IEKP-KA/96-02

Observation of Orbitally Excited B Mesons with the DELPHI Detector at LEP

Christof J. Kreuter

Zur Erlangung des akademischen Grades eines

DOKTORS DER NATURWISSENSCHAFTEN

von der Fakultät für Physik der Universität (TH) Karlsruhe

genehmigte

DISSERTATION

Tag der mündlichen Prüfung:	26.01. 1996
Referent:	*Prof. Dr. W. de Boer*
Korreferent:	*Prof. Dr. Th. Müller*

Diese Arbeit wurde gefördert vom Land Baden-Württemberg.

Abstract

First experimental evidence for the existence of orbitally excited B meson states [1,2] is obtained by investigating the $B\pi$ and $B^*\pi$ Q-value distributions ($Q = m(B^{**}) - m(B^{(*)}) - m(\pi)$) using Z^0 decay data taken with the DELPHI detector at LEP. The mean Q-value of the decays $B^{**} \to B^{(*)}\pi$ is measured to be $283 \pm 5\,(\text{stat.}) \pm 12\,(\text{syst.})$ MeV/c^2. The Gaussian width of the signal is $68 \pm 5\,(\text{stat.}) \pm 8\,(\text{syst.})$ MeV/c^2. The observed shape is consistent with the production of several broad states and several narrow states as predicted by the quark model and HQET, and which have been observed in the D meson sector. The mean mass for B^{**} mesons is extracted to be $5732 \pm 5\,(\text{stat.}) \pm 17\,(\text{syst.})$ MeV/c^2, and the production rate of B^{**} mesons per b-jet is measured to be $0.241 \pm 0.015\,(\text{stat.}) \pm 0.058\,(\text{syst.})$. In addition, the helicity distribution of B^{**} mesons is investigated.

A search is performed for orbitally excited strange B meson states in the decay $B_s^{**} \to B^{(*)}K$. A two-peak structure in the $B^{(*)}K$ Q-value distribution ($Q = m(B_s^{**}) - m(B^{(*)}) - m(K)$) is observed which can be described by the production of the predicted narrow B_s^{**} states B_{s1} and B_{s2}^*. The mass of the B_{s1} state is determined to be $5888 \pm 4\,(\text{stat.}) \pm 8\,(\text{syst.})$ while the mass of the B_{s2}^* state is determined to be $5914 \pm 4\,(\text{stat.}) \pm 8\,(\text{syst.})$. The production rates per b-jet are $0.021 \pm 0.005\,(\text{stat.}) \pm 0.006\,(\text{syst.})$ for the B_{s1} state and $0.016 \pm 0.005\,(\text{stat.}) \pm 0.007\,(\text{syst.})$ for the B_{s2}^* state.

First experimental evidence for the beauty baryons $\Sigma_b^{\pm}$ and $\Sigma_b^{*\pm}$ is presented in an analysis of the $\Lambda_b\pi$ Q-value distribution ($Q = m(\Sigma_b^{(*)}) - m(\Lambda_b) - m(\pi)$). A two-peak structure is observed on top of a flat background which can be described by the production of $\Sigma_b^{\pm}$ and $\Sigma_b^{*\pm}$ baryons. The mean Q-value of the decays $\Sigma_b^{\pm} \to \Lambda_b\pi$ is determined to be $33 \pm 3\,(\text{stat.}) \pm 14\,(\text{syst.})$ MeV/c^2, and that of the decays $\Sigma_b^{*\pm} \to \Lambda_b\pi$ is determined to be $89 \pm 3\,(\text{stat.}) \pm 8\,(\text{syst.})$ MeV/c^2. The production rate of Σ_b and Σ_b^* baryons per b-jet is measured to be $0.048 \pm 0.006\,(\text{stat.}) \pm 0.015\,(\text{syst.})$. The production ratio $\sigma_{\Sigma_b}/(\sigma_{\Sigma_b} + \sigma_{\Sigma_b^*})$ is found to be $0.24 \pm 0.06\,(\text{stat.}) \pm 0.10\,(\text{syst.})$. The helicity angle distribution of the signal identified as Σ_b^* suggests a suppression of the $\pm 3/2$ helicity states.

Contents

List of Figures

List of Tables

Chapter 1

Introduction

The present knowledge of particle physics considers the observed matter in the surrounding nature to be constructed from six different types of quarks and leptons. The quark types are called d, u, s, c, b, and t, the lepton types are called e^-, ν_e, μ^-, ν_μ, τ^-, and ν_τ. Quarks and leptons are fermions with spin 1/2. The fundamental interactions between these particles are understood by the exchange of so-called gauge bosons. The describing theory is known as the Standard Model of particle physics. It basically consists of the following:

The theory of strong interactions which is called Quantum Chromodynamics (QCD) describes the effects of quark interactions. The gauge bosons of the strong interaction, the gluons, have been discovered in three-jet events at the electron-positron ring PETRA[1] at DESY[2]. Since the gluon carries colour charge, this leads to the observed quark-gluon confinement at lower energies. Because of this effect, the theory (QCD) has to be a non-Abelian theory.

The theory of the electro-weak interactions has been developed by Glashow, Salam and Weinberg [3]. It is often called GSW theory. It unifies the first modern gauge theory, Quantum Electrodynamics (QED), which was first constructed by Schwinger and Feynman [4], with the weak interaction which is responsible for radioactive β-decays. This electro-weak theory predicted the existence of three new gauge bosons, the $W^\pm$ and the Z^0. They were discovered in the predicted mass range in 1983 and 1984 in proton-antiproton collisions by the UA1 and UA2 collaborations at CERN[3] [5].

In order to investigate the properties of the electro-weak gauge bosons Z^0 and $W^\pm$ the Large Electron Positron (LEP) collider at CERN has been built. The collider produced in the years 1989-1995 approximately 17 million multi-hadronic Z^0 events from the annihilation of electrons and positrons in resonance at a center of mass energy of $m_{Z^0} = 91.2$ GeV. Four detectors (ALEPH, DELPHI, L3 and OPAL) collected the data from the Z^0 decay products. In a second stage of LEP starting from 1996 the collider is being upgraded to an energy of twice the $W^\pm$ mass, in order to produce $W^\pm$ pairs. In this way the charged electro-weak bosons can be investigated. This second stage of LEP is called LEP200.

[1] PETRA = Positron Electron Tandem Ring Accelerator

[2] DESY = Deutsches Electronen Synchrotron

[3] CERN: Conseil Européen pour la Researche Nucléaire

The produced Z^0 bosons at LEP can decay either into lepton pairs ($Z^0 \to \ell\bar{\ell}$) or into quark antiquark pairs ($Z^0 \to q\bar{q}$), i.e. $d\bar{d}$, $u\bar{u}$, $s\bar{s}$, $c\bar{c}$, and $b\bar{b}$. The Z^0 bosons cannot decay into $t\bar{t}$ pairs, due to the large top quark mass[4]. The studies in this thesis focus on the properties of the lighter b quark. It was discovered in 1977 by the group of L. Lederman in the CFS experiment at Fermilab (Chicago) in proton collisions with a beryllium target [7]. They observed a narrow resonance in the invariant mass spectrum of muon pairs at 9.46 GeV/c^2 ($p + Be \to \mu^+\mu^- + X$). This state was identified as the $1S$ state of the so-called bottomonium system consisting of a $b\bar{b}$ pair. It was named $\Upsilon(1S)$. Later, radial excitations of this system were discovered, e.g. $\Upsilon(2S)$, $\Upsilon(3S)$, $\Upsilon(4S)$, and $\Upsilon(5S)$. Furthermore, states with orbital excitations have been identified, e.g. $h_b(1P)$, $\chi_{b0}(1P)$, $\chi_{b1}(1P)$, and $\chi_{b2}(1P)$. The excitation spectrum of this system was successfully described using QCD-inspired potential models in analogy to the description of positronium.

B mesons are bound states of a b quark and a $\bar{u}$ or $\bar{d}$ quark with spin parity $J^P = 0^-$. In 1983 it was confirmed by CESR, and later at DORIS, that $\Upsilon(4S)$ decays into a pair of $B\bar{B}$ mesons. Several experiments (e.g. ARGUS and CLEO) which study the weak decays of B mesons, run at the $\Upsilon(4S)$ resonance in e^+e^- annihilation. Apart from the ground state B meson with spin parity $J^P = 0^-$, only the B^* meson with $J^P = 1^-$ has been experimentally established. Both states are investigated in $Z^0 \to b\bar{b}$ decays at LEP.

The main goal of this analysis is the search for and first observation of orbitally excited B mesons (commonly labeled as B^{**} mesons) with the DELPHI detector at LEP [1]. The first evidence was obtained in parallel with an independent analysis in the OPAL collaboration [2]. The expected main decay channel of B^{**} mesons is into $B^{(*)}\pi$. The analysis starts with a multi-hadronic event selection. This is followed by the tagging of $b\bar{b}$ events exploiting the long lifetime of the b hadrons of 1.5 ps. The four-vectors of the B or B^* mesons are reconstructed in an inclusive fashion using the hard fragmentation of b hadrons. Since B^{**} mesons decay rapidly through the strong interaction, decay pions originate from the primary vertex and not from a secondary B-decay vertex. Due to the long lifetime of B mesons, the secondary vertex lies on average about 3 mm apart from the primary event vertex. A significant background reduction is achieved by the reconstruction of primary and secondary vertices. The obtained signal is consistent with theoretical expectations for B^{**} states. The helicity distribution of B^{**} mesons is analyzed and a charge analysis is performed. In addition, the B^{**} fragmentation is investigated.

Furthermore, a search for B_s^{**} mesons decaying into $B^{(*)}K$ is performed, exploiting the good kaon identification capabilities of the DELPHI RICH detector. Two narrow signals, consistent with the production of two narrow B_s^{**} states, are extracted from the data [8].

The last part of the analysis is dedicated to a search for the baryons Σ_b and Σ_b^*. Their expected main decay channel is into $\Lambda_b\pi$. The Λ_b is reconstructed in an inclusive fashion. It is combined with pions from the primary vertex. In order to enhance the signal to background ratio, a baryon enrichment is achieved by using proton tagging and Λ reconstruction. First evidence for the existence of the baryons Σ_b and Σ_b^* is extracted from the data [9].

The presented analysis is performed using approximately 3.4 million multi-hadronic Z^0 events taken with the DELPHI Detector at LEP in the years 1991-1994. The results obtained have been published in Refs. [1], [8] and [9]. Some review articles are given in Ref. [10].

[4] The top quark has recently been discovered in proton antiproton collisions by the CDF and D0 collaborations. The CDF collaboration measure a mass for the t quark of $176 \pm 8 \pm 10$ GeV/c^2. The D0 collaboration quote a value of $199^{+19}_{-21} \pm 22$ GeV/c^2 [6].

Chapter 2

The Theoretical Background

This section gives the main theoretical background which is needed for the understanding of the analysis in this thesis. Starting from the static quark model for mesons and baryons, the basic concepts of Quantum Chromodynamics (QCD) are developed. Emphasis is given to the symmetries of QCD. Mainly, *heavy quark* symmetry is discussed, which leads to an effective theory of QCD, the Heavy Quark Effective Theory (HQET).

Then, the four phases of hadron formation in e^+e^- annihilation are described (electroweak phase, perturbative QCD phase, confinement phase, and particle decay phase). This is followed by detailed descriptions of the phenomenology of B meson and b baryon spectroscopy. Lastly, the present experimental status in this field is reviewed.

2.1 The Static Quark Model

Today it is well known that the proton is not an elementary particle, since it consists of three fundamental particles which are called quarks[1]. The name quarks originates from the 1960's when Gell-Mann and Ne'emen [11] discovered symmetries in the spectrum of particles, which lead first to a classification of all known hadrons into meson and baryon octets and baryon decuplet, and later to the proposal of the existence of new fundamental particles, the quarks. At that time the known hadrons could be constructed with the three quark *flavours* up(u), down(d) and strange(s). Today, three more quarks are known: charm(c), bottom(b) and top(t).

Each quark has spin 1/2 and baryon number 1/3. Tab. 2.1 gives the additive quantum numbers (except the baryon number) of the three generations of quarks. The convention is that the flavour of a quark (described by I_3, S, C, B and T) has the *same sign* as the charge. With this convention, any flavour carried by a charged meson has the same sign as its charge; e.g. the strangeness of the K^+ is $+1$, the bottomness of the B^+ is $+1$ and the charm and strangeness of the D_s^- are each -1. By convention, each quark has positive parity. Thus, each antiquark must have negative parity as they are fermions.

[1] Sea quarks and gluons are neglected for the moment.

Property / Quark	d	u	s	c	b	t
Q electric charge	$-\frac{1}{3}$	$+\frac{2}{3}$	$-\frac{1}{3}$	$+\frac{2}{3}$	$-\frac{1}{3}$	$+\frac{2}{3}$
I_3 isospin (3rd component)	$-\frac{1}{2}$	$+\frac{1}{2}$	0	0	0	0
S strangeness	0	0	-1	0	0	0
C charm	0	0	0	$+1$	0	0
B bottomness	0	0	0	0	-1	0
T topness	0	0	0	0	0	$+1$

Table 2.1: *Additive quantum numbers of the quarks. The u and d quarks belong to the first family, the s and c quarks to the second family, and the b and t quarks to the third family.*

2.1.1 Mesons: $q\bar{q}$ states

Nearly all known mesons are bound states of a quark q and an antiquark $\bar{q}'$ (the flavours of q and q' can be different). If the orbital angular momentum of the $q\bar{q}'$ system is L, then the parity P is $(-1)^{L+1}$. A state $q\bar{q}$ of a quark and its own antiquark is also an eigenstate of charge conjugation, with $C = (-1)^{L+S}$, where the total spin S is 0 or 1. The $L = 0$ states are the pseudoscalars ($J^P = 0^-$), and the vectors ($J^P = 1^-$). According to this, states in the normal spin-parity series, $P = (-1)^J$, must have $S = 1$ and hence $CP = +1$. That means that mesons with normal spin-parity and $CP = -1$ are forbidden in the $q\bar{q}'$ model. The $J^{PC} = 0^{--}$ state is forbidden as well. Mesons with such J^{PC} values would lie outside the additive quark model [12].

For fixed J^{PC} nine possible $q\bar{q}'$ combinations containing u, d and s quarks group themselves into an octet and a singlet according to SU(3) symmetry:

$$\mathbf{3} \otimes \bar{\mathbf{3}} = \mathbf{8} \oplus \mathbf{1} \ . \tag{2.1}$$

States with the same IJ^P (I = Isospin) and the same additive quantum numbers can mix. If they are eigenstates of charge conjugation, they must also have the same value of C. As an example consider the $I = 0$ member of the ground-state pseudoscalar octet η_8. It mixes with the corresponding pseudoscalar singlet η_1 to produce the η and η' mesons. They appear as members of a nonet which is shown as the middle plane of Fig. 2.1(a). The heavier charm and bottom quarks can be included in this scheme by extending the symmetry to SU(5). The significant mass differences between the various flavour states indicate that this symmetry is badly broken. Fig. 2.1 shows the SU(4) sub-group of the pseudoscalar and vector mesons made of u, d, s and b quarks. The drawing of the full SU(5) multiplets would require four dimensions.

All the mesons shown (except the η_b) have been observed experimentally. The work of this thesis is mainly devoted to B meson spectroscopy. The present experimental status in this field as well as the theoretical background of B meson ground states and excited states is discussed in detail in section 2.4.

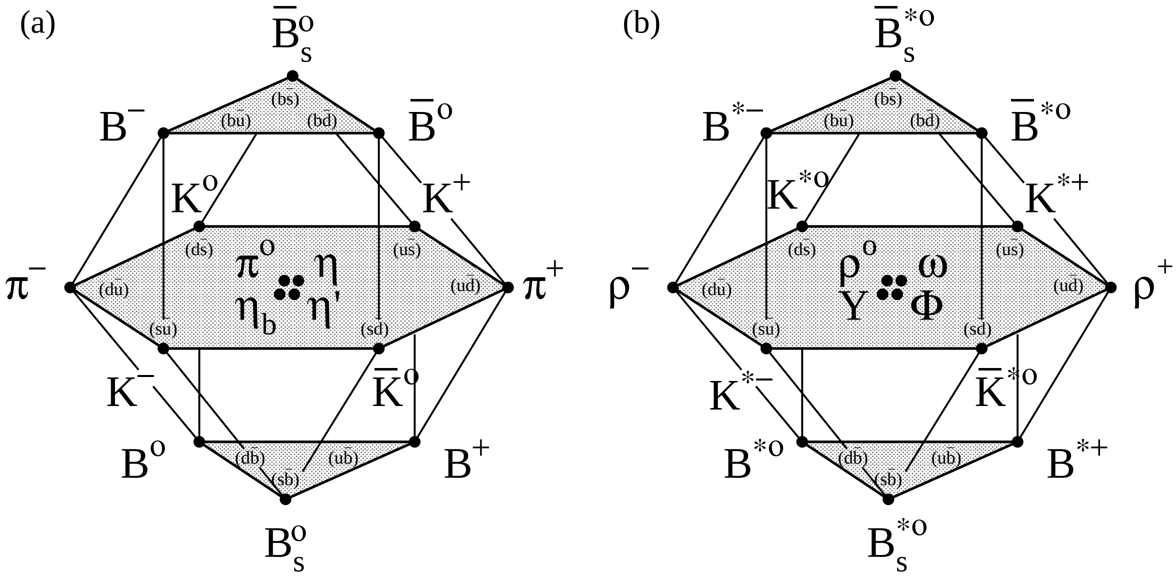

Figure 2.1: *SU(4) 16-plets for (a) pseudoscalar and (b) vector mesons made of u, d, s, and b quarks. The nonets of the light mesons occupy the central planes, to which the $b\bar{b}$ have been added. The neutral mesons at the centers of these planes are mixtures of $u\bar{u}$, $d\bar{d}$, $s\bar{s}$ and $b\bar{b}$. States involving the c quark are not shown.*

2.1.2 Baryons: qqq states

All the established baryons are 3-quark (qqq) states, and each such state is a SU(3) colour singlet, a completely antisymmetric state of the three possible colours. Since the quarks are fermions, the state function for any baryon must be antisymmetric under interchange of any two equal-mass quarks (up and down quarks in the limit of isospin symmetry). Thus, the state function can be written as:

$$|qqq\rangle_A = |\text{colour}\rangle_A \times |\text{space, spin, flavour}\rangle_S \ , \tag{2.2}$$

where the subscripts S and A indicate symmetry or antisymmetry under the interchange of any two of the equal-mass quarks.

The "ordinary" baryons are made up of u, d and s quarks. Assuming an approximate flavour SU(3) symmetry for the three flavours, implies that baryons made of these quarks belong to the multiplets on the right side of

$$\mathbf{3} \otimes \mathbf{3} \otimes \mathbf{3} = \mathbf{10_S} \oplus \mathbf{8_M} \oplus \mathbf{8_M} \oplus \mathbf{1_A} \ . \tag{2.3}$$

Here the subscripts indicate symmetric, mixed-symmetry, or antisymmetric states under interchange of any two quarks. Including the c and b quarks in addition to the light quarks would extend the flavour symmetry to the badly broken SU(5) symmetry. Again, it would require four dimensions to draw the multiplets of SU(5). The Figures 2.2 (a) and 2.2 (b) show the multiplets containing only u, d, s and b quarks (SU(4) sub-group). All the particles in a given multiplet have the same spin and parity ($J^P = 1/2^+$ for Fig. 2.2 (a) and $J^P = 3/2^+$ for Fig. 2.2 (b)). The *ground floors* of the shown multiplets represent the SU(3) octet that

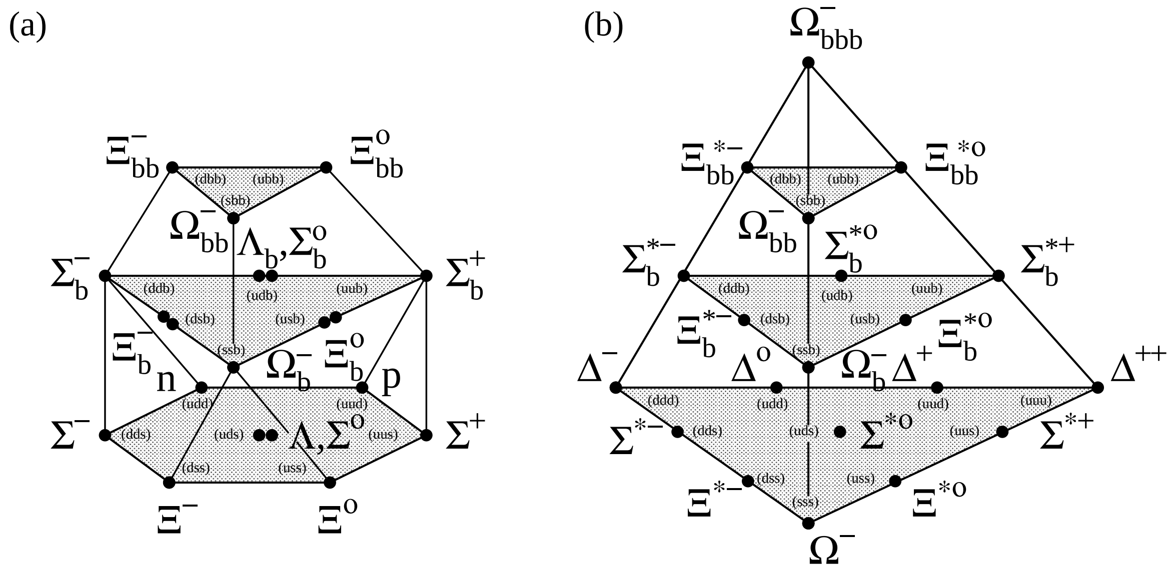

Figure 2.2: *SU(4) multiplets of baryons made of u, d, s and b quarks. (a) The 20-plet with a SU(3) octet. (b) The 20-plet with a SU(3) decuplet.*

contains the nucleon, and the SU(3) decuplet that contains the $\Delta(1232)$. All these particles have been observed in former experiments. Most of the baryons containing a b quark are not yet established experimentally apart from the Λ_b and the Ξ_b. Parts of this thesis will focus on the search for the charged Σ_b and Σ_b^* baryon.

2.2 Quantum Chromodynamics

The static quark model successfully describes symmetries and quantum numbers of the known hadrons. It cannot explain why mesons ($q\bar{q}$) and baryons (qqq) are the only bound states. Other combinations of q and $\bar{q}$ are possible as well in this model but are not observed in nature[2]. Inspired by this mystery a dynamical model for the strong interaction was developed, called Quantum Chromodynamics (QCD).

2.2.1 The QCD Lagrangian

Quantum Chromodynamics (QCD), the gauge field theory which describes the strong interactions of coloured quarks and gluons, is one of the components of $SU(3)_C \times SU(2)_L \times U(1)_Y$, called the Standard Model. As already mentioned in section 2.1.2, a quark of specific flavour (such as the bottom quark) can have any one of three colours: often called *red*(r), *green*(g), or *blue*(b). The gluons span the $3 \times \bar{3}$ colour space, which would lead to nine different types of

[2] This statement is true, although some exotic states are known which do not fit easily in the meson / baryon picture. E.g. the $a_0(980)$ is interpreted as $K\bar{K}$ molecule by some authors.

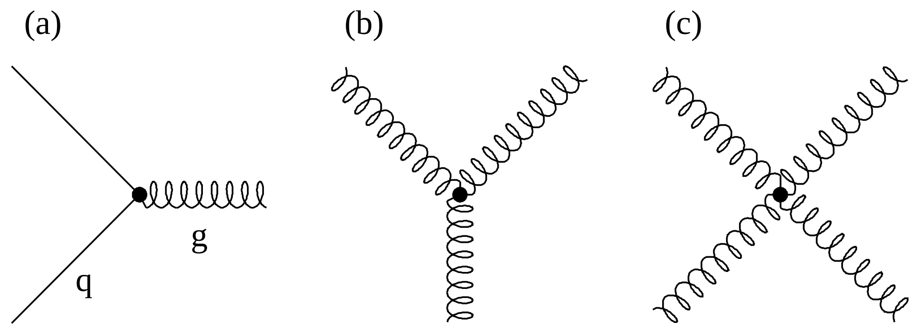

Figure 2.3: *The Feynman graphs of the fundamental processes of QCD. (a) quark-gluon-interaction (b) triple-gluon-vertex (c) 4-gluon-vertex.*

gluons. However, according to SU(3) symmetry[3], these nine states decompose into an octet

$$r\bar{g},\ r\bar{b},\ g\bar{r},\ g\bar{b},\ b\bar{r},\ b\bar{g},\ (r\bar{r}-g\bar{g})/\sqrt{2},\ (r\bar{r}+g\bar{g}-2b\bar{b})/\sqrt{6} \tag{2.4}$$

and a singlet

$$(r\bar{r}+g\bar{g}+b\bar{b})/\sqrt{3}\ . \tag{2.5}$$

Note that the singlet combination does not carry net colour, and therefore it does not transmit any colour. The eight other gluons involve the net transmission of colour. Hadrons are colour-singlet combinations of quarks, antiquarks and gluons.

The Lagrangian of QCD (up to gauge fixing terms) is given by this formula [12]

$$\mathcal{L}_{QCD} = i\sum_q \bar{\psi}_q^i \gamma^\mu (D_\mu)_{ij} \psi_q^j - \sum_q m_q \bar{\psi}_q^i \psi_{qi} - \frac{1}{4} F_{\mu\nu}^{(a)} F^{(a)\mu\nu}\ , \tag{2.6}$$

with

$$F_{\mu\nu}^{(a)} = \partial_\mu A_\nu^a - \partial_\nu A_\mu^a + g_s f_{abc} A_\mu^b A_\nu^c\ , \tag{2.7}$$

and

$$(D_\mu)_{ij} = \delta_{ij}\partial_\mu - i g_s \sum_a \frac{\lambda_{ij}^a}{2} A_\mu^a\ , \tag{2.8}$$

where g_s is the QCD coupling constant, and the f_{abc} are the structure constants of the SU(3) algebra. The λ_{ij}^a are known as Gell-Mann matrices. The $\psi_q^i(x)$ are the 4-component Dirac spinors associated with each quark field of colour i and flavour q. The $A_\mu^a(x)$ are the eight Yang-Mills (gluon) fields. The first term in the Lagrangian is the *kinetic* term, the second term corresponds to the *mass* term, and the third term is known as the *field* term. This form of the Lagrangian leads to the three fundamental processes of QCD: the quark-gluon-interaction, the triple-gluon-vertex and the 4-gluon-vertex. The Feynman graphs of these processes are shown in Fig. 2.3.

2.2.2 The Running Coupling Constant α_s

Calculations in lowest order perturbation theory have finite results. Higher order calculations of Feynman diagrams are divergent and would lead to unphysical results. In order to obtain

[3] $3 \otimes \bar{3} = 8 \oplus 1$

finite physical values one has to perform a regularization and renormalization procedure. This leads to the result that the effective QCD coupling constant $\alpha_s = g_s/4\pi$ is not constant but depends on an energy scale μ. The renormalization scale dependence of the effective QCD coupling α_s is described by the Renormalization Group Equation (RGE):

$$\mu\frac{\partial \alpha_s}{\partial \mu} = -\frac{\beta_0}{2\pi}{\alpha_s}^2 - \frac{\beta_1}{4\pi^2}{\alpha_s}^3 - \frac{\beta_2}{64\pi^3}{\alpha_s}^3 - \dots \; . \tag{2.9}$$

The β functions contain some QCD intrinsic coefficients:

$$\beta_0 = 11 - \frac{2}{3}n_f \; , \tag{2.10}$$

$$\beta_1 = 51 - \frac{19}{3}n_f \; , \tag{2.11}$$

$$\beta_2 = 2857 - \frac{5033}{9}n_f - \frac{325}{27}n_f^2 \; , \tag{2.12}$$

where n_f is the number of quark flavours with mass less than the energy scale μ. In solving this differential equation for α_s, a constant of integration is introduced. This constant is the one fundamental constant of QCD that must be determined from experiment. The most sensible choice for this constant is the value of α_s at a fixed reference scale μ_0 (e.g. $\mu_0 = m_{Z_0}$), but it is more conventional to introduce the dimensional parameter Λ_{QCD} since this provides a parametrization of the μ dependence of α_s. The definition of Λ_{QCD} is arbitrary. One way of defining it is to write the solution of Eq. 2.9 as an expansion in inverse powers of $\ln(\mu^2)$. The solution to first order is:

$$\alpha_s(\mu) = \frac{4\pi}{\beta_0 \cdot \ln(\mu^2/\Lambda^2_{QCD})} \; . \tag{2.13}$$

The solution illustrates the property of *asymptotic freedom*, i.e. that $\alpha_s \rightarrow 0$ as $\mu \rightarrow \infty$. From this equation it can also be seen, that α_s reaches infinity at the scale Λ_{QCD}. The increase of α_s at small scales μ reflects the *confinement* property of QCD. This behaviour of α_s is remarkably different from the behaviour in QED, where a decrease of the coupling constant α with the scale μ is observed. Fig. 2.4 illustrates the one-loop contribution to the vacuum polarisation in QCD. In contrast to QED, gluons also participate in these loops, which leads to an increase in α_s with decreasing scale μ. This property reflects the non-Abelian character of QCD. The solution of the RGE in second order gives [12]:

$$\alpha_s(\mu) = \frac{4\pi}{\beta_0 \cdot \ln(\mu^2/\Lambda^2_{QCD})} \cdot \left[1 - \frac{2\beta_1}{\beta_0^2}\frac{\ln[\ln(\mu^2/\Lambda^2_{QCD})]}{\ln(\mu^2/\Lambda^2_{QCD})}\right] \; . \tag{2.14}$$

2.2.3 Symmetries in QCD

There are very few cases in which it is possible, using analytic methods, to make systematic predictions based on QCD in the low-energy nonperturbative regime. In fact, QCD has been shown to be so intractable to analytic methods, that all such predictions are based not on dynamical calculations, but on some symmetry of QCD.

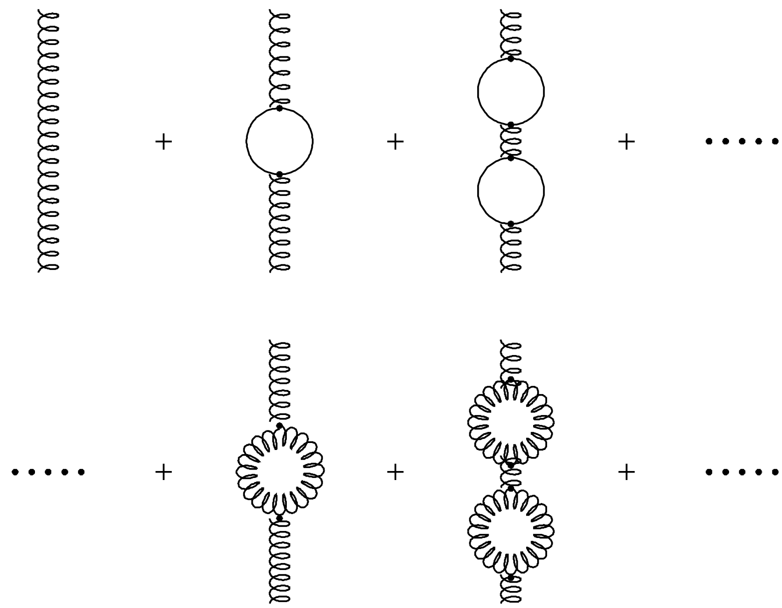

Figure 2.4: *One-loop contribution to the vacuum polarisation. All strong interacting particles can participate in these loops. In contrast to QED there are also contributions from gluons.*

Isospin Symmetry: Isospin symmetry was the first such symmetry discovered. It is now understood as an approximate symmetry which arises because the light quark mass difference $m_d - m_u$ is much smaller than the mass associated with confinement, which is set by the scale Λ_{QCD}. The predictions based on isospin symmetry would, in a world with only strong interactions, be exact in the limit $m_d - m_u \to 0$. Corrections to this limit can be studied in an expansion in the small parameter $(m_d - m_u)/\Lambda_{QCD}$. SU(3) flavour symmetry is similar, but the corrections are larger since $(m_s - m_u)/\Lambda_{QCD}$ is not small.

Chiral Symmetry: Chiral symmetry $SU(2)_L \times SU(2)_R$ arises in QCD because both m_d and m_u are small compared to Λ_{QCD}. It is associated with the separate conservation of vector and axial vector currents. Although spontaneously broken in nature, the existence of this underlying symmetry allows the expansion of chiral perturbation theory in which many low-energy properties of QCD are related to a few reduced matrix elements. If the strange quark is also treated as small compared to Λ_{QCD}, then the chiral symmetry group becomes $SU(3)_L \times SU(3)_R$.

Heavy Quark Symmetry: Over the last years there has been progress in understanding systems containing a single heavy quark. The mass m_Q of the heavy quark is much greater than the scale Λ_{QCD} of the strong interaction. It was discovered that there is a new symmetry of QCD, similar to isospin and chiral symmetry, in the behaviour of such systems. This symmetry arises because once a quark becomes sufficiently heavy, its mass becomes irrelevant to the nonperturbative dynamics of the light degrees of freedom of QCD. This symmetry is called heavy quark symmetry and the underlying theory is known as Heavy Quark Effective Theory (HQET) [13].

2.2.4 Heavy Quark Symmetry

The most important predictions from heavy quark effective theory are for semileptonic B-meson decay form-factors. These play an important role in the accurate determination of the values of the Cabibbo-Kobayashi-Maskawa[4] matrix elements V_{cb} and V_{ub} from experimental data. The properties of hadrons containing a single heavy quark have been studied since a long time using phenomenological models. Now it is understood, that this physics arises from symmetries of an effective theory that is a systematic limit of QCD. Consequently, model independent predictions are possible using HQET.

Heavy Flavour Symmetry

As an extreme example consider two very heavy quarks of masses one and ten kilograms. Although these quarks will live in the usual hadronic sea of light quarks and gluons, they will hardly notice it. Their motion will suffer only slight fluctuations compared to the motion of a free heavy quark. Such quarks define with great precision their own center of mass system. Therefore, hadronic systems containing a heavy quark can be studied in the frame where the heavy quark acts as static source of colour localized at the origin. The equations of QCD in the neighborhood of such an isolated heavy quark are therefore those of the light quarks and gluons with the boundary condition that there is a static triplet source of colour-electric field at the origin. Since the boundary condition is essentially the same for both of our hypothetical heavy quarks, the solutions for the states of the light degrees of freedom in their presence will be the same. Thus, the light degrees of freedom will be symmetric under an isospin-like rotation of the heavy quark flavour into one another even if the quark masses are not almost equal[5]. In particular, the heavy *meson* and *baryon* excitation spectra built on any heavy quark will be the same.

Heavy Spin Symmetry

The preceding discussion ignored the spin of the heavy quark. This is appropriate in QCD since the spin of the heavy quark decouples from the gluonic field, i.e. all heavy quarks look like scalar heavy quarks to the light degrees of freedom. Since the flavour and spin of a heavy quark are irrelevant, the static heavy quark symmetry is actually $SU(2N_h)$, where N_h is the number of heavy quarks. At the spectroscopic level this additional symmetry means that each spectral level built on a heavy quark (unless the light degrees of freedom combine to spin zero) will be a degenerate doublet in total spin.

Heavy flavour symmetry is analogous to the fact that the different isotopes of a given element have the same chemistry, i.e. their electronic structure is almost identical because they have the same nuclear charge. The spin symmetry is analogous to the near degeneracy of hyperfine levels in atoms and the electronic structure of the states of a hyperfine multiplet are almost the same because nuclear magnetic moments are small.

[4] The Cabibbo-Kobayashi-Maskawa (CKM) matrix is the quark mixing matrix of the weak interactions [12].

[5] In first approximation hadronic states containing a c or a b quark are treated in that way. The t quark with its mass around 180 GeV/c^2 would form an almost ideal heavy quark system. Unfortunately it decays rapidly through the weak interaction before the hadronisation takes place ($t \rightarrow Wb$).

The Effective Theory

In the situation described above where the light degrees of freedom typically have four-momenta small compared with the heavy quark mass, it is appropriate to go over to an effective theory where the heavy quark mass goes to infinity, with its four-velocity fixed. The heavy quark path is a straight world-line described by a four-velocity v^μ satisfying $v^2 = 1$. The $SU(2N_h)$ spin-flavour symmetry of the heavy quark effective theory is not present in the full theory of QCD. It becomes apparent only in the effective theory where the heavy quark masses are taken to infinity. The situation is very similar to the chiral symmetry which is only apparent in the limit where the light quark masses are taken to zero. Perturbations to the predictions from heavy quark effective theory with $m_Q \to \infty$ can be calculated in powers of Λ_{QCD}/m_Q.

One can derive the Feynman rules for the effective theory by taking the above limit of the Feynman rules for QCD. In the full theory of QCD the heavy quark propagator is

$$\frac{i(\gamma_\mu p_Q^\mu + m_Q)}{p_Q^2 - M_Q^2} \ . \qquad (2.15)$$

In order to go over to the effective theory, we write $p_Q^\mu = m_Q v^\mu + k^\mu$, where k^μ is a residual momentum that is small compared to the heavy quark mass. In the limit $m_Q \to \infty$ the heavy quark propagator becomes [14]

$$\frac{i}{v \cdot k} \ . \qquad (2.16)$$

Furthermore, in the full theory of QCD the vertex for heavy quark-gluon interaction is

$$-ig_s \gamma_\mu \lambda^a \ , \qquad (2.17)$$

where g_s is the strong coupling constant and λ^a are the SU(3) colour generators (Gell-Mann matrices). For the vertex in the effective theory one obtains [14]

$$-ig_s \lambda^a v_\mu \ . \qquad (2.18)$$

In this derivation factors of $(\gamma^\mu v_\mu + 1)/2$ in the numerators of propagators and in vertex definitions have been moved to the outside of any Feynman graph, where they give unity when acting on the on-shell spinors $u(v, s)$. Equations 2.16 and 2.18 can be taken as definitions of the effective heavy quark theory.

A different but equivalent approach starts from the QCD Lagrangian (Eq. 2.6). The heavy quark spinor with velocity v (as an approximation for $m_Q \to \infty$) can be written as [14]

$$\psi_Q = e^{-im_q v \cdot x} h_Q^{(v)} \ , \qquad (2.19)$$

where the field $h_Q^{(v)}$ is constrained to satisfy

$$\gamma^\mu v_\mu h_Q^{(v)} = h_Q^{(v)} \ . \qquad (2.20)$$

Inserting this in Eq. 2.6 leads to the Lagrangian of heavy quark effective theory [14]:

$$\mathcal{L}_{HQET} = i\bar{h}_Q^{(v)i} v^\mu (D_\mu)_{ij} h_Q^{(v)j} - \frac{1}{4} F_{\mu\nu}^{(a)} F^{(a)\mu\nu} \ . \qquad (2.21)$$

For simplicity the Lagrange density is given for a system containing just one heavy quark. The effective Lagrangian 2.21 reproduces the Feynman rules in Eqs. 2.16 and 2.18. The heavy quark effective theory has symmetries which are not manifest in the Lagrangian of QCD. Since there is no pair creation in the effective theory, there is a U(1) symmetry of the effective Lagrangian associated with heavy-quark conservation. Since gamma matrices no longer appear in the gluon/heavy-quark interaction, the spin of the heavy quark is conserved. Associated with this is a SU(2) symmetry group of the Lagrangian in Eq. 2.21.

2.2.5 Potential Models

The quark potential model is the most successful tool enabling physicists to calculate masses and properties of mesons and baryons. However, potential models suffer from the fact that, although motivated by QCD, so far they have not been derived from basic theory. The most general non-relativistic ansatz for a quark-antiquark system (with masses m_1 and m_2) leads to the *Breit-Fermi Hamilton function* [15]:

$$H = \frac{\vec{p}^{\,2}}{2\mu} + V + H_{LS} + H_{SS} + H_T \ . \tag{2.22}$$

The first term represents the kinetic energy with $\mu = m_1 m_2/(m_1+m_2)$. The specific potential model enters in V, which usually contains an *attractive* and a *repulsive* term. The remaining terms reflect the couplings between total spin $\vec{S}$ and orbital angular momentum $\vec{L}$, and the coupling between the quark spins S_1 and S_2. H_T is known as tensor term[6]. Some examples for frequently used potential models are given below. The different models have certain domains of applicability.

Authors	Potential
Eichten [16]	$V = -\frac{4}{3}\frac{\alpha_s}{r} + ar$
Quigg, Rosner [17]	$V = a\ln(r/r_0)$
Martin [18]	$V = A + Br^{0.1}$
Buchmüller [19]	$V = -\frac{4}{3}\frac{1}{(2\pi)^3}\int d^3q \exp(i\vec{q}\vec{r})\frac{4\pi\alpha_s(\vec{q}^{\,2})}{\vec{q}^{\,2}}$

The energy levels of a quark-antiquark system can be calculated by solving the eigenvalue equation

$$H|\psi\rangle = E|\psi\rangle \ , \tag{2.23}$$

where E is the energy level and $|\psi\rangle$ the wave-function of the state. In the early times of potential models, spectroscopy was very successful in heavy quark systems e.g. charmonium($c\bar{c}$) or bottomonium($b\bar{b}$), since non-relativistic approaches were justified[7]. Then, the spin dependent terms in the Hamilton function can be treated by perturbation theory. For light mesons a non-relativistic approach cannot be justified[8]. Furthermore, perturbation theory for the spin

[6] Explicit expressions for these terms can be found in Ref. [15].

[7] Describing the charmonium system with a potential of type $V = -\frac{4}{3}\frac{\alpha_s}{r} + ar$ leads to $v^2/c^2 \simeq 0.4$. The bottomonium system will be even less relativistic.

[8] The non-relativistic approach in light meson systems is normally only justified by its phenomenological success.

dependent terms cannot be used, since e.g. spin-spin effects cannot be treated as small. The importance of spin-spin effects can be seen in the $\rho - \pi$ system, where the pion with spin 0 ($\uparrow\downarrow$) has a mass of 140 MeV/c^2 and the ρ meson with spin 1 ($\uparrow\uparrow$) has a mass of 770 MeV/c^2.

An interesting application of potential models is to study the difference of the squared masses between spin singlet and triplet states $\Delta m^2 = m^2(^3S_1) - m^2(^1S_0)$. From experiment one finds nearly constant values for $\Delta m^2(\rho/\pi) = 0.57\text{GeV}^2$, $\Delta m^2(K^*/K) = 0.55\text{GeV}^2$, $\Delta m^2(D^*/D) = 0.55\text{GeV}^2$, $\Delta m^2(D_s^*/D_s) = 0.58\text{GeV}^2$ and $\Delta m^2(B^*/B) = 0.55\text{GeV}^2$ [12]. Potential models predict $\Delta m^2 = 32/9\alpha_s\langle\partial V/\partial r\rangle$ [15]. Demanding the result to be mass independent (as motivated by observation), and by using a potential of type $V = -\frac{4}{3}\frac{\alpha_s}{r} + ar$ leads to $\Delta m^2 \simeq 32/9\alpha_s a$. This means that the light quarks in this systems mainly feel the linear term of the potential. From this the strong coupling constant is extracted to be $\alpha_s \simeq 0.6$.

For practical calculations it is sometimes useful to know how the energy of a state changes with a parameter λ. This means that one is interested in the derivative of the energy with respect to the parameter λ. This leads to the so-called *Feynman-Hellmann-Theorem*

$$\frac{\partial E(\lambda)}{\partial\lambda} = \langle\psi|\frac{\partial H(\lambda)}{\partial\lambda}|\psi\rangle \ . \tag{2.24}$$

The proof of this theorem can be found in Ref. [15]. If we consider e.g. a linear potential

$$H = \frac{\vec{p}^2}{2\mu} + ar \ , \tag{2.25}$$

the Feynman-Hellman-Theorem leads to

$$\frac{\partial E(a)}{\partial a} = \langle r\rangle \ . \tag{2.26}$$

Since the right side of the equation is always positive, it is evident that the energy rises with increasing parameter a.

2.3 From Quarks to Hadrons

The formation of hadrons from highly energetic quarks is theoretically not understood in all details. A combined model consisting of exactly calculable parton[9] cross sections, phenomenological algorithms and a variety of experimentally known hadron-decay properties is used to describe the evolution of a multi-hadronic Z^0 decay.

The model can be divided into four time ordered phases which are schematically shown in Fig. 2.5. The process starts with e^+e^- annihilation into the strongly interacting quark and antiquark. Phase I (in Fig. 2.5) is governed by the electroweak force. Phase II is the phase of small-distance strong interactions which is calculable exactly in perturbative QCD. Phase III is the domain of long-distance strong interaction (linear confinement) and hadron formation. Due to the large strong coupling constant α_s no perturbative calculations are possible for this period. Phase IV is the era in which the primary hadron resonances, formed in phase III, decay into the final state particles (hadrons, leptons, photons) which are observable in the detector.

[9] Quarks and gluons are partons.

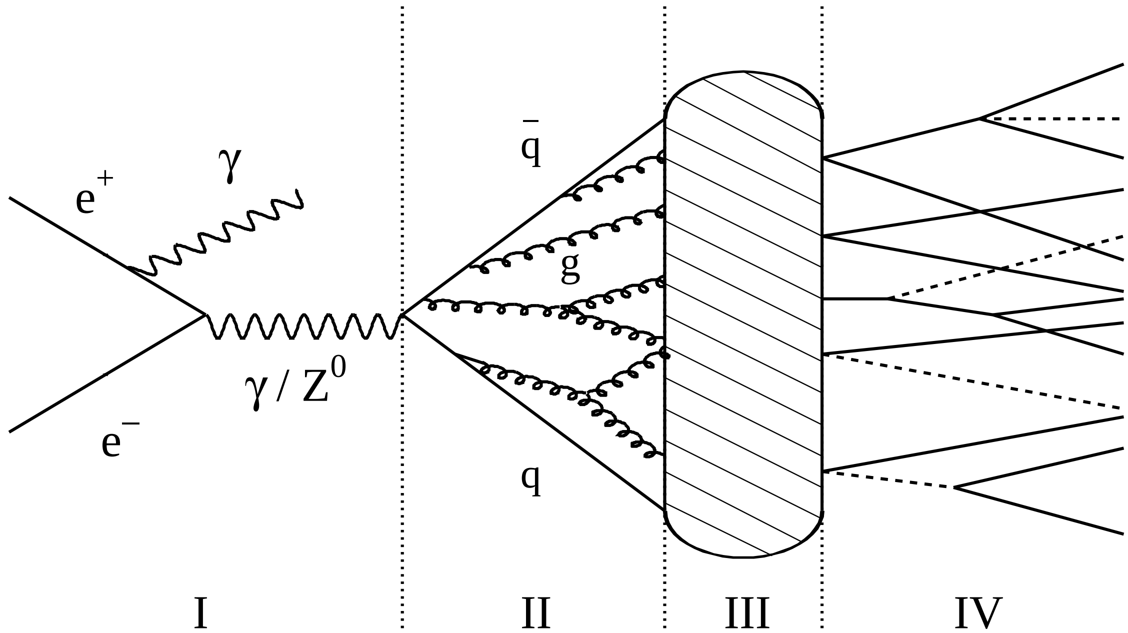

Figure 2.5: *The four phases of e^+e^- annihilation: I. electro-weak phase with initial state radiation, II. perturbative QCD phase with gluon radiation off the leading quarks, III. confinement phase where colour singlet hadrons emerge and IV. decay into final state particles.*

2.3.1 The Electroweak Phase

The first phase in e^+e^- annihilation is governed by the Standard Model of electroweak interactions, which has been developed by Glashow, Salam and Weinberg [3]. It is often called GSW theory[10]. For QCD studies at LEP the process $e^+e^- \to q\bar{q}$ is of main importance. In first order (Born approximation), this process is described by the exchange of a photon or a Z^0 boson. By neglecting fermion masses the total cross section can be derived as [20]:

$$\begin{aligned}\sigma(e^+e^- \to q\bar{q}) = N_C \cdot \frac{4\pi}{3} \cdot \frac{\alpha^2}{s} \quad & \cdot \quad [Q_e^2 \cdot Q_q^2 \\ & + \quad (V_e^2 + A_e^2) \cdot (V_q^2 + A_q^2) \cdot |\chi|^2 \\ & + \quad 2Q_eQ_qV_eV_q \cdot Re(\chi)] \;, \end{aligned} \tag{2.27}$$

where

$$\chi = \frac{1}{4\sin^2\theta_w \cdot \cos^2\theta_w} \cdot \frac{s}{s - M_Z^2 + iM_Z\Gamma_Z} \;. \tag{2.28}$$

The first term originates from γ exchange, the second from Z^0 exchange and the third from γ/Z^0 interference. $V_f = I_{3f} - 2Q_f\sin^2\theta_w$ and $A_f = I_{3f}$ are the vector and axial vector couplings of the fermions to the Z^0, where $\sin^2\theta_w$ is known as the *weak mixing* angle. The fine structure constant is $\alpha = e^2/4\pi$ and $N_C = 3$ is the number of colours. Fig. 2.6 shows

[10] Details on this theory can be extracted from many standard textbooks.

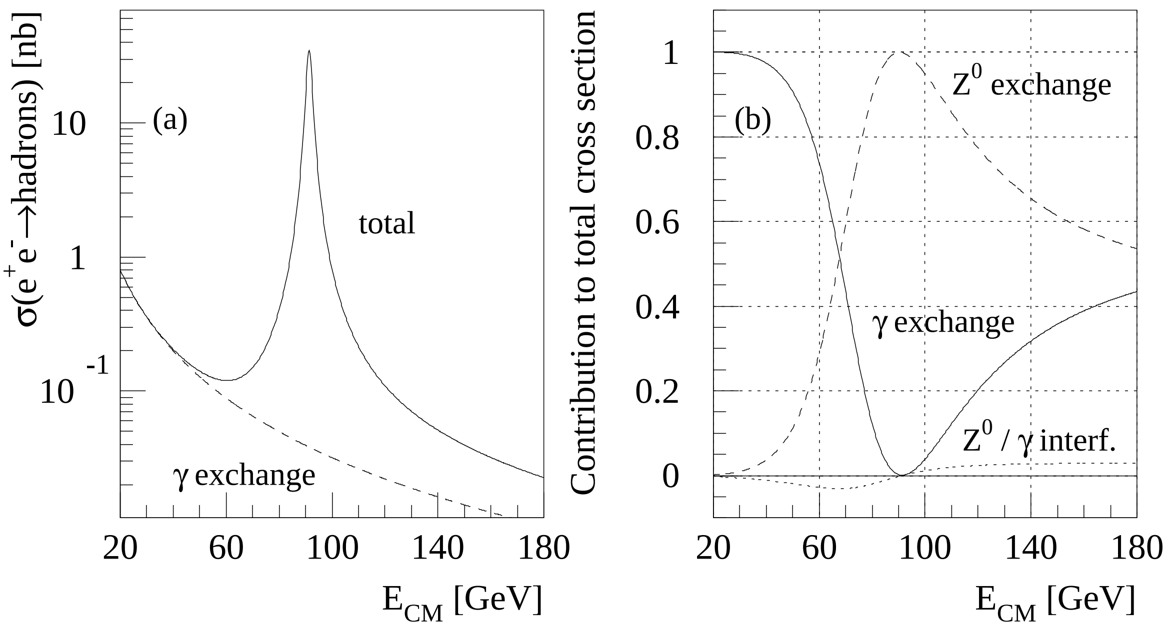

Figure 2.6: *Hadron production in e^+e^- annihilation. (a) The total hadronic cross section as a function of center of mass energy E_{CM}. (b) The relative contributions of γ, Z^0 exchange and γ/Z^0 interference to the total hadronic cross section.*

the total cross section for hadron production in Born approximation as a function of center of mass energy, as well as the relative contributions of γ/Z^0 exchange and interference term to the total cross section. At a center of mass energy, which corresponds to the Z^0 mass (91.2 GeV), the Z^0 exchange dominates completely.

Formula 2.27 is modified by electro-weak and strong interaction corrections of higher order. These are partly virtual corrections (vertex and propagator corrections), and partly radiative corrections of photons in the initial and final state and gluons in the final state. The latter will be discussed in the next section.

Furthermore, the Standard Model provides predictions for the partial widths of the Z^0 boson [12]:

$$Br(Z^0 \to e^+e^-, \mu^+\mu^-, \tau^+\tau^-) \simeq 10.1\% \quad (2.29)$$

$$Br(Z^0 \to \nu\bar{\nu}) \simeq 20.1\% \quad (2.30)$$

$$Br(Z^0 \to q\bar{q}) \simeq 69.8\% \,. \quad (2.31)$$

The produced neutrinos will not be observed in the detector, while the other decays are experimentally accessible. Roughly 22.1% of the hadronic Z^0 decays will go into $b\bar{b}$ pairs. The study of these events is the subject of this thesis.

2.3.2 The Perturbative Phase

Two perturbative approaches are commonly used to calculate the quark and gluon cross sections in phase II. The first method is the complete second order QCD matrix element (ME) calculation, and the second is the parton shower (PS) approach in leading log approximation.

QCD Matrix Elements

The Born term annihilation process $e^+e^- \rightarrow q\bar{q}$ is modified through the possible gluon radiation off coloured quarks. The exact cross section in second order α_s for three-parton final states ($e^+e^- \rightarrow q\bar{q}g$) has been calculated by several groups [21]. Two of these ME calculations are available in the JETSET program [22]. The four-parton final states ($e^+e^- \rightarrow q\bar{q}gg$ or $e^+e^- \rightarrow q\bar{q}q\bar{q}$) cross section in second order α_s contain just the tree level diagrams. With the total cross sections known from the optical theorem, the two-parton cross section follows from a unitarity argument, once the three and four jet cross sections are calculated by direct Feynman graph techniques. Thus, the ME calculation is able to describe two-, three- and four-parton final states i.e. cross sections for the processes $e^+e^- \rightarrow q\bar{q}$, $e^+e^- \rightarrow q\bar{q}g$, $e^+e^- \rightarrow q\bar{q}q\bar{q}$ and $e^+e^- \rightarrow q\bar{q}gg$.

Parton Shower Model

In order to calculate multi-parton final states a vast number of Feynman diagrams has to be considered. An alternative to these excessive calculations is available in terms of the leading logarithm approximation. In this approach only the leading terms of the perturbative expansion are kept, thus neglecting non-leading terms. The parton shower model (PS) is based on the picture of a time ordered cascade of subsequent splitting processes of the partons ($q \rightarrow qg$, $g \rightarrow q\bar{q}$ and $g \rightarrow gg$). The allowed splittings coincide with the $O(\alpha_s)$ vertices which are displayed in Fig. 2.3. Instead of calculating a single transition amplitude $A(e^+e^- \rightarrow q\bar{q}ggq\bar{q}ggg...)$, two primary quarks are produced according to a modified electroweak muon cross section [23] including initial state radiation. Then, the (massless) quarks are assumed to be at rest and thus completely off shell (maximal virtuality: $Q^2 = -m_q^2 = s/2$). During the following chain of incoherent parton splittings the probability $\mathcal{P}_{a\rightarrow bc}$ for a branching $a \rightarrow bc$ results from *splitting functions* which are taken from the Altarelli-Parisi equations [24].

The main difference between ME and PS lies in the fact that ME cannot take into account higher order effects since it is restricted to a maximal number of four partons. PS produces multi-gluon events with an average of nine (comparably soft) gluons per Z^0 event.

2.3.3 The Fragmentation Phase

The formation of bound state systems from quarks and gluons cannot be calculated with perturbative techniques (even if all higher orders could be obtained easily), because of the large coupling constant if Q^2 is of the order of Λ_{QCD}^2. Therefore, the hadronisation is described by QCD motivated phenomenological models. The commonly used models are *independent, string* and *cluster* fragmentation, which are discussed in this section. Emphasis is given to the string fragmentation model, since the standard DELPHI Monte Carlo generator is based on that [22].

Independent Fragmentation

One of the first fragmentation models was the so-called independent fragmentation model [25]. The ansatz assumes that every parton fragments into hadrons independently of the other partons in the event. The algorithm is based on an iterative ansatz in which the available energy is divided in a branching according to a longitudinal splitting function. The iteration stops when the remaining energy is below a certain cutoff energy $\mathcal{E}_{IF}$, which is typically above the pion mass. The fragmentation is performed in the center of mass frame of the whole process. Therefore, the independent fragmentation model is not Lorentz invariant. Also, the remaining energy of each individual jet has to be balanced at the end of each fragmentation procedure.

String Fragmentation

The simplest version of string fragmentation [26] starts with a pair of massless quarks and antiquarks moving in opposite directions with $v = c$. The self coupling of the gluons leads to a linear field configuration of typical size of 1 fm, which is spanned between the quarks. This object is called *string*. The idea originates from the magnetic flux-tubes in superconductors. The effect is therefore called the *chromoelectric Meissner* effect. The linear energy density in the colour field is a constant $a \simeq 1$ GeV/fm $\simeq 0.2$ GeV^{-2} leading to a linear growing potential between the quarks. As soon as the energy stored in the field exceeds the quark pair creation threshold, a new meson is formed leaving the rest of the string as an exact copy of the original, scaled down by the energy taken by the meson. Figure 2.7 shows schematically this procedure. The fraction of energy and momentum z which is given to the meson is distributed according to the longitudinal fragmentation function $f(z)$. Experimental data for the heavy flavours (c and b) can be described best by the *Peterson* function

$$f(z) = \frac{1}{z}\left(1 - \frac{1}{z} - \frac{\epsilon}{1-z}\right)^{-2} \quad , \tag{2.32}$$

and for the light flavours (u, d and s) by the *Lund symmetric* function

$$f(z) = \frac{(1-z)^a}{z} \cdot \exp\left(\frac{-bm_T^2}{z}\right) \quad . \tag{2.33}$$

The Peterson function has the free parameter ϵ. It is the squared ratio of the masses of heavy to light quarks. However, since the light quark masses are not precisely known, in practice the value of ϵ is evaluated from the data. Once it is known for one heavy flavour, the appropriate value for the other can be obtained from the quark mass relation $m_c^2\epsilon_c = m_b^2\epsilon_b$. The Lund symmetric function has two parameters, a and b, which have to be fitted to the data.

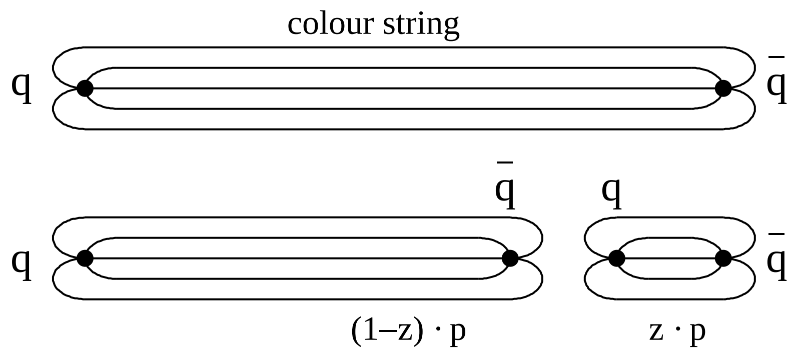

Figure 2.7: *Schematical view of the string fragmentation algorithm. The self interaction of the colour field leads to a linear field of constant energy density (the string). The string breaks and a meson is formed. The rest of the string is left as an exact copy of the original scaled down by the energy taken by the meson.*

The transverse mass $m_T^2 = m^2 + p_T^2$ is calculated from the mass and the average transverse momentum of the produced meson. Fig. 2.8 shows the longitudinal fragmentation functions for the different quark flavours. The heavy flavours are described by the Peterson function with $\epsilon_b = 0.006$ and $\epsilon_c = 0.054$. For the light flavours the Lund symmetric function is plotted with the values $a = 0.18$, $b = 0.34$, $\sigma_{p_T} = 395$ MeV/c and the masses of pion and kaon as typical representations for a light and strange meson.

The gluons can be incorporated into the string fragmentation picture in an universal and simple way. They are treated as transverse excitations of the colour flux tube. Without the introduction of additional free parameters any number of soft and hard gluons can be modeled as a string with several kinks.

The flavour content of the new hadrons depends on the probability of creating a quark-antiquark pair within the thin linear colour flux tube. The rest mass $2m$ of the produced pair has to be provided by the field energy stored in the string. Assuming constant linear energy density a, the two new quarks have to be at a distance $2l$ with $l = m/a$, when appearing as on-shell particles. If the model includes also the transverse movement of the produced object, this additional energy requires an even further separation. The probability for such a pair creation process can be calculated by a simple quantum mechanical approach treating the effect as a tunneling phenomenon. The tunneling feature becomes evident if the reaction is imagined to proceed in the time reversed direction, starting with two quarks (at rest at $\pm l$) attached to two strings of string constant a. By a short violation of energy conservation, they travel a distance l, meet each other at the middle and connect the two strings thereby restoring the amount of potential energy $2la$ they "borrowed" in their annihilation. A wave-function intruding a linearly growing potential exceeding the classical turning point will have an exponentially decreasing intensity. This yields for the pair creation probability [27]

$$\mathcal{P} \propto \exp\left(-\frac{\pi(m^2 + p_T^2)}{a}\right) \ . \tag{2.34}$$

The tunneling picture predicts in a natural way a *unique* Gaussian p_T distribution for all hadrons. The width σ_{p_T} is a free parameter since neither the string constant nor the quark masses are precisely known. It automatically accounts for the suppression of heavy flavours

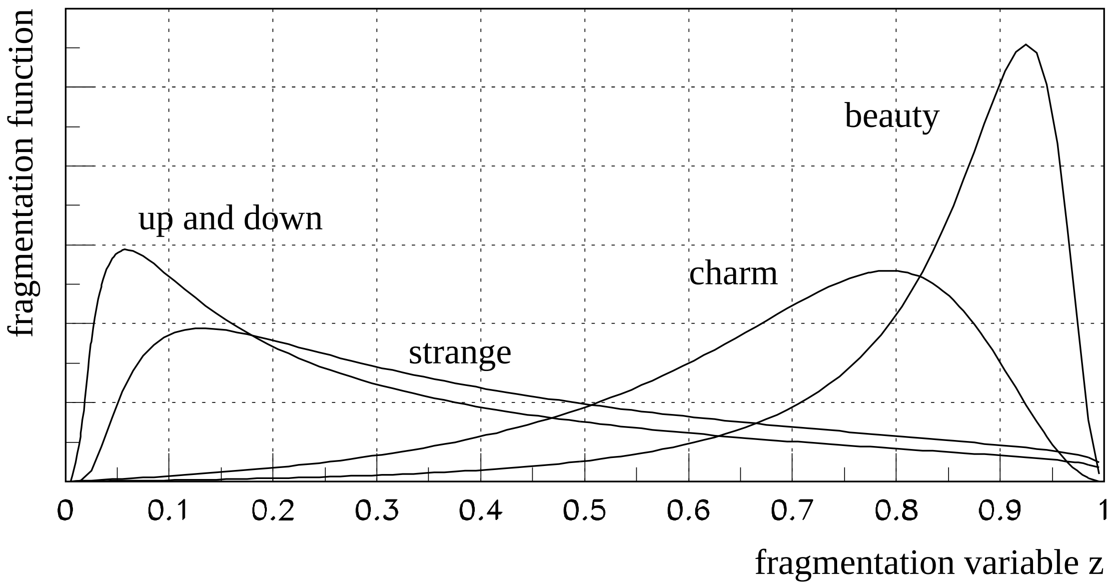

Figure 2.8: *The longitudinal fragmentation functions for the different quark flavours. The heavy flavours are described by the Peterson function with* $\epsilon_b = 0.006$ *and* $\epsilon_c = 0.054$*. For the light flavours the Lund symmetric function is plotted with the values* $a = 0.18$, $b = 0.34$, $\sigma_{p_T} = 395$ *MeV/c and the masses of pion and kaon as typical representations for a light and strange meson.*

during the fragmentation. The expected rates are

$$u : d : s : c : b = 1 : 1 : \frac{1}{3} : 10^{-12} : 10^{-100} \,. \tag{2.35}$$

This means that c and b quarks are practically never produced by the soft hadronisation mechanism[11]. Since the light quark masses are only known with large errors the s quark suppression is a free parameter of the model.

The creation of a *diquark* in the fragmentation phase leads to baryon production. For this case the same statement is true about the suppression factors for heavy flavours. In order to conserve quantum numbers a second diquark has to be produced *near* to the first diquark. It can either be produced immediately next to the first diquark or with some mesons in between. The latter case is known as *pop-corn* effect.

Cluster Fragmentation

A particular version of the so-called cluster fragmentation [28] is implemented in the HERWIG program [29]. The basic idea is the following. The parton shower evolution develops up to a certain virtuality Q_0. Then, all gluons are forced to split into quark-antiquark pairs thus forming clusters of partons. An effective gluon mass m_g^{eff} is introduced to enforce this process.

[11]The heavy quarks can either be produced primarily or during the perturbative phase.

m_g^{eff} is a parameter which must be adjusted in order to fit the model to the data. Conservation of energy and momentum requires m_g^{eff} to be at least twice the mass of the lightest quarks. If the mass of a formed cluster is above a certain cluster mass C_{max}, it will decay into two clusters by creation of a $q\bar{q}$ pair. The clusters are colour singlets which then turn into hadrons. The invariant mass of a cluster M is calculated by using effective masses m_i^{eff} for the quarks in a cluster. The effective masses for up, down, strange charm and bottom quarks are 0.32, 0.32, 0.5, 1.8 and 5.2 GeV/c^2 respectively.

2.3.4 Hadron Decays

After the fragmentation phase no particles[12] created during the perturbative phase have survived. They were confined in primary mesons and baryons, which now start to decay into stable final state particles. The commonly used simulation programs here refer to *experimentally* measured branching ratios. However, at LEP energies, especially within the domain of bottom hadrons, a number of states are produced where only a few or no experimental data exist. The modeling of their production and decay is inspired by predictions, observations in analogous systems[13], quantum number conservation and simple *spin* and *state counting* arguments. Fig. 2.9 gives two examples for particle decays visualized in the so-called spectator model.

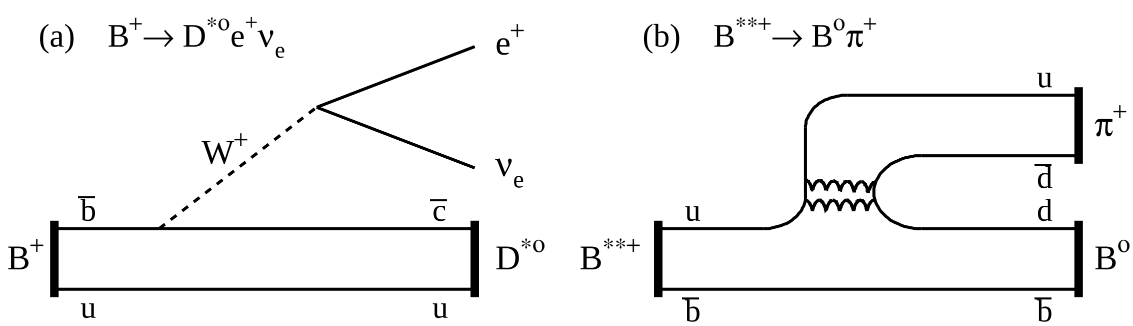

Figure 2.9: *Two examples for particle decays in the spectator model. (a) Weak decay of a B meson in a D^* and a $e^+\nu_e$ pair. (b) Strong decay of an orbitally excited B meson (B^{**}) into a B meson and a pion.*

[12] The only exception are initial or final state photons which are colourless and thus escape from confinement.

[13] The D meson and its excitations e.g. can serve as a model for the B system.

Quantity	Experiment	Measurement	Ref.
m_{B+} [MeV/c^2]	PDG 94	5278.7 ± 2.0	[12]
$\tau_{B+}[ps]$	PDG 94	1.54 ± 0.11	[12]
$\Delta m_{B^*/B}$ [MeV/c^2]	L3	46.3 ± 1.9	[30]
	DELPHI	$45.5 \pm 0.3 \pm 0.8$	[31]
	ALEPH	$45.3 \pm 0.4 \pm 0.9$	[32]
	PDG 94	46.0 ± 0.6	[12]
	average	45.7 ± 0.4	
production ratio $\sigma_{B^*}/(\sigma_{B^*} + \sigma_B)$	L3 publ.	$0.76 \pm 0.08 \pm 0.06$	[30]
	L3 update	$0.76 \pm 0.04 \pm 0.06$	[33]
	DELPHI	$0.72 \pm 0.03 \pm 0.06$	[31]
	ALEPH	$0.77 \pm 0.03 \pm 0.07$	[32]
	average	0.75 ± 0.04	

Table 2.2: *Selected experimental results on B and B^* mesons as given by the Particle Data Group and the LEP collaborations.*

2.4 *B* Meson Spectroscopy

For hadrons containing a heavy quark Q, quantum chromodynamics displays additional symmetries in the limit as the heavy quark mass m_Q becomes large compared with a typical QCD scale. These heavy quark symmetries are powerful aids in understanding the spectrum and decay of heavy-light ($Q\bar{q}$) mesons (see also section 2.2.4). Because $m_b \gg \Lambda_{QCD}$, heavy quark symmetry should provide an excellent description of the B and B_s meson and their excited states. It is plausible that the properties of the D mesons and even of the K mesons should also reflect approximate heavy quark symmetry.

2.4.1 Ground State *B* Mesons

The pseudoscalar B meson ($J^P = 0^-$) and the vector B^* meson ($J^P = 1^-$) have been established experimentally for several years. The B^* meson decays electromagnetically into a B meson and a photon ($B^* \to B\gamma$). A fraction of the experimentally available results is shown in Tab. 2.2. The Hilbert space of these states can be represented conveniently in a tensor product notation $|\pm 1/2, \pm 1/2\rangle$, where the first $\pm 1/2$ is the 3rd component of the spin of the heavy quark and the second $\pm 1/2$ is the 3rd component of the light degrees of freedom:

$$|B^*, +1\rangle = |+1/2, +1/2\rangle \tag{2.36}$$

$$|B^*, 0\rangle = \frac{1}{\sqrt{2}}(|+1/2, -1/2\rangle + |-1/2, +1/2\rangle) \tag{2.37}$$

$$|B^*, -1\rangle = |-1/2, -1/2\rangle \tag{2.38}$$

$$|B\rangle = \frac{1}{\sqrt{2}}(|+1/2, -1/2\rangle - |-1/2, +1/2\rangle)\,. \tag{2.39}$$

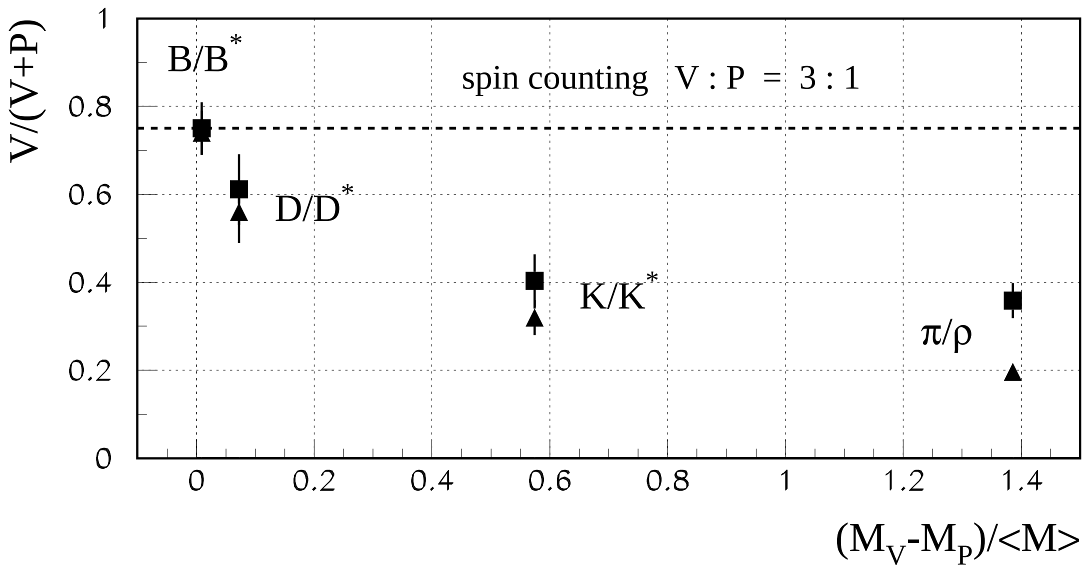

Figure 2.10: *Production ratio V/(V+P) of vector (V) and pseudoscalar (P) mesons as a function of $(M_V - M_P)/\langle M\rangle$ at LEP. The triangles show the ratio including primary and secondary produced mesons [12]. The squares give the same ratio where secondary mesons from particle decays have been subtracted using the* JETSET *7.3 model [22] with DELPHI tuning [34]. A vector meson suppression is evident for the light mesons.*

It can be seen that the pseudoscalar B meson belongs to a singlet, while the vector B^* meson belongs to a triplet. From a simple *spin counting* argument, one would expect a production ratio of $B^* : B$ mesons of $3:1$ in e^+e^- collisions[14]. This expectation is in accord with LEP measurements: $\sigma_{B^*}/(\sigma_B + \sigma_{B^*}) = 0.75 \pm 0.04$ (see Tab. 2.2).

However, this simple spin counting argument, which seems to work well in the B/B^* system, fails for light meson systems. A vector meson suppression is observed here. The production ratio V/(V+P) of vector (V) and pseudoscalar (P) mesons as a function of $(M_V - M_P)/\langle M\rangle$ is shown in Fig. 2.10. The triangles show the ratio including primary and secondary produced mesons. The squares give the same ratio where secondary mesons from particle decays have been subtracted.

2.4.2 *B* Mesons with Orbital Excitation

For the discussion of orbitally excited meson states, the usual spectroscopic notation is used: $n^{2S+1}L_J$, where n is the principle quantum number, S the total spin, L the orbital angular momentum between the quarks and $\vec{J} = \vec{L} + \vec{S}$. Tab. 2.3 gives the suggested $q\bar{q}$ quark model assignments for most of the known mesons.

In the strict sense this notation is valid only if S and L are conserved quantum numbers. In the limit of equal-mass quarks ($q_1\bar{q}_2$) this situation is rather well fulfilled (first column in Fig. 2.11). In this case the total spin $\vec{S} = \vec{s}_{q_1} + \vec{s}_{q_2}$ and the orbital angular momentum $\vec{L}$ are

[14] This simple argument needs slight corrections due to the production of higher excited states (e.g. B^{**} mesons). This will be discussed in the next sections.

$N^{2S+1}L_J$	J^{PC}	$u\bar{d}, u\bar{u}, d\bar{d}$ $I=1$	$u\bar{u}, d\bar{d}, s\bar{s}$ $I=0$	$\bar{s}u, \bar{s}d$ $I=1/2$	$c\bar{c}$ $I=0$	$c\bar{u}, c\bar{d}$ $I=1/2$	$c\bar{s}$ $I=0$	$b\bar{b}$ $I=0$	$\bar{b}u, \bar{b}d$ $I=1/2$	$\bar{b}s$ $I=0$
1^1S_0	0^{-+}	π	η, η'	K	η_c	D	D_s	–	B	B_s
1^3S_1	1^{--}	ρ	ω, Φ	$K^*(892)$	$J/\psi(1S)$	$D^*(2010)$	$D_s^*(2110)$	$\Upsilon(1S)$	B^*	B_s^*
1^1P_1	1^{+-}	$b_1(1235)$	$h_1(1170), h_1(1380)$	K_{1B} [15]	$h_c(1P)$	$D_1(2420)$	$D_{s1}(2536)$	–	–	–
1^3P_0	0^{++}	$a_0(980)$ [16]	$f_0(1300), f_0(980)$ [16]	$K_0^*(1430)$	$\chi_{c0}(1P)$	–	–	$\chi_{b0}(1P)$	–	–
1^3P_1	1^{++}	$a_1(1260)$	$f_1(1285), f_1(1510)$	K_{1A} [15]	$\chi_{c1}(1P)$	–	–	$\chi_{b1}(1P)$	–	–
1^3P_2	2^{++}	$a_2(1320)$	$f_2(1270), f_2'(1525)$	$K_2^*(1430)$	$\chi_{c2}(1P)$	$D_2^*(2460)$	$D_{s2}^*(2573)$	$\chi_{b2}(1P)$	–	–
1^1D_2	2^{-+}	$\pi_2(1670)$	–	$K_2(1770)$	–	–	–	–	–	–
1^3D_1	1^{--}	$\rho(1700)$	$\omega(1600)$	$K^*(1680)$	$\psi(3770)$	–	–	–	–	–
1^3D_2	2^{--}	–	–	$K_2(1820)$	–	–	–	–	–	–
1^3D_3	3^{--}	$\rho_3(1690)$	$\omega_3(1670), \Phi_3(1850)$	$K_3^*(1780)$	–	–	–	–	–	–

Table 2.3: *Suggested $q\bar{q}$ quark model assignments for most of the known mesons [12]. Some assignments, especially of the 0^{++} multiplet and for some of the higher multiplets, are still controversial. Some of the light mesons are not listed in this table, since they are usually interpreted as glueball candidates, $K\bar{K}$ molecules or other exotic states.*

[15] The K_{1A} and K_{1B} are nearly equal (45°) mixtures of $K_1(1270)$ and $K_1(1400)$.

[16] The assignment of these particles is still under discussion. The classification follows the suggestion of the PDG. Other authors suggest these states to be interpreted as $K\bar{K}$ molecules.

conserved separately. For the case of u or d quarks, the ground state pseudoscalar and vector meson correspond to the pion ($J^P = 0^-$) and the ρ meson ($J^P = 1^-$). Orbital excitations are formed by coupling the total spin $\vec{S}$ to the orbital angular momentum $\vec{L}$, leading to a *singlet* and a *triplet*. For the case of $L = 1$ the b_1 is identified as the singlet, and the particles a_0, a_1 and a_2 are identified as belonging to the triplet (see Fig. 2.11).

This situation changes drastically if one quark becomes much heavier than Λ_{QCD} (second column of Fig. 2.11). One essential idea of the heavy quark limit is that the spin of the heavy quark $\vec{s}_Q$ and the total (spin + orbital) angular momentum $\vec{j}_q = \vec{s}_q + \vec{L}$ of the light degrees of freedom are conserved separately. Accordingly, each energy level in the excitation spectrum of $Q\bar{q}$ mesons is composed of a degenerate pair of states characterized by $\vec{j}_q$ and the total angular momentum $\vec{J} = \vec{j}_q + \vec{s}_Q$. The ground-state pseudoscalar and vector mesons, which are degenerate in the heavy quark limit, correspond to $j_q = \frac{1}{2}$, with $J^P = 0^-$ (B) and $J^P = 1^-$ (B^*). Orbital excitations lead to *two* distinct *doublets* associated with $j_q = L \pm \frac{1}{2}$. For the special case of $L = 1$ four different states are expected:

$$
\begin{array}{ll}
j_q = 1/2 & \left\{ \begin{array}{ll} J^P = 0^+ & B_0^* \\ J^P = 1^+ & B_1^* \end{array} \right. \\
j_q = 3/2 & \left\{ \begin{array}{ll} J^P = 1^+ & B_1 \\ J^P = 2^+ & B_2^* \end{array} \right.
\end{array}
$$

The official notation for the four states is given in the third column. All four states are commonly labeled as B^{**}. In order to describe whether the b quark in the meson is accompanied by a $\bar{u}$, $\bar{d}$ or a $\bar{s}$ quark, the notation is extented by the subscript u, d or s (B_u^{**}, B_d^{**} and B_s^{**}). In the literature the symbol B^{**} usually refers to the states B_u^{**} and B_d^{**}, sometimes it also includes the state B_s^{**}. The meaning becomes apparent from the context. Before the start of the work described in this thesis, none of the B^{**} mesons was observed experimentally. The main part of this thesis will focus on the search for and observation of these states.

Properties of Orbitally Excited B Mesons

Orbitally excited B mesons will decay due to the strong interaction. The expected main decay modes of $B_{u,d}^{**}$ mesons are $B\pi$ and $B^*\pi$. If the B_s^{**} meson mass is above the BK or B^*K threshold, these will be the prominent decay modes, since the decay into $B_s\pi^0$ is forbidden by isospin conservation. The members of the first doublet ($j_q = 3/2$) should be narrow compared to the typical strong decay width, because only $L = 2$ (d-wave) decays are allowed. This is due to the conservation of angular momentum and parity for the 2^+ state and a dynamical prediction of HQET for the 1^+ partner. The members of the second doublet ($j_q = 1/2$) are expected to be broad (of the order of the typical strong decay width ≥ 150 MeV/c^2), because $L = 0$ (s-wave) decays are allowed. HQET predicts the two 1^+ eigenstates to be 45° mixtures of the states with $S = 0$ and $S = 1$. This results in the property that the 1^+ ($j_q = 1/2$) state decays via s-wave, while the 1^+ ($j_q = 3/2$) state decays via d-wave. The situation is similar to the D and K meson sector. Spin-parity rules govern the possible decay modes for the different states. In general,

symmetric mesons	heavy-light mesons
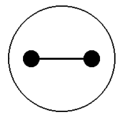 $q_1 \quad q_2$	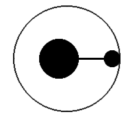 $Q \quad q$
conventional quark model $m_{q_1} = m_{q_2}$	Heavy Quark Effective Theory $m_q << m_Q, \;\; m_Q \to \infty$
Parity $P = (-1)^{L+1}$	
Charge Conjugation $C = (-1)^{L+S}$	C not defined
$s_{q1} \oplus s_{q2} \to S$ $L \oplus S \to J$	$s_q \oplus L \to j_q$ $s_Q \oplus j_q \to J$
ground state, orbital angular momentum L=0:	
$1/2 \oplus 1/2 \to \begin{cases} 0 \\ 1 \end{cases}$	$1/2 \oplus 0 \to 1/2$
$0 \oplus \begin{cases} 0 \to 0^{-+} \quad (\pi) \\ 1 \to 1^{--} \quad (\rho) \end{cases}$	$1/2 \oplus 1/2 \to \begin{cases} 0^- \quad (B) \\ 1^- \quad (B^*) \end{cases}$
excited state, orbital angular momentum L=1:	
$1/2 \oplus 1/2 \to \begin{cases} 0 \\ 1 \end{cases}$	$1/2 \oplus 1 \to \begin{cases} 1/2 \\ 3/2 \end{cases}$
$1 \oplus \begin{cases} 0 \to 1^{+-} \quad (b_1) \\ 1 \to \begin{cases} 0^{++} \quad (a_0) \\ 1^{++} \quad (a_1) \\ 2^{++} \quad (a_2) \end{cases} \end{cases}$	$1/2 \oplus \begin{cases} 1/2 \to \begin{cases} 0^+ \quad (B_0^*) \\ 1^+ \quad (B_1^*) \end{cases} \\ 3/2 \to \begin{cases} 1^+ \quad (B_1) \\ 2^+ \quad (B_2^*) \end{cases} \end{cases}$

Figure 2.11: *The different coupling schemes of symmetric and heavy-light mesons. For symmetric mesons (first column) the total spin S and the orbital angular momentum L are conserved separately. Heavy-light mesons (second column) are governed by HQET. The spin of the heavy quark s_Q and the total angular momentum of the light degrees of freedom j_q are conserved separately.*

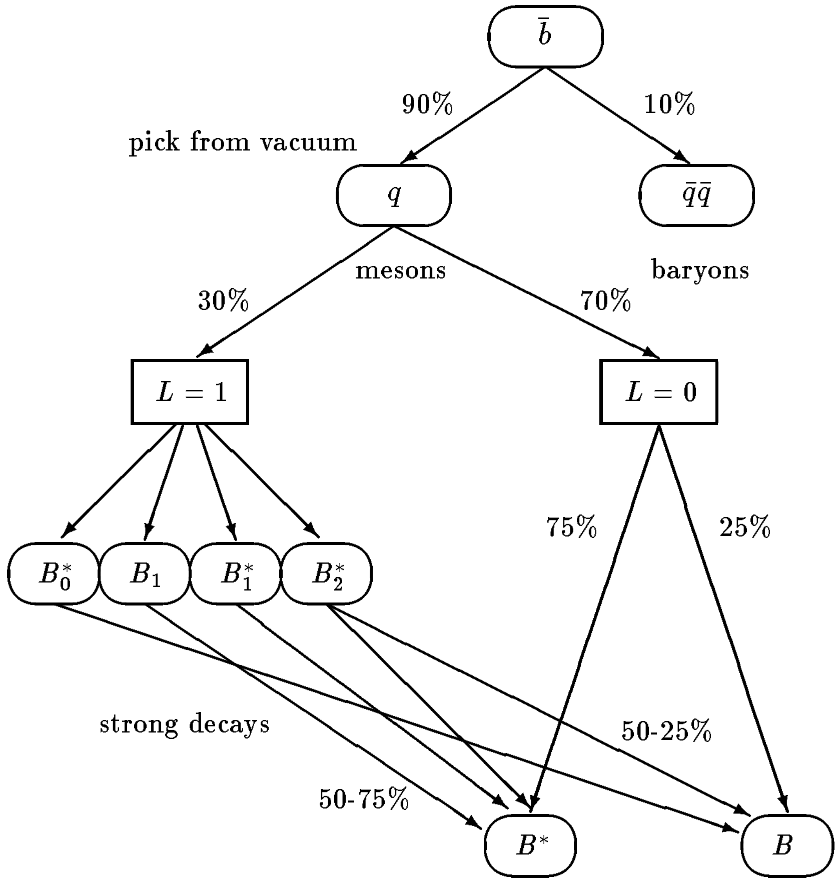

Figure 2.12: *Production and decay properties of orbitally excited B mesons. Details concerning this diagram are given in the text.*

$B_0^* \to B\pi$	$B_{0s}^* \to BK$	broad states
$B_1^* \to B^*\pi$	$B_{1s}^* \to B^*K$	s-wave decay
$B_1 \to B^*\pi$	$B_{1s} \to B^*K$	narrow states
$B_2^* \to B^{(*)}\pi$	$B_{2s}^* \to B^{(*)}K$	d-wave decay

where the symbol $B^{(*)}$ denotes B *or* B^* meson. Fig. 2.12 gives an overview of production and decay properties of orbitally excited B mesons. A primary produced $\bar{b}$ quark will pick a quark q from the vacuum 90% of the time to form a meson, while 10% of the time a baryon is formed. From the D meson sector it is expected that roughly 30% of the mesons will be produced with $L = 1$, 70% with $L = 0$. According to simple spin counting rules the states with $L = 0$ will be manifest in 75% of the cases as B^* mesons and in 25% as B mesons. The four B^{**} states $(2^+, 1^+, 1^+$ and $0^+)$ with $L = 1$ will decay according to spin-parity rules into B and B^* mesons. Depending on the production mechanism assumed for these states (spin counting 5 : 3 : 3 : 1, state counting 1 : 1 : 1 : 1 or anything in between), the ratio of B^* : B mesons produced from B^{**} decays can vary from 50% : 50% to 75% : 25%. For this calculation it is assumed that the 2^+ state decays only in B^* mesons for the spin-counting argument and only into B mesons for the state counting argument. The B^* meson then decays electromagnetically into a B meson and a photon.

Influence of B^{**} Production on the Ratio B^*/B

As discussed in section 2.4.1, the production ratio of B^* mesons per primary produced meson was measured by the LEP experiments to be: $\sigma_{B^*}/(\sigma_B + \sigma_{B^*}) = 0.75 \pm 0.04$. In the absence of B^{**} production, this ratio is equal to the parameter $V/(V+P)$ in the JETSET fragmentation model [22], where V and P are the production rates of primary vector and pseudoscalar B mesons. However, production of a sizeable amount of B^{**} mesons can alter the ratio of B^* to B mesons depending on the relative production rates and branching fractions into $B^*\pi$ and $B\pi$ of the four individual B^{**} spin-parity states. A further complication arises from the way JETSET treats the production of the two 1^+ states: one state is made from the P $(S=0)$ fraction, and the other state, together with the 0^+ and the 2^+ states, is made from the V $(S=1)$ fraction. However, HQET predicts the two 1^+ eigenstates to be equal mixtures of $S=0$ and $S=1$. Different assumptions, such as relative $2^+ : 1^+ : 1^+ : 0^+$ production ratios varying between $1:1:1:1$ (state counting) and $5:3:3:1$ (spin counting), and unknown 2^+ decay branching ratios into $B^*\pi$, may change the effective branching fraction of B^{**} to $B^*\pi$ to anything within the range 50% to 75%. This implies that

$$\frac{V}{V+P} = \frac{1}{1-f^{**}}\left(\frac{\sigma_{B^*}}{\sigma_B + \sigma_{B^*}} - f^{**} \cdot Br(B^{**} \to B^*)\right) \ , \tag{2.40}$$

where f^{**} denotes the production ratio of B^{**} mesons per primary produced meson [31].

Influence of B_s^{**} Production for Mixing Studies

The flavour change[17] in B^{**} decays is shown schematically in Fig. 2.13. According to isospin rules B_u^{**} and B_d^{**} will decay 67% of the time with the emission of a charged pion, and in 33% with the emission of a neutral pion (for the moment the $B^{(*)}\rho$ channel is neglected). In the analysis presented here, only the charged pion decay channel is investigated. It is worth noting that B_s^{**} mesons cannot decay into $B_s^{(*)}\pi^0$, since it is forbidden by isospin conservation. B_s^{**} mesons decay with the emission of a kaon (50% K^+, 50% K^0).

This fact is important for B_s mixing studies, which are being performed at LEP [35]. These analyses look for oscillations of a primary produced B_s to a $\bar{B}_s$ meson. The Standard Model describes such processes in analogy to the $K^0\bar{K}^0$ system with *box diagrams*. In the $B_d\bar{B}_d$ system clear evidence for time dependent and integrated mixing has been extracted from data at LEP [35]. Assuming the usual strangeness suppression factor

$$u : d : s = 3 : 3 : 1 \tag{2.41}$$

for the production of B_s mesons in B events leads to a production ratio of $\sigma_{B_s}/(\sigma_B + \sigma_{B_s}) =$ 14.3%. This production ratio has to be corrected if sizeable amounts of B_s^{**} mesons are

[17] The flavour here refers to the quark (antiquark) which forms the B^{**} meson together with the $\bar{b}$ (b) quark.

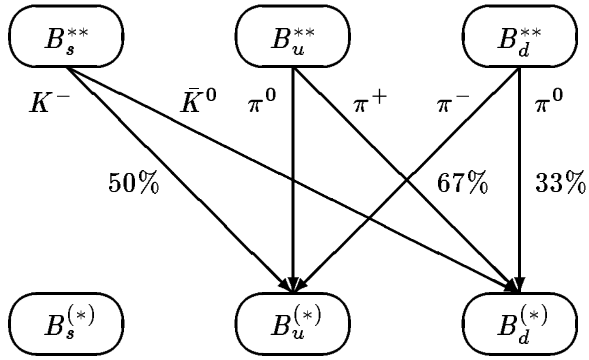

Figure 2.13: *Flavour change in B^{**} decays. According to isospin rules B_u^{**} and B_d^{**} will decay 67% of the time with the emission of a charged pion, and 33% with the emission of a neutral pion. B_s^{**} mesons cannot decay into $B_s^{(*)}\pi^0$ mesons since this is forbidden by isospin conservation.*

produced, since they do not decay in B_s mesons[18]. One obtains

$$\frac{\sigma_{B_s}}{(\sigma_B + \sigma_{B_s})} = 14.3\% \cdot (1 - f_s^{**}) \ , \tag{2.42}$$

where f_s^{**} is the production ratio of B_s^{**} mesons per primary produced $(b\bar{s})$ state. This effect makes it more difficult to observe B_s mixing at LEP.

The decay properties and suspected mass relations of orbitally excited B and B_s mesons are summarized in Fig. 2.14. The ordinate shows schematically the mass of the different states. The arrows give the possible decay modes. The decays of the ground state mesons $(L = 0)$ are not shown.

2.4.3 Motivations from the D Meson Sector

Orbitally excited D and D_s mesons have been established experimentally for the past few years. The evidence has been obtained by experiments running on the $\Upsilon(4S)$ resonance (mainly CLEO and ARGUS). The results from the CLEO collaboration dominate the world average. All narrow orbitally excited D meson states ($j_q = 3/2$ with $J^P = 1^+, 2^+$) have been observed in the channels $D\pi$ and $D^*\pi$. Furthermore, in the D_s meson sector, all the narrow states have been identified in the channels DK and D^*K. Spin-parity and decay characteristics have been shown to be in accord with HQET predictions by studying decay angular distributions. However, until now none of the broad states ($j_q = 1/2$ with $J^P = 0^+, 1^+$) has been identified. Tab. 2.4 summarizes the measurements of masses and widths for the known excited D meson states, as published by the CLEO collaboration [36–39]. The observed mass splitting between 2^+ and 1^+ states is given as well.

Heavy quark symmetry predictions e.g. by Eichten, Hill and Quigg [40, 41] use the measured D_1 and D_2^* masses as input and predict the masses of the corresponding B states. This

[18] Note, that only B_s mesons live long enough to mix. It does not matter if a B_s meson is primary or comes from the decay of a primary B_s^* meson ($B_s^* \to B_s\gamma$).

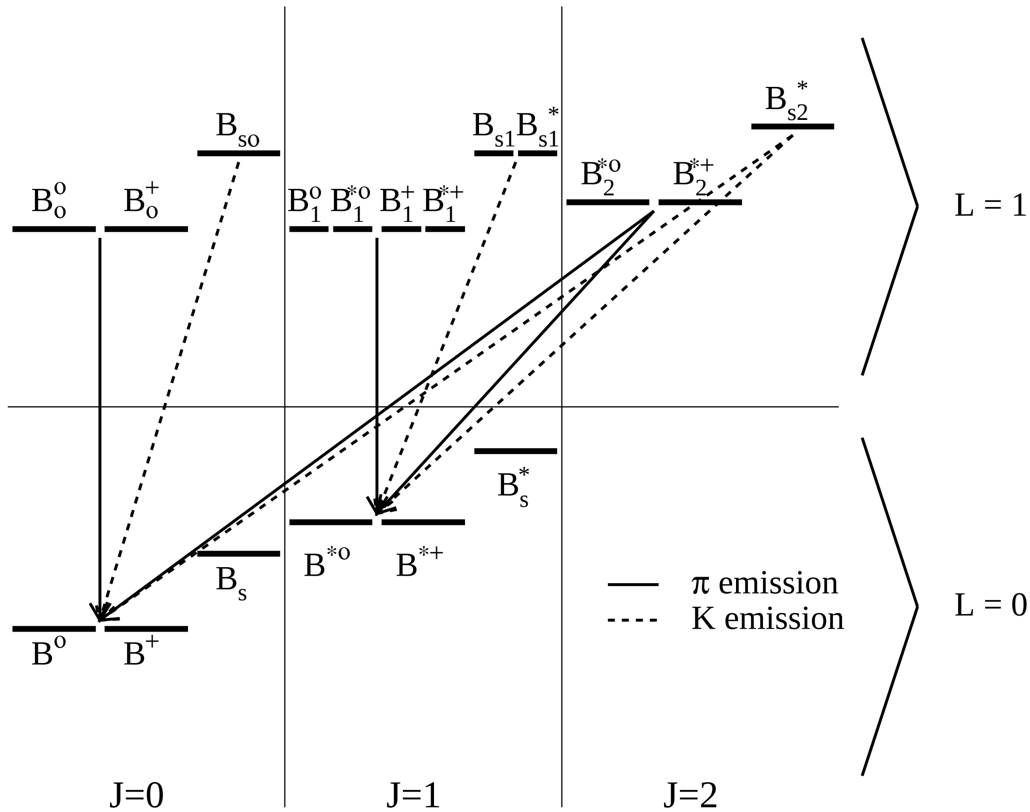

Figure 2.14: *Decay properties and suspected mass relations of orbitally excited B mesons. The ordinate shows schematically the mass of the different states. The arrows give the possible decay modes. The decays of the ground state mesons ($L = 0$) are not shown.*

will be discussed in the following section. Furthermore, they predict masses and decay widths for the D_{s1} and D^*_{s2} mesons. Their prediction for the 1^+ D_s meson lies 9 MeV/c^2 below the level observed at 2535.1 ± 0.5 MeV/c^2 [38]. The prediction for the 2^+ D_s meson lies 12 MeV/c^2 below the level observed at 2573.2 ± 1.7 MeV/c^2 [39]. It was suggested by the authors to take the discrepancies between the calculated and the observed masses as a measure of the limitations of their model. The accuracy for the B_s system predictions is lower, since none of the unknown orbitally excited $B_{u,d}$ states could be used as input (at the time the model was developed).

Recently, the LEP experiments reported evidence for D^{**} production in c events as well as in b events [42–44]. The D^{**} mesons in b events appear due to weak decays of B mesons, e.g. $B^0 \rightarrow D^{**-}\ell^+\nu$. The measured production ratios of the LEP experiments are summarized in Tab. 2.5 together with the corresponding measurements from ARGUS and CLEO. Although experimental errors are large, it becomes clear that sizeable fractions of D^{**} mesons are produced in B meson decays (roughly 30%). Moreover, sizeable fractions of D^{**} mesons (roughly 25%) are observed in c quark fragmentation, thus proving that quark fragmentation is capable of producing mesons with orbital excitation. These facts motivate a search for B^{**} mesons at LEP.

State	Channel	Mass [MeV/c²]	Width [MeV/c²]	Δ [MeV/c²]	Ref.
$D_1(2420)^{\pm}$	$D^{*0}\pi^+$	$2425 \pm 2 \pm 2$	$26^{+8}_{-7} \pm 4$	38 ± 5	[36]
$D_2^*(2460)^{\pm}$	$D^0\pi^+$	$2463 \pm 3 \pm 3$	$27^{+11}_{-8} \pm 5$		[36]
$D_1(2420)^0$	$D^{*+}\pi^-$	$2421^{+1}_{-2} \pm 2$	$20^{+6}_{-5} \pm 3$	44 ± 5	[37]
$D_2^*(2460)^0$	$D^{*+}\pi^-/D^+\pi^-$	$2465 \pm 3 \pm 3$	$28^{+8}_{-7} \pm 6$		[37]
$D_{s1}(2536)^{\pm}$	$D^{*0}K^+/D^{*+}K^0$	$2535.1 \pm 0.2 \pm 0.5$	< 2.3 (90% c.l.)	38 ± 2	[38]
$D_{s2}^*(2573)^{\pm}$	D^0K^+	$2573.2^{+1.7}_{-1.6} \pm 0.5$	$16^{+5}_{-4} \pm 3$		[39]

Table 2.4: *Experimental results for orbitally excited D mesons obtained by the CLEO collaboration. Given are masses, widths and mass splitting between 2^+ and 1^+ states.*

Quantity	Experiment	Measurement	Ref.
$\frac{\sigma(c \to D^{**}X)\cdot Br(D^{**}\to D^{(*)}\pi)}{\sigma(c-jet)}$	ARGUS	$0.460 \pm 0.080 \pm 0.120$	[45,46]
	CLEO	$0.230 \pm 0.020 \pm 0.020$	[37]
	DELPHI	$0.248 \pm 0.068 \pm 0.051$	[42]
	ALEPH	$0.189 \pm 0.054 \pm 0.057$	[43]
$\frac{\sigma(b \to D^{**}X)\cdot Br(D^{**}\to D^{(*)}\pi)}{\sigma(b\to D^{(*)}X)}$	ALEPH	$0.318 \pm 0.096 \pm 0.062$	[43]
	DELPHI	$0.340 \pm 0.120 \pm 0.060$	[42]
$\frac{Br(B^0\to D^{**-}\ell^+\nu)}{Br(B^0\to(D^-,D^{*-},D^{**-})\ell^+\nu)}$	ARGUS	0.31 ± 0.15	[12,47,48]
	CLEO	0.36 ± 0.12	[49]
	DELPHI	0.21 ± 0.09	[12,48]
	OPAL	0.34 ± 0.07	[44]

Table 2.5: *D^{**} production in e^+e^- annihilation experiments. Note, that ARGUS and CLEO run on the $\Upsilon(4S)$ resonance, while the ALEPH, DELPHI and OPAL experiments operate at the Z^0 pole.*

2.4.4 Predictions for Orbitally Excited B Mesons

Predictions of Masses

The heavy spin symmetry can be combined with the heavy flavour symmetry to predict masses of the narrow orbitally excited B mesons in terms of meson masses in the charm sector. The relevant derivation may be found in a paper by Falk and Mehen [50]. The splittings between excited doublets and the ground state should be independent of heavy quark mass, while the spin symmetry violating splitting within the doublet scales like $1/m_Q$. If one defines the spin averaged masses and mass splittings to be

$$\bar{m}_B = \frac{3}{4}m_{B^*} + \frac{1}{4}m_B \ , \tag{2.43}$$
$$\bar{m}_{B^{**}} = \frac{5}{8}m_{B_2^*} + \frac{3}{8}m_{B_1} \ , \tag{2.44}$$
$$\Delta m_{B^{**}} = m_{B_2^*} - m_{B_1} \ , \tag{2.45}$$

and analogous relations for charm mesons, the heavy quark symmetries predict that

$$\bar{m}_{B^{**}} - \bar{m}_B = \bar{m}_{D^{**}} - \bar{m}_D \ , \tag{2.46}$$
$$\Delta m_{B^{**}} = \frac{m_c}{m_b}\Delta m_{D^{**}} \ . \tag{2.47}$$

With the assumption $m_c/m_b = 1/3$, and averaging over the charged and neutral charmed mesons, these relations yield [50]:

$$\boxed{\begin{array}{rcl} m(B_2^*) &=& 5794 \text{ MeV/c}^2 \\ m(B_1) &=& 5780 \text{ MeV/c}^2 \\ m(B_{2s}^*) &=& 5899 \text{ MeV/c}^2 \\ m(B_{1s}) &=& 5886 \text{ MeV/c}^2 \end{array}}$$

The leading corrections to the predictions for $\bar{m}_{B^{**}}$ and $\bar{m}_{B_s^{**}}$ are of the order

$$\delta \sim \Lambda_{QCD}^2 \left(\frac{1}{2m_c} - \frac{1}{2m_b}\right) \sim 40\text{MeV} \ , \tag{2.48}$$

where a QCD-scale of $\Lambda_{QCD} \simeq 400$ MeV has been assumed. It becomes evident that heavy quark symmetry together with measurements in the charm system provide powerful tools for predictions in excited B systems. The simpleness of these considerations increases the confidence in the predictions.

A more sophisticated model has been developed in two papers by Eichten, Hill and Quigg [40, 41]. In a more general concept, they write the mass of a heavy-light meson in the from

$$m(nL_J(j_q)) = m(1S) + E(nL(j_q)) + \frac{C(nL_J(j_q))}{m_Q} \tag{2.49}$$

where $m(1S) = (3m(1S_1) + m(1S_0))/4$ is the mass of the ground state, $E(nL(J_q))$ is the excitation energy and $C(nL_J(j_q))$ are constants. The excitation energy $E(nL(j_q))$ has a weak dependence on the heavy quark mass. Referring to non-relativistic (*Buchmüller type*) potential models to estimate the variation of the excitation spectrum as a function of heavy quark mass, and using meson masses of already observed states[19], the following mass predictions have been determined for orbitally excited B mesons:

[19] The following particles were used as an input: $K, K^*, K_{1A}, K_2^*, D, D^*, D_1, D_2^*, D_s, D_s^*, B$ and B^*.

$$\begin{array}{rcl} m(B_2^*) & = & 5771 \text{ MeV/c}^2 \\ m(B_1) & = & 5759 \text{ MeV/c}^2 \\ m(B_{2s}^*) & = & 5861 \text{ MeV/c}^2 \\ m(B_{1s}) & = & 5849 \text{ MeV/c}^2 \end{array}$$

Thus, the mass splitting between the 2^+ and the 1^+ state is predicted to be 12 MeV/c^2 for the $B_{u,d}^{**}$ case and 12 MeV/c^2 for the B_s^{**} case. Similar mass splittings (14 MeV/c^2 for the $B_{u,d}^{**}$ and 13 MeV/c^2 for the B_s^{**}) are predicted by Falk and Mehen, although their absolute mass predictions are significantly different from the above.

There are no detailed predictions for the masses of the broad ($j_q = 1/2$) B^{**} states since they decay immediately via s-wave due to strong interactions. In first approximation, they should have the same masses as the narrow ($j_q = 3/2$) states. Other models predict their masses to split from the narrow states by an amount, of the order of 100 MeV/c^2, whose magnitude and sign gives valuable information on the spin structure of the long-range interquark force [51].

Predictions of Decay Widths

It is somewhat more delicate to make predictions for the widths of the excited B mesons than for their masses, since the widths depend on the available phase space, and hence on the values of the heavy meson masses. The argument presented here follows the ideas of Eichten, Hill and Quigg [40,41]. Consider the decay of an excited heavy-light meson H, characterized by $L_J(j_q)$, to a heavy-light meson $H'(L'_{J'}(j'_q))$, and a light hadron h with spin s_h. The amplitude for the emission of h with orbital angular momentum l relative to H' satisfies certain symmetry relations because the decay dynamics becomes independent of the heavy quark spin in the $m_Q \to \infty$ limit of QCD. The decay amplitude can be factored into a reduced amplitude $\mathcal{A}_R$ times a normalized $6-j$ symbol:

$$\mathcal{A}(H \to H'h) = (-1)^{s_Q+j_h+J'+j_q} \cdot C_{j_h,J,j_q}^{s_Q,j'_q,J'} \cdot \mathcal{A}_R(j_h, l, j_q, j'_q) \ , \tag{2.50}$$

where

$$C_{j_h,J,j_q}^{s_Q,j'_q,J'} = \sqrt{(2J'+1)(2j_q+1)} \cdot \begin{Bmatrix} s_Q j'_q J' \\ j_h J j_q \end{Bmatrix} \tag{2.51}$$

and

$$\vec{j}_h = \vec{s}_h + \vec{l} \ . \tag{2.52}$$

The coefficients C depend only upon the total angular momentum j_h of the light hadron and not separately on its spin s_h and the orbital angular momentum wave l of the decay. The two-body decay rate may be written as

$$\Gamma_{j_h,l}^{H \to H'h} = (C_{j_h,J,j_q}^{s_Q,j'_q,J'})^2 \cdot p^{2l+1} \cdot F_{j_h,l}^{j_q,j'_q}(p^2), \tag{2.53}$$

where p is the three-momentum of a decay product in the rest frame of H. Heavy quark symmetry does not predict the reduced $\mathcal{A}_R$ or the related $F_{j_h,l}^{j_q,j'_q}(p^2)$ for a particular decay.

However, once determined from the strange and charmed mesons, these dynamical quantities are used to predict related decays, e.g. those of orbitally excited B mesons. For each independent decay process, a modified Gaussian form is assumed

$$F_{j_h,l}^{j_q,j'_q}(p^2) = F_{j_h,l}^{j_q,j'_q}(0) \cdot \exp(-p^2/\kappa^2) \cdot \left[\frac{M_\rho^2}{M_\rho^2 + p^2}\right]^l, \qquad (2.54)$$

and the overall strength of the decay and the momentum scale κ is determined by fitting to existing data. The ability to predict decay rates depend on the quality of the information used to set these parameters. The following list gives the predicted decay widths, Γ, for orbitally excited B mesons [40,41].

$\Gamma(B_2^* \to B^*\pi)$	$=$	11 MeV/c^2
$\Gamma(B_2^* \to B\pi)$	$=$	11 MeV/c^2
$\Gamma(B_2^* \to B^*\rho)$	$=$	3 MeV/c^2
$\Gamma(B_2^* \to B\rho)$	$<$	1 MeV/c^2
$\Gamma(B_2^* \to all)$	$=$	25 MeV/c^2
$\Gamma(B_1 \to B^*\pi)$	$=$	17 MeV/c^2
$\Gamma(B_1 \to B^*\rho)$	$=$	1 MeV/c^2
$\Gamma(B_1 \to B\rho)$	$=$	3 MeV/c^2
$\Gamma(B_1 \to all)$	$=$	21 MeV/c^2
$\Gamma(B_{s2}^* \to B^*K)$	$\approx$	1 MeV/c^2
$\Gamma(B_{s2}^* \to BK)$	$=$	2.6 MeV/c^2
$\Gamma(B_{s2}^* \to all)$	$=$	4 MeV/c^2
$\Gamma(B_{s1} \to B^*K)$	$\approx$	1 MeV/c^2

Chiral symmetry and heavy quark symmetry combined suggest that the heavy-light $j_q = 1/2$ states should have large widths for pionic decay to the ground states ($\geq$ 150 MeV/c^2) [52]. This will make the discovery and study of these states challenging, and will limit their utility for B^{**} tagging.

2.4.5 Flavour Tagging and CP-Violation

Inclusive studies of particle-antiparticle mixing and CP-violation for neutral B mesons require that the quantum numbers of the meson have to be identified at the time of production. This identification can be made by observing the decay of a B ($\bar{B}$) produced in association with the neutral $\bar{B}$ (B) of interest. The efficiency of flavour identification might be significantly enhanced if the neutral B mesons under study were self-tagging [53].

Charmed mesons have been observed as (strong) decay products of orbitally excited ($c\bar{q}$) states, in the decay channels $D^{**} \to D\pi$ and $D^{**} \to D^*\pi$. The charge of the pion signals the flavour content of the charmed meson. If a significant number of B mesons were produced through one or two narrow excited states, then the strong decay $B^{**\pm} \to B^{(*)0}\pi^\pm$ tags the neutral meson as $\bar{b}q$ or $b\bar{q}$. This B^{**} tagging may resolve kinematical ambiguities in semileptonic decays of charged and neutral B mesons by choosing between two solutions for the momentum of the undetected neutrino. In hadron colliders and Z^0 factories this technique may make high statistics determination of the form factors in semileptonic decays possible, and would enable precise measurements of V_{cb} and V_{ub} [40].

However, the primary application of B^{**} tagging would be in the expected large CP-violation asymmetry[20] [53]. Theoretically these asymmetries can be interpreted most easily in the decays of the neutral B meson into CP eigenstates f, such as $J/\psi K_s$. A state which was produced as B^0 at time $t = 0$ decays into a CP eigenstate f with probability D_f, while a state which was $\bar{B}^0$ at $t = 0$ decays into f with probability $\bar{D}_f$. The time integrated asymmetry can be written as

$$A(f) \equiv \frac{\Gamma(B^0_{t=0} \to f) - \Gamma(\bar{B}^0_{t=0} \to f)}{\Gamma(B^0_{t=0} \to f) + \Gamma(\bar{B}^0_{t=0} \to f)} = \frac{D_f - \bar{D}_f}{D_f + \bar{D}_f} \ . \tag{2.55}$$

For the final state $f = J/\psi K_s$, it has been shown that the asymmetry $A(f)$ measures the angle β of the unitarity triangle (a fundamental parameter of the CKM matrix) to a very good approximation [54] (for notation see, e.g. Ref. [12])

$$A(J/\psi K_s) = -\frac{x_d}{1 + x_d^2} \cdot \sin 2\beta \ , \tag{2.56}$$

since a single amplitude contributes to each decay $B^0 \to J/\psi K_s$ and $\bar{B}^0 \to J/\psi \bar{K}_s$. The parameter x_d is known as the mass mixing parameter and has been extracted from time integrated B^0_d-$\bar{B}^0_d$ mixing analyses [35].

This discussion shows the importance of B^{**} tagging for future experiments on CP-violation in the B system. The work of this thesis is dedicated to the first observation of the B^{**} meson and to the investigation of its properties.

2.5 *b* Baryon Spectroscopy

2.5.1 Heavy Baryons

Heavy baryons are bound states formed from a heavy quark and a light diquark system. The spin-parity quantum numbers J^P of the light diquark system are determined from the spin and orbital degrees of freedom of the two light quarks that make up the diquark system. From the spin degrees of freedom of the two light quarks one obtains both spin 0 and spin 1 states. The total orbital state of the diquark system is characterized by two angular degrees of freedom which we take to be the two independent relative momenta $k = (p_1 - p_2)/2$ and $K = (p_1 + p_2 - 2p_3)/2$ which can be formed from the two light momenta p_1 and p_2 and the heavy quark momentum p_3. The k-orbital momentum describes relative orbital excitations of the two light quarks, and the K-orbital momentum describes orbital excitation of the center of mass of the two light quarks relative to the heavy quark as shown in Fig. 2.15.

The wave function may be viewed as if the heavy quark (charm or bottom) at the center is surrounded by a cloud corresponding to a light diquark system. The only communication between the cloud and the center is via gluons. But since the gluons are flavour-blind the light cloud knows nothing about the flavour of the center. Also, for infinitely heavy quarks, there

[20] Up till now CP-violation has only been observed in the $K^0\bar{K}^0$ system.

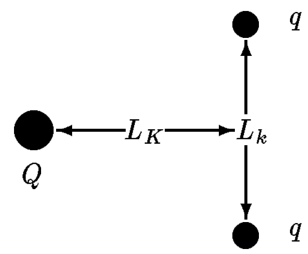

Figure 2.15: *Orbital angular momenta of a light diquark system. L_k describes relative orbital momentum of the two light quarks and L_K describes orbital momentum of the center of mass of the light quarks relative to the heavy quark.*

is no spin communication between the cloud and the center. Thus, one concludes that, in the heavy mass limit, a bottom baryon at rest is identical to a charm baryon at rest regardless of the spin orientation of the heavy quarks. First order corrections to this limit would be proportional to $1/m_Q$ (as discussed in section 2.2.4) [21].

The ground state heavy baryons ($L_k = L_K = 0$) are made from the heavy quark Q with spin-parity $J^P = 1/2^+$ and a light diquark system with spin-parity 0^+ and 1^+ moving in an s-wave state relative to the heavy quark. When one combines the diquark spin with the heavy quark's spin one obtains the ground state heavy baryons Λ_Q and Σ_Q/Σ_Q^* according to the following coupling scheme:

$$\begin{array}{cccc} 0^+ \otimes \frac{1}{2}^+ & \rightarrow & J^P = \frac{1}{2}^+ & : \ \Lambda_Q \\ & \nearrow & J^P = \frac{1}{2}^+ & : \ \Sigma_Q \\ 1^+ \otimes \frac{1}{2}^+ & & & \\ & \searrow & J^P = \frac{3}{2}^+ & : \ \Sigma_Q^* \end{array}$$

The two states Σ_Q and Σ_Q^* are exactly degenerate in the heavy quark limit since the heavy quark possesses no spin interaction with the light diquark system as $m_Q \to \infty$. Parts of the work on this thesis will focus on the search for the charged Σ_b and Σ_b^* baryons, with quark content (uub) for the $\Sigma_b^{(*)+}$ and (ddb) for the $\Sigma_b^{(*)-}$. They are expected to decay strongly into $\Lambda_b\pi$.

2.5.2 Present Knowledge about *b* Baryons

The present experimental knowledge about b baryons is very limited. First measurements show that roughly $(10 \pm 4)\%$ [56] of primary b quarks in e^+e^- annihilation fragment into baryons, while the remaining b quarks fragment into B mesons (see also Fig. 2.12). Fig. 2.2 shows the SU(4) baryon multiplets made of u, d, s and b quarks, where picture (a) corresponds

[21] A comprehensive theoretical review about heavy baryons is given in Ref. [55].

Quantity	Experiment	Measurement	Ref.
Mass m_{Λ_b} [MeV/c^2]	ALEPH	$5621 \pm 17 \pm 15$	[57]
	DELPHI	$5656 \pm 22 \pm 6$	[58]
	PDG Average	5641 ± 50	[12]
Lifetime τ_{Λ_b} [ps]	ALEPH	$1.02^{+0.23}_{-0.18} \pm 0.06$	[59]
	DELPHI	$1.10^{+0.16+0.05}_{-0.14-0.08}$	[60]
	OPAL	$1.14^{+0.22}_{-0.19} \pm 0.07$	[61]
Polarisation P_{Λ_b}	ALEPH	$-0.26^{+0.23+0.13}_{-0.20-0.12}$	[62]
Rate $f(b \to \Lambda_b) \cdot Br(\Lambda_b \to \Lambda \ell \bar{\nu} X)$	DELPHI	$(3.0 \pm 0.6 \pm 0.4) \cdot 10^{-3}$	[63]
	OPAL	$(2.91 \pm 0.23 \pm 0.25) \cdot 10^{-3}$	[64]
Rate $f(b \to \Lambda_b) \cdot Br(\Lambda_b \to \Lambda_c \ell \bar{\nu} X)$	ALEPH	$(15.1 \pm 2.9 \pm 2.3) \cdot 10^{-3}$	[59]
	DELPHI	$(11.8 \pm 2.6^{+3.1}_{-2.1}) \cdot 10^{-3}$	[63]
Lifetime τ_{Ξ_b} [ps]	DELPHI	$1.5^{+0.7}_{-0.4} \pm 0.3$	[65]
Rate $f(b \to \Xi_b) \cdot Br(\Xi_b \to \Xi^- \ell \bar{\nu} X)$	ALEPH	$(5.3 \pm 1.3 \pm 0.7) \cdot 10^{-4}$	[66]
	DELPHI	$(6.6 \pm 1.7 \pm 1.0) \cdot 10^{-4}$	[60]
	OPAL	$< 5.1 \cdot 10^{-4}$ (95% c.l.)	[67]

Table 2.6: *Present knowledge about b baryons. Properties of Λ_b and Ξ_b baryons as measured by the LEP experiments.*

to the 20-plet with SU(3) octet ($J^P = 1/2^+$), and picture (b) corresponds to the 20-plet with SU(3) decuplet ($J^P = 3/2^+$). The present knowledge on b baryons is summarized in Tab. 2.6. From the b baryons only the Λ_b state is experimentally established. Most of the b baryons are expected to decay into Λ_b by strong or electromagnetic interactions. Since the Λ_b is the lightest b baryon, it decays weakly. It has been observed in the final states $\Lambda_b \to \Lambda J/\psi$, $\to pD^0\pi^-$, $\to \Lambda_c^+\pi^+\pi^-\pi^-$, $\to \Lambda\ell^- X$ and $\to \Lambda_c^+\ell^- X$ [12]. Note that the Λ_b lifetime is roughly 30% lower than the lifetime of the B meson [59–61]. Some evidence has also been obtained for the existence of the Ξ_b baryon [65–67], otherwise there is nothing known about excited b baryons.

The spectroscopy in the c baryon sector can serve as a guide in the searches for new b baryons. The Λ_c^+ has been observed in many channels e.g. $\Lambda_c^+ \to p\bar{K}^0$, $\to pK^-\pi^+$, $\to p\bar{K}^0\pi^+\pi^-$ and $\to \Lambda\pi^+\pi^0$. It has a mass of 2285.1 ± 0.6 MeV/c^2 [12]. Furthermore, the $\Sigma_c(2455)$ has been identified, decaying to almost hundred percent into $\Lambda_c\pi$. The following masses have been measured: $m(\Sigma_c(2455)^{++}) = 2453.1 \pm 0.6$MeV/c^2, $m(\Sigma_c(2455)^+) = 2453.8 \pm 0.9$MeV/c^2 and $m(\Sigma_c(2455)^0) = 2452.4 \pm 0.7$MeV/c^2 [12]. The Σ_c^* has not yet been discovered.

2.5.3 Predictions for Σ_b and Σ_b^* Baryons

Predictions of Masses

The simplest approach in predicting the mass difference between Σ_b and Λ_b consists of a simple extrapolation from the c baryon sector ignoring all $1/m_b$ corrections. Taking the Particle-Data-Group [12] mass values for the Σ_c and Λ_c leads to

$$m(\Sigma_b) - m(\Lambda_b) = 168\,\mathrm{MeV/c^2}\ . \tag{2.57}$$

As already said, in this simple approach the state Σ_b^* would have the same mass as Σ_b, since there is no spin communication between the b quark and the diquark.

A more sophisticated model for the masses of Σ_b and Σ_b^* (dealing with corrections in $1/m_b$) has recently (1995) been published by Roncaglia, Dzierba, Lichtenberg and Predazzi [68]. They argue that the quark potential model has been the most successful tool enabling physicists to calculate the masses of normal mesons and baryons containing heavy quarks. However, potential models suffer from the fact that, although motivated by QCD, they have not been derived from basic theory (QCD). Therefore, predictions about hadron masses are made with complementary methods which use general properties of the potential but not its specific form. Complementary constraints are obtained from (1) hadron (and quark) masses from the Feynman-Hellman theorem, (2) theorems which relate the ordering of bound state energy levels to certain properties of potentials, and (3) regularities in known hadron masses, which yield estimates of undiscovered hadrons using either interpolation or semi-empirical mass formulae. Exploiting these methods, the following mass predictions for the Σ_b and Σ_b^* baryon are obtained [68]:

$$m(\Sigma_b) - m(\Lambda_b) = 200 \pm 20\,\mathrm{MeV/c^2}\ , \tag{2.58}$$

$$m(\Sigma_b^*) - m(\Lambda_b) = 230 \pm 20\,\mathrm{MeV/c^2}\ . \tag{2.59}$$

A similar mass prediction for the Σ_b baryon has already been obtained in a paper from 1981 by A. Martin [69]:

$$m(\Sigma_b) - m(\Lambda_b) = 197 \pm 20\,\mathrm{MeV/c^2}\ . \tag{2.60}$$

Predictions of Widths

The widths for the transitions $\Sigma_b/\Sigma_b^* \to \Lambda_b\pi$ can be estimated in the nonrelativistic quark model by using a pion quark coupling estimated from the *Goldberger-Trieman* relation. This computation has been done by Yan *et al.* [70]. They find

$$\Gamma = \frac{g_A^2}{6\pi f_\pi^2} \cdot p_\pi^3 = 28\,\mathrm{MeV/c^2} \cdot \left(\frac{p_\pi}{200\,\mathrm{MeV/c}}\right)^3\ , \tag{2.61}$$

where p_π is the pion three momentum in the $\Sigma_b^{(*)}$ rest frame, $f_\pi = 93\mathrm{MeV/c^{1/2}}$, and g_A is the axial vector coupling of the constituent quark. In the numerical estimate, we take $g_A = 0.75$ to give the correct g_A for the nucleon [71]. The Σ_b and the Σ_b^* have the same decay rate up to kinematic factors, since the decay mechanism does not directly involve the heavy quark.

2.6 Summary of the Chapter

- The static quark model describes nearly all experimentally known meson and baryon states. Furthermore, predictions for the quantum numbers of unknown meson and baryon states can be derived.

- The dynamic theory of the strong interaction is Quantum Chromodynamics (QCD). The non-Abelian structure of the theory provides the key point for the understanding of confinement and asymptotic freedom.

- Quantum chromodynamics reveals additional symmetries in the limit of $m_d - m_u \to 0$ (Isospin Symmetry), as well as in the limit of $m_q \to 0$ (Chiral Symmetry), and in the heavy quark limit $m_Q \to \infty$ (Heavy Quark Symmetry). The latter symmetry is described mathematically by Heavy Quark Effective Theory (HQET).

- In the heavy quark limit the spin of a heavy quark decouples from the light quark degrees of freedom (Heavy Spin Symmetry), and the flavour of the heavy quark becomes irrelevant to the system (Heavy Flavour Symmetry). Heavy Quark Effective Theory can be constructed by taking the limit $m_Q \to \infty$ (with four-momenta fixed) of the Feynman rules of QCD. In an equivalent approach the same limit is taken for the QCD Lagrangian leading to the same Feynman rules.

- The non-relativistic quark potential model is the most successful tool enabling physicists to calculate masses and properties of mesons and baryons. The most general non-relativistic ansatz for a quark-antiquark system starts with the Breit-Fermi Hamilton function. For heavy quark systems, e.g. charmonium ($c\bar{c}$) or bottomonium ($b\bar{b}$), spin dependent terms in the Hamilton function can be treated by perturbation theory.

- Hadronic Z^0 decays in e^+e^- annihilation can be described by four phases, which are implemented in the JETSET [22] simulation program (Electroweak Phase, Perturbative Phase, Fragmentation Phase and Particle Decay Phase). The perturbative phase of short distance QCD is modeled either by the parton cross sections obtained by the exact second order QCD matrix element at an optimized scale or by the parton shower algorithm. The low Q^2 QCD processes of hadron formation in JETSET are described by the string fragmentation model.

- Quark model and dynamical implications from HQET provide predictions for orbitally excited B mesons. They are commonly labeled as B^{**} (B_s^{**}) mesons, and are grouped into two doublets with $j_q = 1/2$ ($J^P = 0^+, 1^+$) and $j_q = 3/2$ ($J^P = 1^+, 2^+$). Two of these states ($j_q = 3/2$) are expected to have narrow width ($\Gamma \simeq 20$ MeV/c^2), since they decay through d-wave transitions. The expected main decay modes are $B^{**} \to B^{(*)}\pi$ ($B_s^{**} \to B^{(*)}K$). Masses and decay widths of these states have been predicted. Observations from the D meson sector motivate the search for orbitally excited B mesons.

- The present knowledge about b baryons is very limited. Only the Λ_b is experimentally established. Predictions for the baryon masses of Σ_b and Σ_b^* are made using constraints on hadron (and quark) masses from the Feynman-Hellman theorem, theorems which relate the ordering of bound state energy levels to certain properties of potentials, and regularities in known hadron masses. The principal decay mode for Σ_b and Σ_b^* is expected be into $\Lambda_b\pi$.

Chapter 3

The Experiment

This chapter describes the experimental setup of the Large Electron Positron (LEP) collider at CERN. After an introduction to the LEP machine, the DELPHI detector, one of the four LEP experiments, is discussed in more detail. This is followed by a description of the DELPHI online and offline systems.

3.1 The LEP Collider

The LEP storage ring with a circumference of about 26.7 km is installed in the LEP tunnel, which has a diameter of 3.80 m and lies 50 to 175 meters below the surface across the frontiers between France (Pays de Gex) and Switzerland (Canton Genève) [72]. A schematic map of the local area is given in Fig 3.1. The LEP ring consists basically of a beam pipe, a set of magnets, acceleration sections and their power supplies. The magnets either bend or focus the electron beam, while the acceleration sections, consisting of several radio frequency cavities, provide the energy for the acceleration of the electrons and positrons. In total, there are 3 392 dipole magnets (for bending), and 876 quadrupole, 520 sextupole and 700 correction magnets (for focussing). Since the electrons and positrons have opposite electric charge and equal mass, they can circulate in opposite directions in a single beam pipe with the same arrangement of focussing and bending magnets. Therefore, unlike proton-proton colliding beam accelerators, LEP has only one beam pipe.

The energy of the electrons and positrons in the LEP100 phase is around 45.6 GeV ($\sqrt{s} = m_{Z^0}$). This is achieved in a several step procedure as shown in Fig. 3.2. In the first step of positron generation, electrons are accelerated at the LEP Injector Linacs (LIL) to an energy of about 200 MeV. Collisions with a target of high atomic number Z lead to the production of positrons with an average energy of 10 MeV. A small fraction ($\simeq 0.001$) of the positrons is accelerated by the second stage LIL to 600 MeV. The electrons for the electron beam are produced by a 10 MeV electron gun and are injected directly into the second stage LIL. In the next step the electrons and positrons are accumulated in the Electron Positron Accumulator (EPA) to increase the current of each beam. The Proton Synchrotron (PS) then accelerates the beams to 3.5 GeV followed by the Super Proton Synchrotron (SPS) which accelerates

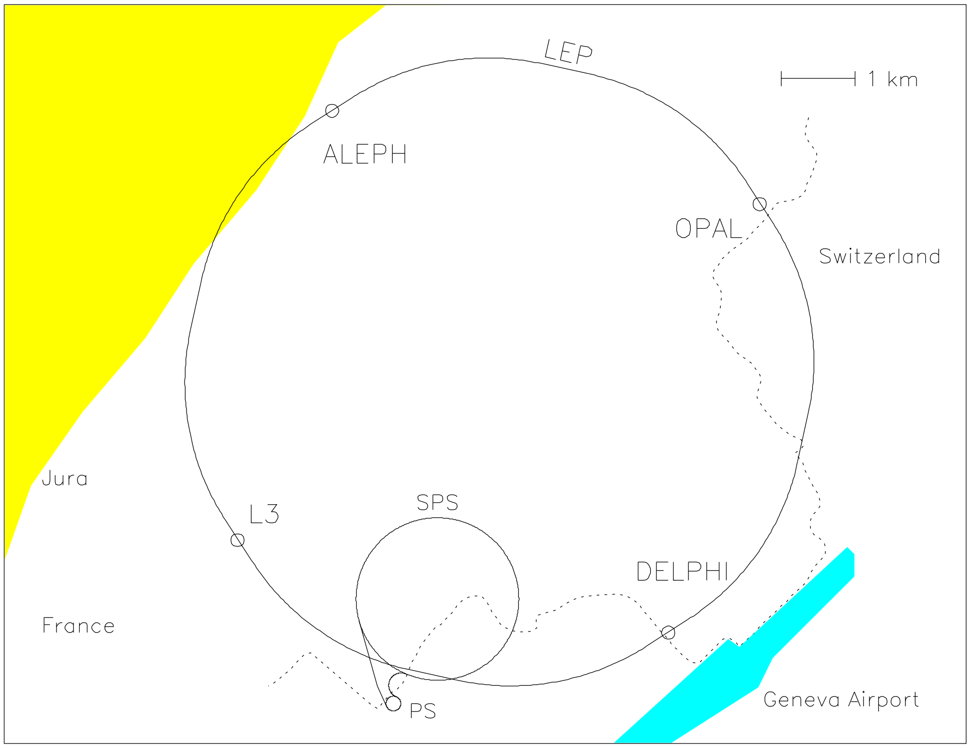

Figure 3.1: *Schematic map of the local area near the LEP collider. PS, SPS and the LEP rings are shown, together with the four LEP experiments ALEPH, DELPHI, L3 and OPAL.*

them to an energy of 20 GeV. Finally the beams are injected into LEP where the particles are accelerated to about 45.6 GeV. The energy loss ΔU due to synchrotron radiation is given by

$$\Delta U = 8.85 \cdot 10^{-5} \, \frac{E^4}{r} \cdot \frac{\mathrm{m}}{\mathrm{GeV}^3} \,, \tag{3.1}$$

where E is the beam energy and r the bending radius of the ring. The synchrotron radiation loss in LEP is not negligible and consumes about 1.2 MW of power. It is the major constraint on the maximum beam energy for LEP100 with the present accelerator sections.

Each beam is concentrated in short time bunches with a length of ≈ 4.5 cm. The transverse dimensions are $\sigma_x \approx 100$ μm and $\sigma_y \approx 10$ μm (corresponding to an elliptic beam profile). Each bunch contains roughly $2.5 \cdot 10^{11}$ electrons or positrons and circulates around the ring 11 250 times a second. Until mid 1992 four bunches for electrons and positrons were used. Starting in 1993 LEP also operates in an eight bunch (so-called *pretzel*) mode, and it has been tested successfully to run with *bunch trains*[1]. Both bunch systems are synchronized so that they cross each other at the four interaction points each of which is surrounded by one of the detectors ALEPH, DELPHI, L3 and OPAL. The rate of production of Z^0 events at the interaction points is increased, because the transverse size of the bunches is squeezed by strong superconducting quadrupole magnets close to the detectors.

[1] The running with 4 bunches, dividing each bunch into a train of several (mostly 4) bunches, is called bunch train mode.

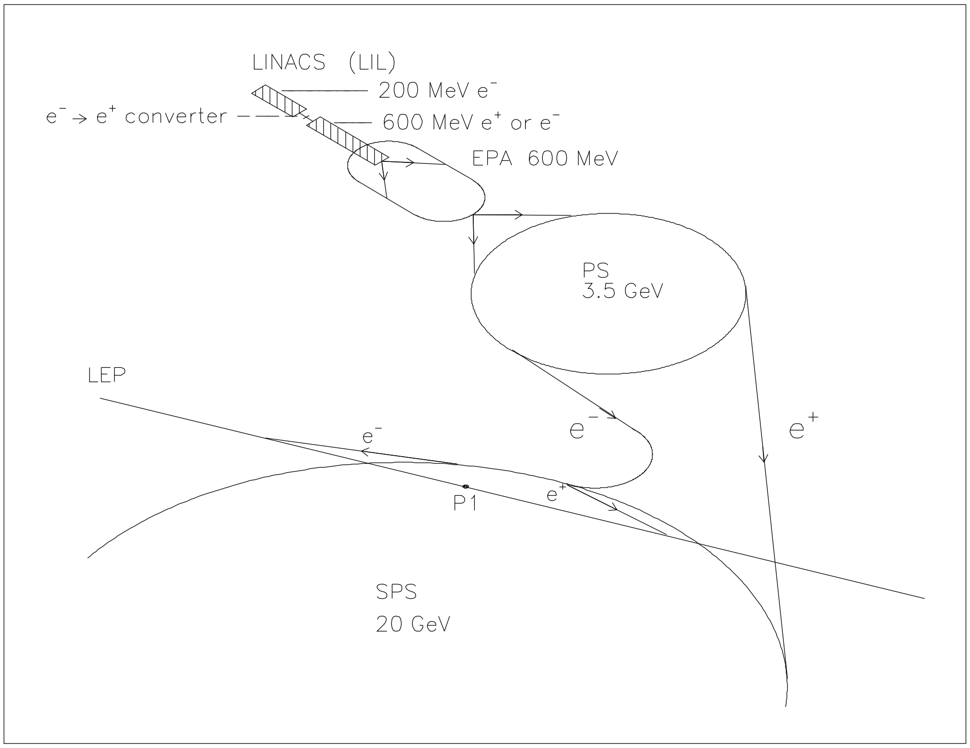

Figure 3.2: *Schematic view of the LEP injection system, which shows the two stage LEP Injector Linacs (LIL), the Electron Positron Accumulator (EPA), the Proton Synchrotron (PS), the Super Proton Synchrotron (SPS) and the LEP ring itself. The 10 MeV electron gun close to the $e^- \rightarrow e^+$ converter is not shown.*

From the physics point of view, two important machine parameters are the center of mass energy $\sqrt{s}$ and the luminosity $\mathcal{L}$. The center of mass energy $\sqrt{s}$ of an e^+e^- storage ring of two beams with exactly the same energy is twice the beam energy. This is the most economical way of achieving the highest possible center of mass energy. In order to get a stable beam several effects such as betatron oscillations[2], or beam-beam interactions[3], must be considered. An additional small effect which influences the beam energy on the per mill level is the phase of the moon. The surface of the earth is subject to the gravitational attraction of the moon. It moves since the rocks that make it up are elastic. At the new moon and when the moon is full, the earth's crust rises by some 25 cm in the Geneva area under the effect of these tides. This movement causes a variation of 1 mm in the circumference of LEP (for a total circumference of 26.7 km), which shifts the beam energy up to $\Delta E \approx 14$ MeV [74].

The luminosity $\mathcal{L}$ can be defined by

$$n = \sigma \cdot \mathcal{L} \ , \tag{3.2}$$

where n is the number of events per second of a given process and σ is the corresponding cross section. The luminosity depends on some specific machine parameters and can be expressed

[2] Oscillations of the beam around the ideal orbit of the machine are called betatron oscillations.

[3] Electromagnetic interactions between the beams lead to an increased betatron frequency.

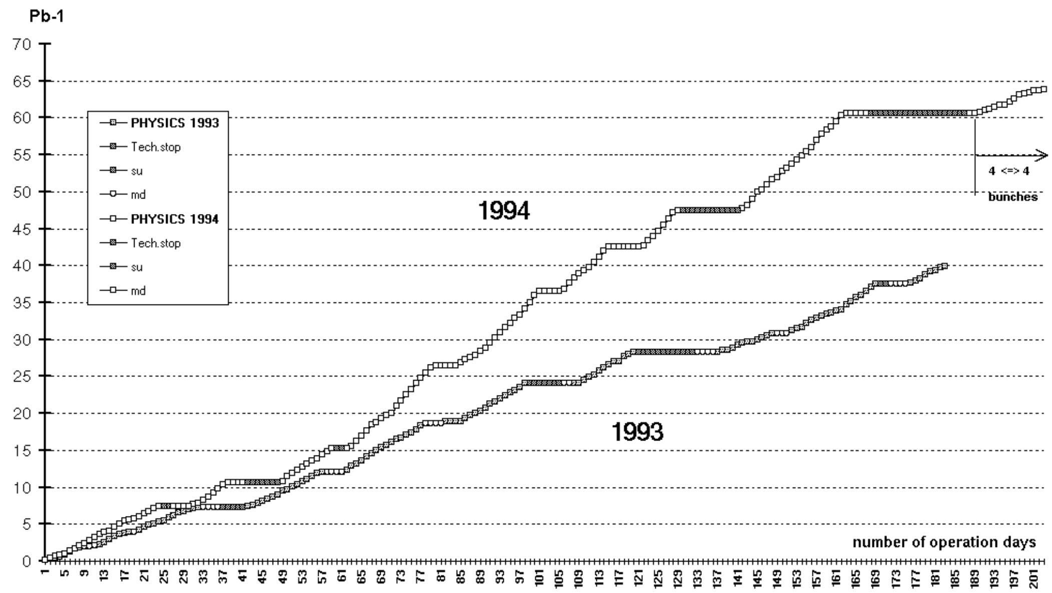

Figure 3.3: *Integrated luminosity averaged over the LEP experiments in the years 1993 and 1994. The horizontal plateaus correspond to technical stops and machine developments [73].*

in the following way

$$\mathcal{L} = \frac{N^+ \cdot N^- \cdot k \cdot f}{4\pi \cdot \sigma_x \cdot \sigma_y} \ , \tag{3.3}$$

where $N^\pm$ denotes the number of electrons or positrons in a bunch, k is the number of bunches, f is the revolution frequency and σ_x and σ_y are the horizontal and vertical widths of the beams at the collision point. The maximum luminosity obtained at LEP in 1994 was approximately 2.2 $\text{nb}^{-1}\text{s}^{-1}$. The integrated luminosity averaged over the four LEP experiments for the years 1993 and 1994 is shown in Fig. 3.3. In summary, an integrated luminosity of roughly 145 pb^{-1} has been collected in the years 1990-94 by each experiment. The beam current for an e^+e^- collider is defined as

$$I^\pm = N^\pm \cdot k \cdot f \cdot e^\pm \ , \tag{3.4}$$

where $e^\pm$ is the elementary charge of the electrons and positrons. Typical beam currents for LEP during the 1994 running period were 2.5 mA.

The operational phase of LEP100 ended in October 1995. Starting from 1996 the center of mass energy of LEP will be increased up to 180 GeV in order to produce W^+W^- pairs. With a scheduled integrated luminosity of 500 pb^{-1} roughly 10 000 $W^\pm$ pairs are expected per experiment. The main physics goals are investigations of the properties of the $W^\pm$ boson (e.g. a precise measurement of its mass), and searches for new physics (e.g. Higgs or supersymmetric particles). A serious problem for LEP200 is the energy consumption of the ring. Due to synchrotron radiation an energy loss of about 38 MW is expected for running in the eight bunch mode. This corresponds to roughly 10% of the production of a modern power station. In order to optimize the acceleration sections of LEP the conventional radio-frequency (RF) cavities are being exchanged with superconducting RF cavities.

3.2 The DELPHI Detector

The DELPHI detector is one of the four multi-purpose 4π detectors at LEP. DELPHI stands for DEtector with Lepton, Photon and Hadron Identification. A schematic view of the apparatus is given in Figs. 3.4 and 3.5. It was constructed and it is run by a collaboration of 540 physicists coming from 52 different universities and national laboratories. The construction time of DELPHI was roughly 7 years. The costs for the construction of DELPHI not including the manpower provided by the institutes were in the order of 150 MSFr. Since the operational beginning of LEP in November 1989 DELPHI has collected over 3 400 000 hadronic Z^0 events.

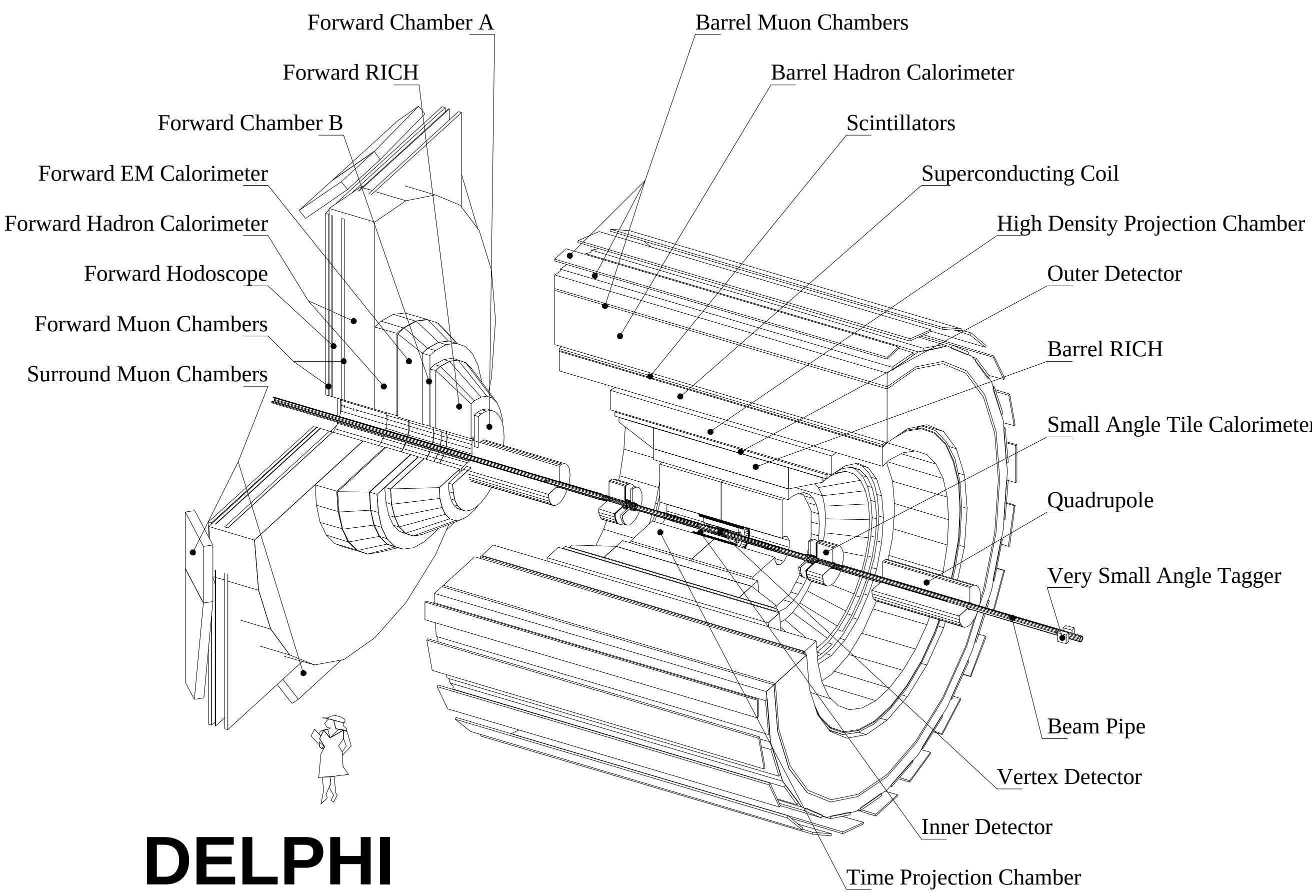

Figure 3.4: *Schematic view of the DELPHI detector: Vertex Detector (VD), Inner Detector (ID), Time Projection Chamber (TPC), Ring Imaging Cherenkov Counter (RICH), Outer Detector (OD), High density Projection Chamber (HPC), Superconducting Solenoid, Time-of-Flight Scintillators (TOF), Hadron Calorimeter (HAC), Muon Chambers (MUB, MUF and MUS), Forward Drift Chambers (FCA and FCB), Small Angle Tile Calorimeter (STIC), Forward Electromagnetic Calorimeter (FEMC).*

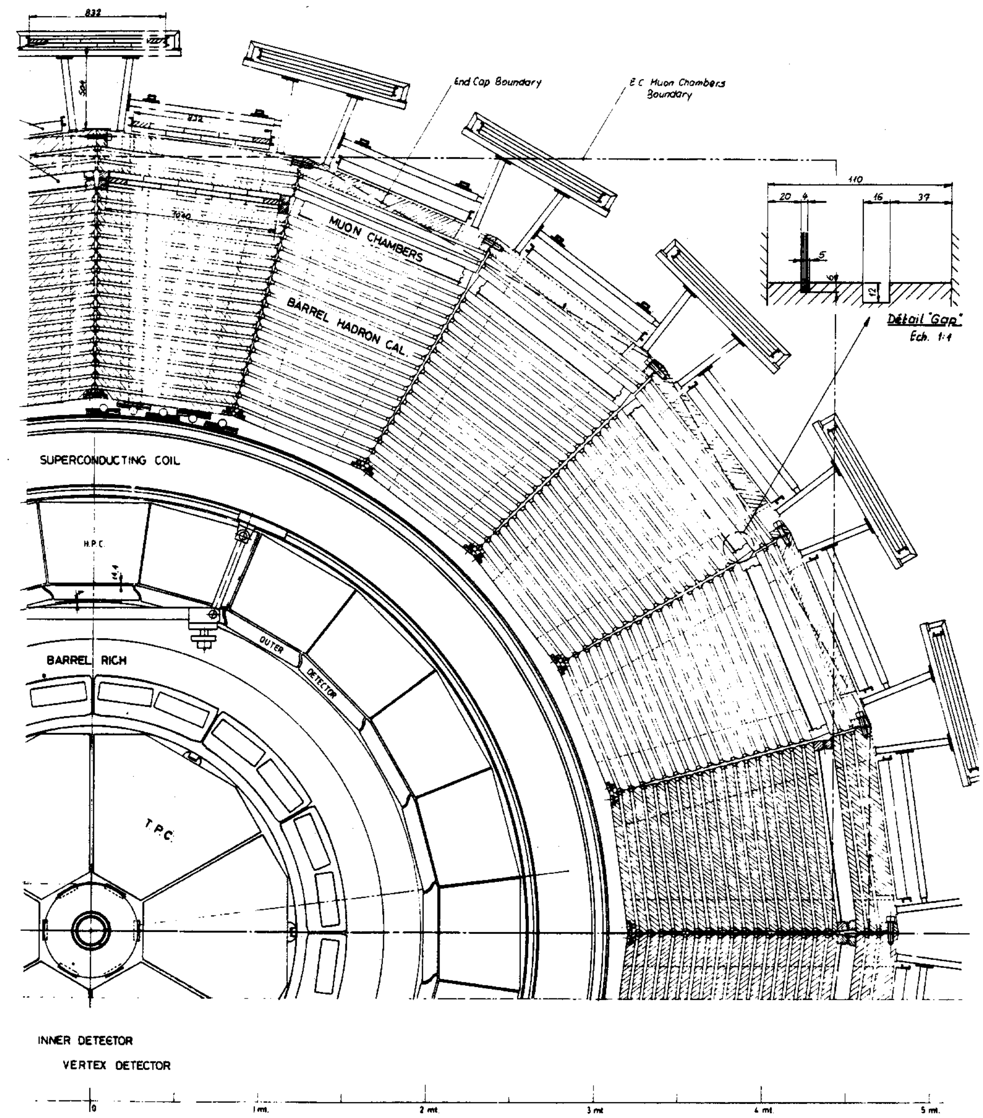

Figure 3.5: *Schematic view of the DELPHI detector (barrel part) along the beam pipe.*

The apparatus can be divided into three main parts: the cylindrical barrel-part with a total length of 8 m and a diameter of 10 m which lies axially symmetric to the beam pipe, and two large end-caps (3 m long and 10 m diameter). It has a total weight of approximately 3 500 tons. The detector architecture has, besides some conventional components of an e^+e^- detector, additional features for particle identification, e.g. the Ring Imaging CHerenkov (RICH) detectors, which allow a separation of kaons, pions and protons in certain momentum regions. Most of the elements in DELPHI provide direct three-dimensional information, which is read out via some 250 000 channels, 14 dedicated computers and one main computer. This section reviews the main (barrel) detector components of DELPHI and provides information concerning the performance. More details can be found in Refs. [75–78].

3.2.1 The Tracking System

The Solenoid

A large part of the barrel detector is embedded in the magnetic field (1.2 T) of the large superconducting coil (length 7.2 m, inner diameter 5.2 m), made of copper-packed Ni-Ti filaments operating at $T = 4.5$ K with a total current of 5 000 A. The magnetic field allows a precise momentum determination of charged particles from the curvature of their tracks in the $R\phi$ plane[4]. Moreover, it plays an essential role in reducing the transverse diffusion of the gas drift devices, e.g. in the central Time Projection Chamber (TPC) and in the High density Projection Chamber (HPC).

The Vertex Detector

The DELPHI Vertex Detector (VD) consists of three layers of silicon micro-strip detectors which surround the interaction point at radii of 6.3, 9.0 and 10.9 cm parallel to the beam-pipe (see Fig. 3.6 and 3.7). Each layer consists of 24 modules covering a length of 23 cm (27 cm for the closer layer). In 1994 two layers of the VD were equipped with double-sided micro-strip detectors which provide measurements in $R\phi$ and Z direction. The intrinsic resolution of the VD is 7.6 μm in $R\phi$ and 9 μm in Z (for perpendicular tracks). The short lever arm to the interaction point results in an excellent impact parameter[5] resolution in $R\phi$ and Z.

The impact parameter uncertainty, σ_{IP}, has contributions from three independent sources. There is a purely geometric extrapolation uncertainty, σ_0, due to the point measurement error in the VD, the uncertainty due to multiple scattering in the beam-pipe and the layers of the VD, σ_{MS}, and the uncertainty on the position of the primary vertex, σ_V. Thus, $\sigma_{IP}^2 = \sigma_0^2 + \sigma_{MS}^2 + \sigma_V^2$. The impact parameter uncertainty has successfully been parametrized for the $R\phi$ direction

$$\sigma_{IP}(R\phi) = \sqrt{\left(\frac{65\ \mathrm{GeV}\mu\mathrm{m/c}}{p \cdot \sin^{3/2}\Theta}\right)^2 + (20\,\mu\mathrm{m})^2} \quad , \tag{3.5}$$

and for the Z direction

$$\sigma_{IP}(Z) = \sqrt{\left(\frac{71\ \mathrm{GeV}\mu\mathrm{m/c}}{p \cdot \sin^{5/2}\Theta}\right)^2 + (34\,\mu\mathrm{m})^2} \quad , \tag{3.6}$$

where p is the track momentum [GeV/c] and Θ the corresponding polar angle [77]. To achieve the extremely high precision, which is of the order of the inhomogenities of a smooth surface, a careful alignment of each layer is necessary. Measurements on high momentum particle trajectories (e.g. $Z^0 \to \mu^+\mu^-$) as well as the overlaps between the neighboring wafers in each layer are very useful in this respect.

[4]DELPHI has a cylinder coordinate system with the Z axis coinciding with the electron beam direction.

[5]The impact parameter is defined as the distance of closest approach of a track to the primary vertex.

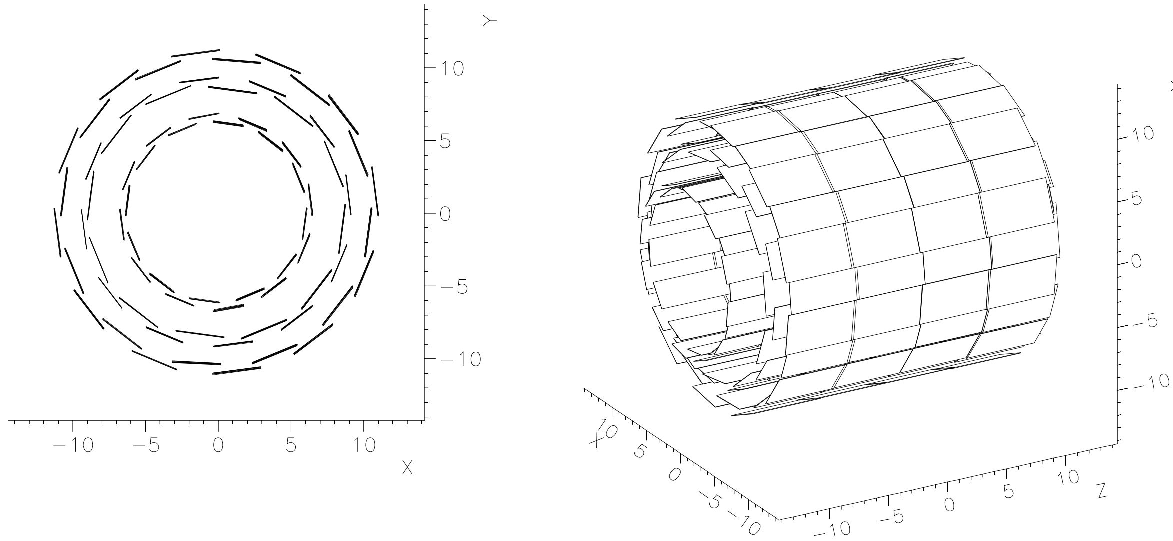

Figure 3.6: *Schematic layout of the DELPHI microvertex detector (in cm). (a) Projection on the plane transverse to the beam. (b) Perspective view.*

The Inner Detector

The Inner Detector (ID) is used for fast trigger decisions and it yields some redundancy for the vertex reconstruction and track separation done by the VD. It covers a cylindrical volume between the radii 12 cm and 28 cm and a total length of 1 m. The apparatus is split into an inner drift chamber part with a jet-chamber architecture pointing to the interaction point, and an outer MWPC[6] for radii greater 23 cm. All wires are parallel to the beam. The jet chamber is divided into 24 sectors in ϕ with 24 wires each. The high voltage is chosen so that the drift velocity rises in the same way as the drift distance e.g. linearly with R. Due to this architecture ideal tracks stemming from the interaction point lead to pulses arriving on the 24 wires all at once. This allows a fast trigger decision (3μs) weather tracks come from the interaction point. Five layers of 192 field wires in the MWPC part serve to resolve the left-right ambiguity of the jet-chamber, while 192 circular cathode strips (pitch = 5 mm) give Z information. The resolutions obtained for $Z^0 \rightarrow \mu^+\mu^-$ events is $\sigma(R\phi) = 50$ μm and $\sigma(\phi) = 1.5$ mrad [78]. The two track separation is about 1 mm. In the 1995 shutdown the ID was replaced by an extendet device with a total length of 1.40 m.

The Time Projection Chamber

The Time Projection Chamber (TPC) is the main tracking device of DELPHI. It covers the active volume from $R = 35$ cm to 111 cm ($|Z| \leq 134$ cm) and is filled by an argone-methane gas mixture (Ar/CH_4 : 80/20%). The TPC is divided into two hemispheres of six sectors in ϕ. It is read out at the end-caps by 16 concentric pad rows and 192 anode wires. A track passing

[6]MWPC = Multi Wire Proportional Chamber.

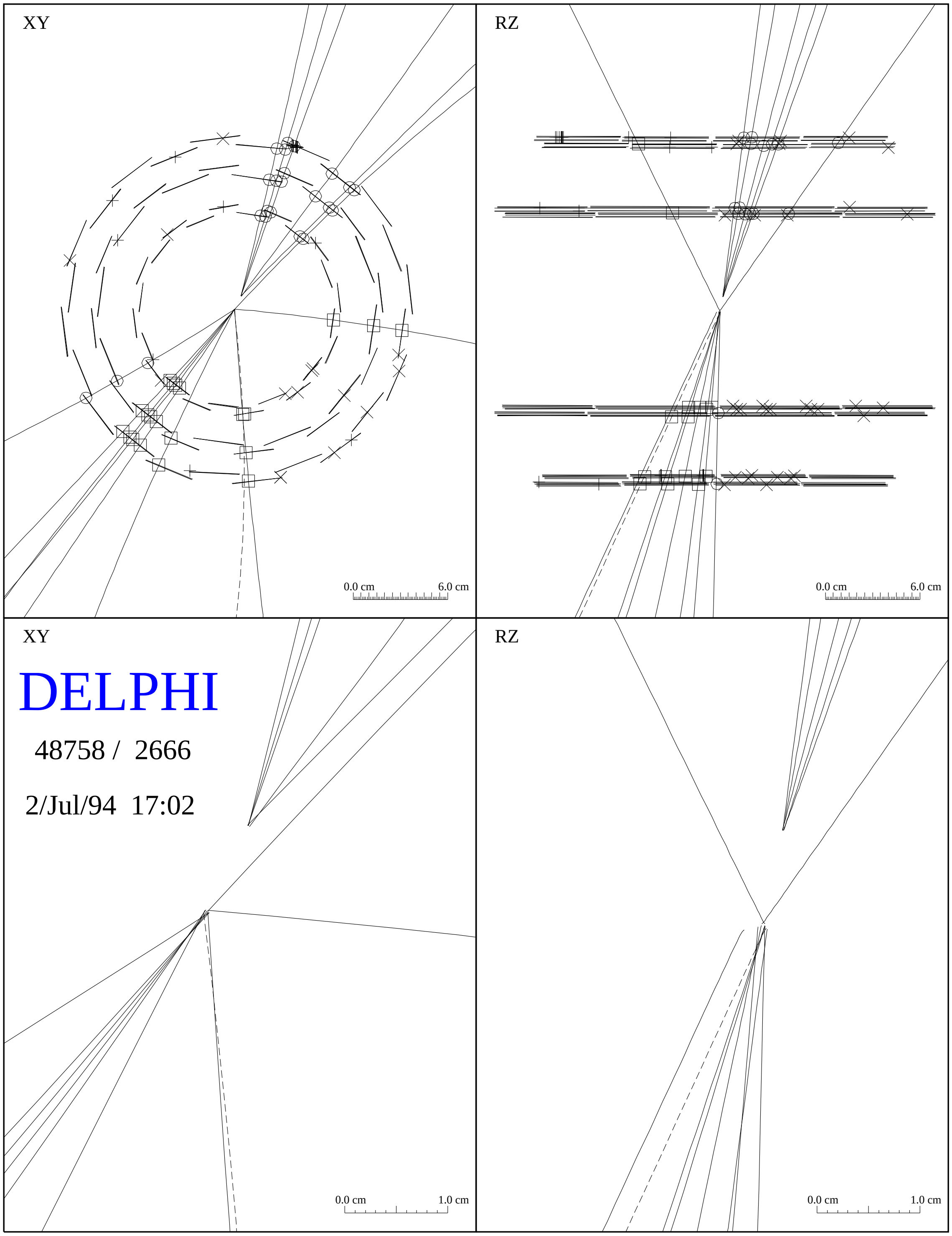

Figure 3.7: *The XY and the RZ projection of a hadronic Z^0 decay observed in the DELPHI vertex detector. Circles and squares indicate vertex detector hits associated to tracks, crosses correspond to unassociated hits.*

through the gas volume leaves a tube of ionization along its way. Due to a homogeneous electric field along the Z direction, the charges are drifted in the gas with a drift velocity of $v_D = 6.7$ cm/μs to the end-caps. The $R\phi$ resolution is governed by the segmentation of the read-out structure, while the Z coordinate is measured by the drift time. In this way up to 16 three-dimensional space points can be measured per track. The single point resolution for tracks from multi-hadronic Z^0 decays is 250 μm in the $R\phi$ plane and 880 μm in the RZ plane [78]. The two-point separation is of the order of 1 cm. Particle identification with the TPC is performed using the dE/dx measurement for charged tracks. This is described in detail in section 4.5.

The Outer Detector

The Outer Detector (OD) is a drift chamber which essentially provides a fast trigger information in $R\phi$ as well as in Z. It consists of five layers of drift tubes at a radius between 198 and 206 cm, covering an angular region in Θ between 42^o and 138^o. The OD gives points with good spatial resolution at a radius of 2 m from the interaction point, which increases the lever arm for the track reconstruction. All five layers provide precise $R\phi$ measurements with a resolution of $\sigma_{R\phi} = 110$ μm [78]. The longitudinal information in Z is obtained by the relative timing of the signals from both ends. A resolution of $\sigma_Z = 3.5$ cm is achieved [78].

The Performance of the Tracking System

The design of the DELPHI detector which includes the RICH detectors for particle identification limits the size of the central tracking devices. Therefore, a system of several tracking components (e.g. VD, ID, TPC and OD for the barrel part) has been constructed. The alignment of the different components and the disentangling of systematic effects (e.g. shifts or torsions) is essential for a good momentum resolution. By using $Z^0 \to \mu^+\mu^-$ events the total momentum resolution in the barrel part of the detector is determined to be

$$\sigma(1/p) = 0.57 \times 10^{-3} (\mathrm{GeV/c})^{-1} , \tag{3.7}$$

combining VD, ID, TPC and OD track elements [78]. The momentum resolution in the forward region with $20^o \leq \Theta \leq 35^o$ is

$$\sigma(1/p) = 1.31 \times 10^{-3} (\mathrm{GeV/c})^{-1} , \tag{3.8}$$

using at least VD and FCB[7] information [78].

3.2.2 The Calorimeters

The High Density Projection Chamber

The High density Projection Chamber (HPC) is the barrel electromagnetic calorimeter in DELPHI [79]. It is the first large time-projection gas calorimeter, which provides a full

[7] The Forward Chambers (FCA and FCB) are the main tracking devices in the forward region (see Fig. 3.4).

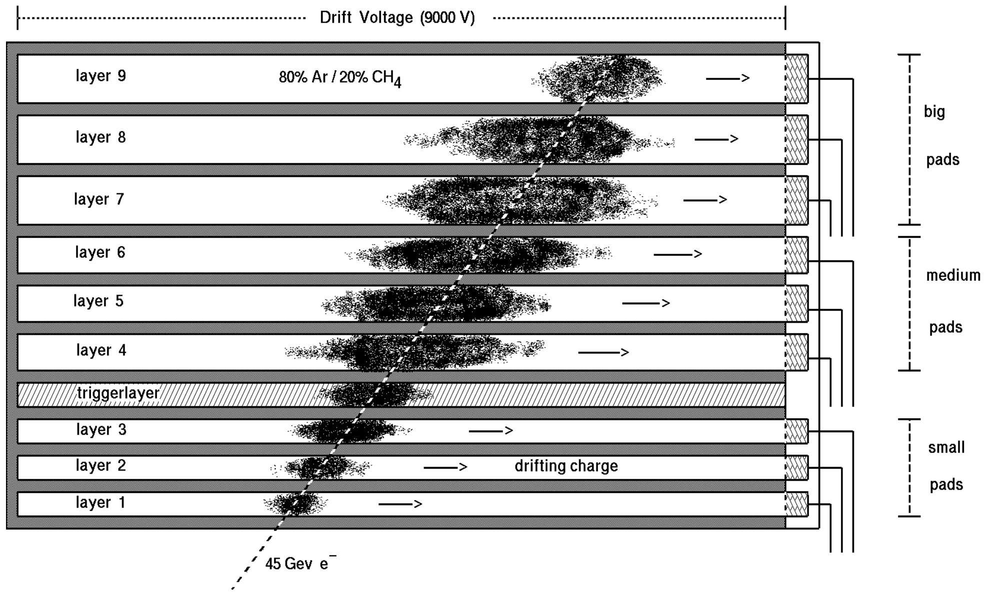

Figure 3.8: *Schematic view of the layer structure of a single HPC module. An entering electron initiates an electromagnetic shower in the converter. The produced charge is drifted to a planar MWPC. The full detector consists of 144 such modules.*

three-dimensional reconstruction of an electromagnetic shower. It covers the angular region $42^\circ < \Theta < 138^\circ$. The HPC consists of 144 modules arranged in 6 rings inside the cryostat of the magnet. Each ring consists of 24 modules concentrically arranged around the Z axis with an inner radius of 208 cm and an outer radius of 260 cm. In principle, each HPC module is a TPC, with layers of a high dense material (lead) in the gas volume, where electromagnetic showers are initiated (see Fig. 3.8). The converter thickness varies between 18 and 22 radiation length depending on the polar angle Θ. It consists of 40 planes of lead with a thickness of about 3 mm. The 39 gas gaps are filled with an argone-methane gas mixture (Ar/CH_4 : 80/20%). The produced cloud of electric charge form an electromagnetic shower. It is drifted with a velocity of $v_D = 5.5$ cm/μs in a homogeneous electric field ($E = 106$ V/cm), which is parallel to the $\vec{B}$ field. The read-out of a single module is performed at the end of each module by a planar MWPC, which consists of 39 sense wires and is segmented in 128 pads. Each pad is read out in 256 time buckets. This leads to a total number of $144 \times 128 \times 256 = 4.7 \cdot 10^6$ ADC signals which are available per event. The energy resolution of the HPC for photons has been found to be

$$\frac{\sigma_E}{E} = \frac{32\%}{\sqrt{E[\mathrm{GeV}]}} \oplus 4.3\% \;, \tag{3.9}$$

using neutral pions reconstructed from one photon converted before the TPC, reconstructed with high precision, and one photon reconstructed in the HPC [78]. The angular resolution in ϕ is given by the segmentation of the read out ($\sigma_\phi = 3.1$ mrad). The Z information is evaluated from the drift time (leading to $\sigma_\Theta = 1.0$ mrad) [78].

The Hadron Calorimeter

The return yoke of the DELPHI superconducting solenoid is designed as an iron/gas hadron calorimeter (HAC). The angular acceptance of the instrument is $43^o < \Theta < 137^o$ in the barrel part, and $11^o < \Theta < 50^o$ and $130^o < \Theta < 169^o$ in the two forward parts. The active components of the HAC consist of 20 layers (19 in the forward region) of plastic-made wire chambers of 2 cm depth interleaved by 5 cm of iron. The energy resolution obtained from multi-hadronic Z^0 decays using the momentum information from the TPC is described by [78]

$$\frac{\sigma_E}{E} = \frac{112\%}{\sqrt{E[\mathrm{GeV}]}} \oplus 21\% \, . \tag{3.10}$$

The average depth of 1.5 m of the HAC together with the other detectors make DELPHI self-shielding so that even during runtime the detector is accessible.

The Luminosity Monitoring Detectors

The luminosity is measured via low Q^2 Bhabha scatter events which emerge from the interaction largely at small polar angles. Therefore, the Small angle Tile Calorimeter[8] (STIC) and the Very Small Angle Tagger (VSAT) are mounted 2.5 m and 7.7 m, respectively, from the interaction point close to the beam-pipe. The STIC is a lead/scintillator sampling calorimeter read out with wavelength shifting fibres and photoelectrode tubes. VSAT is a W-Si calorimeter of 24 radiation length sensitive between the polar angles of 5 and 7 mrad.

3.2.3 Particle Identification Devices

The identification of photons, electrons, muons and hadrons is generally done in a combined offline analysis of many detector components. This section emphasizes the subdetectors which are dedicated to particle identification.

The Ring Imaging Cherenkov Detectors

Charged particles traversing a dielectric medium with a velocity larger than the speed of light in that medium produce a cone of Cherenkov light. The emission angle Θ_{Ch} depends on the mass M and momentum p of the particle via the relation

$$\cos\Theta_{Ch} = \frac{\sqrt{1 + M^2/p^2}}{n} \, , \tag{3.11}$$

where n is the refractive index of the radiator medium. The number of photons emitted is proportional to $\sin^2\Theta_{Ch}$. This information (Cherenkov angle and number of photons) is used to evaluate masses of charged particles. The main goal of the RICH detectors is to separate

[8] The STIC detector replaced in 1994 the Small Angle Tagger (SAT) [76].

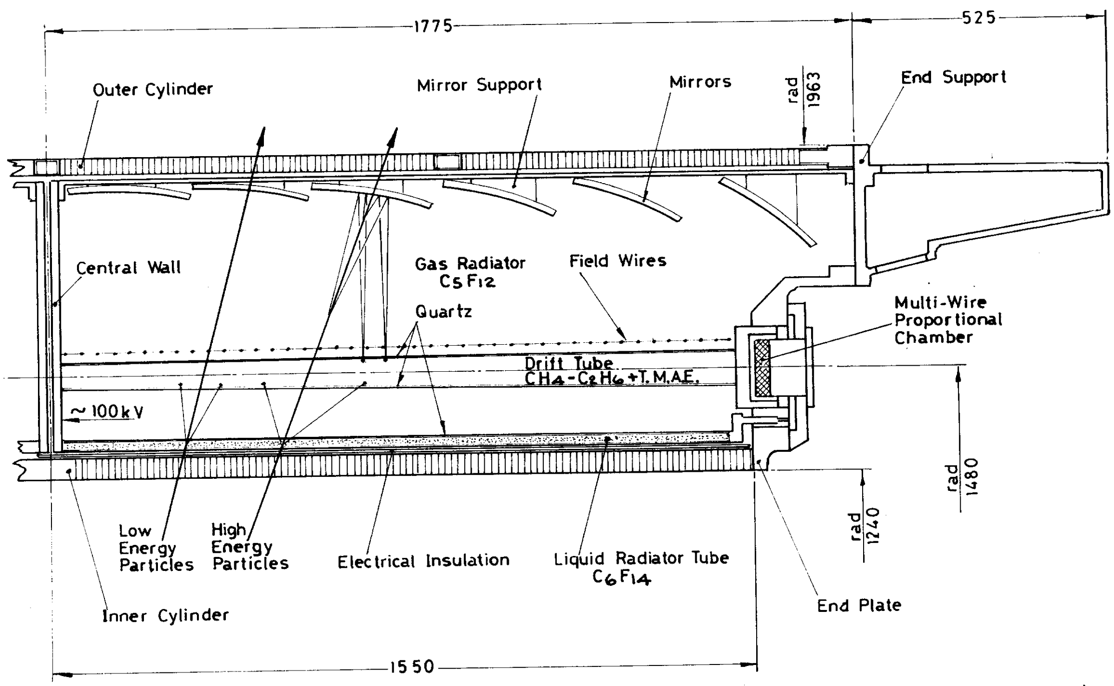

Figure 3.9: *Schematic view of the barrel RICH detector. The upper volume shows the gas radiator system filled with C_5F_{12}. The liquid radiator volume filled with C_6F_{14} is indicated as well. The Cherenkov photons are converted in $CH_4 - C_2H_6$+T.M.A.E. gas. The converted electrons drift for both systems to the proportional chamber, indicated on the right hand side. Note that the rings of the liquid and of the gas systems are displaced with respect to each other.*

kaons and protons form the large pion background. In the momentum range where kaons and protons are below the Cherenkov threshold, they do not emit light while lighter particles do. This property can also be used in the so-called *veto mode*.

The DELPHI RICH [80] contains two radiator systems of different refractive indices. A liquid radiator is used for particle identification in the momentum range from 0.7-4.0 GeV/c, and a gaseous radiator is used from 2.5-25.0 GeV/c. The full solid angle coverage is provided by two independent detectors (the forward and the barrel RICH). Perfluorocarbons were chosen as radiator media, both in the forward (liquid C_6F_{14}, gaseous C_4F_{10}) and in the barrel (liquid C_6F_{14}, gaseous C_5F_{12}). Photons in the range from 170-220 nm are focused onto photosensitive Time Projection Chambers, 48 in number in the barrel and 24 in each arm of the forward RICH. A schematic view of the DELPHI barrel RICH is given in Figure 3.9. More details on the operation of the RICH and the corresponding particle identification software are given in section 4.5.

The Muon Chambers

The DELPHI muon chambers are drift chambers which are located behind the hadron calorimeter. They provide a muon identification with an efficiency of about 95%. The Barrel, Forward and Surround MUon (BMU, FMU and SMU) chambers cover the polar angular region between 15^o and 165^o. Resolution measurements on isolated tracks give $\sigma_{R\phi} = 4$ mm. The Z coordinate is evaluated from delay time measurements (with a digitization window of 2 ns) obtaining a resolution of $\sigma_Z = 2.5$ cm [78].

The Time-of-Flight Counters

The Time-of-Flight (TOF) system is installed on the outer surface of the solenoid. It consists of a layer of 172 scintillation counters. The modules (19×2 cm^2 cross section and 3.5 m long) are read out at both ends by photo-multipliers connected by light guides. In the forward part of the DELPHI detector a similar system is installed as well. In the polar angle region from 15^o to 165^o the TOF system serves as a cosmic muon trigger as well as a cosmic veto during beam crossings. Cosmic ray runs show the time resolution to be 1.2 ns [78].

3.3 The DELPHI Online System

The DELPHI online system has to manage several functions during runtime: analyse the events on an elementary level and supply a fast trigger decision; read out all detector components and write the data on storage media (disks, tapes); run the power supplies, gas and cooling systems of the detector and control and log all slowly varying detector parameters (e.g. temperatures, pressures, high voltages, drift velocities etc.).

3.3.1 The Slow Control System

The DELPHI slow control architecture allows a single operator to monitor and control the complete status (high and low voltages, gas supplies etc.) of the entire detector. The performance comprises the display of the detector status, error messages and the continuous updating of the detector database for calibration and offline analysis. The 16 gas-filled subdetectors of DELPHI are supplied by a standardized gas flow control system including automatic survey of relative mixtures, cleaning and drying of the media. This system is realized using VAXstation computers shared with the DELPHI data aquisition. The hardware link is realized by G64-computers for the subdetectors connected by an ethernet link [81].

3.3.2 The Trigger

The time between two bunch crossovers is 22 μs (11 μs in 8-bunch mode). The DELPHI trigger system [82] is designed to handle large luminosities with large background event rates.

The four level hierarchy starts with two hardware triggers T1 and T2. The first level decision is made within 3 μs using e.g. the charged track condition of the ID and OD or correlated wires in the FCA and FCB. Other first level trigger conditions are provided by scintillator modules mounted inside in the HPC. If T1 fires, T2 decides within 39 μs, reanalyzing the slow drifting devices to confirm the T1 decision, e.g. the TPC for charged tracks and the HPC for electromagnetic energies. The T1 rate is usually around 400 Hz, the T2 rate around 4 Hz. T3 and T4 are software triggers running in real time. T3 confirms the T2 decision using the full granularity and resolution rejecting roughly half of the T2 events. The fourth level trigger program suppresses remaining background, flags events for physics analyses and provides an online event display for monitoring purposes [83]. There are at least 15 different trigger conditions for the levels 1 and 2 and further logical combinations are possible. The trigger system is highly redundant so that the efficiency can be tested by data itself. The efficiency for multi-hadronic events is almost 100%.

3.3.3 The Data Aquisition System

The heart of the DELPHI Data Aquisition System (DAS) [84] is a VAX8700 computer supported by a VAX4000 and several VAX and DEC5000 workstations. All T2 events are stored as raw data on IBM-3480 cassettes using the ZEBRA[9] bank structure. The typical size of a multi-hadronic event is 50 Kbyte. The events are flagged with the *fill number* of the LEP machine and with the DELPHI *run number*. A run is defined as a period of stable conditions e.g. constant temperature, pressure, high voltages and other detector parameters. Each run is a separate file on the output tapes.

3.4 The DELPHI Offline Analysis Chain

This section gives an overview over the DELPHI offline analysis chain. The main components are shown in Fig. 3.10.

3.4.1 The DELANA Package

The main reconstruction program is the DELPHI ANAlysis program DELANA [85]. It contains one module for each subdetector which performs the necessary alignment and calibration of the raw data. The data format inside DELANA is based on ZEBRA and is called TANAGRA. The event reconstruction proceeds in the following steps:

- A local pattern recognition is performed independently and separately for each subdetector resulting in so-called Track Elements (TE's) e.g. space points and directions, energy depositions and so on. This step is known as *first stage pattern recognition.*

[9] ZEBRA is a memory management program which offers the possibility of handling dynamic data structures.

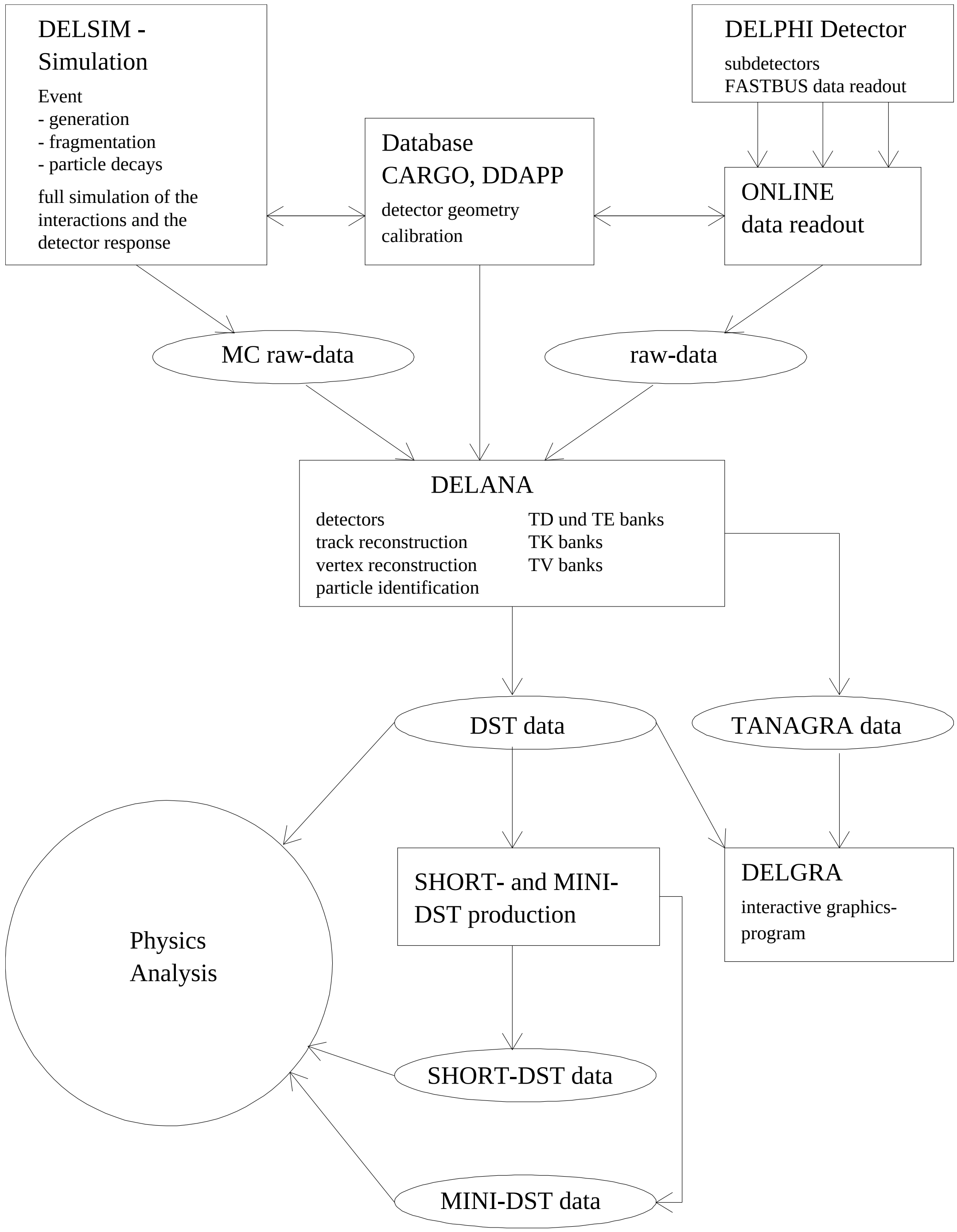

Figure 3.10: *The DELPHI offline analysis chain.*

- The track elements from several detectors are grouped into track candidates and a first track fit is performed.
- After resolving ambiguities, the tracks are extrapolated to obtain precise estimates for their passage through the subdetectors.
- A *second stage pattern recognition* is performed, where the local pattern recognition is redone using the appropriate extrapolated information from the other subdetectors.
- Energy depositions in the calorimeter are either successfully linked to charged tracks or are marked as neutral energy.
- Primary event vertices are fitted from the reconstructed tracks.

The output of this procedure is the so-called DST[10] data format containing a tree structure of banks based on the reconstructed vertices. All information related to physics analysis (e.g. four-vectors of particles, calorimeter information, matches to the simulation etc.) is stored here. The size of a multi-hadronic Z^0 DST event is roughly 80 kbyte.

3.4.2 The SDST Creation

In order to improve data quality and to provide reasonable particle identification for the collaboration, an additional processing is performed. It reduces the amount of data by a factor of three and is called Short DST (SDST). It contains the following:

- Track and vertex fits are redone after fixes for alignment and calibration have been applied on the TE basis (DSTFIX).
- Running of the AABTAG package (tagging of $b\bar{b}$ events)
- Running of the ELEPHANT package (e, γ and π^0 identification)
- Running of the MUFLAG package (μ identification)
- Running of the RECV0 package (Λ and K^0 identification)
- Running of the HADIDENT package ($K^{\pm}$ and p identification)

In order to reduce the volume of data by an additional factor of three, a subsample of the SDST data is produced which is called Mini DST (MDST). The MDST data format contains just the basic information which is needed for an analysis, e.g. track refits are not possible using this format.

The time consuming processings (DELANA and SDST production) are done on the DELFARM computer cluster consisting of 15 ALPHA-OSF, DEC-ULTRIX and VAX-VMS workstations. The analyses presented in this thesis are based on the SDST data format. The programs analysing the SDST data ran on the DELPHI SHIFT system consisting of seven HP-UX and four ALPHA-OSF workstations.

[10]DST = Data Summary Tape [86]. The DST data format is based on ZEBRA and is produced from TANAGRA data by the program package PXDST.

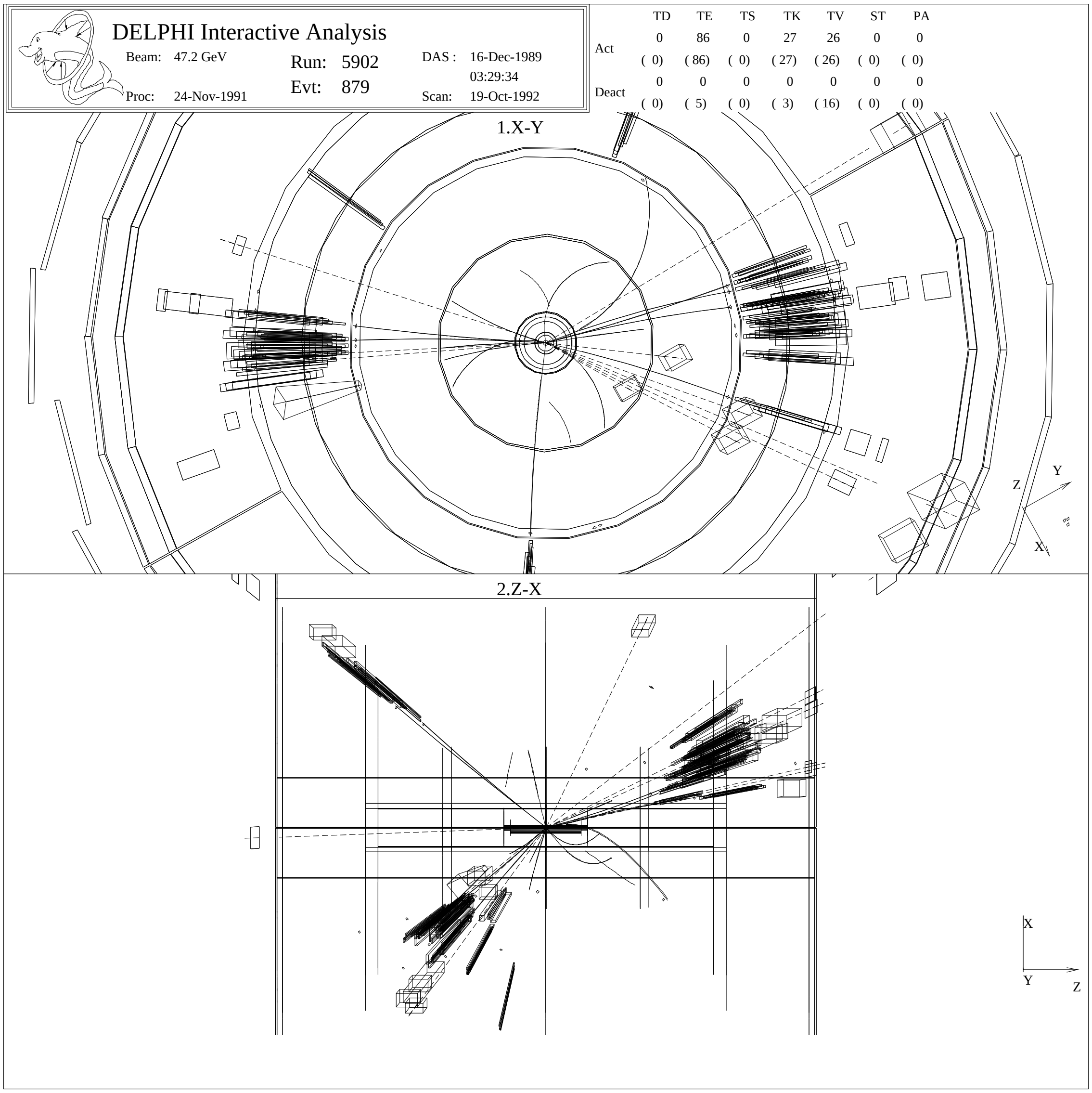

Figure 3.11: *A three-jet event recorded with the DELPHI detector and visualized with the DELGRA event display program. Individual charged tracks are drawn as lines and energy depositions in the calorimeters as boxes. The upper and lower plot show the views in direction and perpendicular to the direction of the beam pipe.*

3.4.3 The DELPHI Event Display

The DELPHI GRAphics program DELGRA is a 3-D interactive colour display facility to visualize the detector response of an event. It is very useful for investigations of the detector performance and for checks of event reconstruction programs, e.g. shower reconstructions and track fits. Especially in the LEP200 phase, where very low event rates are expected and new physics could show up, the DELGRA program will be of major importance. A three-jet event visualized by DELGRA is shown in Fig. 3.11.

3.5 The Detector Simulation

The primary aim of a simulation program is to produce "data" for a particular reaction which are as close as possible to the real raw data from the detector. These "data" are then processed through the reconstruction program DELANA and the subsequent analysis programs in exactly the same way as for real data. This procedure models the detailed response of the complete detector to a particular physics subject. The DELPHI simulation (DELSIM) [87] is based on three components which can be summarized as follows:

- A model for the generation of the primary physics process: In most cases, this is performed by external programs, like JETSET [22] for quark final states, DYMU3 [23] for $e^+e^- \rightarrow \mu^+\mu^-$, BABAMC [88] for $e^+e^- \rightarrow e^+e^-$, KORALZ [89] for $e^+e^- \rightarrow \tau^+\tau^-$. The DELPHI collaboration uses its own parameter tuning for the different generators determined from the latest available data [34].
- The general task of following particles through the DELPHI detector up to the point where they hit an active detector component: This is done by stepping through the magnetic field including the possibility that these particles give rise to secondary interactions. In order to reach the required accuracy for the results, a very detailed description of the material inside the detector is necessary.
- Following the particles inside the active detector components and the simulation of the detector response as recorded in reality: This part is specific to every detector component and the modularity of the code is such that each of them corresponds to an independent software module.

The particle tracking through the DELPHI detector includes energy loss, multiple scattering and the following secondary processes:

- the photoelectric effect
- the emission of Delta rays
- bremsstrahlung
- annihilation of positrons
- pair production
- Compton scattering
- weak decays
- nuclear interactions, using GEANTH [90]

The material parameters which determine the rates of the above processes are extracted from the CARGO data base. When a particle enters an active detector component the control of the track-following is given to the corresponding software module. Most modules follow the particles by using tools provided by the general routines outlined above. Some modules use different methods, for example the HPC which needs a very accurate description of the electromagnetic effects and is based on EGS4 [91]. When a particle crosses the sensitive volume of a detector the relevant information is stored to compute the detector response in the form of electronic signals, as for real data.

The simulation of events for physics analyses and detector studies is produced in several production centers in the DELPHI member states. The achieved statistics is comparable with or larger than the statistics for the actual LEP data.

3.6 Summary of the Chapter

- LEP is the largest storage ring ever built. The luminosity of 2.2 nb^{-1} s^{-1} was reached using 8 bunches per e^+e^- beam in pretzel orbits. LEP is operating on the Z^0 resonance with good performance close to the design values.

- DELPHI is one of the four LEP experiments. It is equipped with a large superconducting coil producing a magnetic field of 1.2 T. The electromagnetic calorimeter HPC and the RICH systems are located inside the superconducting coil which restricts the volumes of the central tracking devices.

- In the years 1991-1994 DELPHI collected an integrated luminosity of roughly 145 pb^{-1}. About 3.4 million hadronic Z^0 decays have been recorded on tape.

- The track resolution is dominated by the DELPHI vertex detector consisting of three layers of silicon microstrip diodes. The impact parameter resolution can be parametrized as $\sigma_{IP}(R\phi)[\mu\text{m}] = \sqrt{\left(65/p/\sin^{3/2}\Theta\right)^2 + 20^2}$ for $R\phi$. The corresponding resolution in the Z direction is given by $\sigma_{IP}(Z)[\mu\text{m}] = \sqrt{\left(71/p/\sin^{5/2}\Theta\right)^2 + 34^2}$.

- The momentum resolution of the DELPHI tracking system was determined to be $\sigma(1/p) = 0.57\times10^{-3}(\text{GeV/c})^{-1}$ for the barrel and $\sigma(1/p) = 1.31\times10^{-3}(\text{GeV/c})^{-1}$ for the forward region.

- The energy resolution of the electromagnetic calorimeter HPC was found to be $\sigma_E/E = 26\%/\sqrt{E[\text{GeV}]} \oplus 4.6\%$. The energy resolution of the hadron calorimeter is described by $\sigma_E/E = 112\%/\sqrt{E[\text{GeV}]} \oplus 21\%$.

- Special emphasis during the construction of DELPHI was given to the particle identification devices. Good separation between kaons, protons and pions is achieved by using the barrel and forward RICH detectors. Furthermore, DELPHI is equipped with 4π muon chambers.

- The DELPHI online system manages several functions during runtime: analyse the events on an elementary level and supply a fast trigger decision; read out all detector components and write the data on storage media; run the power supplies, gas and cooling systems of the detector and control and log all slowly varying detector parameters.

- The offline analysis (DELANA, SDST production) is done on the DELFARM computer cluster, consisting of 15 DEC-ALPHA workstations. The processed data are stored for physics analysis in the DST (Data Summary Tape), SDST (Short DST) and MDST (Mini DST) format. The presented analyses were performed at CERN using the SDST format and the DELPHI SHIFT computer system.

- The simulation for physics analyses and detector studies is produced in several production centers in the DELPHI member states. The achieved statistics is comparable with LEP statistics.

Chapter 4

Analysis Tools

The main goal of this thesis is the search for and observation of orbitally excited B mesons in the decay channel $B^{**} \to B\pi$ or $B^{**} \to B^*\pi$. This chapter describes the main analysis tools while the next chapter is dedicated to the actual analysis. The analysis starts with a multi-hadronic event selection (section 4.1), followed by a tagging of $b\bar{b}$ events (section 4.2). The four-vectors of the B or B^* mesons are reconstructed in an inclusive fashion using an algorithm based on a simple rapidity argument (section 4.3). Since B^{**} mesons decay rapidly through the strong interaction, decay pions originate from the primary vertex. A significant reduction of background from B decay products is achieved by using a vertex reconstruction algorithm (section 4.4).

Furthermore, a search for B_s^{**} mesons decaying into $B^{(*)}K$ as well as a search for the b baryons Σ_b and Σ_b^* is performed. Significant kaon identification is essential for the observation of B_s^{**} mesons (section 4.5). In order to achieve baryon enrichment for the $\Sigma_b^{(*)}$ analysis, methods of proton tagging and Λ reconstruction are used (sections 4.5 and 4.6).

4.1 Hadronic Event Selection

The hadronic event selection in DELPHI is based on the reconstruction of charged particle tracks and neutral energy deposition in the calorimeters. Prior to the actual event selection, a track selection takes place which removes badly reconstructed tracks or tracks originating from secondary interactions with the detector material. The following track quality cuts are applied:

- track length > 30 cm
- track momentum > 0.1 GeV/c
- radius of first measured point < 35 cm
- $R\phi$ impact parameter < 4 cm
- relative error on $R\phi$ impact parameter < 2
- Z impact parameter < 4 cm

Electromagnetic showers are selected by using the default quality cuts from the ELEPHANT package [92]. Neutral showers reconstructed in the hadron calorimeter (HAC) are accepted if their energy exceeds 10 GeV. The multi-hadronic event selection comprises the following standard selection cuts (for details see Ref. [93]):

- number of charged tracks in the event ≥ 6
- number of neutral particles in the event ≥ 1
- $|\text{positive} - \text{negative}|$ charged particles in the event ≤ 5
- charged energy in the event ≥ 20 GeV
- total energy in the event ≥ 30 GeV

After these cuts one obtains a sample of 2 943K multi-hadronic events taken with the DELPHI detector in the years 1991-1994. The following SDST data sets are used: **91F1** - 255K, **92D2** - 700K, **93C1** - 708K and **94B1** - 1280K. Background originating from *beam-gas* and *beam-wall* events is significantly suppressed. The contribution of these backgrounds to the event sample is estimated to be of the order of 0.1%. The background from $\tau^+\tau^-$ events is of the order of 0.2%.

For each multi-hadronic event the main event axis (given by the thrust axis $\vec{t}$) is calculated. The quantity thrust T is defined by [94]

$$T = \max_{|\vec{n}|=1} \frac{\sum_i |\vec{n} \cdot \vec{p}_i|}{\sum_i |\vec{p}_i|} \tag{4.1}$$

and the thrust axis $\vec{t}$ is given by the vector $\vec{n}$ for which the maximum is attained. The allowed range is $1/2 \leq T \leq 1$, with a two-jet event corresponding to $T \approx 1$ and an isotropic event to $T \approx 1/2$. Each event is divided into two hemispheres as defined by the thrust axis. The analysis is restricted to the barrel region where there is complete vertex detector coverage ($|\cos(\Theta_{thrust})| \leq 0.75$ with Θ_{thrust} being the angle between the thrust axis $\vec{t}$ and the Z axis).

Furthermore, the jet structure of each event is analyzed using the LUCLUS algorithm [95] with a transverse momentum cutoff of 5 GeV/c, leading to a classification of all events into two-, three-, four-, or five-jet event samples[1]. In simulation studies this transverse momentum cutoff is found to give the best reconstruction of the initial b hadron direction. Depending on the particular analysis performed, different cuts for the number of jets are used.

4.2 Tagging of $b\bar{b}$ Events

The cross section for $b\bar{b}$ production in e^+e^- annihilation on the Z^0 resonance is 6.6 nb which corresponds roughly to 22.1% of the hadronic cross section $Z^0 \rightarrow q\bar{q}$ [12]. Several methods

[1] The following parameter settings are used for the LUCLUS algorithm [95]: PARU(44)=5.0, MSTU(46)=1, MSTU(47)=2 and MSTU(48)=0.

are used by the LEP collaborations in order to isolate $b\bar{b}$ events from the remaining multi-hadronic backgrounds $Z^0 \to c\bar{c}$, $s\bar{s}$, $u\bar{u}$ and $d\bar{d}$. A b hadron can either be reconstructed in a fully exclusive way from its decay products, or it can be tagged by a measured high p_t lepton from its weak decay. These methods suffer from low efficiencies and small branching ratios in the observable decay channels (e.g. $\mathrm{Br}(B^0 \to e^+ \nu_e X) \approx 10\%$).

The method used in this analysis is based on the long lifetime of b hadrons (about 1.6 ps for the mixture of B mesons and b baryons produced at LEP), their large mass (5.28 GeV/c^2) and their sizeable energy ($\langle E_b \rangle \approx 0.7 \cdot E_{beam}$). These facts lead to a mean flight distance for b hadrons in the laboratory frame of $d = \beta\gamma c\tau \approx 3$ mm. In order to identify $b\bar{b}$ events, one may try to reconstruct a secondary b-decay vertex from charged particle tracks in a hemisphere (see section 4.4). However, studies of impact parameter distributions of b decay products lead to methods with higher tagging efficiencies. Such methods are standard in DELPHI [96] and are discussed below.

The impact parameter[2] is defined as the distance of closest approach of the trajectory of a charged particle to the primary reconstructed vertex. It is evaluated separately in the $R\phi$ plane and in Z. The sign of the impact parameter is defined with respect to the jet direction. It is positive if the vector joining the primary vertex and the point of closest approach to the track lies in the same direction as the jet to which the given track belongs. The sign is computed in two dimensions when only $R\phi$ measurements from the VD are available, otherwise it is done in three dimensions[3]. The sign of $R\phi$ and Z impact parameters are the same for a given track. The impact parameter error arises from the error on the point of closest approach and the error on the vertex position. The significance S_0 of a given track is defined as the impact parameter divided by its error.

The impact parameter is used as the only tagging variable for the separation of events with b quarks from the rest of the hadronic events. With the given definition of the impact parameter and of its sign, it follows that the tracks from the decays of b hadrons have positive impact parameters, whereas non-zero impact parameters, arising from the inaccurate reconstruction of particle trajectories, are equally likely to be positive or negative. Therefore, the use of tracks with positive impact parameters increases the tagging efficiency.

For the tagging of b hadrons, the probability method proposed originally in [97] is used. It gives the possibility of constructing one tagging variable from all impact parameter values observed in the event. This is achieved by the following algorithm. The negative significance distribution mainly reflects the detector resolution and is used to build the track probability function $\mathcal{P}(S_0)$, which is by definition the probability for a track from the primary interaction to have a significance with absolute value S_0 or greater. By construction, the distribution of $\mathcal{P}(S_0)$ for tracks with positive impact parameters should have a peak at low values. Using the track probability function, the probability for each track in the event can be computed according to the value of the significance. Thus, for any group of N tracks the N-track probability is defined as:

$$\mathcal{P}_N \equiv \Pi \cdot \sum_{j=0}^{N-1} (-\ln \Pi)^j / j! \;, \text{ where } \Pi \equiv \prod_{i=1}^{N} \mathcal{P}(S_i) \;. \tag{4.2}$$

This variable gives the probability for a group of N tracks with the observed values of significance to come from the primary vertex. By construction, a flat distribution of $\mathcal{P}_N$ is

[2] The impact parameter and the obtained resolutions in DELPHI are also discussed in section 3.2.1.

[3] Starting from 1994 the DELPHI vertex detector provides both $R\phi$ and Z information.

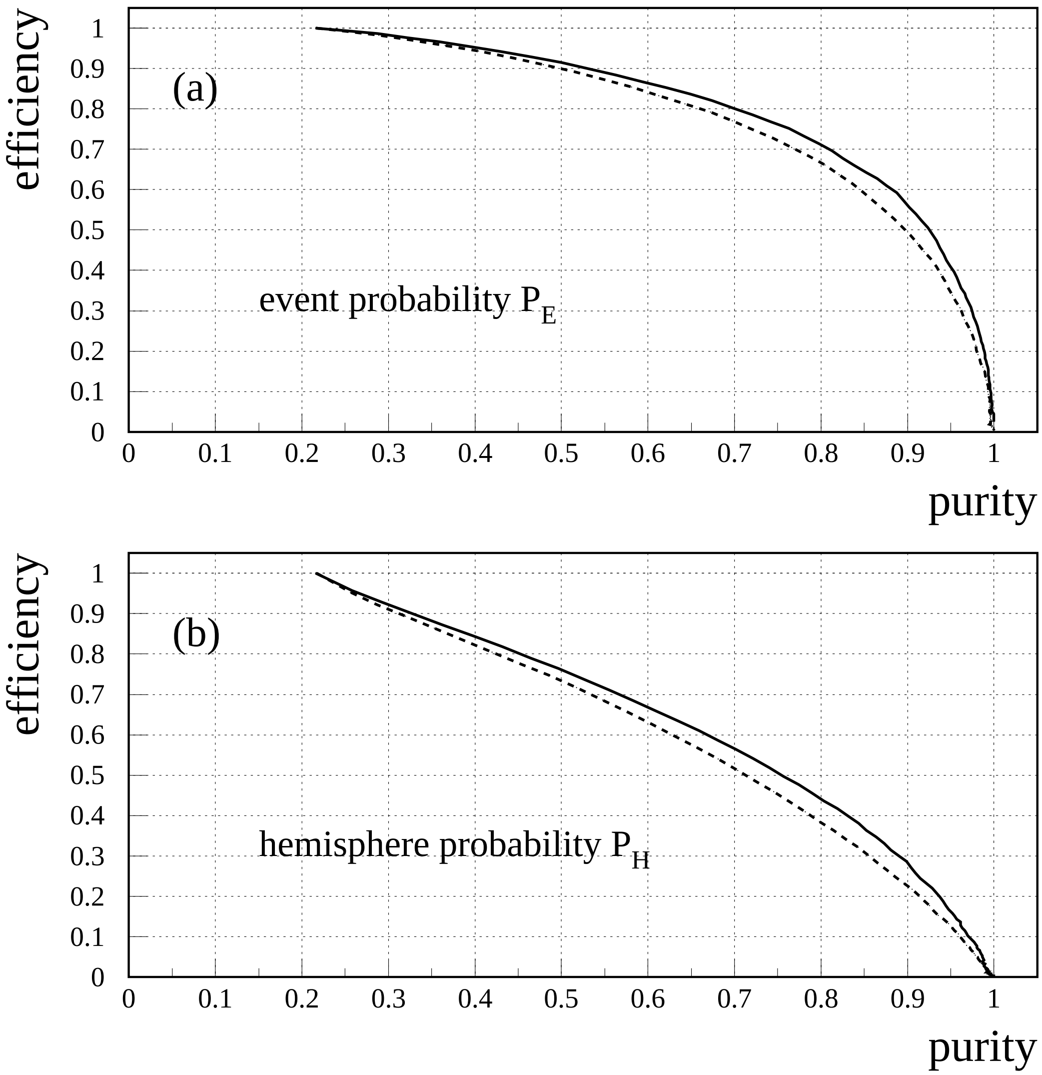

Figure 4.1: *b-tagging efficiency as a function of purity for different values of the cut on (a) the event probability and (b) on the hemisphere probability for three-dimensional VD (full line) and for two-dimensional VD (dashed line) [78].*

expected for a group of tracks from the primary vertex, provided the significances of these tracks are uncorrelated, while tracks from b-hadron decays should have a sharp peak at 0. In the case that the Z impact parameter is measured, the probability $\mathcal{P}(S_0)_Z$ is computed in the same way as for the $R\phi$ impact parameter. The N-track probability is then given by a combination of both $\mathcal{P}_{R\phi}$ and $\mathcal{P}_Z$ probabilities. The event probability, $\mathcal{P}_E$, is the probability computed using all the N-tracks of the event and, similarly, the hemisphere probability $\mathcal{P}_H$ is the probability computed from the tracks belonging to that hemisphere. Furthermore, in order to decide if a single track originates from the primary vertex or from a b-decay vertex, the track probability $\mathcal{P}_T$ is provided by the b-tagging package. Fig. 4.1 shows the b-tagging efficiency as a function of purity for the event probability and for the hemisphere probability for three-dimensional VD (full line) and for two-dimensional VD (dashed line). It can be seen that the possibility to measure both $R\phi$ and Z increases the efficiency for a given purity. The

year	multi-hadronic Z^0 events	$b\bar{b}$ events purity: $(83 \pm 4)\%$	$b\bar{b}$ events purity: $(94 \pm 4)\%$
1991	255 K	32 K	17 K
1992	700 K	85 K	45 K
1993	708 K	100 K	55 K
1994	1280 K	154 K	82 K

Table 4.1: *Number of multi-hadronic Z^0 events and b-tagged events for DELPHI data taken in the years 1991-1994.*

results have been extracted from simulation for a sample of multi-hadronic events selected within the acceptance of the vertex detector ($|\cos(\Theta_{thrust})| < 0.75$). The working points for the different presented analyses are stated explicitly in the next chapter. Some typical values for event numbers and purities are given in Tab. 4.1. A cut on the event probability $\mathcal{P}_E < 0.01$ corresponds to an efficiency of $(65 \pm 3)\%$ and a purity of $(83 \pm 4)\%$. A cut $\mathcal{P}_E < 0.001$ leads to an efficiency of $(44 \pm 3)\%$ and a purity of $(94 \pm 4)\%$.

4.3 Inclusive B Meson Reconstruction

The algorithm of inclusive B meson reconstruction [98] was developed and successfully applied in the DELPHI B^* analysis [31], combining inclusive reconstructed B mesons with converted photons ($B^* \to B\gamma$). Additionally, it lead to an inclusive measurement of the B fragmentation function in DELPHI [99].

The algorithm is based *only* on the measured momenta and angles of the B decay products. This works well for B mesons due to their large mass and their hard fragmentation function. Simulation studies at the Z^0 resonance show that the rapidity[4] $y = 0.5 \cdot \log((E+p_z)/(E-p_z))$ of B mesons along the event thrust axis should be strongly peaked at $y = \pm 2.4$, with some spread towards lower $|y|$ due to hard gluon radiation (see Fig. 4.2(a)). Another observation is that the B meson decay products should have a Gaussian distribution in rapidity space with a width of about 0.8 units. In b events the fragmentation process generates particles mostly at low rapidity, and their distribution can be described by two Gaussians of width 1.05 units, centered at ± 1.03. The model dependence of these distributions has been analyzed by comparing the predictions of JETSET 7.4 [22] and HERWIG 5.8 [29] (with the JETSET particle decays), both with default parameters. In general these two predictions differ by less than 10% at any value of y in the inclusive y distribution from fragmentation, and by less than 4% in the distribution from B decays.

Detector acceptance and resolution effects have only a small influence on these distributions, the most important effect being that the loss of low energy particles leads to a suppression of the population at low $|y|$. The inclusive rapidity distributions for DELPHI data and simulation are shown in Fig. 4.2(b). Excellent agreement is observed for both charged and neutral particles.

[4] The definition of the rapidity originates from a parametrization of the Lorentz invariant phase space element $dLips = 1/4(2\pi)^3 dy d\phi dp_\perp^2$ for a single particle. A longitudinal Lorentz boost is a linear transformation in rapidity.

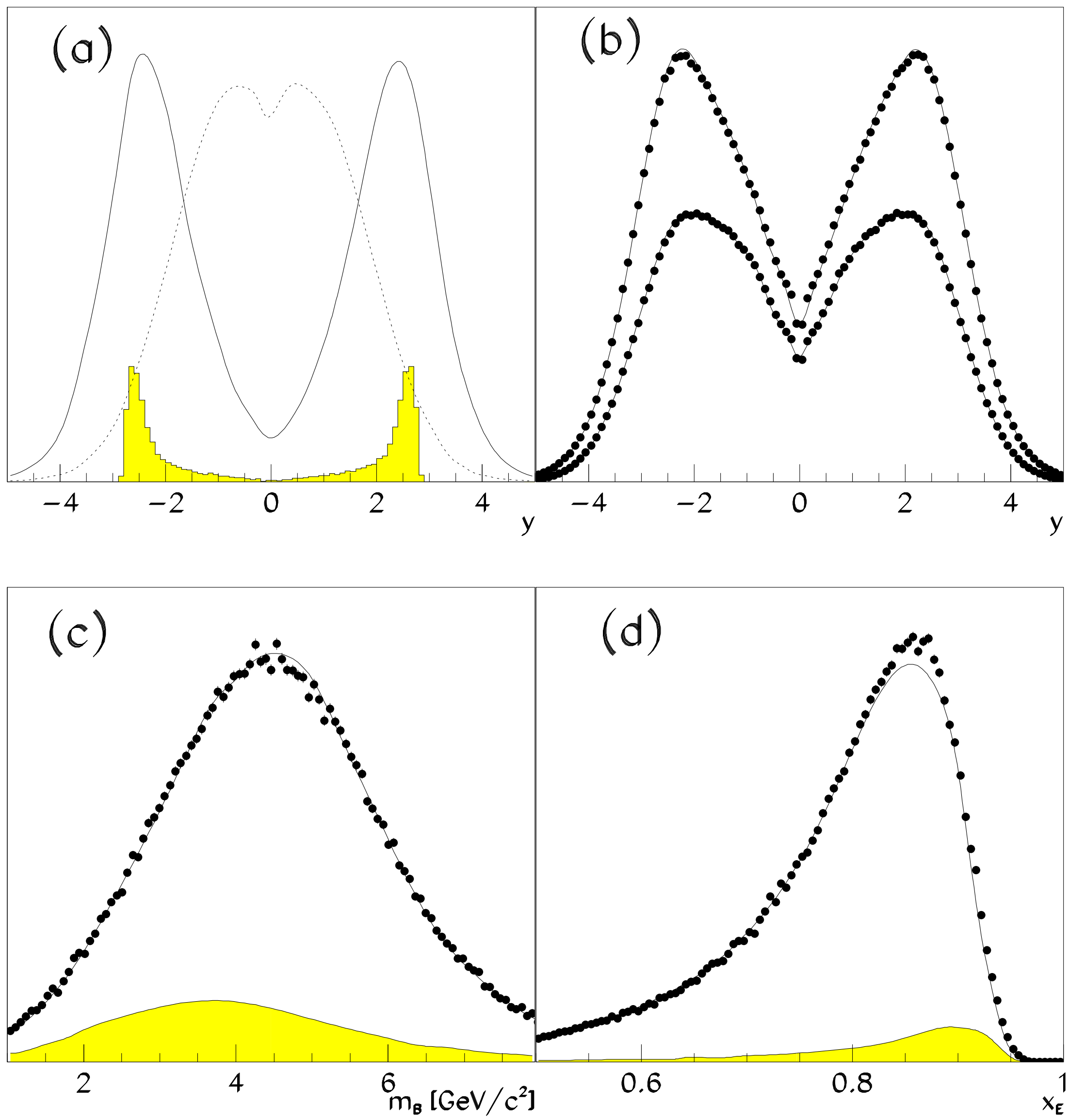

Figure 4.2: *(a) Rapidity distributions for B mesons (shaded area), particles stemming from B decay (solid curve) and particles from fragmentation (dotted curve) in $b\bar{b}$ events as expected from the* JETSET *7.4 model.*
(b) Comparison between the rapidity distributions of all particles (upper curves) and charged particles (lower curves) in a b-enriched sample of data (points) and Monte Carlo simulation (lines).
(c) Reconstructed B mass spectrum for data (points) and simulation (solid line).
(d) Corrected fractional B energy spectrum for data (points) and simulation (solid line). The shaded area in (c) and (d) corresponds to the background due to non-$b\bar{b}$ events.

Each event is divided into two hemispheres as defined by the thrust axis. The rapidity of each reconstructed charged particle (assuming the pion mass) and neutral particle (assuming the photon mass) with respect to the thrust axis is calculated. Particles outside a central rapidity window of ± 1.6 units are considered to be B meson decay products. The four-momenta of these particles are added together in each hemisphere to arrive at a B meson energy estimate E_y for each side of the event.

Given the inclusive nature of this reconstruction technique there are events that are not well reconstructed. However, most of these poorly reconstructed events are removed by requiring that:

- a minimum energy of 20 GeV is reconstructed for the B candidate in the rapidity-gathering algorithm
- the reconstructed mass m_y lies within ± 2.5 GeV/c^2 of the average reconstructed B meson mass
- the ratio of hemisphere energy, E_{hem}, to beam energy, E_{beam}, lies in the range $0.6 < x_h = E_{hem}/E_{beam} < 1.1$

Enforcing these requirements results in a loss of 26% of B decays. Studies using simulation showed a strong correlation between the generated B meson energy, E_{Btrue}, and the initial estimate E_y from the rapidity-gathering algorithm described above. There is a further correlation between the energy residuals $\Delta E = E_y - E_{Btrue}$ and the reconstructed B meson mass m_y, which is approximately linear in m_y. Also a correlation between ΔE and the ratio of the energy seen in the hemisphere to the beam energy $x_h = E_{hem}/E_{beam}$ is observed, reflecting global inefficiencies and neutrino losses. Since the mass and hemisphere energy dependences are not independent, a correction technique taking into account their correlations is applied.

The correction function is determined using simulated events in the following way. After applying all cuts, the simulated data are divided into several samples according to the measured ratio x_h. For each of these classes the energy residual ΔE is plotted as a function of the reconstructed mass m_y. The median values of ΔE in each bin of m_y are calculated, and their m_y dependence fitted by a second order polynomial, $\Delta E(m_y; x_h\text{-bin}) = a + b \cdot (m_y - \langle m_y \rangle) + c \cdot (m_y - \langle m_y \rangle)^2$. The three coefficients in the fit, a, b and c, in each x_h class are then plotted as function of x_h and their dependence fitted using second order polynomials, $a(x_h) = a_1 + a_2 \cdot x_h + a_3 \cdot x_h^2$, and similarly for $b(x_h)$ and $c(x_h)$. Thus one obtains a smooth correction function describing the mean dependence on m_y and the hemisphere energy, characterized by 9 parameters $a_i, b_i, c_i, i = 1, 3$. Finally, a small *bias correction* is applied for the mean remaining energy residual as a function of the corrected energy, as determined from simulation.

The good agreement between data and Monte Carlo simulation for the reconstructed B mass m_y and corrected fractional B energy x_E distributions is shown in Figs. 4.2(c) and 4.2(d). The attainable precision of this inclusive technique depends on the cuts on the b-tagging probability, the event shape variables (e.g. thrust and number of jets) and on the B quality (E_y, m_y and x_h). For the standard cuts described above the energy precision is 7% for 75% of the B mesons, the remainder constituting a non-Gaussian tail towards higher energies. The angular resolution in Θ and ϕ can be parameterized as double-Gaussians with widths of 15 mrad for 60% of the data and 38 mrad for the remaining 40%. Fig. 4.3 shows the energy and angular resolutions of the inclusive reconstruction method.

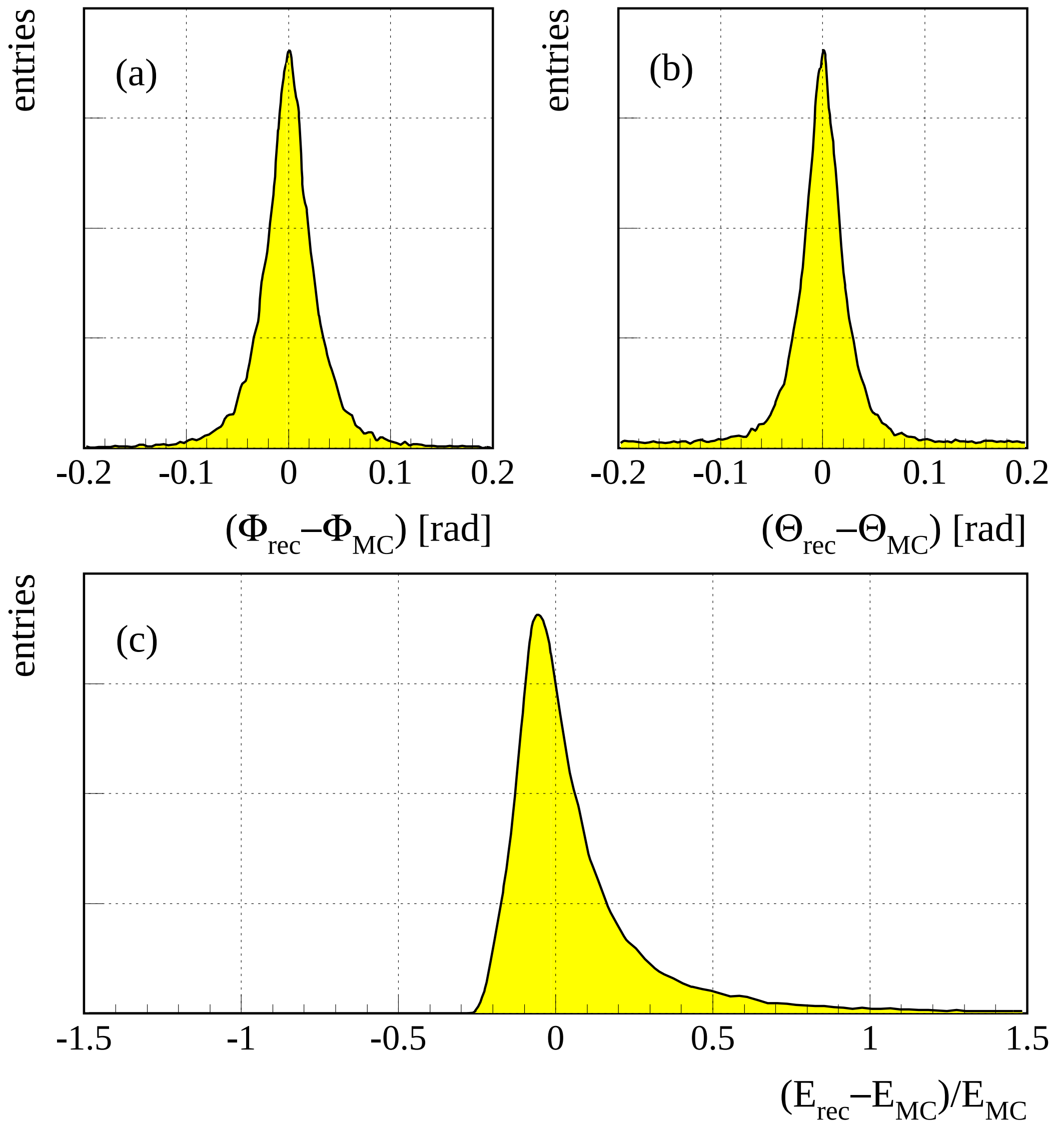

Figure 4.3: *Inclusive B reconstruction algorithm. (a) $\phi_{rec} - \phi_{MC}$, (b) $\Theta_{rec} - \Theta_{MC}$ and (c) $(E_{rec} - E_{MC})/E_{MC}$. The angular resolutions can be parametrized by double-Gaussians, the energy resolution consists of a Gaussian part with a tail towards higher energy.*

The simulation prediction of the resolutions of the inclusive B reconstruction algorithm is verified by the good agreement in the width of the $B^* \to B\gamma$ mass difference peak [31].

4.4 *B*-Decay Vertex Reconstruction

In order to reconstruct orbitally excited B meson in the decay channel $B^{**} \to B^{(*)}\pi$, the four-vectors of the reconstructed B or B^* mesons are combined with possible B^{**} decay pions. This section describes a tool for the reduction of the combinatorial background from the

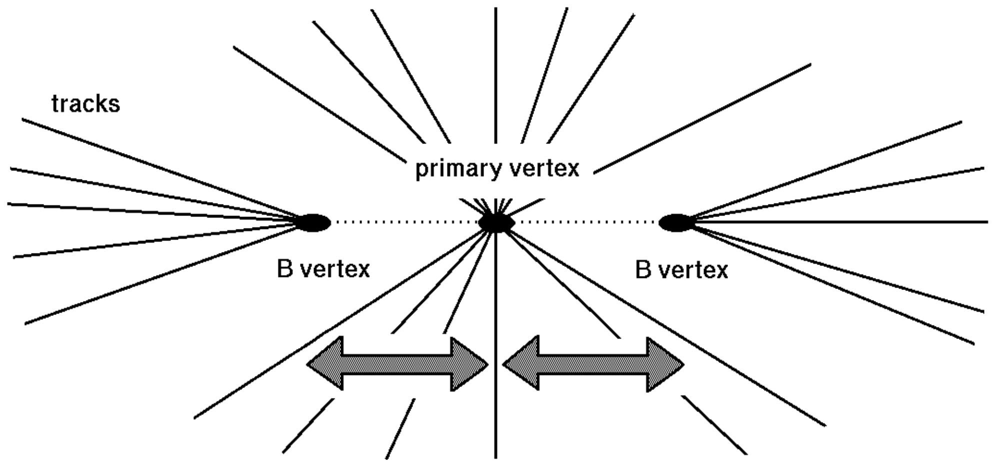

Figure 4.4: *Iteration procedure for the reconstruction of two B-decay vertices and one primary vertex. The rapidity assignment serves as a starting point for the iteration.*

many fragmentation pions present. Since B^{**} mesons decay due to the strong interaction, decay pions originate from the primary vertex and not from the B-decay vertex which lies on average about 3 mm away from the primary vertex. An iterative procedure is described which provides a fit of three vertices in an event (two B-decay vertices and one primary vertex). In the analysis only pion candidates are accepted which are assigned to the primary vertex.

Only well measured tracks with momentum greater than 0.1 GeV/c and two associated vertex detector hits are used for this algorithm. The alignment of the various tracking detector components as well as an accurate description of efficiencies, resolutions and covariance matrix elements of charged tracks, which are crucial for the analysis, are monitored and adjusted using $Z^0 \to \mu^+\mu^-$ decays and primary vertex fits of non-$b\bar{b}$ hadronic events.

The algorithm is as follows: All well measured tracks are classified into three vertices: the primary vertex which has to be compatible with the known beam spot, and two B-decay vertices. The rapidity classification serves as a starting point: all particles with $|y| < 1.6$ are assigned to the primary vertex, and those with $y < -1.6$ and $y > 1.6$ to the two secondary vertices respectively. Three vertex fits are then performed. In a first step all tracks are reassigned to the three vertices according to their impact parameters with respect to primary and secondary vertex. Three vertex fits are performed with the new assignments. The track contributing the largest χ^2 is then tried at the other kinematically allowed vertex (i.e. the primary vertex if it was a secondary before and vice versa). The new vertex distribution is accepted if the χ^2 gets better, otherwise the old distribution is kept. If the track gives the largest χ^2 contribution in both situations, it is discarded. The iteration process is illustrated in Fig. 4.4. This procedure is continued until no track gives a χ^2 contribution larger than 5. On average about sixteen iteration steps are performed. Fig. 4.5 shows an example for an event where a primary and two B-decay vertices have been reconstructed.

In order to get a sensible distinction between primary and secondary vertices, the reconstructed decay length (in the signal hemisphere) is required to exceed $d = 1.5$ mm. Additional cleaning is achieved by placing a cut on the acolinearity, defined by the coordinates of the two

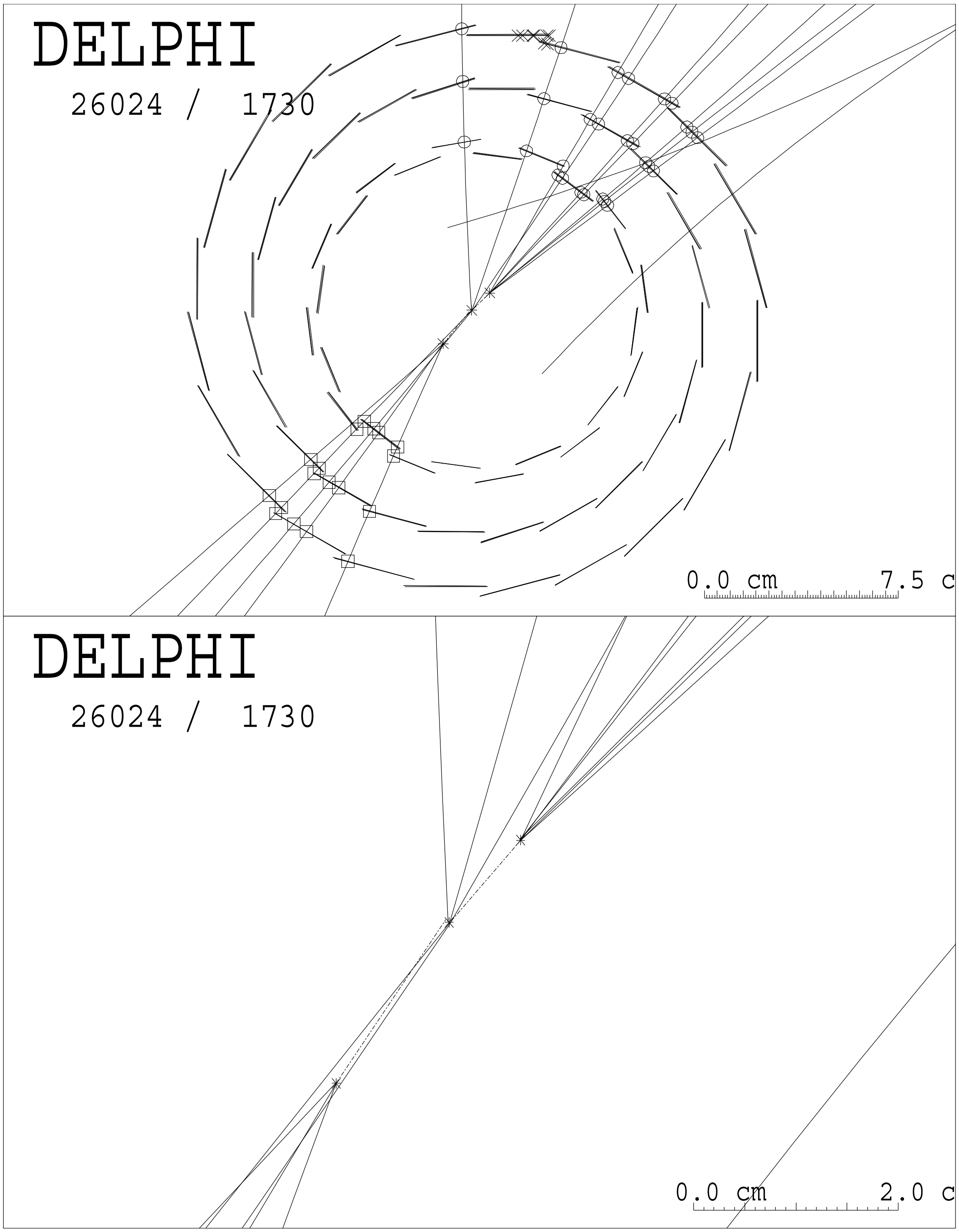

Figure 4.5: *Selected event with reconstruction of a primary vertex and two B-decay vertices. The vertices are marked with stars. The upper plot also shows the three layers of the DELPHI vertex detector. The lower plot magnifies the situation near to the interaction point.*

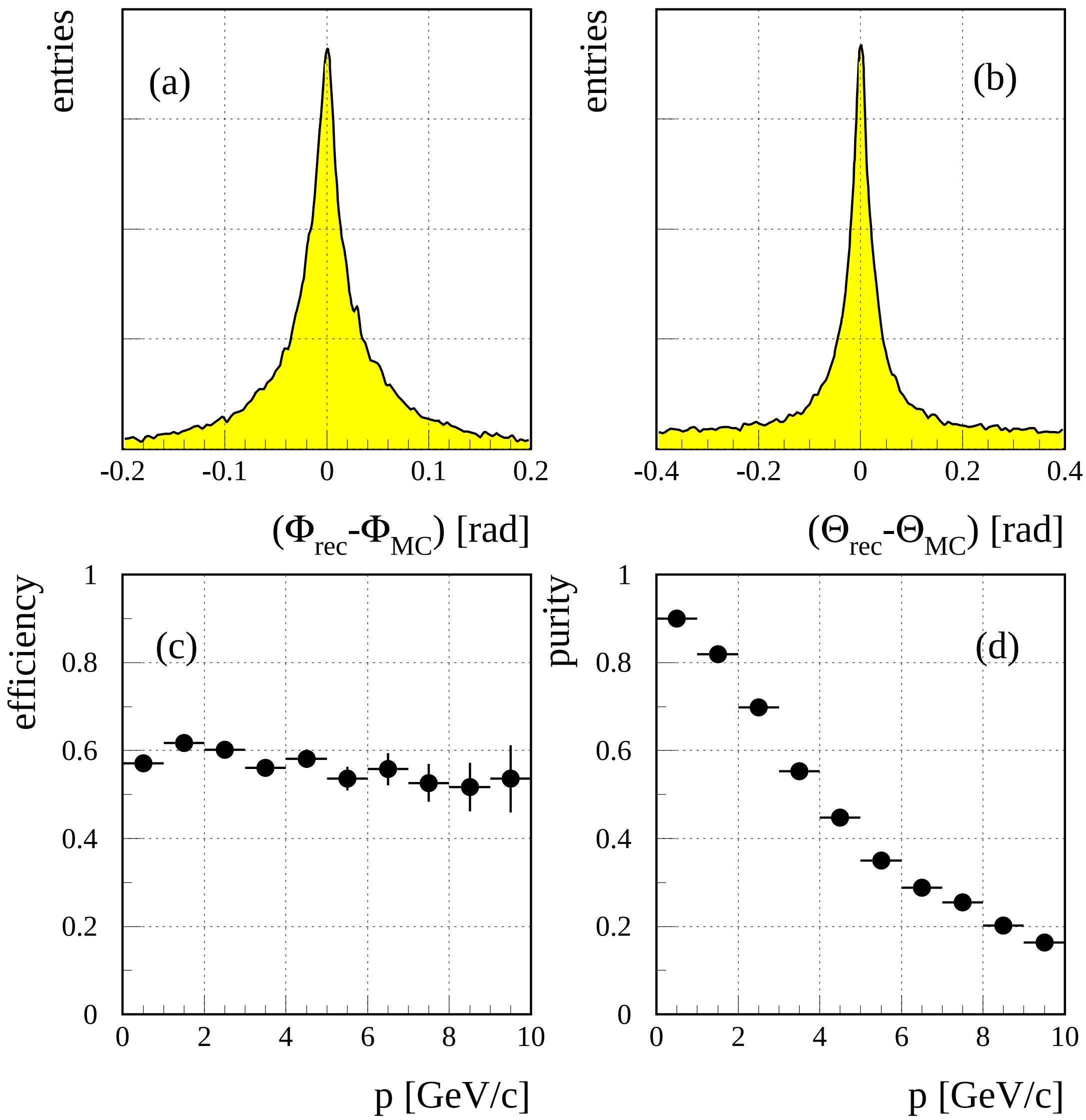

Figure 4.6: *Performance of the vertex reconstruction algorithm. (a) $\phi_{rec} - \phi_{MC}$ and (b) $\Theta_{rec} - \Theta_{MC}$ obtained from the coordinates of the reconstructed vertices. (c) Efficiency for particles, originating from fragmentation, to be assigned to the primary vertex as a function of momentum. (d) Purity as a function of momentum.*

B-decay vertices and the primary vertex ($\cos\Theta_V \geq 0.8$). The performance of the algorithm depends on the required event topology (e.g. on the number of jets in the event[5]).

The following quantities have been extracted from a Monte Carlo sample containing two- and three-jet events ($\mathcal{P}_E < 0.01$). A mean number of 4.9 particles per hemisphere belonging to the primary vertex is found. For the B-decay vertex a mean number of 2.6 particles is observed. Both numbers are in agreement with the results in real data. The angular resolution in ϕ can be parameterized as a double-Gaussian with a width of 18 mrad for 65% of the data and 85 mrad for the remaining 35% (see Fig. 4.6(a)). It is compatible with the

[5]The cut on the number of jets is different in each particular analysis and is stated explicitly in chapter 5.

resolution obtained from the inclusive B reconstruction algorithm. The angular resolution in Θ is somewhat worse. It can be parameterized as a double-Gaussian with a width of 25 mrad for 70% of the data and 260 mrad for the remaining 30% (see Fig. 4.6(b)) [6]. Furthermore, the resolution on the flight distance of the reconstructed B meson has been studied. By using a double-Gaussian function, one obtains a resolution of 0.05 cm for 60% of the data and of 0.29 cm for the remaining 40%. The efficiency for particles from fragmentation to be assigned to the primary vertex as a function of momentum is shown in Fig. 4.6(c). It is approximately constant at $(60 \pm 3)\%$. The purity of fragmentation particles which are assigned to the main vertex reveals a strong dependence on momentum (see Fig. 4.6(d)). For particles between 0.1-2.0 GeV/c a purity of $(86 \pm 3)\%$ is found.

4.5 Hadron Identification

In order to obtain evidence for B^{**} mesons inclusively reconstructed $B^{(*)}$ mesons are combined with pions. Since the dominant fraction of charged particles in an event are pions, no sophisticated hadron identification is needed. However, B_s^{**} mesons are expected to decay into $B^{(*)}K$. Good particle identification is essential for this kind of analysis. Furthermore, in order to study Σ_b and Σ_b^* baryons, an enrichment in baryons can be achieved by proton tagging. The algorithm and performance of the DELPHI hadron identification is discussed in this section. It is based on the specific ionization measured by the TPC and the reconstructed Cherenkov angles in the RICH detectors.

Specific Ionization from the TPC

In addition to providing a three-dimensional track reconstruction, the DELPHI TPC is useful for charged particle identification by measuring the energy loss per unit length, dE/dx. The sense wires of its proportional chambers provide up to 192 ionization measurements per track. The signals collected by the sense wires are associated to the tracks reconstructed by the TPC pads. This association is done by comparing the time of arrival of the pad and sense wire signals. Hits too close in time to be correctly separated are not used for the dE/dx calculation. This requirement corresponds, for tracks orthogonal to the drift direction Z, to a separation of at least 2 cm.

It should be noted that an average of 5% of the signals collected by the sense wires are below the electronic threshold. The fraction of the Landau distribution lost due to this effect is a function of the drift length and gap size. To reduce this dependence an effective threshold is applied which depends on these quantities [78].

To be used in the physics analysis, the truncated dE/dx is required to have at least 30 measurements. The efficiency obtained after these requirements is 61% for tracks in multi-hadronic events with momentum greater than 1 GeV/c and $|\cos\Theta_{thrust}| < 0.7$ [78]. The measured signals are corrected to take into account the usual dependence on parameters like gap size or drift length. The dependence of dE/dx on the ratio p/m of the track is measured from the data using various samples, and the final result can be seen in Fig. 4.7. The position

[6] These quantities have been extracted with a vertex detector providing full three-dimensional information.

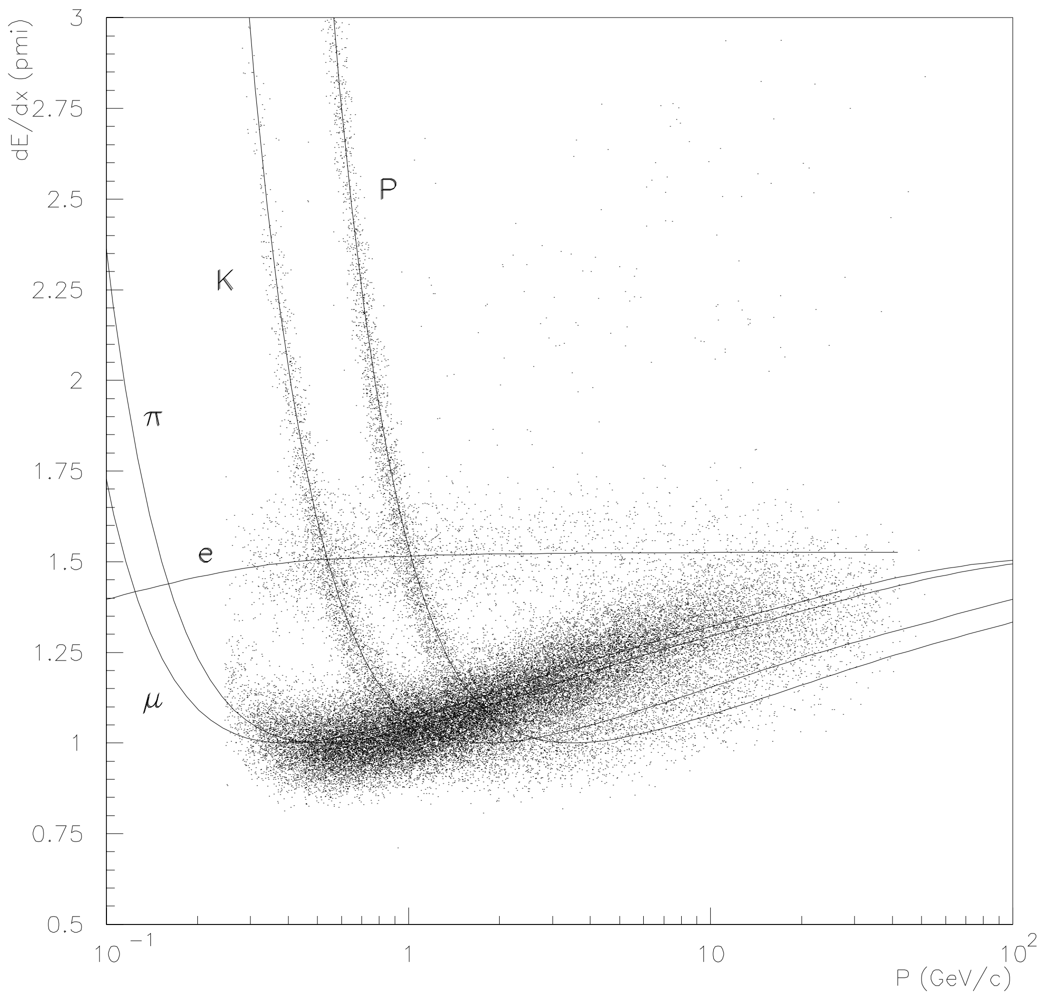

Figure 4.7: *Specific energy loss dE/dx in the TPC as a function of momentum. The full lines correspond to the expectations for e, μ, π, K and p tracks [78].*

of the Fermi plateau when normalized to the minimum ionizing particle is found at 1.52.

The resolution on dE/dx estimated from data is 6.7% for pions ($p > 2$ GeV/c) coming from K^0_s decays in multi-hadronic events, and 5% for muons ($p = 45$ GeV/c) from dimuon events ($Z^0 \to \mu^+\mu^-$) [78]. With the obtained resolution and dependence of dE/dx on p/m, the separation between electron and pion is above 3 standard deviations for momenta below 4.5 GeV/c. A pion/kaon separation can be achieved at the 1σ level above 2 GeV/c [78].

Detection of Cherenkov Radiation

The detection of Cherenkov light with the RICH detectors has already been described in section 3.2.3. In the 1994 data taking period 1.5 million events were recorded with a fully operational RICH detector. In previous years, the Barrel RICH recorded 0.24 million events with both radiators, and 0.73 million events with the gas radiator only. The identification power of the RICH depends on the accuracy of the Cherenkov angle measurement and on the detected number of photoelectrons. Stable operation of the different subsystems and monitoring of the relevant detector parameters is therefore very important. Table 4.2 shows averaged resolutions for both single photoelectrons and the resulting average Cherenkov angle

	B. liquid	B. gas	F. liquid	F. gas
number of photoelectrons per track	14	8	7	8
resolution (per photoelectron, mrad)	13.3	4.3	11.4	2.5
resolution (average angle, mrad)	5.2	1.5	5.0	1.2

Table 4.2: *Number of photoelectrons and angular resolutions (in mrad) for the Barrel (B) and Forward (F) RICH obtained with $Z^0 \to \mu^+\mu^-$ events [78].*

per track. A detailed simulation program that takes into account all known detector effects was tuned to reproduce the data.

Several particle identification algorithms have been developed in order to fulfill very different requirements. Some physics analyses need individual track tagging, while others measure statistically the content of a given sample, without associating tags to each track. For track by track tagging, the observed signal is compared with that expected for known particle types, namely e, μ, π, K and p, at the measured momentum. Depending on the decay mode analyzed, the priority may be high rejection or high efficiency. The requirements also depend on the dominant source of combinatorial background: pion rejection only, or proton/kaon separation. For statistical analyses, one needs a continuous estimator of the observed Cherenkov angle, independent of any mass hypothesis, such that the number of particles of a given type can be determined.

In a hadronic event, the main difficulty is to deal with the background under the Cherenkov signal, whose shape and level is different for each track and is a priori unknown. The algorithms developed so far follow two mains approaches. In the first, a flat background is fitted and no attempt is made to separate it from the signal. For each mass hypothesis, the expected signal is calculated. A flat background is adjusted in order to build and maximize a likelihood probability. The probabilities corresponding to the known particle types are then used for tagging. For statistical analyses, the likelihood probability is computed as a function of the Cherenkov angle, and the best one is retained. For further details on the HADSIGN algorithm see Ref. [100].

In the other approach, one uses a clustering algorithm to distinguish between background and signal photoelectrons. Photoelectrons are grouped into clusters, and given a weight according to quality criteria such as measurement errors or possible ambiguities between several tracks. The best cluster is retained, and weights are used to measure the average Cherenkov angle, its error and the estimated number of photoelectrons. Quality flags are set to allow different rejection levels. They are based on the detector status and the cluster quality. For further details on the RIBMEAN algorithm see Refs. [100, 101].

The distribution of the average Cherenkov angle as a function of the momentum in multi-hadronic events is shown in Fig. 4.8 for the liquid (top) and gaseous (bottom) radiators.

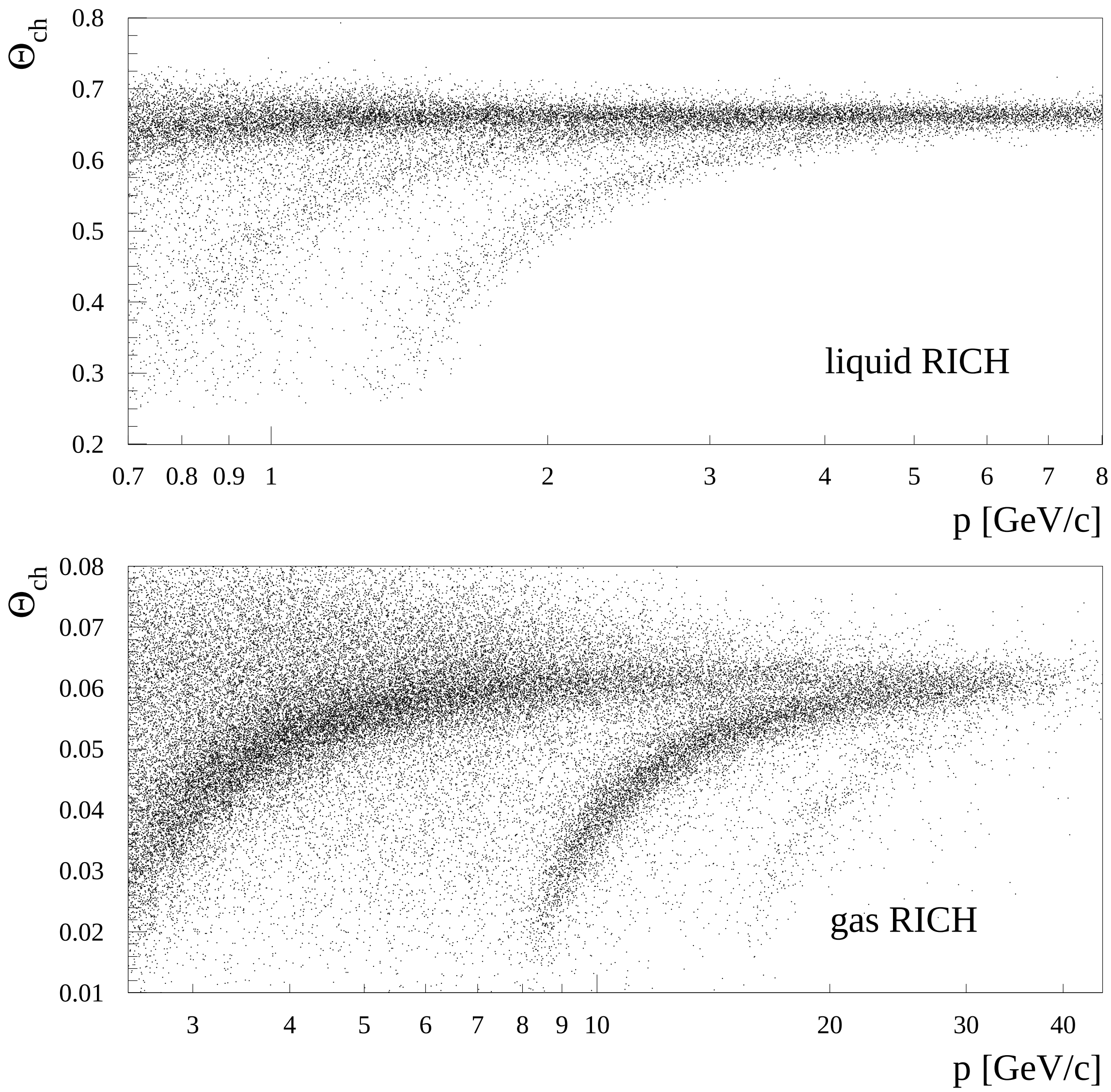

Figure 4.8: *Average Cherenkov angle per track as a function of the momentum in multi-hadronic events in the Barrel RICH, for the liquid (top) and gaseous (bottom) radiators. The three bands on both plots correspond to pions (upmost band), kaons (middle) and protons (lowest band) [78].*

Combination of TPC and RICH

The information originating from TPC and RICH are combined providing three different tagging levels (loose, standard and tight) for the separation of protons and kaons from pion background. Since the analysis presented is restricted to the barrel part of the detector, this discussion leaves out the performance in the forward part of DELPHI. The algorithm discussed is based on the official DELPHI hadron identification software (HADSIGN). The liquid radiator is used for particle identification in the momentum range from 0.7-4.0 GeV/c,

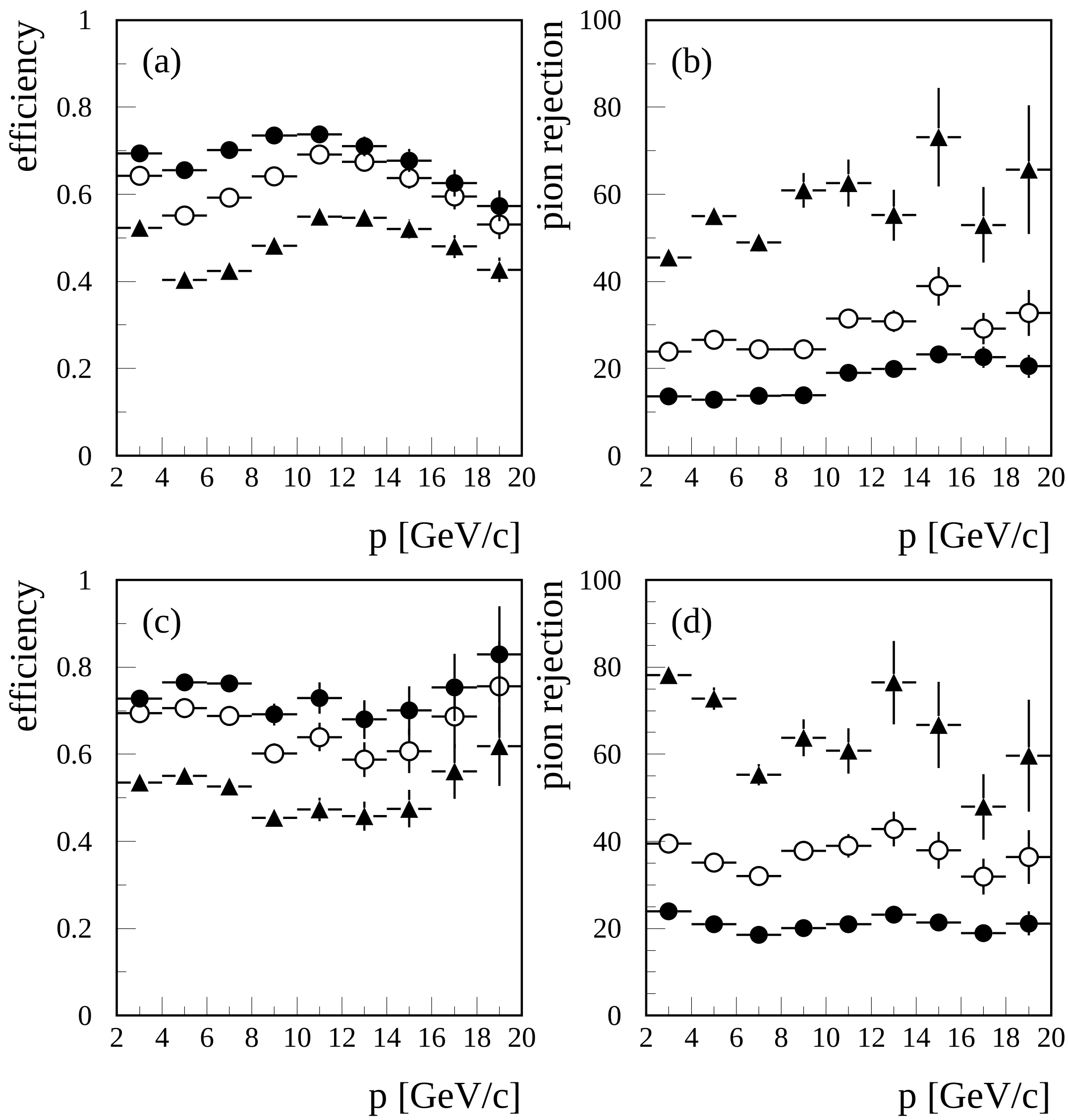

Figure 4.9: *Performance of the DELPHI hadron identification (HADSIGN) in multi-hadronic events. (a) Efficiency and (b) pion rejection power for the three different kaon tags as a function of momentum (full circles - loose tag, open circles - standard tag, triangles - tight tag). (c) Efficiency and (d) pion rejection power for proton identification.*

and the gaseous radiator is used from 2.5-25.0 GeV/c. Different operational modes of the RICH detector have to be considered, e.g. for the kaon tag it must be considered that the kaon band in the gas RICH starts at 8.5 GeV/c (see Fig. 4.8), which means that the gas RICH information below 8.5 GeV/c can be used *only* in the so-called veto mode. In the region between 8.5 and 25.0 GeV/c kaons can be tagged positively from the kaon band. The performance of the tagging routines has been tested using a multi-hadronic Monte Carlo sample. The efficiency and pion rejection power for kaon tagging (loose tag - KTAG $>$ 0.5, standard tag - KTAG $>$ 1 and tight tag - KTAG $>$ 2) as a function of track momentum is shown in Fig. 4.9(a) and (b). Analogous data for proton tagging (loose tag - PTAG $>$ 0.5, standard tag - PTAG $>$ 1 and tight tag - PTAG $>$ 2) are given in Fig. 4.9(c) and (d). For a typical multi-hadronic momentum spectrum above 0.7 GeV/c one obtains by demanding a standard kaon tag (KTAG $>$ 1) a sample containing approximately $(68 \pm 4)\%$ kaons. The average efficiency is estimated to be $(54 \pm 4)\%$. Similar estimations for the standard proton tag (PTAG $>$ 1) lead to a sample composition containing approximately $(43 \pm 4)\%$ protons. The main background in this case originates from misidentified kaons. The average efficiency is estimated to be $(60 \pm 4)\%$. All these quantities have been extracted from simulation. Systematic studies comparing data and simulation show the misidentification probability for kaon identification in Monte Carlo to be approximately a factor of two lower than in data [100].

4.6 V^0 Reconstruction

This section describes the standard DELPHI algorithm for Λ and K^0_s reconstruction [78]. By demanding a reconstructed Λ in a hemisphere a baryon enriched sample can be obtained (similar to demanding an identified proton). This method is used in the Σ_b and Σ_b^* analysis described in the next chapter.

Candidate V^0 decays in the sample of hadronic events are found by considering all pairs of oppositely charged particles. The vertex defined by each pair is determined such that the χ^2 obtained from the distances of the vertex to the extrapolated tracks (considered as ellipsoids in 5D space of perigee parameters[7]) is minimized.

The V^0 decay vertex candidates are required to satisfy the following criteria [78]:

- The angle $\Delta\phi$ in the XY plane between the V^0 momentum and the line joining the primary to the secondary vertex is less than $(0.01 + 0.02/p_t)$ rad, where p_t [GeV/c] is the transverse momentum of the V^0 candidate relative to the beam axis.
- The radial separation R of the primary and secondary vertex in the XY plane is greater than 4 standard deviations.
- The probability of the χ^2 fit to the secondary vertex is larger than 0.01.
- The transverse momentum of each particle of the V^0 with respect to the line of flight is greater than 0.02 GeV/c and the invariant mass for the e^+e^- hypothesis is less than 0.16 GeV/c^2.
- When the reconstructed decay point of the V^0 is beyond the VD radius, there is no signal in the VD consistent with association to the decay vertex.

The $\pi^+\pi^-$ and $p\pi^-$ ($\bar{p}\pi^+$) invariant masses (attributing the proton mass to the particle of larger momentum) are calculated. When a pair is consistent within three standard deviations with both K^0 and Λ ($\bar{\Lambda}$) hypotheses, the pair with the smaller mass pull (the absolute value of mass shift with respect to the nominal mass divided by the overall resolution) is selected. Finally, K^0 and Λ ($\bar{\Lambda}$) samples are defined if the probability to have decayed within the fitted

[7] A charged particle track can be described as a helix defined by five parameters ($\Theta, \phi, \kappa, \varepsilon$ and Z). These parameters evaluated at the point of closest approach to the primary vertex are called perigee parameters.

distance lies between 0.02 and 0.95 and if the difference between the invariant mass and the nominal mass is within two standard deviations. The mean resolution, defined as the FWHM of the fitted distributions, is 4.3 MeV/c^2 for K^0's and 1.8 MeV/c^2 for Λ's (using 94B data). The efficiency is strongly dependent on the V^0 momentum. For Λ's the efficiency rises from 10% at 0.5 GeV/c to 32% at 3.6 GeV/c and then drops to 6% at 17 GeV/c. For K^0's the efficiency rises from 9% at 0.5 GeV/c to 38% at 3.6 GeV/c and then drops to 10% at 17 GeV/c [78]. The efficiency for $K^0 \rightarrow \pi^+\pi^-$ in this selection averaged over the momentum spectrum is about 36% with a contamination of 3%. The average efficiency for $\Lambda \rightarrow p\pi$ is 30% with a contamination of about 10% [78].

4.7 Summary of the Chapter

- The presented analysis starts with a sample of 2 943 K multi-hadronic events taken with the DELPHI detector at LEP in the years 1991-1994. The multi-hadronic event selection is based on the reconstruction of charged particle tracks and neutral energy depositions in the calorimeters.

- The topology of each event is analyzed by calculating the thrust axis and evaluating the jet structure with the LUCLUS algorithm.

- Exploiting the long lifetime (1.6 ps) and the large mass (5.28 GeV/c^2) of b hadrons and using the good spatial resolution of the DELPHI vertex detector, a sample of $b\bar{b}$ events is enriched. With a purity of 83% (94%) one obtains approximately 371 K (199 K) events.

- The inclusive reconstruction of B mesons is based on the measured rapidity distribution of charged and neutral particles in an event. The rapidity of a particle is defined as $y = 0.5 \cdot \log((E + p_z)/(E - p_z))$, where E is the energy and p_z is the longitudinal momentum with respect to the thrust axis.

- Motivated by simulation studies, a first estimate for the B four-vector is given by the sum over all particles in a hemisphere with rapidity greater than 1.6. The estimated B energy E_y is corrected by a function, determined from simulation, which depends on the reconstructed mass m_y and the reconstructed energy E_h in the hemisphere.

- For standard cuts ($E_y > 20$ GeV, $|m_y - \langle m_y \rangle| < 2.5$ GeV/c^2 and $0.6 < E_{hem}/E_{beam} < 1.1$) an energy resolution for B mesons of 7% for 75% of the data is achieved, the remainder constituting a non-Gaussian tail towards higher energies. The angular resolution in Θ and ϕ can be parameterized as double-Gaussians with widths of 15 mrad for 60% of the data and 38 mrad for the remaining 40%.

- A vertex reconstruction algorithm is used in order to separate B^{**} pions originating from the primary vertex from B decay products. All well measured tracks, with at least two vertex detector hits associated, are classified into three vertices: the primary vertex, which has to be compatible with the known beam spot, and two B-decay vertices. The rapidity classification serves as a starting point. An iterative procedure reassigns tracks between the three vertices until a minimal χ^2 is found.

- The vertex reconstruction algorithm provides a resolution in ϕ compatible with the resolution from the inclusive B reconstruction algorithm (18 mrad for 65% of the data). The efficiency for particles from fragmentation to be assigned to the primary vertex is approximately constant at 35%. The purity of fragmentation particles which are assigned to the main vertex reveals a strong dependence on momentum. For particles between 0.1-2.0 GeV/c a purity of 86% is found.

- The DELPHI hadron identification is based on the dE/dx measurement of the TPC and the Cherenkov angle reconstruction of liquid and gas RICH. For a typical multi-hadronic momentum spectrum above 0.7 GeV/c one obtains a sample containing approximately $(68 \pm 4)\%$ kaons ($(43 \pm 4)\%$ protons) by demanding a standard kaon (proton) tag. The average efficiency for kaons (protons) is estimated to be $(54 \pm 4)\%$ ($(60 \pm 4)\%$).

Chapter 5

The Analysis

The main goal of this thesis is the search for and observation of orbitally excited B mesons in the decay channel $B^{**} \rightarrow B^{(*)}\pi$. The analysis starts with a multi-hadronic event selection, followed by the tagging of $b\bar{b}$ events. The four-vectors of the B or B^* mesons are reconstructed in an inclusive fashion using an algorithm based on a simple rapidity argument. The combination of inclusively reconstructed $B^{(*)}$ mesons with pions from the primary vertex leads to the first observation[1] of B^{**} mesons [1,8]. The obtained signal can consistently be described with theoretical expectations for B^{**} states. The helicity distribution of B^{**} mesons is analyzed and a charge analysis is performed. In addition, the B^{**} fragmentation is investigated.

A search for B_s^{**} mesons decaying into $B^{(*)}K$ is performed, exploiting the good kaon identification capabilities of the barrel RICH detector. Two narrow signals, consistent with the production of two narrow B_s^{**} states, are extracted from the data [8].

The third part of this chapter is dedicated to a search for the baryons Σ_b and Σ_b^*. Their expected main decay channel is into $\Lambda_b\pi$. The Λ_b is reconstructed in an inclusive fashion using the rapidity algorithm. In order to enhance the signal to background ratio, a baryon enrichment is achieved by using proton tagging and Λ reconstruction. An indication for the Σ_b baryon and first evidence for the Σ_b^* baryon are extracted from the data [9].

5.1 Observation of Orbitally Excited B Mesons ($B^{**} \rightarrow B^{(*)}\pi^{\pm}$)

If the mass of B^{**} mesons is above the $B^*\pi$ but below the $B\rho$ threshold, B^{**} mesons decay mainly into $B\pi$ *or* $B^*\pi$. Heavy Quark Effective Theory [13] groups the different B^{**} states into two doublets per B flavour according to the vector sum of the light quark's spin and the orbital angular momentum $\vec{j}_q = \vec{s}_q + \vec{L}$; where if $j_q = 3/2$, then $J^P = 1^+, 2^+$, and if $j_q = 1/2$, then $J^P = 0^+, 1^+$. The members of the first doublet should be very narrow compared to typical strong decay widths because only $L = 2$ decays are allowed. This is due to angular momentum and parity conservation for the 2^+ state and a dynamical prediction of HQET [13,51] for the 1^+ partner. Parity conservation also restricts the expected main decay

[1] The first evidence for B^{**} Mesons was obtained in parallel by two independent analyses in DELPHI [1] and OPAL [2]. The DELPHI analysis is presented here.

modes of the single states. The spin-parity state 0^+ would decay into $B\pi$ (s-wave), the two 1^+ states into $B^*\pi$ (s- or d-wave), and the 2^+ state into both $B\pi$ and $B^*\pi$ (both d-wave). Before the start of this work none of the orbitally excited B meson states was experimentally known. In the D meson sector, the two narrow states have been identified experimentally, and spin/parity and decay characteristics have been shown to be in accord with the HQET predictions [102] (see section 2.4.3).

5.1.1 Experimental Procedure and Results

Most of the experimental tools (e.g. multi-hadron selection, b-tagging, inclusive B reconstruction and vertex reconstruction) which are needed for this analysis have been discussed in the previous chapter. The analysis concentrates on the decay channels $B^{**} \to B^*\pi$ and $B^{**} \to B\pi$. The B or B^* four-momentum is evaluated using the inclusive B reconstruction algorithm described in section 4.3. Note that with the present experimental methods there is no distinction between B and B^* mesons. Therefore they are labeled as $B^{(*)}$. Both the B decay particles as well as the B^{**} decay pion have large rapidities. However, since the B^{**} decays strongly, the pion should originate from the primary vertex and not from the B-decay vertex (see section 4.4). The cuts used in this analysis are the following:

- Multi-hadron event selection (see section 4.1)
- Event topology cuts (see section 4.1)
  - restrict analysis to barrel: $|\cos(\Theta_{thrust})| \leq 0.75$
  - accept only two-jet events: NJET = 2
- Tagging of b hemispheres (see section 4.2)
  - event tag $\mathcal{P}_E < 0.01$, efficiency = $(65 \pm 3)\%$ purity = $(83 \pm 4)\%$
  - hemisphere tag $\mathcal{P}_H < 0.01$, efficiency = $(43 \pm 3)\%$ purity = $(78 \pm 4)\%$
- Inclusive B reconstruction (see section 4.3)
  - quality cuts: $E_y > 28$ GeV, $|m_y - \langle m_y \rangle| < 1.2$ GeV/c^2 and $0.6 < E_{hem}/E_{beam} < 1.1$
  - restrict B vector to barrel: $|\cos\Theta_B| > 0.02$, $|\cos\Theta_B| < 0.7$
- Vertex reconstruction algorithm (see section 4.4)
  - quality of vertex reconstruction: $|\cos\Theta_V| > 0.8$
  - flight distance: $d > 1.5$ mm
- Pion track selection cuts (see sections 4.2, 4.4 and 4.5)
  - accept only pions which are assigned to the primary vertex
  - cut on the b-tagging signed track probability: $-0.85 < \mathcal{P}_T^* < 0.85$ [2]
  - restrict pion vector to barrel: $|\cos\Theta_\pi| > 0.05$, $|\cos\Theta_\pi| < 0.7$
  - veto kaons and protons: KTAG ≤ 1, PTAG ≤ 1 (HADSIGN)
  - standard veto on electrons or muons
  - pion momentum cut: $p_\pi > 1.5$ GeV/c

[2] The quantity $\mathcal{P}_T^*$ originates from the b-tagging package (see section 4.2). It is defined as the $+\mathcal{P}_T$ for tracks with positive impact parameter, and $-\mathcal{P}_T$ for tracks with negative impact parameter, where $\mathcal{P}_T$ is the probability for a track to originate from the primary vertex.

The quantity which is best accessible experimentally with inclusive B reconstruction methods is the Q-value[3] of the decay:

$$\boxed{Q = m(B^{(*)}\pi) - m(B^{(*)}) - m(\pi) \equiv m(B^{**}) - m(B^{(*)}) - m(\pi)\ .} \qquad (5.1)$$

The resolution of the present method as obtained from simulation can be parameterized as $\sigma(Q) = 23\ \mathrm{MeV/c^2}\ + 87\ \mathrm{MeV/c^2}\ \times (Q[\mathrm{GeV/c^2}])$. It is dominated by the energy and angular resolution of the B meson. Whether the decay was actually into B or B^* and whether the B^* decay photon has been reconstructed, only has a negligible effect on the resolution in the Q-value. However, the decay of a B^{**} of a given mass to a $B^*\pi$ gives rise to a Q-value which is shifted downwards by the B^*-B mass difference of 46 MeV/c^2 compared to the Q-value of a $B\pi$ decay. Therefore, for the determination of a B^{**} mass from the measurable Q-value an assumption about the B^*/B ratio in the signal has to be employed.

The distribution of the measured $B^{(*)}\pi$ Q-values obtained with the DELPHI detector is shown as data points in Fig. 5.1(a). The analysis is performed with a sample of 2 943K multi-hadronic events taken with the DELPHI detector in the years 1991-1994 using the SDST data sets: 91F1 - 255K, 92D2 - 700K, 93C1 - 708K and 94B1 - 1280K (see section 4.1). There is a large excess of combinations on top of a smoothly falling background. The background, described by the Monte Carlo prediction in which B^{**} decay pions have been suppressed, is shown as the shaded area in Fig. 5.1(a). The normalization is extracted from the sideband in the range between 0.5 GeV/c^2 and 1.2 GeV/c^2. The Monte Carlo statistics corresponds to 1.43 times the data statistics.

Deviations of the background model from the measured data are observed at low Q-value. The origin of this difference is not yet fully understood, but it might be related to the rate of inclusive D^* mesons, the relative b baryon to B meson production, possible decays of B^{**} mesons into $B\rho$, the modelling of yet unmeasured B hadron decays, or to general limitations of the JETSET string fragmentation model. It is worth noting that the HERWIG 5.8 generator predicts a much less steep rise of the background at small Q-values. The reason for this originates from the fragmentation model (cluster instead of string) rather than the different modelling of the parton shower. This has been inferred from a Monte Carlo study with the HERWIG parton shower generator interfaced to LUND string fragmentation. The difference between the JETSET and HERWIG generator is larger than the observed deviation between data and JETSET . However, note that the whole excess of entries originating from $B^{**} \to B^{(*)}\pi$ decays was not known before the start of this analysis and thus was not simulated in the Monte Carlo.

Fig. 5.1(b) shows the background subtracted $B^{(*)}\pi$ pair Q-value distribution obtained from Fig. 5.1(a). The solid line originates from a model containing two narrow and two broad states. Details of this model and further comparisons with predictions are discussed in section 5.1.2. The yield of the signal and its mean Q-value can be extracted using different methods, e.g. the signal can be fitted to a simple Gaussian or a Breit-Wigner function. A fit of the signal to a simple Gaussian with central value

$$\boxed{Q(B^{**} \to B^{(*)}\pi) = 283\ \pm\ 5\,(\mathrm{stat.})\ \pm\ 12\,(\mathrm{syst.})\ \mathrm{MeV/c^2}} \qquad (5.2)$$

and Gaussian width

$$\boxed{\sigma(Q) = 68\ \pm\ 5\,(\mathrm{stat.})\ \pm\ 8\,(\mathrm{syst.})\ \mathrm{MeV/c^2}} \qquad (5.3)$$

[3] In the calculation of the Q-value the pion candidate is excluded from the inclusive B reconstruction.

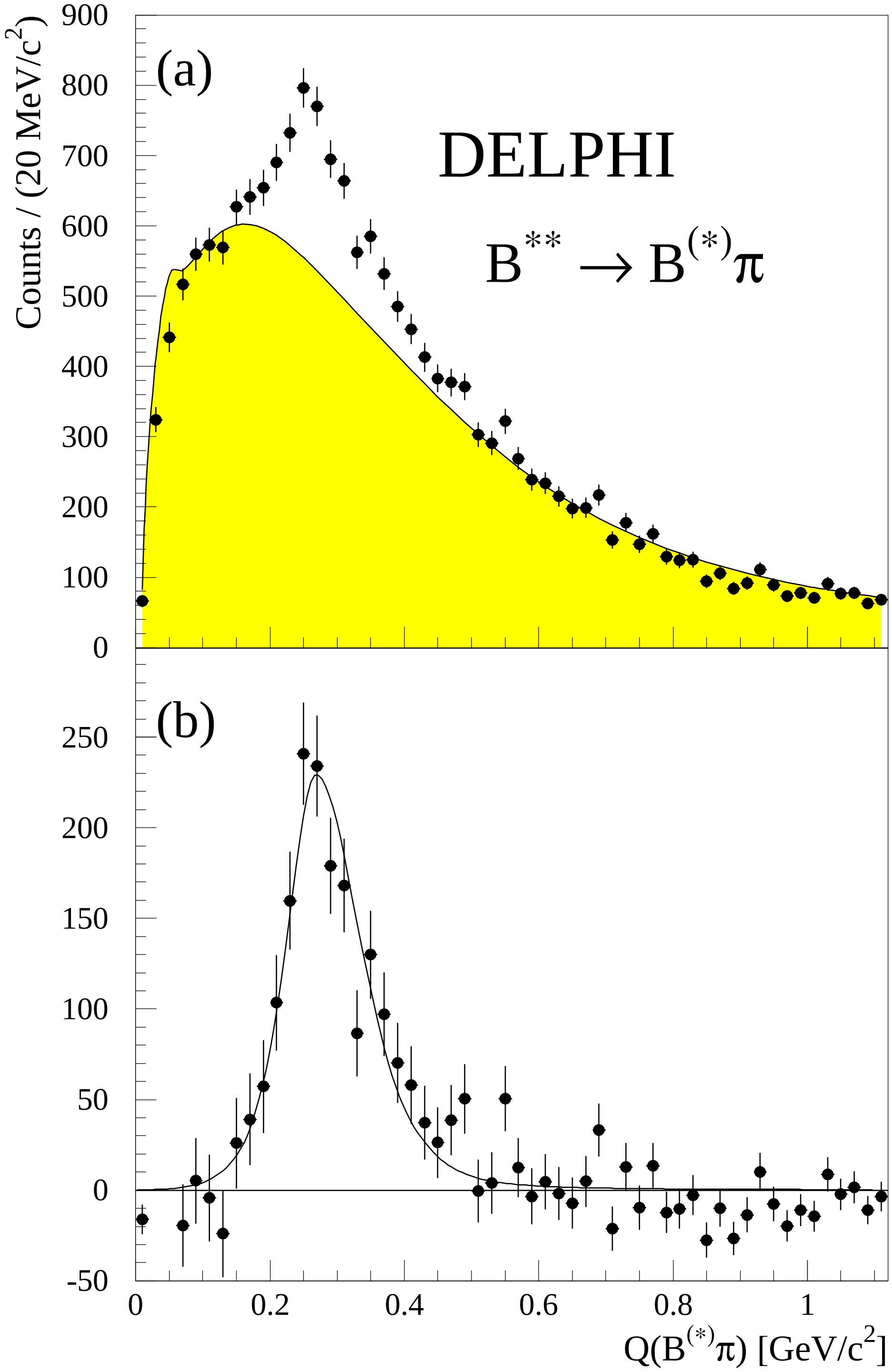

Figure 5.1: *(a) Distribution of the Q-value of $B^{(*)}\pi$ pairs (data points) along with the Monte Carlo expectation without B^{**} production (shaded area). Q is defined as $Q = m(B^{(*)}\pi) - m(B^{(*)}) - m(\pi)$. (b) Background subtracted $B^{(*)}\pi$ pair Q-value distribution. The solid line originates from a model containing two narrow and two broad states (see Fig. 5.2(f)).*

contains

$$\boxed{N = 1704 \pm 101\,(\text{stat.}) \pm 323\,(\text{syst.})} \tag{5.4}$$

events. This corresponds to a statistical significance of approximately 17 standard deviations. The main systematics on the number of events and on the width of the Gaussian originates from the modelling and the normalization of the background.

B^{**} Production Rate

Extracting the acceptance for B^{**} pions from simulation, the total $B^{**}_{u,d}$ production cross section is determined to be

$$\boxed{\sigma_{B^{**}_{u,d}}/\sigma_b = 0.241 \pm 0.015\,(\text{stat.}) \pm 0.058\,(\text{syst.})\,.} \tag{5.5}$$

In this rate calculation it is assumed that 2/3 of all B^{**} decay into charged pions and 1/3 into (unobserved) π^0, according to isospin rules for an $I = 1/2$ decay into an isovector and an isospinor. From this the total number of $B^{**}_{u,d}$ mesons per hadronic Z decay is determined to be

$$\boxed{N_{B^{**}_{u,d}}/Z_{had} = 0.097 \pm 0.006\,(\text{stat.}) \pm 0.022\,(\text{syst.})\,.} \tag{5.6}$$

Assuming the b baryon rate to be $(10\pm 4)\%$ [56] and the $B_s^{(*)}$ rate to be $(13\pm 2)\%$ (see section 2.4.2), the relative amount of $B_{u,d}$ mesons which originate from $B^{**}_{u,d}$ decay is

$$\boxed{\sigma_{B^{**}_{u,d}}/\sigma_{B_{u,d}} = 0.302 \pm 0.015\,(\text{stat.}) \pm 0.074\,(\text{syst.})\,.} \tag{5.7}$$

Systematic Uncertainties

Systematic uncertainties dominate in the measurements of all these quantities. Different systematic checks have been performed leading to a determination of the systematic errors. The main sources are discussed here.

- The modelling and the normalization of the background is the dominant source of the systematic error. Different background shapes originating from simulation and various phenomenological background models (e.g. $f(Q) = a_1 \cdot Q^{a_2} \cdot \exp(-a_3 \cdot Q - a_4 \cdot Q^2 - a_5 \cdot Q^3)$) are fitted to the data. The normalization is extracted from the sideband in the range between 0.5 GeV/c^2 and 1.2 GeV/c^2. These bounds are varied by $\pm$0.1 GeV/c^2. Furthermore, the normalization is extract from the left sideband ($0.0 < Q < 0.15$ GeV/c^2) *and* the right sideband ($0.5 < Q < 1.2$ GeV/c^2) of the B^{**} signal. This method suffers from deviations between data and simulation at low Q-values. Employing the simulation prediction for the background shape, the normalization has to be adjusted by the factor $0.95 \pm 0.01\,(\text{stat.}) \pm 0.04$ (syst., depending on cuts, see below) in order to describe well the data at large Q-values. These studies lead to a systematic error of $\pm$189 entries on the yield, $\pm$7 MeV/c^2 on the Q-value, and $\pm$6 MeV/c^2 on the width.

- The complete analysis is repeated several times with different sets of B and π selection cuts. This is realized in an automatic procedure providing hundreds of histograms with different cuts and automatic fitting algorithms. The minimum B momentum cut is varied between 20 GeV and 30 GeV, the cut on the difference between the reconstructed and the mean B mass is varied between 1.0 GeV/c^2 and 3.0 GeV/c^2. Furthermore, the cut on the momentum of the pion candidate is varied between 0.5 GeV/c^2 and 2.0 GeV/c^2. The quoted systematic errors on the Q-value, $\sigma(Q)$ and the number of events N correspond to half the observed width in each case. The systematic error on the yield is ± 176, the error on the Q-value is ± 7 MeV/c^2, and the error on the width is ± 4 MeV/c^2.

- A further systematic uncertainty originates from the way the yield is extracted from the data. The result of a simple Gaussian fit to the signal are given above, consistent with the results of a Breit-Wigner fit or a simple counting method. The systematic error on the yield from this source is ± 105.

- The limited Monte Carlo statistics of 4.1 million multi-hadronic Z^0 events as well as the modelling of B^{**} decays in simulation account for a systematic error of ± 112 entries on the yield, ± 2 MeV/c^2 on the Q-value, and on ± 2 MeV/c^2 on the width $\sigma(Q)$.

- To check whether the signal could be an artifact of the employed vertex procedure (since it depends crucially on the correct modelling of the perigee parameter and the covariance matrices of the tracks), the selection cuts are varied over wide ranges. The cut on the flight distance is varied from 0.05 cm to 0.2 cm, while the cut on $|\cos\Theta_V|$ is varied between 0.0 and 0.9. Furthermore, by using simpler analysis techniques without vertex reconstruction (based on different cuts on $\mathcal{P}_T^*$), a clear excess with the same characteristics is observed, but it is on top of a larger combinatorial background. The systematic errors are ± 78 on the yield, ± 2 MeV/c^2 on the Q-value and ± 2 MeV/c^2 on the width $\sigma(Q)$.

- In order to test the stability of the results as a function of b-purity, the cut on the event b-tagging probability $\mathcal{P}_E$ is varied in the range between 10^{-6} and 0.05. This range corresponds to a variation in b-purity between $(99 \pm 1)\%$ and $(63 \pm 3)\%$. The extracted systematic error on the yield is ± 89 and the error on the mass is ± 4 MeV/c^2.

- Possible reflections from $B_s^{**} \to B^{(*)}K$ decays are expected to contribute in the Q-value range between 50 and 250 MeV/c^2 in the order of 8% to the expected $B_{u,d}^{**}$ signal. Additional uncertainties are introduced by the possible production of $\Sigma_b \to \Lambda_b\pi$ and $\Sigma_b^* \to \Lambda_b\pi$, and reflections from the decay $B_{u,d}^{**} \to B^{(*)}\rho$. Their possible influence in the signal region is found to be small.

In addition, the helicity distribution of the B^{**} signal is investigated by dividing it into eight helicity bins. The distribution is compared with theoretical expectations. This is discussed in detail in section 5.1.3. The charge symmetry of the signal is tested by dividing the sample according to positive and negative pion charge and positive and negative jet charge. More details are given in section 5.1.4. All tests have been passed successfully, no cut being found where the behaviour of the data was different from that expected from the simulation prediction for a strongly decaying isospin $I = 1/2$ $B^{(*)}\pi$ resonance.

5.1.2 Interpretation and Comparison with Predictions

If the signal were due to a single very narrow resonance, the expected Gaussian width would be around $\sigma = 48$ MeV/c^2, as shown in Fig. 5.2(a). This interpretation is unlikely. In order to describe the observed signal with a single resonance, its full width would have to be

$$\boxed{\Gamma = 86 \pm 24 \text{ MeV/c}^2\ .} \tag{5.8}$$

A comparison of the signal with a single resonance of this width is shown in Fig. 5.2(b). The signal could be broadened by the fact that different resonances with possibly different masses contribute, and that some decay into $B\pi$ and others into $B^*\pi$, leading to a 46 MeV/c^2 shift in Q-value. The observed signal shape is consistent with predictions for orbital excitations. According to this model the signal would consist of two narrow (1^+ and 2^+) and two broad (0^+ and 1^+) resonances of roughly the same mass (splittings at the 10 MeV/c^2 level), and decays into $B^*\pi$ or $B\pi$, as dictated by spin-parity rules. The 2^+ is predicted to decay into both $B^*\pi$ and $B\pi$ with about equal rates [40,41].

There is no prediction about the relative production rates of the four B^{**} states, but reasonable assumptions range between 5:3:3:1 (spin counting) and 1:1:1:1 (state counting) for the $2^+ : 1^+ : 1^+ : 0^+$ states. In the D meson sector the production ratios $D_2^* \to D\pi$: $D_2^* \to D^*\pi$: $D_1 \to D^*\pi$ have been measured by CLEO [36,37] to be roughly 2:1:3. This is compatible with the state counting picture for the narrow states. It also confirms the ratio $D_2^* \to D\pi : D_2^* \to D^*\pi = 1.8 : 1$ decay branching ratio prediction from HQET [40,41]. These facts motivate the use of state counting and HQET predictions.

Fig. 5.2(c) and 5.2(d) compare the background subtracted Q-value distribution with models of two narrow states (of width $\Gamma \approx 20$ MeV/c^2) based on the HQET predictions of Eichten, et al. [40,41]. In order to obtain better agreement with observations the predicted masses are shifted downwards by 37 MeV/c^2 [4]. In Fig. 5.2(c) state counting is assumed for the relative production ratio between 2^+ and 1^+ states ($2^+ : 1^+ = 1 : 1$). Fig. 5.2(d) shows the same comparison but using the spin counting model ($2^+ : 1^+ = 5 : 3$). Both models give fairly good descriptions of the data. However, an even better agreement would be obtained by implying a somewhat larger mass splitting between the two states.

The observed signal could also contain broad resonances with a full width Γ of about 150 MeV/c^2. Assuming two narrow states with a width of roughly 20 MeV/c^2 and two broad states with a width of 150 MeV/c^2 and a production ratio of $1:1:1:1$ for the four B^{**} states leads to rather good agreement, as shown in Fig. 5.2(e). The broad states are assumed to have the same mass as the narrow states. Similar good agreement is obtained by using the spin counting model, leading to a production ratio of $5:3:3:1$ for the four B^{**} states (see Fig. 5.2(f)).

Furthermore, models with large mass splittings (of the order of ≈ 40 MeV/c^2) between narrow and broad states also lead to fairly good descriptions of the data. Such large mass splittings between the $j_q = 3/2$ and $1/2$ states have been proposed by Rosner et al. [51].

With the current experimental sensitivity the different interpretations in the models in Figs. 5.2(b)-(f) cannot be distinguished, and neither can any of them be discarded. However, due to the large freedom, consistent results can be achieved in a number of possible scenarios based on quark model and HQET.

[4] The measured Q-value is somewhat lower than the predictions by Eichten, et al., but it is consistent within the errors if one assumes a theoretical uncertainty of roughly 30 MeV/c^2.

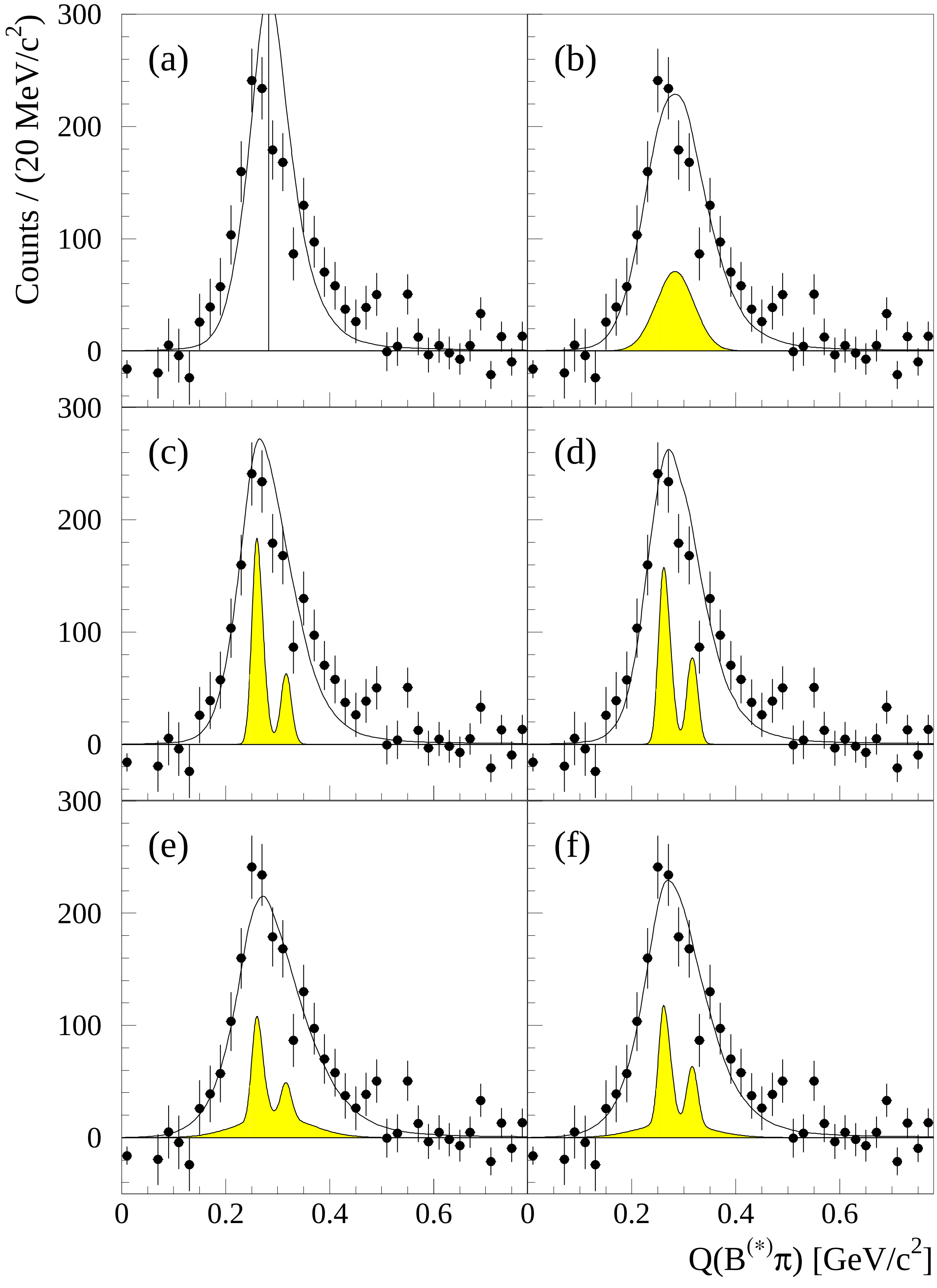

Figure 5.2: *Comparison of the background subtracted Q-value distribution (data points) with various models (solid lines). The shaded area corresponds to the generated distribution (scaled by a factor 0.2) prior to detector resolution effects. The different models in the histograms (a)-(f) are discussed in the text.*

Assuming a $B^*\pi$ to $B\pi$ ratio of 2 : 1, the mean mass difference between the B meson and the cross section weighted mean of the four expected $B^{**}_{u,d}$ resonances is determined to be

$$\boxed{m(B^{**}_{u,d}) - m(B_{u,d}) = 453 \pm 5\,(\text{stat.}) \pm 17\,(\text{syst.})\ \text{MeV/c}^2}\ , \tag{5.9}$$

corresponding to a mass of

$$\boxed{m(B^{**}_{u,d}) = 5732 \pm 5\,(\text{stat.}) \pm 17\,(\text{syst.})\ \text{MeV/c}^2}\ . \tag{5.10}$$

Part of the systematic error is due to the uncertainty in the ratio of decays into B^* and B in the mapping from Q-value to mass difference. Tt can accommodate the two reasonable assumptions 1 : 1 and 3 : 1 (see section 2.4.2). This value is somewhat lower than the predicted values of 5771 MeV/c^2 for the B_2^* and 5759 MeV/c^2 for the B_1 mass differences [40, 41], but it is consistent within the errors if one adds a theoretical uncertainty of roughly 30 MeV/c^2 for the predictions (see section 2.4.3).

5.1.3 B^{**} Helicity Analysis

The angular distribution of the decay pions in the B^{**} helicity frame is investigated. To ensure acceptance in the backward hemisphere, the cuts of the original analysis are loosened, e.g. the cut on the pion momentum is removed. The analysis uses the following cuts:

- Multi-hadron event selection (see section 4.1)
- Event topology cuts (see section 4.1)
  - restrict analysis to barrel: $|\cos(\Theta_{thrust})| \leq 0.75$
  - accept only two-jet events: NJET = 2
- Tagging of b hemispheres (see section 4.2)
  - event tag $\mathcal{P}_E < 0.01$, efficiency = $(65 \pm 3)\%$ purity = $(83 \pm 4)\%$
- Inclusive B reconstruction (see section 4.3)
  - quality cuts: $E_y > 22$ GeV, $|m_y - \langle m_y \rangle| < 1.5$ GeV/c^2 and $0.6 < E_{hem}/E_{beam} < 1.1$
  - restrict B vector to barrel: $|\cos\Theta_B| > 0.02$, $|\cos\Theta_B| < 0.7$
- Vertex reconstruction algorithm (see section 4.4)
  - quality of vertex reconstruction: $|\cos\Theta_V| > 0.8$
  - flight distance: $d > 1.0$ mm
- Pion track selection cuts (see sections 4.2, 4.4 and 4.5)
  - accept only pions which are assigned to the primary vertex
  - cut on the b-tagging signed track probability: $\mathcal{P}_T^* > -0.85$
  - restrict pion vector to barrel: $|\cos\Theta_\pi| > 0.05$, $|\cos\Theta_\pi| < 0.7$
  - veto kaons and protons: KTAG ≤ 1, PTAG ≤ 1 (HADSIGN)
  - standard veto on electrons or muons
  - pion candidate belongs to the two most energetic particles at the primary vertex in a hemisphere

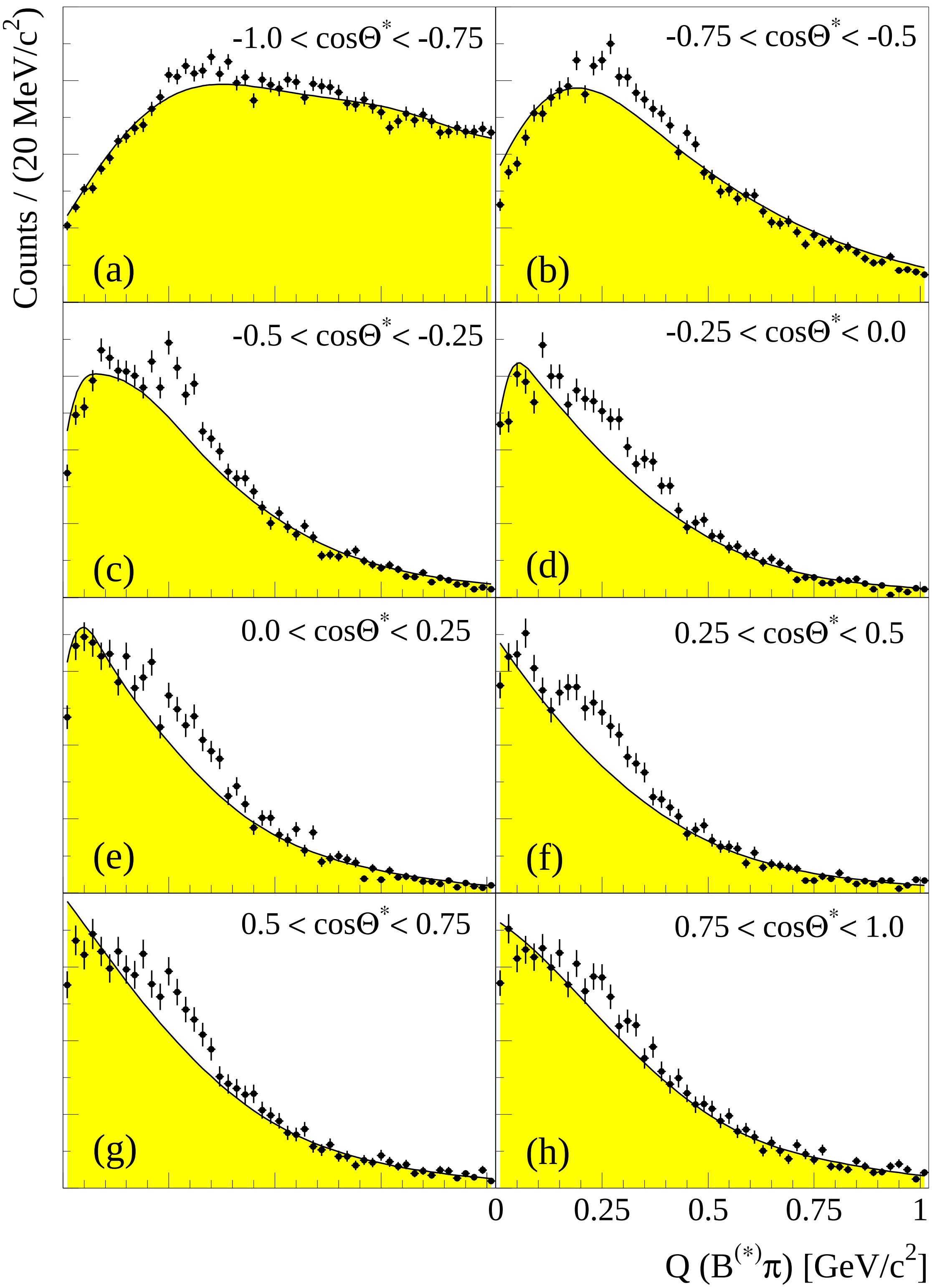

Figure 5.3: *(a)-(h) Q-value distribution of $B^{(*)}\pi$ pairs (data points) along with Monte Carlo expectations without B^{**} production (shaded area) in helicity bins.*

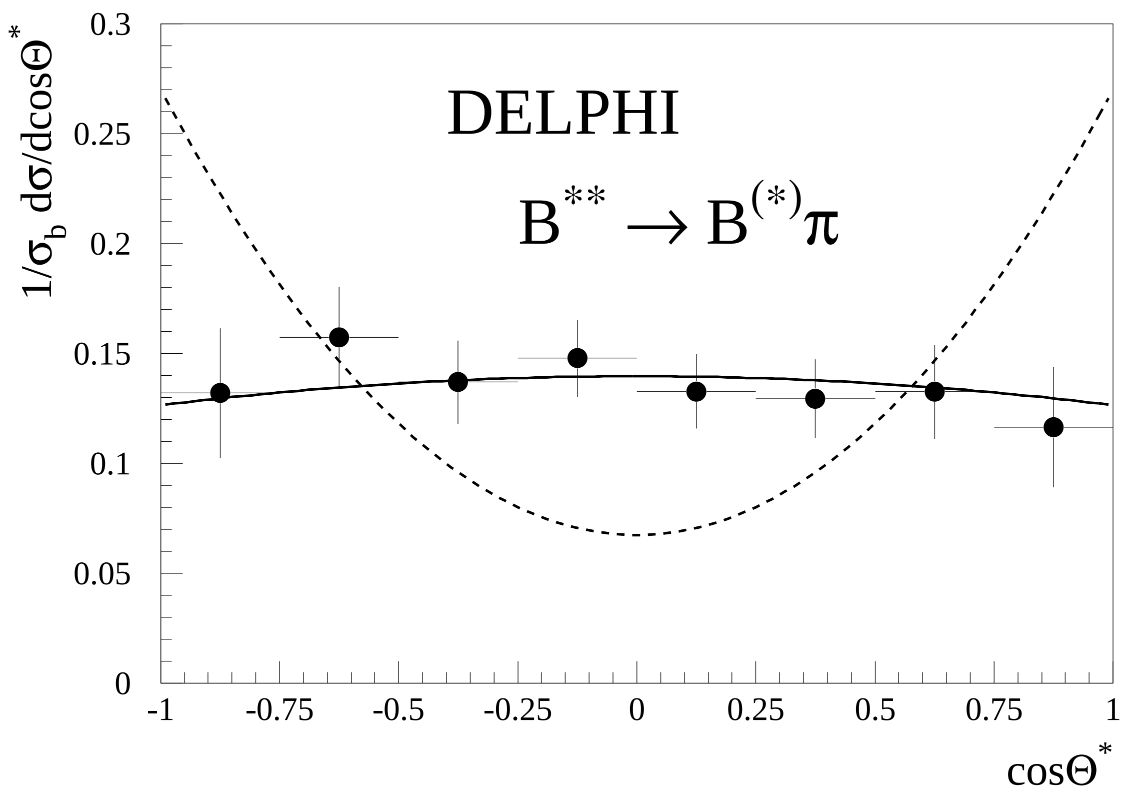

Figure 5.4: *Decay angle distribution for B^{**} pions in the B^{**} rest frame. The solid line is the best fit to the model of Falk and Peskin leading to $w_{3/2} = 0.53 \pm 0.07 \pm 0.10$. The dashed line corresponds to $w_{3/2} = 0$.*

The total data sample is divided into eight bins of cosΘ^*, where Θ^* is the angle between the decay pion in the B^{**} rest frame and the B^{**} line of flight in the laboratory. The B^{**} signal is extracted separately for each bin in cosΘ^* by simple counting of the yield in the Q-value range between 0.14 GeV/c^2 and 0.42 GeV/c^2. From simulation, the resolution on cosΘ^* is found to be 0.05. Even without reconstruction of the B^* helicity, the $B^{**} \to B^{(*)}\pi$ helicity angle distribution is not expected to be flat for all helicity states. However, if all contributing states are completely unpolarized, the distribution will be flat.

The Q-value distributions for the eight helicity bins are shown in Figs. 5.3(a)-(h). A significant change in the shape of the background in different bins is evident from the distributions. Note that low energetic particles ($p < 1.0$ GeV/c) and particles close to the thrust axis contribute mainly in the backward hemisphere at low Q-values. Since the lower end of the particle momentum spectrum and its angular distribution with respect to the thrust axis in b events are not precisely known, this leads to inaccurate descriptions of the background. Deviations of the simulated background from the data especially at low Q-values are visible[5]. The dominant systematic error in the extraction of the yield originates from these deviations and the background normalization. The background has been normalized from the right and left sideband, thereby allowing *only* smooth variations between neighbouring helicity bins.

[5] This fact and possible reasons have already been discussed in section 5.1.

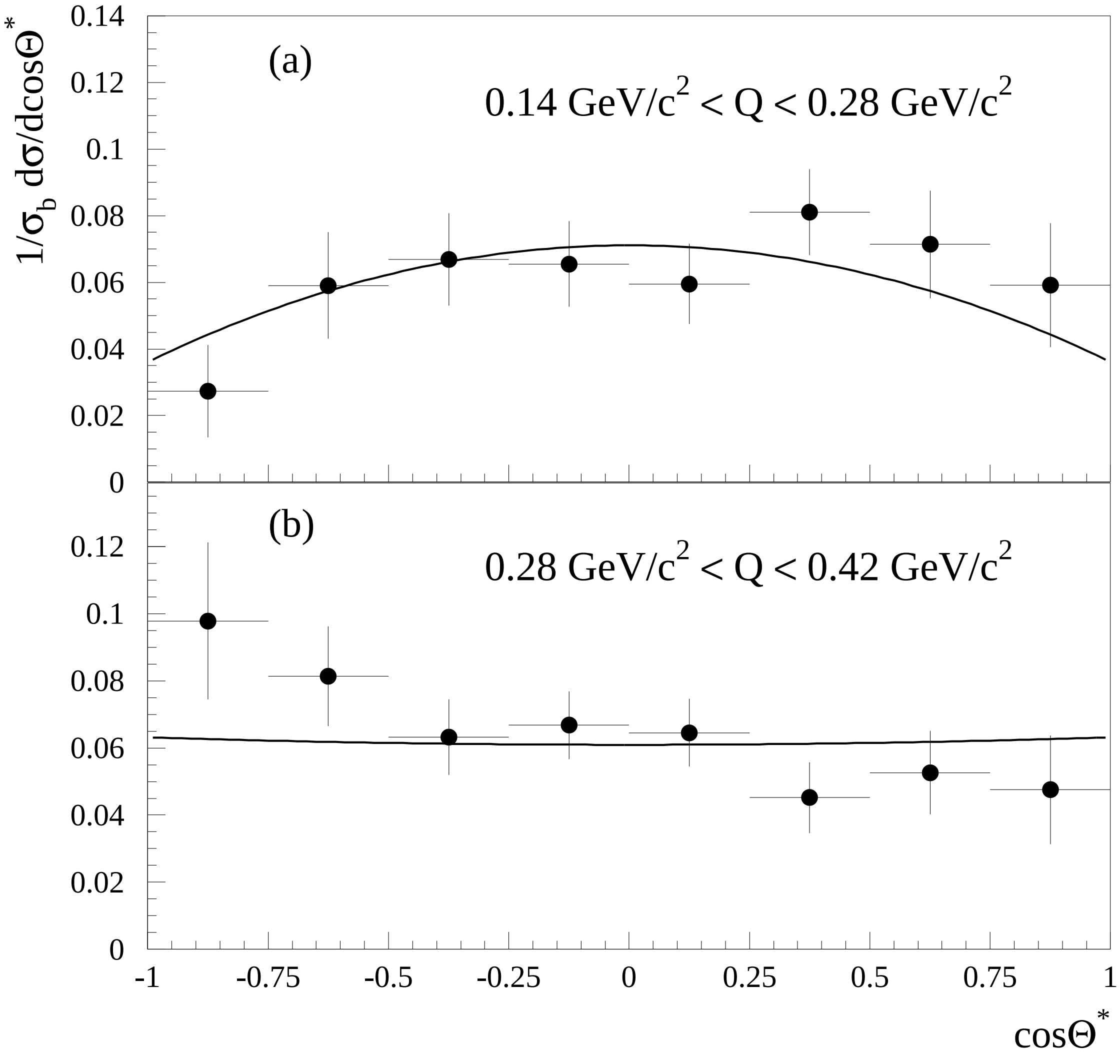

Figure 5.5: *Decay angle distribution for B^{**} pions in the B^{**} rest frame for the first and second half of the signal. The solid lines are the best fits to the model of Falk and Peskin leading to (a) $w_{3/2} = 0.69 \pm 0.11 \pm 0.10$ and (b) $w_{3/2} = 0.49 \pm 0.10 \pm 0.10$.*

The differential production rate $1/\sigma_b \cdot d\sigma/d\cos\Theta^*$ in the eight helicity bins is consistent with being flat, as shown in Fig. 5.4(a), If the model assumption shown in Fig. 5.2(c) or (d) is correct, the upper half of the Q-value distribution should contain mainly the signal from $B_2^* \to B\pi$, whereas the lower half is a mixture of $B_1 \to B^*\pi$ and $B_2^* \to B^*\pi$. If any of the resonances is produced in a preferred helicity state, one expects a deviation from a flat angular distribution. Therefore, the angular distributions are also evaluated separately in the regions $0.14 < Q < 0.28$ GeV/c^2 and $0.28 < Q < 0.42$ GeV/c^2. In both energy regions the angular distributions are consistent with being flat, as shown in Fig. 5.5.

The ARGUS collaboration has obtained some evidence that the helicity ± 2 state of D_2^* production is suppressed in low energy ($\approx$ 5 GeV) c-quark fragmentation [45], which leads to an enrichment at very forward and backward angles. Falk and Peskin [71] attribute the ARGUS result to a suppression of the maximally aligned helicity states $\lambda_{j_q} = \pm 3/2$ of the

helicity bin	$1/\sigma_b \cdot d\sigma/d\cos\Theta^*$ all	$1/\sigma_b \cdot d\sigma/d\cos\Theta^*$ 1st half	$1/\sigma_b \cdot d\sigma/d\cos\Theta^*$ 2nd half
$-1.00 < \cos\Theta^* < -0.75$	$(13.2 \pm 3.0 \pm 3.4)\%$	$(2.7 \pm 1.4 \pm 1.8)\%$	$(9.8 \pm 2.3 \pm 1.8)\%$
$-0.75 < \cos\Theta^* < -0.50$	$(15.7 \pm 2.3 \pm 3.4)\%$	$(5.9 \pm 1.6 \pm 1.8)\%$	$(8.1 \pm 1.5 \pm 1.8)\%$
$-0.50 < \cos\Theta^* < -0.25$	$(13.7 \pm 1.9 \pm 3.4)\%$	$(6.7 \pm 1.4 \pm 1.8)\%$	$(6.3 \pm 1.1 \pm 1.8)\%$
$-0.25 < \cos\Theta^* < \pm 0.00$	$(14.8 \pm 1.7 \pm 3.4)\%$	$(6.6 \pm 1.3 \pm 1.8)\%$	$(6.7 \pm 1.0 \pm 1.8)\%$
$\pm 0.00 < \cos\Theta^* < +0.25$	$(13.3 \pm 1.7 \pm 3.4)\%$	$(5.9 \pm 1.2 \pm 1.8)\%$	$(6.5 \pm 1.0 \pm 1.8)\%$
$+0.25 < \cos\Theta^* < +0.50$	$(13.0 \pm 1.8 \pm 3.4)\%$	$(8.1 \pm 1.3 \pm 1.8)\%$	$(4.5 \pm 1.1 \pm 1.8)\%$
$+0.50 < \cos\Theta^* < +0.75$	$(13.3 \pm 2.1 \pm 3.4)\%$	$(7.1 \pm 1.6 \pm 1.8)\%$	$(5.3 \pm 1.2 \pm 1.8)\%$
$+0.75 < \cos\Theta^* < +1.00$	$(11.6 \pm 2.7 \pm 3.4)\%$	$(5.9 \pm 1.9 \pm 1.8)\%$	$(4.7 \pm 1.6 \pm 1.8)\%$

Table 5.1: *Differential cross section $1/\sigma_b \cdot d\sigma/d\cos\Theta^*$ for eight helicity bins. The second column gives the obtained production rates for the whole signal, while the third and forth columns give the rates for the first and second half of it.*

total angular momentum of the light quark system $j_q = s_q \oplus L = 3/2$, described by a weight factor $w_{3/2}$ which according to the ARGUS result should be near zero. If this model is valid, then the same suppression should hold here for the narrow 1^+ and 2^+ states. Translating from the D to the B system, Falk and Peskin predict the angular distribution of both the B_1 and B_2^*, whether decaying into $B\pi$ or $B^*\pi$ to be of the form

$$\boxed{\frac{1}{\Gamma}\frac{d\Gamma}{d\cos\Theta^*}(B_1, B_2^* \to B, B^*\pi) = \frac{1}{4}\left(1 + 3\cos^2\Theta^* - 6w_{3/2}(\cos^2\Theta^* - \tfrac{1}{3})\right)\ .} \tag{5.11}$$

A fit to the measured angular distribution leads to

$$\boxed{w_{3/2} = 0.53 \pm 0.07(\text{stat.}) \pm 0.10(\text{syst.})\ ,} \tag{5.12}$$

shown as a solid line in Fig. 5.4(a). The systematic error has been estimated from uncertainties in the background modelling in the different $\cos\Theta^*$ bins. The angular distribution corresponding to the ARGUS result $w_{3/2} = 0$ is shown as dashed line in Fig. 5.4(a). It clearly does not describe the data well. If the observed B^{**} signal were due to mainly narrow B^{**} states, there would be a severe *disagreement* with either the model prediction or with the ARGUS data[6]. The angular distributions of the first and second half of the B^{**} signal are also consistent with being flat, corresponding to

$$\boxed{w_{3/2} = 0.69 \pm 0.11\ (\text{stat.})\ \pm 0.10\ (\text{syst.})} \tag{5.13}$$

for the first region, and

$$\boxed{w_{3/2} = 0.49 \pm 0.10\ (\text{stat.})\ \pm 0.10\ (\text{syst.})\ .} \tag{5.14}$$

for the second region (see Fig. 5.5). The systematic error has been estimated from uncertainties in the background modelling in the different $\cos\Theta^*$ bins. The measured differential cross sections $1/\sigma_b \cdot d\sigma/d\cos\Theta^*$ are summarized in Tab. 5.1. The second column corresponds to the production rates in the whole signal, while the third and forth columns give the rates for the first and second half of it.

[6]The CLEO collaboration which dominates the present D_2^* world average doesn't make any statement concerning the D_2^* helicity distribution yet.

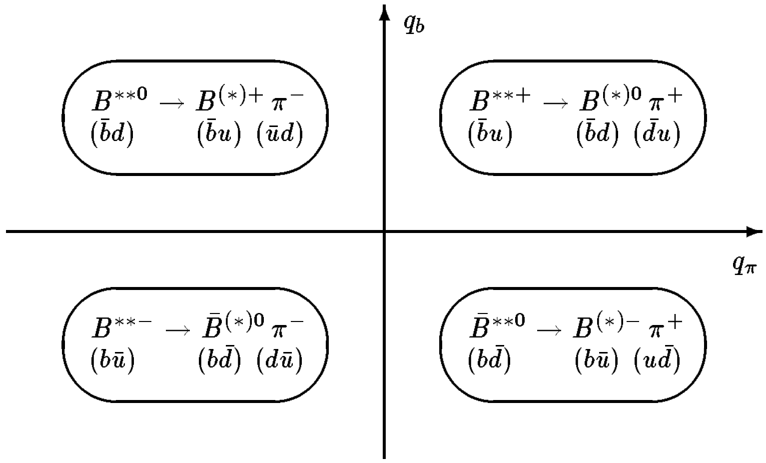

Figure 5.6: *Decay characteristics for the four B^{**} charge states decaying into charged pions. The horizontal axis denotes the pion charge, while the vertical axis denotes the charge of the involved b quark.*

5.1.4 B^{**} Charge Analysis

The charge symmetry of the extracted B^{**} signal is investigated. Positively charged pions can come from decays of the $I_3 = +1/2$ states B^{**+} (containing a $\bar{b}$ quark) and $\bar{B}^{**0}$ (containing a b quark). Therefore, flavour tagging with e.g. inclusive leptons or jet charge cannot be used to enhance the ratio of B^{**} signal to background[7].

However, methods based on flavour tagging and pion charge can be used to check the consistency of the signal. Therefore, the observed signal is divided into four subsamples according to the jet charge of the hemisphere containing the B^{**} candidate and the pion charge. If the signal stems from an $I = 1/2$ resonance, the production rates extracted from all four charge combinations $B^{(*)+}\pi^-$ (enriched by positive jet charge, negative pion), $B^{(*)0}\pi^+$ (positive jet-charge, positive pion), $\bar{B}^{(*)0}\pi^-$ (negative jet charge, negative pion) and $B^{(*)-}\pi^+$ (negative jet charge, positive pion) are expected to be the same. The four possible charge combinations are shown in Fig. 5.6. The horizontal axis denotes the pion charge, while the vertical axis denotes the charge of the involved b quark.

The analysis is based on the same selection cuts as described in section 5.1.3. Furthermore, an additional momentum cut for the B^{**} pion candidate is applied ($p_\pi > 1.5$ GeV/c), in order reduce uncertainties in the background modelling at low Q-values. The jet charge j_c is defined as the (longitudinal) momentum-weighted charge average of all charged particles in an event hemisphere, i.e.

$$\boxed{j_c = \frac{\sum\limits_i q_i \cdot |\vec{p}_i \vec{t}|^\kappa}{\sum\limits_i |\vec{p}_i \vec{t}|^\kappa}}\ , \tag{5.15}$$

where $\vec{p}_i$ and q_i are the three-momentum and charge of a particle with index i in a given hemisphere. The vector $\vec{t}$ denotes the thrust axis as defined in section 4.1. For this summation only particles passing the track selection cuts described in section 4.1 are considered. A

[7] An enhancement of signal to background can be achieved by tagging the B meson charge. Such an algorithm is presently under construction in the DELPHI collaboration.

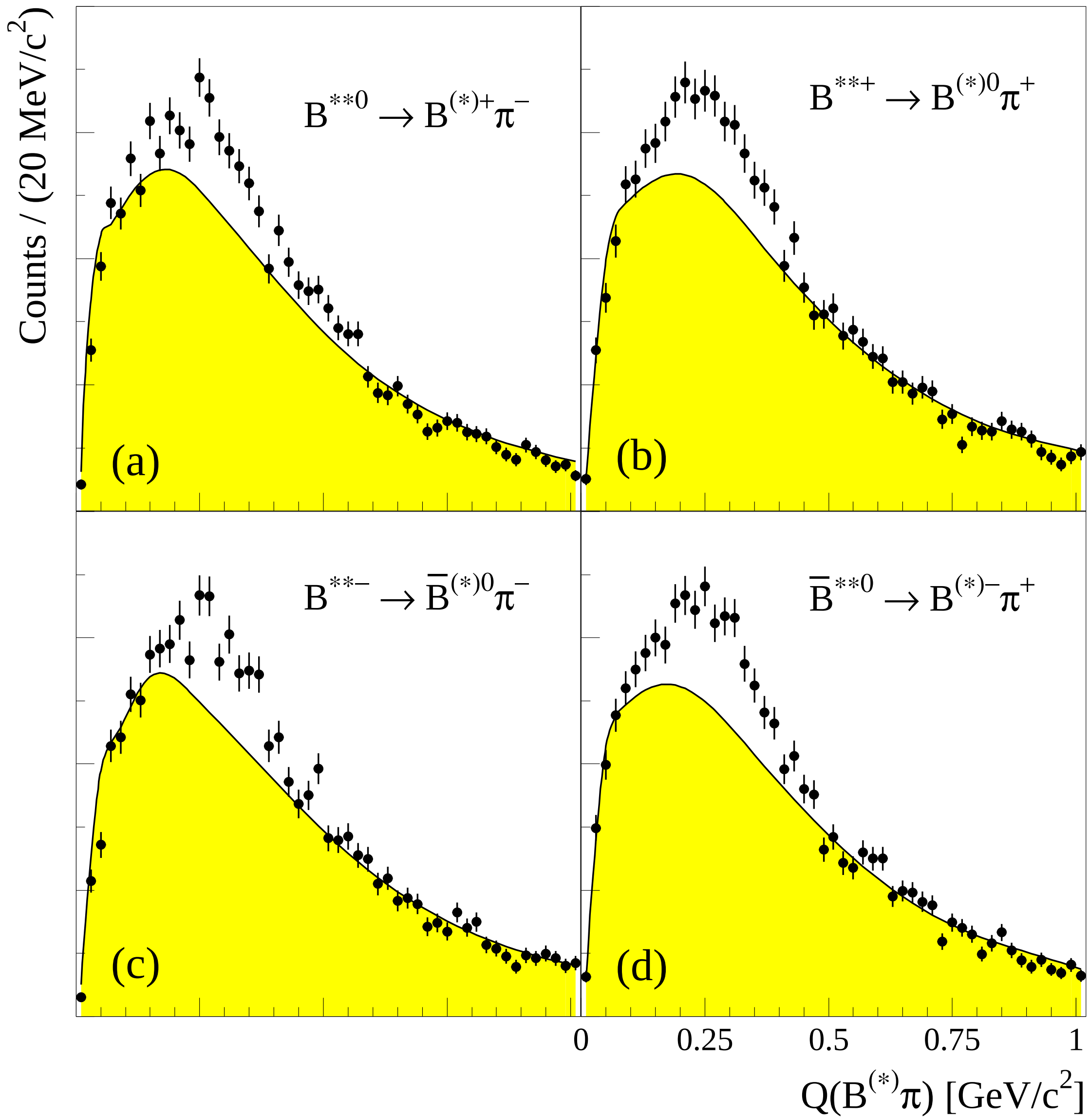

Figure 5.7: *Distribution of the Q-value of $B^{(*)}\pi$ pairs (data points) along with the Monte Carlo background expectation for four different charge combinations: (a) $B^{(*)+}\pi^-$, (b) $B^{(*)0}\pi^+$, (c) $\bar{B}^{(*)0}\pi^-$, and (d) $B^{(*)-}\pi^+$.*

minimal momentum cut of $p_{min} = 0.1$ GeV/c was chosen in that analysis. The free tuning parameter κ allows one to give different weights to the different parts of the momentum spectrum. The width of the jet charge distribution rises with κ. This comes from the fact that a large value of the exponent results in a situation in which the leading particle in the hemisphere completely dominates the value of j_c. In the limit $\kappa \rightarrow \infty$, j_c becomes a binary operator with the possible values ± 1 resulting from the charge of the leading particle. In the limit of $\kappa \rightarrow 0$, j_c simply reflects the average charge in the hemisphere. For this analysis a value of $\kappa = 0.6$ is chosen. In order to increase sensitivity to the charge of the primary

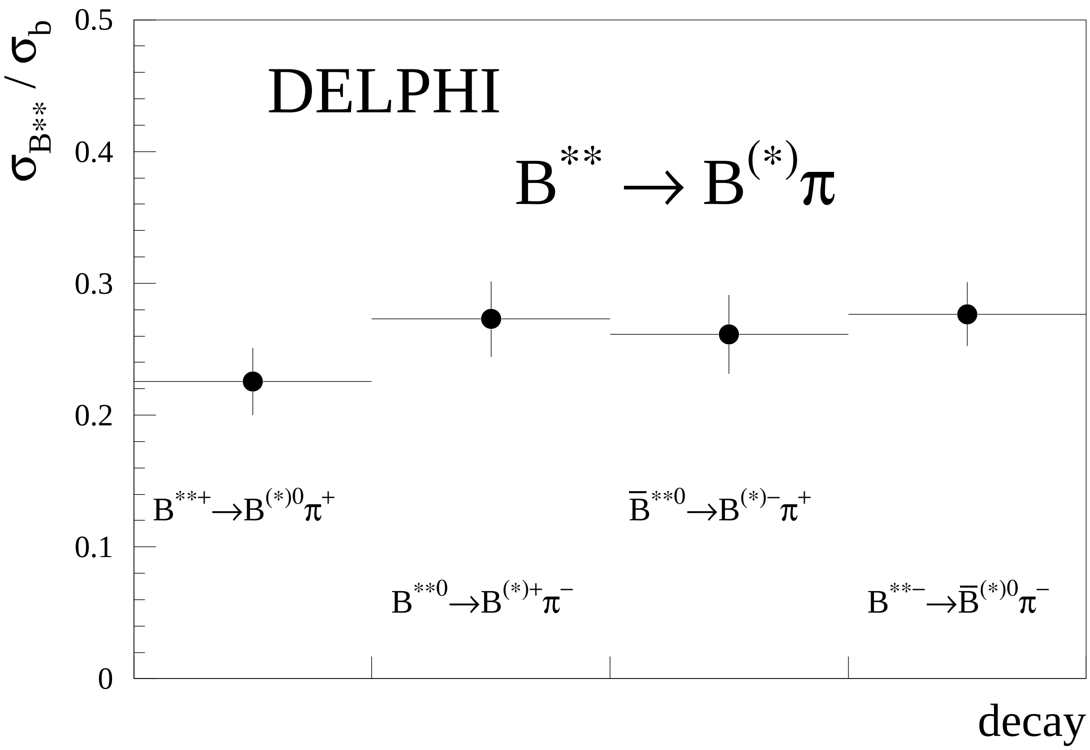

Figure 5.8: *Total production cross section $\sigma_{B^{**}}/\sigma_b$ obtained from the four different charge combinations: $B^{(*)0}\pi^+$, $B^{(*)+}\pi^-$, $B^{(*)-}\pi^+$, and $\bar{B}^{(*)0}\pi^-$. The enrichment for $B^{(*)+}$ is (83 ± 3)%, and for $B^{(*)0}$ it is (70 ± 3)%.*

quark the difference between the jet charge in opposite hemispheres is formed, resulting in the definition of the so-called *charge flow*

$$\boxed{q_b = j_{c,same} - j_{c,oppo}} \ , \tag{5.16}$$

where $j_{c,same}$ denotes the jet charge in the hemisphere of the B^{**} candidate and $j_{c,oppo}$ denotes the jet charge in the opposite hemisphere. From simulation one expects that a positive charge flow will select (83 ± 3)% of $B^{(*)+}$ and (70 ± 3)% of $B^{(*)0}$. The four possible charge subsamples of the B^{**} signal based on pion charge q_π and charge flow q_b are shown in Figs. 5.7(a)-(d). The extracted total cross sections $\sigma_{B^{**}}/\sigma_b$ are shown graphically in Fig. 5.8. The numerical results are given in Tab. 5.2. The data are consistent with the assumption that the B^{**} signal stems from an $I = 1/2$ resonance, i.e the production rates extracted from the four charge combinations $B^{(*)+}\pi^-$, $B^{(*)0}\pi^+$, $\bar{B}^{(*)0}\pi^-$ and $B^{(*)-}\pi^+$ are the same within errors.

5.1.5 B^{**} Fragmentation

The differential cross section $1/\sigma_b \cdot d\sigma/dx_{Etrue}$ is analyzed. The analysis starts with the same cuts as already described in section 5.1.3. The data sample is divided into seven equally populated bins in $x_{Erec} = E_B/E_{beam}$, E_B being the corrected energy as described in section

charge state	cut	enrichment	$\sigma_{B^{**}}/\sigma_b$
$B^{(*)0}\pi^+$	$q_\pi > 0, q_b > 0$	$(70 \pm 3)\%$	$(22.6 \pm 2.5 \pm 5.8)\%$
$B^{(*)+}\pi^-$	$q_\pi < 0, q_b > 0$	$(83 \pm 3)\%$	$(27.3 \pm 2.9 \pm 5.8)\%$
$B^{(*)-}\pi^+$	$q_\pi > 0, q_b < 0$	$(83 \pm 3)\%$	$(26.1 \pm 3.0 \pm 5.8)\%$
$\bar{B}^{(*)0}\pi^-$	$q_\pi < 0, q_b < 0$	$(70 \pm 3)\%$	$(27.6 \pm 2.4 \pm 5.8)\%$

Table 5.2: *Total production cross section $\sigma_{B^{**}}/\sigma_b$ evaluated for the four different charge combinations $B^{(*)0}\pi^+$, $B^{(*)+}\pi^-$, $B^{(*)-}\pi^+$, and $\bar{B}^{(*)0}\pi^-$.*

4.3. The $B^{**} - B^{(*)}$ Q-value plot is fitted in each of these bins. An unfolding procedure is applied that uses a simulated B^{**} sample to generate the reconstructed energy spectrum x_{Erec} in each of five bins of true energy x_{Etrue}. A fit to the data histogram is performed using the five simulation histograms. The fit parameters determine the normalization coefficients of the simulation histograms such that the resulting histogram of the reconstructed energies best describes the data. In order to avoid spurious oscillations that are typical in such unfolding procedures [103], regularization is enforced by adding to the χ^2 a term proportional to the curvature of the unfolding result, as follows:

$$\chi^2 \rightarrow \chi'^2 = \chi^2 + \tau \cdot \int |f''(x)|^2 \, dx \approx \chi^2 + \tau \cdot \sum_{i=2}^{n-1} |f_{i-1} - 2 \cdot f_i + f_{i+1}|^2 \, . \tag{5.17}$$

The regularization parameter, τ, is chosen so as to minimize the condition number (i.e. the ratio of the largest to the smallest eigenvalue) of the correlation matrix ($\tau = 2.5$). Much smaller values lead to oscillating solutions and large negative correlations, whereas too large values lead to too flat solutions, too small errors and strong positive correlations. However, the results are stable in the τ range between 0.1 and 10.

The final differential cross section as a function of the true energy is obtained by multiplying these relative deviations from the simulation prediction by the simulation input cross section. The results are shown as points in Fig. 5.9. The shaded histogram gives the expectation from simulation (JETSET 7.3 [22] with DELPHI tuning [34]). The measured fragmentation is somewhat harder than in simulation. It is also harder than the average b-hadron fragmentation [99]. The measured differential cross section is given separately for each bin in Tab. 5.3. It has been checked that the result is independent of the fragmentation function used in the simulation by repeating the unfolding procedure with Monte Carlo events weighted as a function of x_{Etrue}.

x_{Etrue} bin	$1/\sigma_b \cdot d\sigma/dx_{Etrue}$
$0.5 - 0.6$	$(0.8 \pm 1.3 \pm 0.2)\%$
$0.6 - 0.7$	$(2.4 \pm 0.9 \pm 0.6)\%$
$0.7 - 0.8$	$(6.2 \pm 1.0 \pm 1.6)\%$
$0.8 - 0.9$	$(10.2 \pm 1.0 \pm 2.6)\%$
$0.9 - 1.0$	$(6.3 \pm 1.5 \pm 1.6)\%$

Table 5.3: *Differential cross section $1/\sigma_b \cdot d\sigma/dx_{Etrue}$ for five bins of x_{Etrue}. The data are obtained by using an unfolding procedure.*

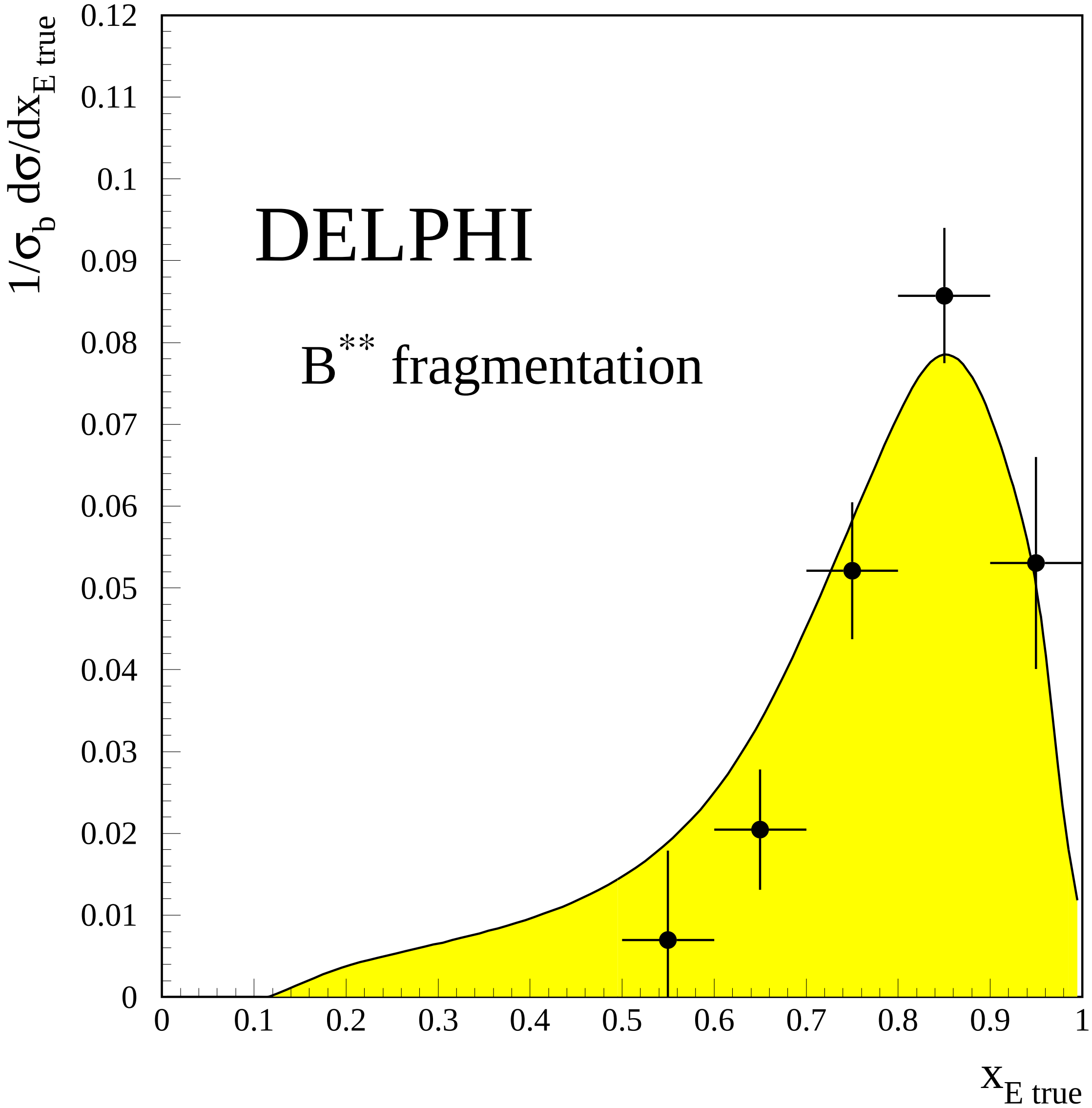

Figure 5.9: *Inclusive B^{**} cross section in bins of x_{Etrue}. The points are unfolded data. The curve shows the expectation from the simulation.*

5.1.6 Comparison with other Experiments

First evidence for B^{**} mesons was obtained in parallel by two independent analyses in the DELPHI [1] and OPAL [2] collaboration. Additional evidence was reported later by the ALEPH collaboration using a technique similar to the DELPHI analysis presented here [32]. Furthermore, ALEPH observed B^{**} mesons using fully exclusive methods [104]. All the results are compatible with each other and are summarized in Tab. 5.4.

For the B^{**} mass values, quoted in Tab. 5.4, a production ratio B^* : B mesons of $2:1$ in B^{**} decays is assumed. The mass values given by the OPAL and ALEPH collaboration are corrected in this way. This leads to a world average of 5730 ± 9 MeV/c^2.

Quantity	Experiment	Measurement	Ref.
mass $m_{B^{**}_{u,d}}$ [MeV/c^2]	OPAL	5712 ± 11 (stat.)	[2]
	DELPHI	$5732 \pm 5 \pm 17$	[8]
	ALEPH	$5734 \pm 3 \pm 17$	[32]
	ALEPH excl.	5734 ± 14	[104]
	average	5730 ± 9	
uncorr. width σ [MeV/c^2]	DELPHI	$68 \pm 5 \pm 8$	[8]
	ALEPH	$53 \pm 3 \pm 9$	[32]
	ALEPH excl.	28^{+18}_{-14}	[104]
single resonance Γ [MeV/c^2]	OPAL	116 ± 24	[2]
	DELPHI	86 ± 24	[8]
rate $\sigma(B^{**}_{u,d})/\sigma(B_{u,d})$ [%]	OPAL	$18 \pm 1.2 \pm 3.5$	[2]
	DELPHI	$30.2 \pm 1.5 \pm 7.4$	[8]
	ALEPH	$27.9 \pm 1.6^{+7.1}_{-8.1}$	[32]
	ALEPH excl.	30 ± 8	[104]
hel. param. $w_{3/2}$, all	DELPHI	$0.53 \pm 0.07 \pm 0.10$	[8]
hel. param. $w_{3/2}$, 1st half	DELPHI	$0.69 \pm 0.11 \pm 0.10$	[8]
hel. param. $w_{3/2}$, 2nd half	DELPHI	$0.49 \pm 0.10 \pm 0.10$	[8]

Table 5.4: *LEP $B^{**}_{u,d} \to B^{(*)}\pi$ results. Masses are recalculated from mass differences or from Q-values using an upward shift of 31 MeV/c^2 in order to account for the average $B^{**} \to B^*$ contribution.*

The uncorrected width of the B^{**} signal is consistent in the inclusive analyses of DELPHI and ALEPH. Differences in this quantity arise from the different models of the background rather than from significant differences in the data. The exclusive ALEPH analysis reveals a much smaller uncorrected width for the signal, which favours the interpretation of narrow resonances. The observed signal in all analyses can be described consistently by the production of two narrow B^{**} states with a mass splitting of the order of 10 MeV/c^2. An interpretation of the B^{**} signal as stemming from only one resonance leads to a width of $\Gamma = 116 \pm 24$ in the OPAL and a width of $\Gamma = 86 \pm 24$ in the DELPHI analysis.

The production cross section $\sigma(B^{**}_{u,d})/\sigma(B_{u,d})$ is found to be approximately 25%. The dominant uncertainty in extracting the rate originates from the modelling and normalization of the unknown background.

The helicity parameter $w_{3/2}$ as well as the B^{**} fragmentation have been investigated only in the DELPHI analysis. A confirmation of the DELPHI results on the B^{**} helicity distribution and the B^{**} fragmentation by the other LEP collaborations would be welcome.

5.2 Search for Orbitally Excited Strange B Mesons ($B_s^{**} \to B^{(*)}K^{\pm}$)

This section reports on a search for orbitally excited strange B mesons, usually labeled B_s^{**}, in the decay mode $B_s^{**} \to B^{(*)}K^{\pm}$. If the B_s^{**} meson mass is above the $B^{(*)}K$ threshold, then this will be the dominant decay mode since the channel $B_s^{(*)}\pi$ is forbidden by isospin conservation. Parity conservation restricts the expected main decay modes of the single states: the spin-parity state 0^+ will decay into BK (s-wave), the two 1^+ states will decay into B^*K (s- or d-wave), and the 2^+ state will decay into both BK and B^*K (both d-wave). If the B_s^{**} meson mass is below the $B^{(*)}K$ threshold, then the decay will be electromagnetic. The expected strangeness suppression factor of 1 : 6 for B_s^{**} mesons compared to $B_{u,d}^{**}$ mesons makes an observation of these states challenging (see section 2.4.2).

5.2.1 Experimental Procedure and Results

The analysis presented here is very similar to the original B^{**} analysis as discussed in section 5.1. Most of the experimental tools (b-tagging, inclusive B reconstruction, vertex reconstruction and hadron identification) which are needed for the analysis have been described in the previous chapter.

Since the B_s^{**} meson decays rapidly through the strong interaction, the kaon should originate from the primary vertex and not from the B-decay vertex. The decay channel $B^{(*)}K_s^0$ is difficult to observe experimentally due to the limited K_s^0 reconstruction efficiency and to the dominant K_s^0 background from B decays[8]. Therefore, the search focuses on B_s^{**} states decaying into charged kaons $K^{\pm}$.

Charged kaons are identified using the dE/dx information measured by the TPC and the Cherenkov angle reconstruction in the gas and liquid RICH. In the momentum range 1 to 3 GeV/c a kaon ring in the liquid RICH is required (HADSIGN: KTAG > 1, liquid ring required), while the veto mode of the gas RICH (RIBMEAN: KTAG > 1) or dE/dx measured by the TPC (Prob.($K^{\pm}$) $>$ Prob.($\pi^{\pm}$)) is used in the momentum range above 3 GeV/c. Monte Carlo studies show an approximately constant kaon tagging efficiency of $(51 \pm 5)\%$ with an average pion rejection factor of 15 ± 2. This corresponds to an average purity of the sample of $(51 \pm 5)\%$. Details of the DELPHI hadron identification software have been discussed in section 4.5.

In the B_s^{**} analysis quark-flavour tagging can be used to suppress background. A B_s^{**} can decay into $B^{(*)-}K^+$ (and $B^{(*)0}K_s^0$), but not into $B^{(*)+}K^-$. Thus, the K^+ will be accompanied by a $B^{(*)-}$ meson (containing a b quark) and the opposite hemisphere will contain a $\bar{b}$ quark. This fact is illustrated in Fig. 5.10. The horizontal axis gives the kaon charge while the vertical axis denotes the charge of the b quark. To enhance the signal to background ratio a cut on $(j_{c,same} - j_{c,oppo}) \cdot q_K$ is applied, where j_c denotes the jet charge calculated using an energy weighting exponent $\kappa = 0.6$ (see section 5.1.4). The symbol $j_{c,same}$ refers to the jet charge in the signal hemisphere, while $j_{c,oppo}$ refers to the jet charge in the opposite hemisphere. In the signal hemisphere the kaon itself is excluded from the jet charge calculation. Fig. 5.11

[8] The reconstruction of the origin (primary or secondary vertex) of a K_s^0 from the decay $K_s^0 \to \pi^+\pi^-$ a few tens of centimeters away from the interaction point is not possible.

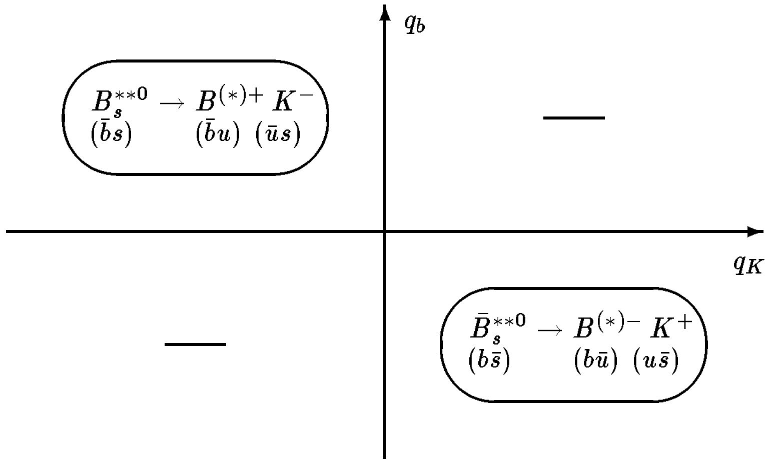

Figure 5.10: *Decay characteristics for the two B_s^{**} charge states decaying into charged kaons. The horizontal axis denotes the kaon charge, while the vertical axis denotes the charge of the involved b quark.*

shows the distribution of $(j_{c,same} - j_{c,oppo}) \cdot q_K$ for simulated B_s^{**} kaons and background from fragmentation. The signal accumulates mostly at negative values, while the background is almost symmetrically distributed around zero. A cut $(j_{c,same} - j_{c,oppo}) \cdot q_K < 0$ is applied. Approximately $(80 \pm 3)\%$ of the B_s^{**} decays fulfill this criterion, whereas only $(60 \pm 1)\%$ of the background pass this cut.

In summary, the analysis uses the following cuts:

- Multi-hadron event selection (see section 4.1)
- Event topology cuts (see section 4.1)
  - restrict analysis to barrel: $|\cos(\Theta_{thrust})| \leq 0.75$
  - accept two-jet events and most energetic jet in three-jet events
- Tagging of b hemispheres (see section 4.2)
  - event tag $\mathcal{P}_E < 0.01$, efficiency $= (65 \pm 3)\%$, purity $= (83 \pm 4)\%$
- Inclusive B reconstruction (see section 4.3)
  - quality cuts: $E_y > 18$ GeV, $|m_y - \langle m_y \rangle| < 2.5$ GeV/c^2 and $0.6 < E_{hem}/E_{beam} < 1.1$
  - restrict B vector to barrel: $|\cos\Theta_B| > 0.02$, $|\cos\Theta_B| < 0.7$
- Kaon track selection cuts (see sections 4.2, 4.4 and 4.5)
  - accept only tracks which are assigned to the primary vertex
  - restrict koan vector to barrel: $|\cos\Theta_K| > 0.05$, $|\cos\Theta_K| < 0.7$
  - standard veto on electrons or muons
  - kaon momentum cut: $p_K > 1.0$ GeV/c
  - perform kaon tagging:
    efficiency $= (51 \pm 5)\%$, purity $= (51 \pm 5)\%$
  - jet charge cut: $(j_{c,same} - j_{c,oppo}) \cdot q_K < 0$
    efficiency $= (80 \pm 3)\%$, background rejection $= (40 \pm 1)\%$

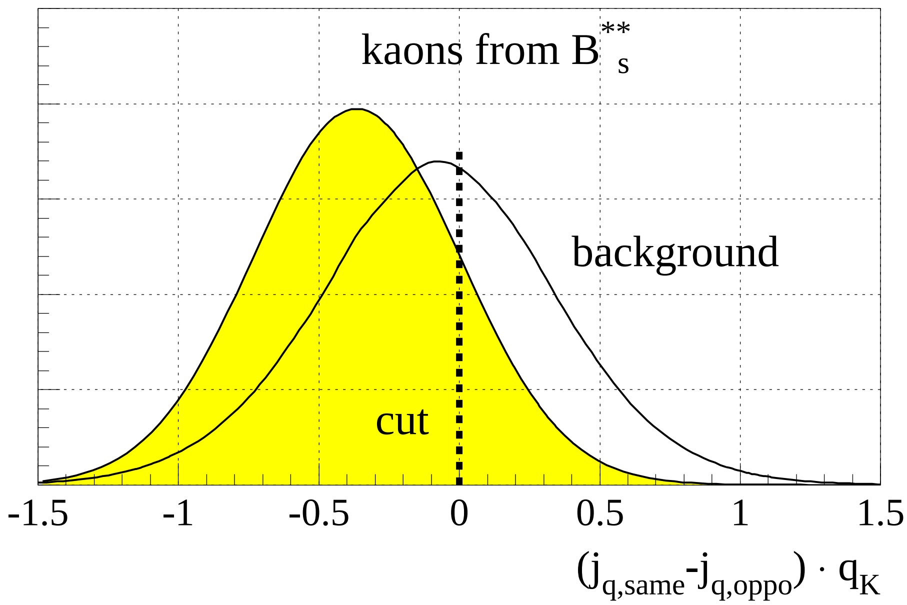

Figure 5.11: *Distribution of* $(j_{c,same} - j_{c,oppo}) \cdot q_K$ *from simulation for kaons originating from* B_s^{**} *decays and for background. An enhancement of the signal to background ratio is achieved by demanding* $(j_{c,same} - j_{c,oppo}) \cdot q_K < 0$.

The quantity which is best accessible experimentally with inclusive B reconstruction methods is the Q-value[9] of the decay:

$$\boxed{Q = m(B^{(*)}K) - m(B^{(*)}) - m(K) \equiv m(B_s^{**}) - m(B^{(*)}) - m(K)\ .} \tag{5.18}$$

The symbol $B^{(*)}$ denotes both B and B^* states, which cannot be distinguished with the present method. The resolution on the Q-value is 18 MeV/c^2 at Q = 70 MeV/c^2. This number has been determined from simulation. The resolution is dominated by the energy and angular resolution of the B meson. Whether the decay was actually into B or B^* and whether the B^* decay photon has been reconstructed, has only a negligible effect on the resolution on the Q-value. However, the decay of a B_s^{**} of a given mass to B^*K gives rise to a Q-value which is shifted downwards by the B^*-B mass difference of 46 MeV/c^2 as compared to the Q-value of a BK decay.

The Q-value plot for DELPHI data taken in the years 1991-94 is shown in Fig. 5.12 together with the Monte Carlo expectation without B_s^{**} production. The data distribution shows two narrow peaks, containing a total of 577 ± 49 (stat.) ± 70 (syst.) events. Simple Gaussian fits to the signal lead to $Q = 70 \pm 4$ (stat.) ± 8 (syst.) MeV/c^2 with a width of $\sigma = 21 \pm 4$ (stat.) ± 4 (syst.) MeV/c^2 for the first peak, and $Q = 142 \pm 4$ (stat.) ± 8 (syst.) MeV/c^2 with a width of $\sigma = 13 \pm 4$ (stat.) ± 4 (syst.) MeV/c^2 for the second peak. The evaluation of the systematic errors is discussed in the next section.

The peaks are naturally explained by B_s^{**} production. The strong pion rejection and the narrowness of the signals exclude an interpretation as a reflection due to $B_{u,d}^{**}$ decays. Several cross checks have been performed in order to check the consistency of the result.

[9] In the calculation of the Q-value the kaon candidate is excluded from the inclusive B reconstruction.

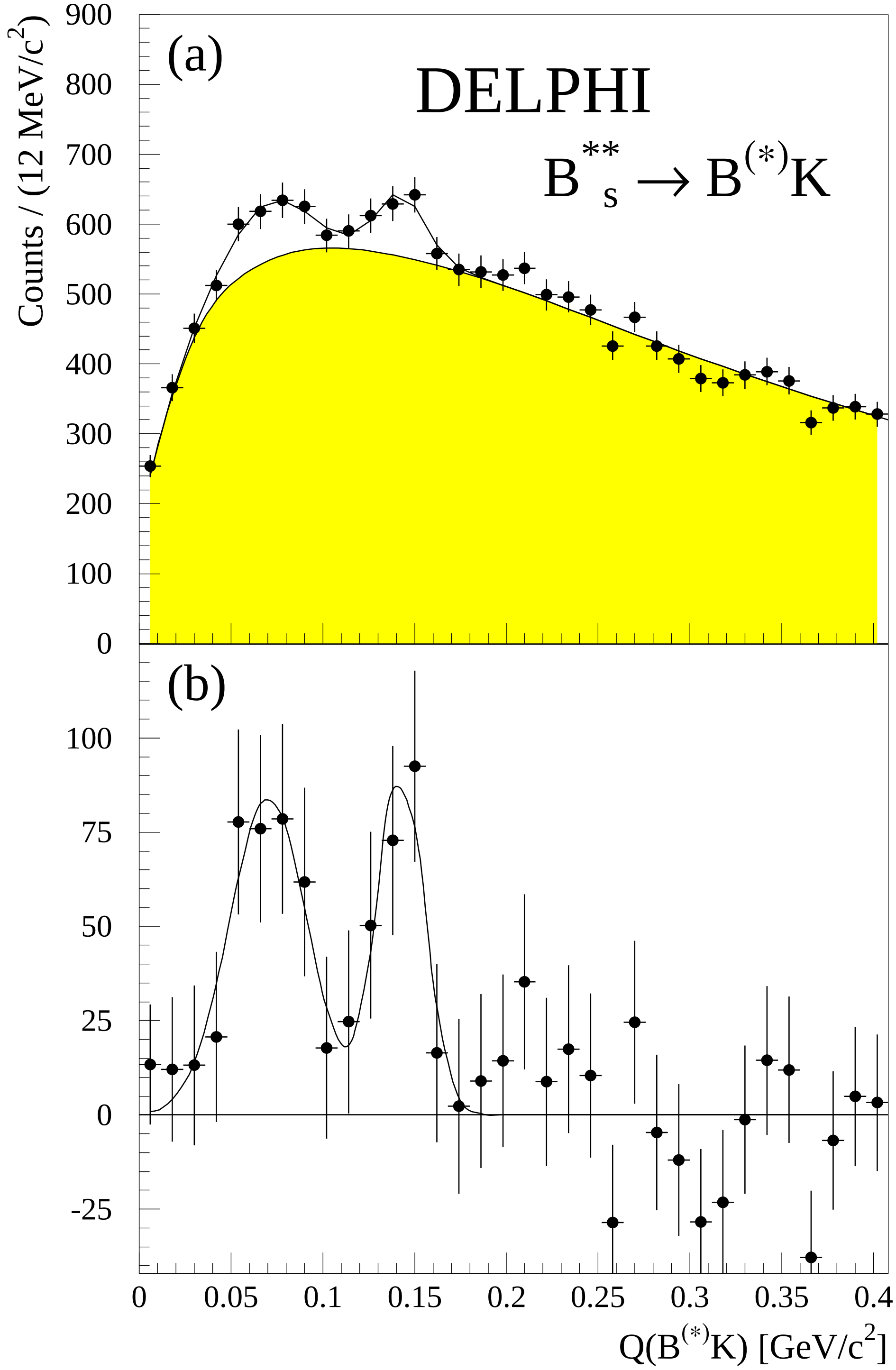

Figure 5.12: *(a) Distribution of the Q-value of $B^{(*)}K$ pairs (data points) along with the Monte Carlo expectation without B_s^{**} production (shaded area). Q is defined as $Q = m(B^{(*)}K^{\pm}) - m(B^{(*)}) - m(K^{\pm})$. (b) Background subtracted $B^{(*)}K^{\pm}$ pair Q-value distribution. The fit is to two simple Gaussians.*

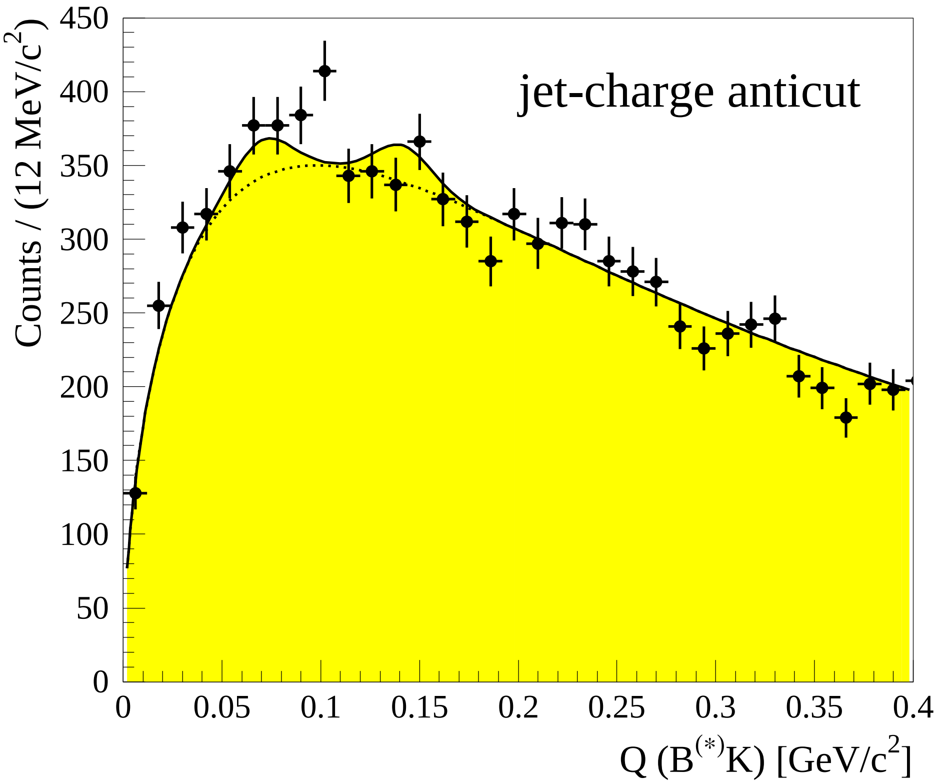

Figure 5.13: *Distribution of the Q-value of $B^{(*)}K$ pairs (data points) along with the Monte Carlo expectation without B_s^{**} production (dotted line) for $(j_{c,same} - j_{c,oppo}) \cdot q_K > 0$. The shaded area shows the expectation including B_s^{**} production. The B_s^{**} production characteristics is simulated in such a way to reproduce the observed signal in Fig. 5.12.*

- To check whether the signal could be an artifact of the employed vertex procedure (since it depends crucially on the correct modelling of the perigee parameter and the covariance matrices of the tracks), the vertex reconstruction procedure is replaced by a simpler analysis techniques without vertex reconstruction (based on different cuts on $\mathcal{P}_T^*$ (see section 5.1.1)). The same two-peak structure with the same characteristics is observed.

- Different kaon enrichment techniques based on the dE/dx measurements of the TPC and the Cherenkov angle reconstruction in gas and liquid RICH have been used, thereby varying the purity of the kaon sample between 40% and 70%. For different purities a similar two-peak structure, as shown in Fig. 5.12, is extracted from the data. These tests are based on the RIBMEAN and HADSIGN software packages (see section 4.5).

- Another cross check consists in reversing the jet charge cut, i.e. $(j_{c,same} - j_{c,oppo}) \cdot q_K > 0$. In that way, $(80 \pm 3)\%$ of the signal originating from B_s^{**} decays is suppressed, while $(20 \pm 3)\%$ is retained. Fig. 5.13 shows the Q-value distribution for data along with the Monte Carlo expectation including B_s^{**} production. The B_s^{**} production characteristics are simulated in such a way to reproduce the observed signal in Fig. 5.12 by adding two appropriate Gaussian distributions. Although some fluctuations are visible around $Q = 90$ MeV/c^2, the agreement between data and expectation is reasonable.

5.2.2 Interpretation and Comparison with Predictions

If the observed two-peak structure in Fig. 5.12 is correct, it can be described consistently by the production of two narrow B_s^{**} states. The first peak is slightly broader than the expected resolution at that low Q-value. It may be explained as stemming from the narrow B_{s1} decaying into B^*K, whereas the second peak could be due to the B_{s2}^* decaying into BK.

Accepting this interpretation, the masses and widths of the two states are determined to be:

$$\boxed{\begin{array}{rcc} m(B_{s1}) & = & 5888 \pm 4\,(\text{stat.}) \pm 8\,(\text{syst.})\ \text{MeV/c}^2 \\ m(B_{s2}^*) & = & 5914 \pm 4\,(\text{stat.}) \pm 8\,(\text{syst.})\ \text{MeV/c}^2 \\ \Gamma(B_{s1}) & < & 60\,\text{MeV/c}^2\ (\text{at }95\%\ \text{c.l.}) \\ \Gamma(B_{s2}^*) & < & 50\,\text{MeV/c}^2\ (\text{at }95\%\ \text{c.l.})\,. \end{array}} \tag{5.19}$$

The measured masses of these states are in good agreement with HQET predictions derived in section 2.4.4. A mass of 5886 MeV/c^2 is predicted for the 1^+ state and 5899 MeV/c^2 for the 2^+ state. The theoretical uncertainties on these predictions are of the order of 40 MeV/c^2.

The measured masses do not agree perfectly with the more sophisticated HQET prediction of Eichten et al. [40, 41] of 5849 MeV/c^2 for the 1^+ state and 5861 MeV/c^2 for the 2^+ state. However, their prediction for the $B_{u,d}^{**}$ meson mass already differs by 37 MeV/c^2 from the observation. Furthermore, the original model [40] predicts the $D_{s1} - D_s$ and $D_{s2} - D_s$ mass differences to be 23 MeV/c^2 *lower* than the corresponding nonstrange mass differences, whereas they have been observed [12] to be 12 MeV/c^2 *higher*. The updated model [41] predicts these mass differences to be about the same as in the nonstrange case, i.e. about 11 MeV/c^2 below the observed values. The same pattern is observed in the B_s^{**} sector. Thus, it seems that the model has problems in predicting the influence of the non-negligible strange quark mass on the orbital excitation energy. If the given interpretation is correct, then the mass splitting between the 2^+ and 1^+ states would be 26 $\pm$ 6 $\pm$ 8 MeV/c^2, which should be compared to the predicted 12 MeV/c^2.

The production cross sections per b-jet are measured to be

$$\boxed{\begin{array}{rcl} \sigma_{B_{s1}} \cdot Br(B_{s1} \to B^*K)/\sigma_b & = & 0.021 \pm 0.005\,(\text{stat.}) \pm 0.006\,(\text{syst.}) \\ \sigma_{B_{s2}^*} \cdot Br(B_{s2}^* \to BK)/\sigma_b & = & 0.016 \pm 0.005\,(\text{stat.}) \pm 0.007\,(\text{syst.})\,. \end{array}} \tag{5.20}$$

Assuming the b baryon rate to be $(10 \pm 4)\%$ and the $B_s^{(*)}$ rate to be $(13 \pm 2)\%$, the relative amount of B_s mesons which is produced with orbital excitation is

$$\boxed{\begin{array}{rcl} \sigma_{B_{s1}} \cdot Br(B_{s1} \to B^*K)/\sigma_{B_s} & = & 0.178 \pm 0.05\,(\text{stat.}) \pm 0.06\,(\text{syst.}) \\ \sigma_{B_{s2}^*} \cdot Br(B_{s2}^* \to BK)/\sigma_{B_s} & = & 0.135 \pm 0.05\,(\text{stat.}) \pm 0.06\,(\text{syst.})\,. \end{array}} \tag{5.21}$$

Combining the results of the $B_{u,d}^{**}$ and B_s^{**} analyses, one can evaluate the production ratio

$$\boxed{\frac{\sigma_{B_{s1}} + \sigma_{B_{s2}^*}}{\sigma_{B_{u,d}^{**}}} = 0.154 \pm 0.030\,(\text{stat.}) \pm 0.054\,(\text{syst.})\,,} \tag{5.22}$$

which is consistent with the expected strangeness suppression factor of 1 : 6 if one assumes that the narrow resonances dominate the $B_{u,d}^{**}$ signal. For the calculation, totally uncorrelated errors have been assumed.

The B_{s2}^* state is allowed to decay into both BK and B^*K. The above interpretation does not give much room for the latter decay. This is in agreement with expectation, since the partial widths scale roughly like $Q^{2L+1} = Q^5$; which leads to a ratio $\Gamma(B_{s2}^* \to BK)/\Gamma(B_{s2}^* \to B^*K) = (0.142/0.096)^5 = 7$ at the measured Q-value.

Systematic Uncertainties

Systematic uncertainties dominate in the measurements of all these quantities. Different systematic checks have been performed leading to a determination of the systematic errors. The main sources are discussed here.

- The complete analysis is repeated several times with different sets of B and $K^{\pm}$ selection cuts. This is realized in an automatic procedure providing hundreds of histograms with different cuts and automatic fitting algorithms. The minimum B momentum cut is varied between 15 GeV and 25 GeV, the cut on the difference between the reconstructed and the mean B mass is varied between 2.0 GeV/c^2 and 3.0 GeV/c^2. Furthermore, the cut on the momentum of the kaon candidate is varied between 0.5 GeV/c^2 and 3.5 GeV/c^2. Two- and three-jet event topologies are studied separately. Different kaon enrichment techniques based on the dE/dx measurements of the TPC and the Cherenkov angle reconstruction in gas and liquid RICH have been used, thereby varying the purity of the kaon sample between 40% and 70%.
- Different background shapes originating from simulation and various phenomenological background models (e.g. $f(Q) = a_1 \cdot Q^{a_2} \cdot \exp(-a_3 \cdot Q - a_4 \cdot Q^2 - a_5 \cdot Q^3)$) are fitted to the data. The normalization is extracted from the sideband in the range between 0.18 GeV/c^2 and 0.6 GeV/c^2. These upper bound is varied by ± 0.2 GeV/c^2. Additionally, the normalization is extracted from the left *and* the right sidebands of the B_s^{**} signal. Furthermore, different techniques of extracting the yield are used, e.g. replacing the fitting of two Gaussians by simple counting methods.
- Possible reflections from $B^{**} \to B^{(*)}\pi$ decays are expected to contribute in the Q-value range between 50 and 350 MeV/c^2 in the order of 6% to the background. Their influence in simulation and their possibly larger influence in data, due to uncertainties in the modelling of the pion rejection capabilities, have been considered in the systematic errors. Additional but smaller uncertainties are introduced by the possible production of $\Sigma_b \to \Lambda_b \pi$ and $\Sigma_b^* \to \Lambda_b \pi$, and reflections from the decay $B_{u,d}^{**} \to B^{(*)}\rho$.
- For cross section calculations the acceptance is extracted from simulation (JETSET [22] with DELPHI tuning [34]). Uncertainties in the modelling of the B_s^{**} decays as well as the limited Monte Carlo statistics of 4.1 million multi-hadronic Z^0 events account for the systematic errors.

5.2.3 Comparison with other Experiments

The present experimental knowledge about orbitally excited strange B mesons is very limited. It is summarized in Tab. 5.5. First experimental evidence for B_s^{**} mesons was reported by the

Quantity	Experiment	Measurement	Ref.
$m_{B_s^{**}}$ [MeV/c^2]	OPAL	5884 ± 15 (stat.)	[2]
$m_{B_{s1}}$ [MeV/c^2]	DELPHI	$5888 \pm 4 \pm 8$	[8]
$m_{B_{s2}^*}$ [MeV/c^2]	DELPHI	$5914 \pm 4 \pm 8$	[8]
width $\Gamma(B_s^{**})$ [MeV/c^2]	OPAL	47 ± 22 (stat.)	[2]
width $\Gamma(B_{s1})$ [MeV/c^2]	DELPHI	< 60 (at 95% c.l.)	[8]
width $\Gamma(B_{s2}^*)$ [MeV/c^2]	DELPHI	< 50 (at 95% c.l.)	[8]
rate $\sigma(B_s^{**})/\sigma(B_s)$ [%]	OPAL	17.5 ± 5.2 (stat.)	[2]
rate $\sigma(B_{s1})/\sigma(B_s)$ [%]	DELPHI	$17.8 \pm 5 \pm 6$	[8]
rate $\sigma(B_{s2}^*)/\sigma(B_s)$ [%]	DELPHI	$13.5 \pm 5 \pm 6$	[8]

Table 5.5: *LEP $B_s^{**} \to B^{(*)}K$ results. The OPAL result is interpreted as an indication for the production of the narrow B_s^{**} states B_{s1} and B_{s2}^*.*

OPAL collaboration [2]. Additional results are provided by the DELPHI collaboration [8]. If the interpretation given in the previous section is correct, then the OPAL signal yields from the narrow B_s^{**} states B_{s1} and B_{s2}^*. The DELPHI analysis resolved both states separately. The mass measurement for the total B_s^{**} signal of 5884 ± 15 (stat.) MeV/c^2 from the OPAL analysis agrees rather well with the DELPHI results of 5888 ± 4 (stat.) ± 8 (syst.) MeV/c^2 for the 1^+ state and 5914 ± 4 (stat.) ± 8 (syst.) MeV/c^2 for the 2^+ state. The published OPAL mass has been shifted by 31 MeV/c^2 to account for the average effect of $B_s^{**} \to B^*$; the error does not contain the uncertainty on this procedure.

The production cross sections in the DELPHI and the OPAL analyses are somewhat different but consistent within errors (OPAL : $\sigma(B_s^{**})/\sigma(B_s) = 17.5 \pm 5.2$(stat.)%; DELPHI: $\sigma(B_{s1})/\sigma(B_s) = 17.8 \pm 5$(stat.)$\pm 6$(syst.)% and $\sigma(B_{s2}^*)/\sigma(B_s) = 13.5 \pm 5$(stat.)$\pm 6$(syst.)%).

Combining the results from the DELPHI $B_{u,d}^{**}$ and B_s^{**} analyses, one obtains the production ratio $(\sigma_{B_{s1}} + \sigma_{B_{s2}^*})/\sigma_{B_{u,d}^{**}} = 15.4 \pm 3.0$ (stat.) $\pm$ 5.4 (syst.)% , which is consistent with the expected strangeness suppression factor of 1 : 6. All these measurements are in agreement with expectations for the production of orbitally excited strange B mesons. However, further studies by the LEP collaborations are necessary to confirm these states.

5.3 Search for Σ_b and Σ_b^* Baryons ($\Sigma_b^{(*)\pm} \to \Lambda_b \pi^\pm$)

This section reports on a search for the b baryons $\Sigma_b^\pm$ and $\Sigma_b^{*\pm}$ which are expected to decay into $\Lambda_b \pi^\pm$. Their quark content in the static quark model is (buu) for the $\Sigma_b^{(*)+}$ baryon and (bdd) for the $\Sigma_b^{(*)-}$ baryon. The Σ_b baryon belongs to an isospin triplet ($I = 1$) with total angular momentum $J = 1/2$ (mixed wave-function), while the Σ_b^* baryon belongs to a triplet with $J = 3/2$ (symmetric wave-function). For further details see section 2.5. It is expected that approximately $(10 \pm 4)\%$ of all primary produced b quarks in Z^0 decays fragment into b baryons. The Λ_b (uds) is the lightest such baryon, and thus it decays weakly. Most other b baryons are expected to decay into Λ_b by strong or electromagnetic interactions; only the Ξ_b states and the Ω_b probably decay weakly. There is evidence for Λ_b and Ξ_b production at LEP (see section 2.5.2), otherwise nothing is known experimentally about excited b baryons.

5.3.1 Experimental Procedure and Results

Most of the experimental tools (b-tagging, inclusive B reconstruction, vertex reconstruction and hadron identification) which are needed for this analysis have been described in the previous chapter.

The analysis presented here is very similar to the original B^{**} analysis. Inclusively reconstructed Λ_b baryons are combined with charged pions. Since the $\Sigma_b^{(*)}$ baryons decay rapidly through the strong interaction, the pion should originate from the primary vertex and not from the Λ_b-decay vertex. The inclusive B reconstruction algorithm is modified in such a way as to force the mass of the reconstructed b hadron to the Λ_b mass (5.620 GeV/c^2). In the original algorithm the mass is forced to B meson mass (5.279 GeV/c^2). However, this change has only a very small influence on the reconstruction of the Q-value.

The main difference to the original B^{**} analysis consists in an enrichment of Λ_b decays. This is accomplished by demanding that there is either a reconstructed Λ, a neutral hadron shower above 10 GeV or that the most energetic particle in the hemisphere is identified as a proton. The Λ reconstruction achieves an average efficiency of $(30 \pm 3)\%$ with a background contamination of $(10 \pm 2)\%$ (see section 4.6). Protons are identified using the standard DELPHI hadron identification code employing the gas RICH, the liquid RICH and dE/dx measurements by the TPC (HADSIGN: PTAG > 1). For the multi-hadronic momentum spectrum the working point chosen leads to an average proton efficiency of $(60 \pm 4)\%$ with a purity of approximately $(43 \pm 4)\%$ (see section 4.5).

In summary, the analysis uses the following cuts:

- Multi-hadron event selection (see section 4.1)
- Event topology cuts (see section 4.1)
  - restrict analysis to barrel: $|\cos(\Theta_{thrust})| \leq 0.75$
  - accept two-jet events and most energetic jet in three-jet events
- Tagging of b hemispheres (see section 4.2)
  - event tag $\mathcal{P}_E < 0.01$, efficiency $= (65 \pm 3)\%$, purity $= (83 \pm 4)\%$

- Inclusive b reconstruction (see section 4.3)
  - mass forced to Λ_b mass ($m_{\Lambda_b} = 5.620$ GeV/c^2)
  - quality cuts: $E_y > 20$ GeV, $|m_y - \langle m_y \rangle| < 2.5$ GeV/c^2 and $0.6 < E_{hem}/E_{beam} < 1.1$
  - restrict B vector to barrel: $|\cos\Theta_B| > 0.02$, $|\cos\Theta_B| < 0.7$

- Pion track selection cuts (see sections 4.2, 4.4 and 4.5)
  - accept only tracks which are assigned to the primary vertex
  - restrict pion vector to barrel: $|\cos\Theta_\pi| > 0.05$, $|\cos\Theta_\pi| < 0.7$
  - standard veto on electrons or muons
  - veto kaons and protons: KTAG ≤ 1, PTAG ≤ 1 (HADSIGN)
  - pion momentum cut: $p_\pi < 3.0$ GeV/c

- Baryon enrichment (see sections 4.5 and 4.6)
  - most energetic particle in hemisphere is identified as proton
    efficiency = $(60 \pm 4)\%$, purity = $(43 \pm 4)\%$
  - reconstructed lambda in hemisphere
    efficiency = $(30 \pm 3)\%$, purity = $(90 \pm 2)\%$
  - reconstructed neutral hardron shower above 10 GeV in hemisphere

The quantity which is best accessible experimentally with inclusive reconstruction methods is the Q-value of the decay:

$$\boxed{Q = m(\Lambda_b\pi) - m(\Lambda_b) - m(\pi) \equiv m(\Sigma_b^{(*)}) - m(\Lambda_b) - m(\pi)\ .} \tag{5.23}$$

The resolution on the Q-value using the present method is 16 MeV/c^2 at Q=85 MeV/c^2. This value has been determined from simulation. The resolution is dominated by the energy and angular resolution of the Λ_b baryon. The distribution of the measured Q-values of $\Lambda_b\pi$ pairs is shown as the data points in Fig. 5.14(a). There is a clear excess on top of an almost constant background which is naturally explained by the production of Σ_b and Σ_b^* baryons. The background from simulation has a flat distribution in the signal range, but a slightly larger slope towards lower Q-values than is observed in the data. The origin of this difference is not yet fully understood, but it might be correlated to the rate of inclusive D^* meson production, the relative b baryon to B meson production ratio, the modelling of yet unmeasured B hadron decays, or general limitations of the JETSET string fragmentation model. It is worth noting that the HERWIG 5.8 generator [29] predicts a less steep rise of the background at small Q-values. The reason for this seems to come from the fragmentation model (cluster instead of string) rather than from the different modelling of the parton shower. This has been inferred from a Monte Carlo study with the HERWIG parton shower generator interfaced to LUND string fragmentation.

However, the background as shown in Fig. 5.14(a) has been determined from real data by reversing the baryon enrichment cut. This procedure is motivated by the simulation. Fig. 5.14(b) shows the corresponding Q-value distribution where no significant excess is observed. A function $f(Q) = a_1 \cdot Q^{a_2} \cdot \exp(-a_3 \cdot Q - a_4 \cdot Q^2 - a_5 \cdot Q^3)$ is fitted to the baryon depleted sample and shown as background in Fig. 5.14(a). The signal to background ratio in the baryon depleted sample is expected to be a factor of three less than in the baryon enriched sample. The efficiency for the baryon enrichment is approximately $(30 \pm 4)\%$.

Several cross checks have been performed in order to check the consistency of the result:

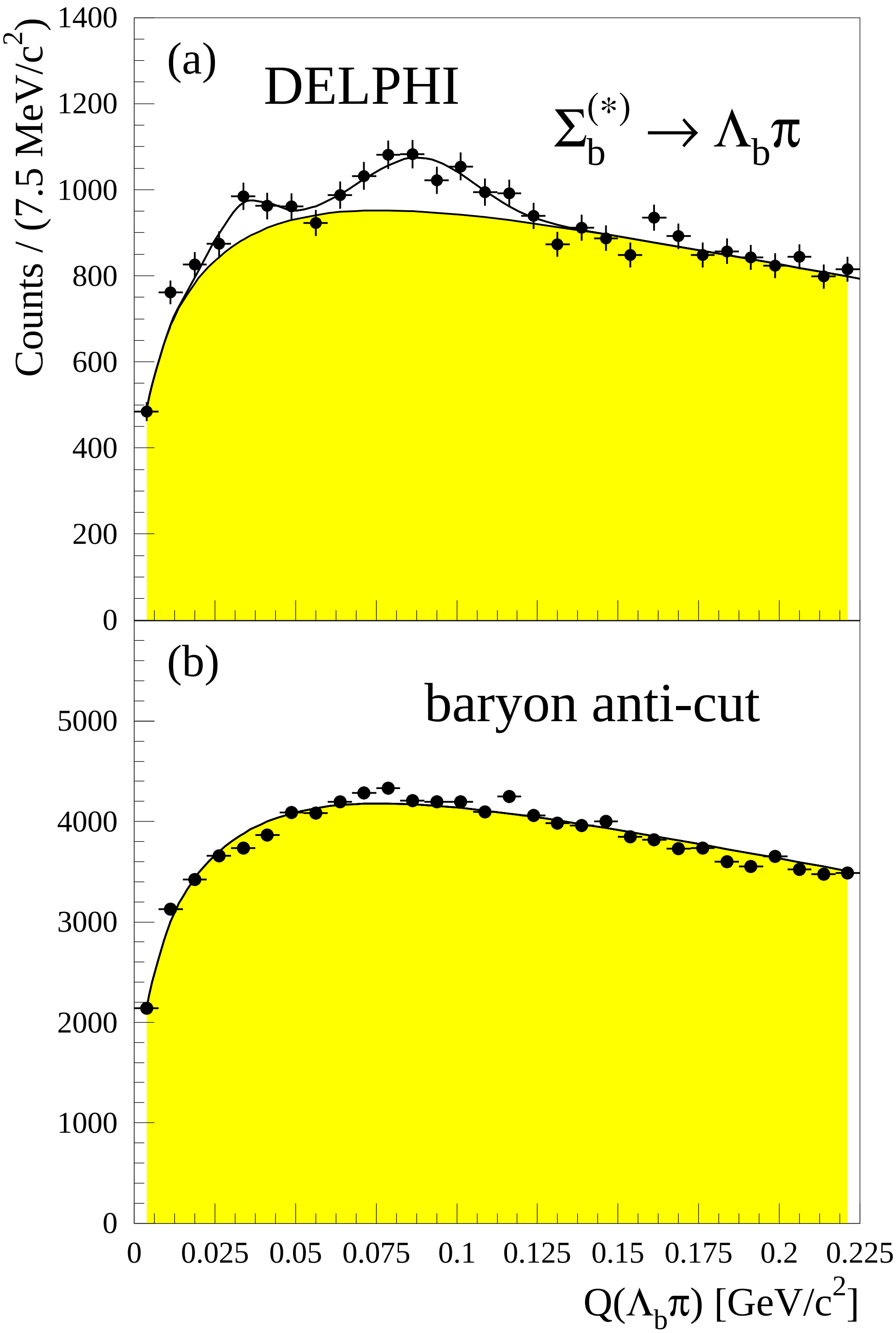

Figure 5.14: *(a) Distribution of the Q-value of $\Lambda_b\pi$ pairs (data points). The background is extracted from the baryon anti-cut (shaded area). The solid line results from a fit of the background and two Gaussians to the data. Q is defined as $Q = m(\Lambda_b\pi) - m(\Lambda_b) - m(\pi)$. (b) Distribution of the Q-value of $\Lambda_b\pi$ pairs (data points) with a baryon anti-cut.*

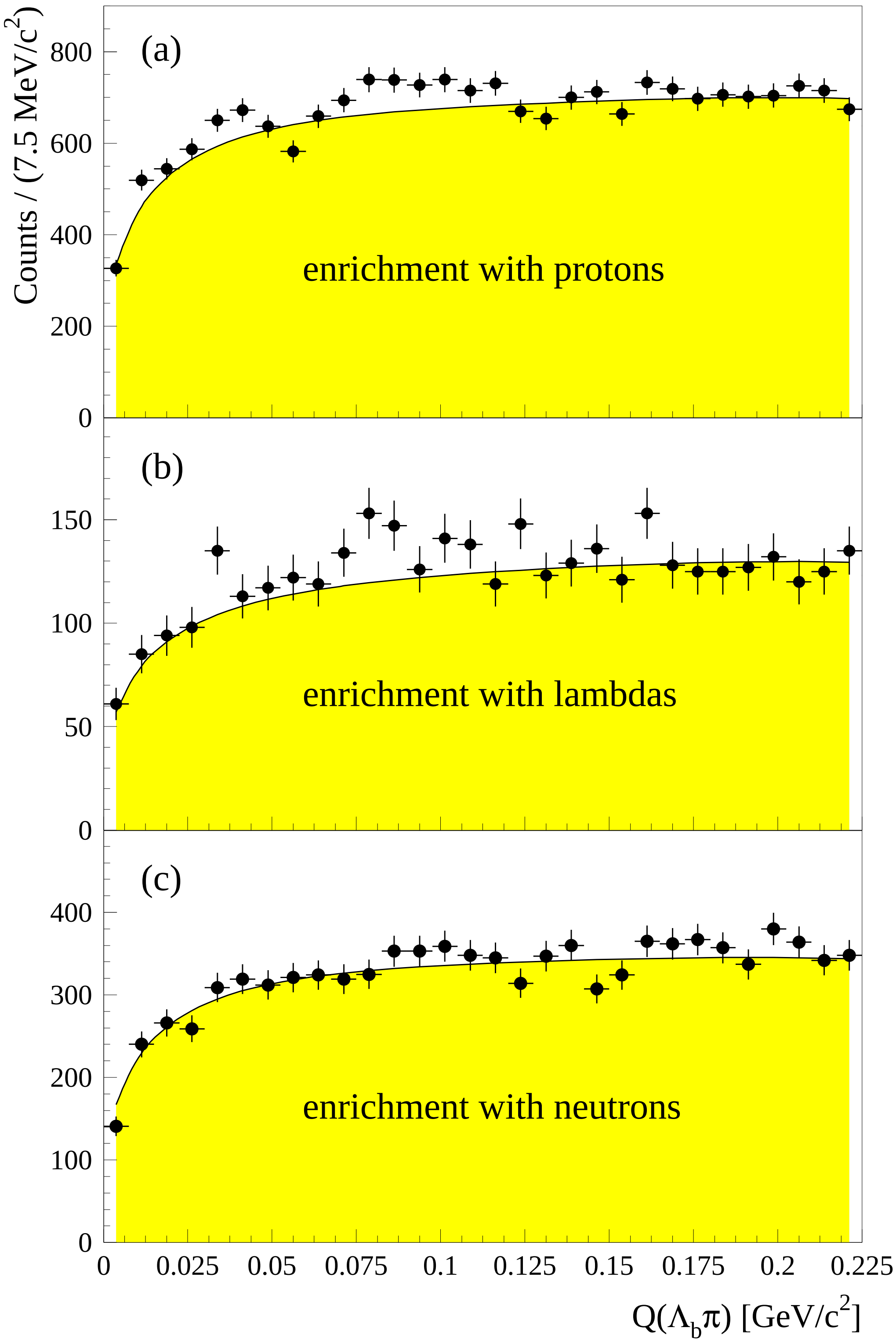

Figure 5.15: *Distribution of the Q-value of $\Lambda_b\pi$ pairs (data points) for (a) enrichment with protons, (b) enrichment with lambdas and (c) enrichment with neutrons. The background (shaded area) is extracted from the baryon anti-cut.*

- To check whether the observed two-peak signal could be an artifact of the employed vertex procedure (since it depends crucially on the correct modelling of the perigee parameter and the covariance matrices of the tracks), the vertex reconstruction procedure is replaced by a simpler analysis techniques without vertex reconstruction (based on different cuts on $\mathcal{P}_T^*$ (see section 5.1.1)). The same two-peak structure with the same characteristics is observed.
- The total sample is divided into three subsamples according to the way the baryon enrichment is achieved: (a) enrichment with protons, (b) enrichment with lambdas and (c) enrichment with neutrons. Due to the small yield of the total signal, the subsamples are expected to show only non-significant structures. The corresponding Q-value distributions for $\Lambda_b\pi$ pairs are shown in Figs. 5.15(a)-(c). In each case the background is extracted from the data by reversing the baryon enrichment cut. Fig. 5.15(a) (corresponding to an enrichment with protons) and Fig. 5.15(b) (corresponding to an enrichment with lambdas) show the same two-peak characteristics as observed in the total sample. Some small indications for the two-peak structure can also be observed in Fig. 5.15(c) (corresponding to an enrichment with neutrons). However, this behaviour is expected due to the crude resolution of the hadron calorimeter ($\sigma_E/E = 112\%/\sqrt{E[\mathrm{GeV}]} \oplus 21\%$ [78]) [10] which spoils the resolution on the Λ_b baryon.
- Another cross check consists in dividing the signal according to jet charge and pion charge. The four $\Sigma_b^{(*)}$ charge states and their decay characteristics are shown in Fig. 5.16. The jet charge is calculated using an energy weighting exponent $\kappa = 0.6$. If the signal stems from an $I = 1$ resonance, the observed structure is expected to appear in all four charge combinations $\Lambda_b\pi^+$ (enriched by negative jet charge, positive pion), $\Lambda_b\pi^-$ (negative jet charge, negative pion), $\bar{\Lambda}_b\pi^+$ (positive jet charge, positive pion) and $\bar{\Lambda}_b\pi^-$ (positive jet charge, negative pion). The achieved enrichment is $(70 \pm 3)\%$. The expectation is confirmed by the data as shown in Fig. 5.17.

5.3.2 Interpretation and Comparison with Predictions

The observed two-peak structure in Fig. 5.14(a) can be described consistently by the production of the b baryons Σ_b (first peak) and Σ_b^* (second peak). Guided by expectations, the excess is fitted to two Gaussians of widths expected from detector resolution at the approximate masses (10 MeV/c^2 and 16 MeV/c^2), with masses and production rates allowed to vary. The results of this fit are:

$$\boxed{\begin{array}{rcl} N(\Sigma_b^\pm + \Sigma_b^{*\pm}) & = & 937 \pm 108\,(\mathrm{stat.}) \pm 270\,(\mathrm{syst.}) \\ Q(\Sigma_b^\pm \to \Lambda_b\pi^\pm) & = & 33 \pm 3\,(\mathrm{stat.}) \pm 14\,(\mathrm{syst.})\ \mathrm{MeV/c^2} \\ Q(\Sigma_b^{*\pm} \to \Lambda_b\pi^\pm) & = & 89 \pm 3\,(\mathrm{stat.}) \pm 8\,(\mathrm{syst.})\ \mathrm{MeV/c^2} \\ (\sigma_{\Sigma_b} + \sigma_{\Sigma_b^*})/\sigma_b & = & 0.048 \pm 0.006\,(\mathrm{stat.}) \pm 0.015\,(\mathrm{syst.}) \\ \sigma_{\Sigma_b}/(\sigma_{\Sigma_b} + \sigma_{\Sigma_b^*}) & = & 0.24 \pm 0.06\,(\mathrm{stat.}) \pm 0.10\,(\mathrm{syst.})\,. \end{array}} \tag{5.24}$$

According to isospin rules, the observed $\Sigma_b^{(*)\pm}$ rate has been multiplied by 1.5 to account for $\Sigma_b^{(*)0}$ production. The production cross sections also have been evaluated separately for the Σ_b

[10] This relation is extracted from the simulation. The correct modelling of the hadron calorimeter resolution is still the subject of intensive studies within the DELPHI collaboration.

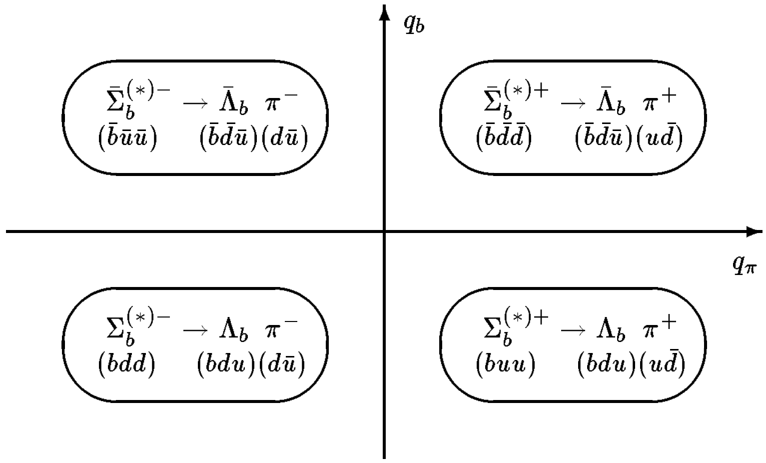

Figure 5.16: *Decay characteristics for the four $\Sigma_b^{(*)}$ charge states decaying into charged pions. The horizontal axis denotes the pion charge, while the vertical axis denotes the charge of the involved b quark.*

and Σ_b^* baryon, leading to $\sigma_{\Sigma_b}/\sigma_b = 0.012 \pm 0.003 \pm 0.006$ and $\sigma_{\Sigma_b^*}/\sigma_b = 0.036 \pm 0.005 \pm 0.011$. The statistical significance for the Σ_b (Σ_b^*) signal corresponds to 4.0 (7.2) standard deviations. The quoted statistical errors are uncorrelated errors, i.e. they have been determined from the χ^2 evolution as a function of the deviation from the minimum, refitting with respect to all other parameters. In particular, fits without signal for Σ_b or Σ_b^* result in χ^2 values larger by 12 and 40, respectively. However, systematic errors dominate in the measurements of all these quantities. Their evaluation will be discussed below. Adding the pion mass to the measured Q-value leads to the following mass differences

$$\boxed{\begin{array}{rcl} m(\Sigma_b^{\pm}) - m(\Lambda_b) & = & 173 \pm 3\,(\text{stat.}) \pm 14\,(\text{syst.})\ \text{MeV/c}^2 \\ m(\Sigma_b^{*\pm}) - m(\Lambda_b) & = & 229 \pm 3\,(\text{stat.}) \pm 8\,(\text{syst.})\ \text{MeV/c}^2\ , \end{array}} \tag{5.25}$$

which compare well with the simple expectations from section 2.5.3 ($m(\Sigma_b) - m(\Lambda_b) = 168$ MeV/c^2) and with previous ($m(\Sigma_b) - m(\Lambda_b) = 197 \pm 20$ MeV/c^2 [69]) and the latest predictions ($m(\Sigma_b) - m(\Lambda_b) = 200 \pm 20$ MeV/c^2; $m(\Sigma_b^*) - m(\Lambda_b) = 230 \pm 20$ MeV/c^2 [68]) [11].

The default mass differences in jetset 7.4 [22] ($m(\Sigma_b) - m(\Lambda_b) = 159$ MeV/c^2; $m(\Sigma_b^*) - m(\Lambda_b) = 169$ MeV/c^2) are somewhat lower than the measured values, whereas the DELPHI JETSET parameter setting [34] used to calculate acceptances uses 180 and 200 MeV/c^2. The rates predicted by both models are $(\sigma_{\Sigma_b} + \sigma_{\Sigma_b^*})/\sigma_b = 0.039$ and $\sigma_{\Sigma_b}/(\sigma_{\Sigma_b} + \sigma_{\Sigma_b^*}) = 0.33$.

From the observed widths of the signals and the known experimental resolution, the upper limits on the full width Γ of the resonances are calculated

$$\boxed{\begin{array}{rcl} \Gamma(\Sigma_b^{\pm}) & < & 32\ \text{MeV/c}^2\ (\text{at } 95\%\ \text{c.l.}) \\ \Gamma(\Sigma_b^{*\pm}) & < & 39\ \text{MeV/c}^2\ (\text{at } 95\%\ \text{c.l.})\ . \end{array}} \tag{5.26}$$

The observed small widths are consistent with a calculation by Yan et al. [70] who find 3.5 MeV/c^2 and 19.0 MeV/c^2 for the Σ_b and Σ_b^* at the observed Q-values (section 2.5.3).

[11] For this discussion only the mass differences are considered, since the present experimental uncertainties on the Λ_b mass are larger than the obtained resolution on the mass differences ($m(\Lambda_b) = 5641 \pm 50$ MeV/c^2 [12]).

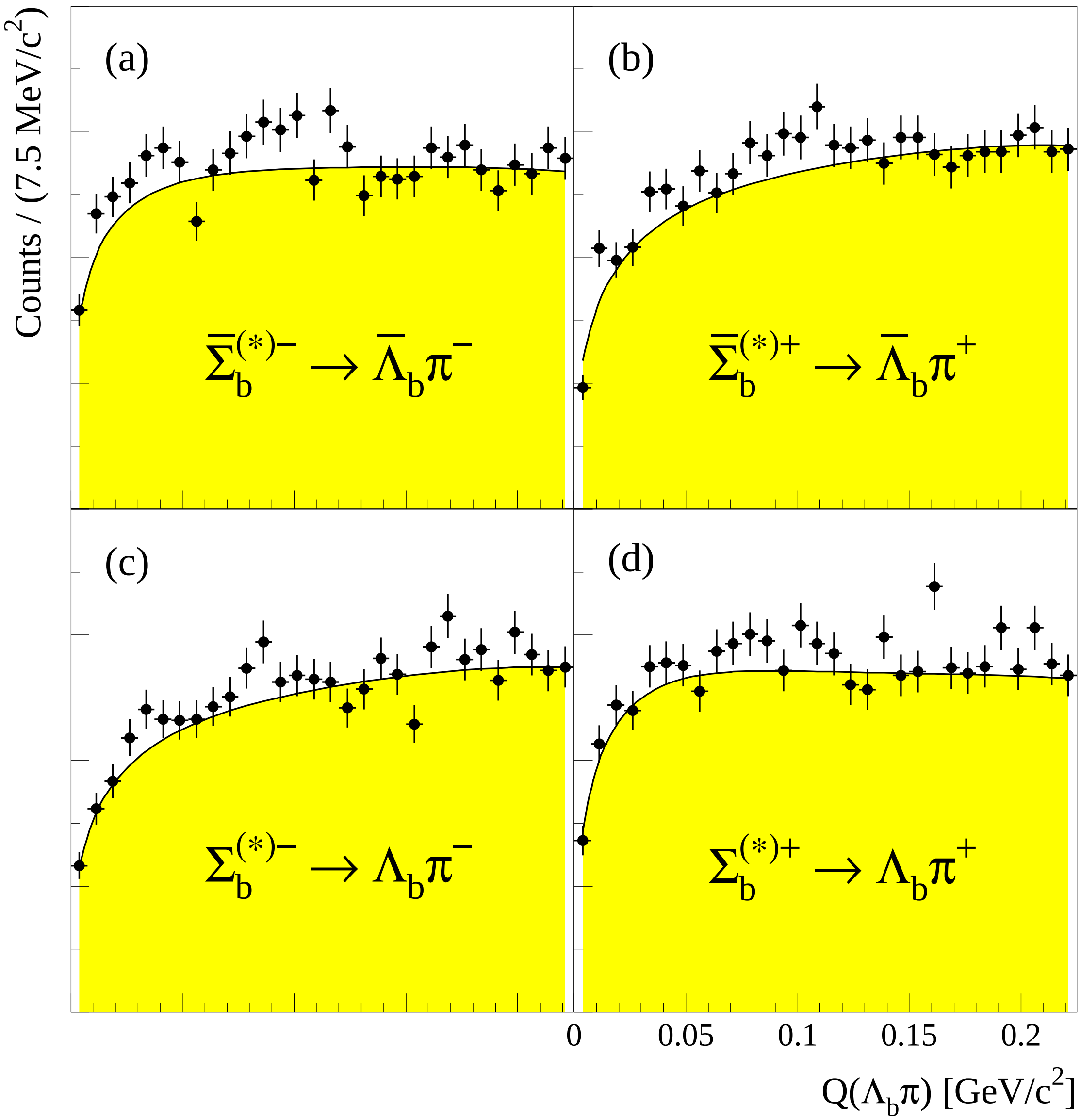

Figure 5.17: *Distribution of the Q-value of $\Lambda_b\pi$ pairs (data points) for the four different $\Sigma_b^{(*)}$ charge combinations: (a) $\bar{\Lambda}_b\pi^-$, (b) $\bar{\Lambda}_b\pi^+$, (c) $\Lambda_b\pi^-$, and (d) $\Lambda_b\pi^+$. The achieved enrichment in the four states is $(70 \pm 3)\%$.*

The interpretation presented leads to consistent results and to good agreement with predictions. However, the total significance of the first peak is only two standard deviations. Thus, one could also try to ascribe the second peak to the production of the Σ_b baryon. This interpretation is excluded by the observed non-flat helicity distribution of the second peak (see section 5.3.3), since the helicity distribution for the Σ_b baryon is expected to be flat [71]. Furthermore, there is no evidence for an additional enhancement above the second peak, which would be expected from Σ_b^* production in this interpretation.

Another hypothesis for the observed signal could be a possible reflection from the decay

$\Lambda_b^* \rightarrow \Lambda_b \pi^+ \pi^-$. The Λ_b^* (udb) is the lightest baryon with orbital excitation denoting two states with $J^P = \frac{1}{2}^-$ $(L_k = 0,\ L_K = 1)$ and $J^P = \frac{3}{2}^-$ $(L_k = 1,\ L_K = 0)$. The orbital angular momentum L_k describes the relative orbital excitations of the two light quarks, and the orbital angular momentum L_K describes orbital excitation of the center of mass of the two light quarks relative to the heavy quark as shown in Fig. 2.15. The Λ_b^* baryon has not yet been observed experimentally. Since the Λ_b^* baryon is orbitally excited, it is expected to be suppressed compared to the production of Σ_b and Σ_b^* baryons. In addition, the Λ_b^* may also have significant radiative branching ratio $(\Lambda_b^* \rightarrow \Lambda_b \gamma)$ [105]. These facts already disfavour an interpretation of the observed signals as originating from Λ_b^* reflections. In the charm sector the two Λ_c^* baryon states $\frac{1}{2}^-$ and $\frac{3}{2}^-$ have been observed experimentally in the expected decay channel $\Lambda_c \pi^+ \pi^-$ [106]. It is found that their decays are mainly non-resonant in the $\Lambda_c \pi$ subsystem, which proofs that narrow reflections cannot be created by this system.

Systematic Uncertainties

Systematic uncertainties dominate in the measurements of all the calculated quantities. Different systematic checks have been performed leading to a determination of the systematic errors.

- The complete analysis is repeated several times with different sets of B and π selection cuts. The minimum B momentum cut is varied between 15 GeV and 25 GeV, the cut on the difference between the reconstructed and the mean B mass is varied between 2.0 GeV/c^2 and 3.0 GeV/c^2. Furthermore the cut on the b-tagging event probability is varied between 0.03 and 0.003. Two- and three-jet event topologies are studied separately. Different proton enrichment techniques based on the dE/dx measurements of the TPC and the Cherenkov angle reconstruction in gas and liquid RICH have been used, thereby varying the purity of the proton sample between 25% and 40%. The uncertainties in the modelling of the baryon enrichment have been assumed to be of the order of 20%.
- Different background shapes originating from the baryon anti-cut and various phenomenological background models (e.g. $f(Q) = a_1 \cdot Q^{a_2} \cdot \exp(-a_3 \cdot Q - a_4 \cdot Q^2 - a_5 \cdot Q^3)$) are fitted to the data. The normalization is extracted from the sideband. Different techniques of extracting the yield from the signals are used, e.g. replacing the fitting of two Gaussians by simple counting methods.
- The influence of the smaller Λ_b lifetime ($\tau = 1.12 \pm 0.09$ ps [12]) compared to the B meson lifetime on the performance of the b-tagging and the vertex separation algorithm is investigated. It is found to be smaller than 3% for the b-tagging and 2% for the vertex reconstruction algorithm.
- For cross section calculations the acceptance is extracted from simulation (JETSET [22] with DELPHI tuning [34]). Uncertainties in the modelling of the decays of the $\Sigma_b^{(*)}$ baryons as well as the limited Monte Carlo statistics of 4.1 million multi-hadronic Z^0 events account for systematic errors.
- The influence on the background shape in the signal region of possible reflections from $B_{u,d}^{**} \rightarrow B^{(*)}\pi/\rho$ and $B_s^{**} \rightarrow B^{(*)}K$ decays has been investigated, and it is found to be negligible.

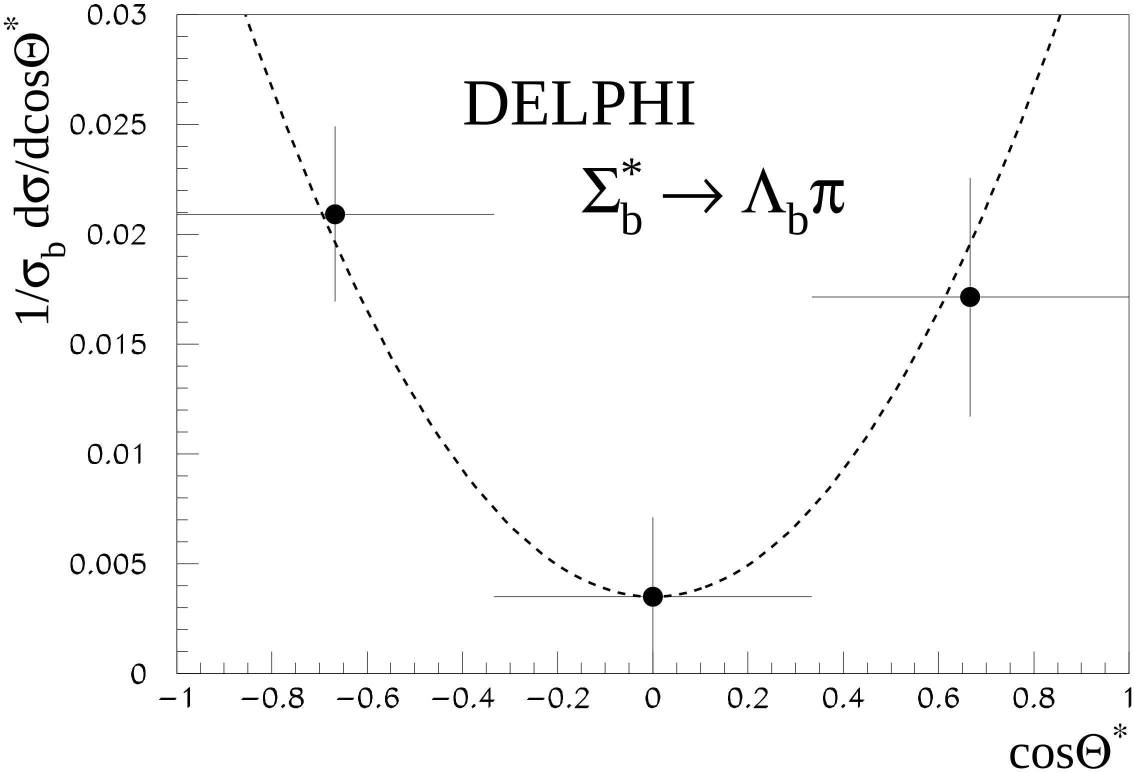

Figure 5.18: *Decay angle distribution for Σ_b^* pions in the Σ_b^* rest frame with respect to the Σ_b^* line of flight in the laboratory. The curve is a fit of the expression given by Falk and Peskin [17], resulting in $w_1 = -0.36 \pm 0.30 \pm 0.30$.*

5.3.3 Σ_b^* Helicity Analysis

An interesting consequence of a large Σ_b and Σ_b^* rate is the depolarization of the Λ_b. If all Λ_b's were primary particles, the standard model predicts a large polarization of -94% [107]. This would be reduced if a substantial fraction of Λ_b's came from decays of heavier baryons [108]. In the quantitative model of Falk and Peskin [71] the resulting polarization is expressed as function of two parameters $\mathcal{A}$ (related to the production rate of Σ_b and Σ_b^*) and w_1 (describing the population of the spin alignment state ±1 of the light quark system). The Σ_b/Σ_b^* production ratio in this model is 1/2, which is smaller than but consistent with the present measurement. w_1 can be deduced from the angular distribution of the Σ_b^* production rate in the helicity frame

$$\boxed{\frac{1}{\Gamma}\frac{d\Gamma}{d\cos\Theta^*}(\Sigma_b^* \to \Lambda_b\pi) = \frac{1}{4}\left(1 + 3\cos^2\Theta^* - \frac{9}{2}w_1(\cos^2\Theta^* - \frac{1}{3})\right)\ .} \tag{5.27}$$

The measured helicity angle distribution is shown in Fig. 5.18. The parameter w_1 deduced from a fit to this distribution is

$$\boxed{w_1 = -0.36 \pm 0.30(\text{stat.}) \pm 0.30(\text{syst.})\ .} \tag{5.28}$$

Quantity	Experiment	Measurement	Ref.
$Q(\Sigma_b)$ [MeV/c^2]	DELPHI	$33 \pm 3 \pm 14$	[9]
$Q(\Sigma_b^*)$ [MeV/c^2]	DELPHI	$89 \pm 3 \pm 8$	[9]
$\Gamma(\Sigma_b)$ [MeV/c^2]	DELPHI	< 32 (at 95% c.l.)	[9]
$\Gamma(\Sigma_b^*)$ [MeV/c^2]	DELPHI	< 39 (at 95% c.l.)	[9]
$(\sigma_{\Sigma_b} + \sigma_{\Sigma_b^*})/\sigma_b$ [%]	DELPHI	$4.8 \pm 0.6 \pm 1.5$	[9]
$\sigma_{\Sigma_b}/(\sigma_{\Sigma_b} + \sigma_{\Sigma_b^*})$ [%]	DELPHI	$24 \pm 6 \pm 10$	[9]
helicity parameter w_1	DELPHI	$-0.36 \pm 0.30 \pm 0.30$	[9]

Table 5.6: *LEP* $\Sigma_b^{(*)} \to \Lambda_b \pi^{\pm}$ *results.*

Negative w_1 are unphysical, $w_1 = 0$ corresponds to a complete suppression of the helicity states $\pm 3/2$. According to Falk and Peskin [71] large Σ_b and Σ_b^* rates and small values of w_1 lead to a substantial reduction of the observable Λ_b polarization in Z^0 decays. This is in qualitative agreement with the apparently small Λ_b polarization $P(\Lambda_b) = -0.26^{+0.23}_{-0.20}$ (stat.) $^{+0.13}_{-0.12}$ (syst.) as measured by the ALEPH collaboration [62].

The decay angle distribution for Σ_b pions in the Σ_b rest frame with respect to the Σ_b line of flight in the laboratory is expected to be flat [71]

$$\boxed{\frac{1}{\Gamma}\frac{d\Gamma}{d\cos\Theta^*}(\Sigma_b \to \Lambda_b \pi) = \frac{1}{2}\ .} \tag{5.29}$$

Within the present sensitivity the data are consistent with this expectation.

This section reported on the search and first evidence for Σ_b^* baryons in the DELPHI experiment. The data obtained are also consistent with the production of the Σ_b baryon. The results are summarized in Tab. 5.6. Further studies by other experiments are needed to confirm these results.

Chapter 6

Summary

First experimental evidence for the existence of orbitally excited B mesons ($B^{**} \rightarrow B^{(*)}\pi^{\pm}$) is obtained, in parallel with an independent analysis by the OPAL collaboration, from the $B^{(*)}\pi$ Q-value distribution using approximately 3.4 million multi-hadronic Z^0 events taken with the DELPHI detector at LEP in the years 1991-1994. By using an inclusive B reconstruction method and secondary vertex reconstruction a large signal is observed in the $B^{(*)}\pi$ Q-value distribution at

$$\boxed{Q(B^{**}) = 283 \pm 5\,(\mathrm{stat.}) \pm 12\,(\mathrm{syst.})\ \mathrm{MeV/c^2}} \tag{6.1}$$

with a Gaussian width of $\sigma(Q) = 68 \pm 5\,(\mathrm{stat.}) \pm 8\,(\mathrm{syst.})\,\mathrm{MeV/c^2}$. The signal can be described consistently as originating from several narrow and broad B^{**} resonances, as predicted by quark models and HQET and observed in the D meson sector. The mass of orbitally excited B mesons is extracted to be

$$\boxed{m(B^{**}) = 5732 \pm 5\,(\mathrm{stat.}) \pm 17\,(\mathrm{syst.})\ \mathrm{MeV/c^2}\ .} \tag{6.2}$$

The signal can also be described as a single resonance of full width $\Gamma = 86 \pm 24$ MeV/c^2. The production rate of B^{**} mesons per b-jet is measured to be

$$\boxed{\sigma_{B^{**}}/\sigma_b = 0.241 \pm 0.015\,(\mathrm{stat.}) \pm 0.058\,(\mathrm{syst.})\ .} \tag{6.3}$$

The helicity distribution of the signal is investigated and found to be flat within errors. Furthermore, the B^{**} fragmentation function is extracted from the data. The charge symmetry of the signal is found to be in agreement with the expectations for an $I = 1/2$ resonance. In conclusion, the existence of orbitally excited B mesons has been experimentally established. The results are in general agreement with predictions and with measurements of other LEP experiments. The existence of B^{**} mesons might open the possibility for future experiments of observing CP-violation in the B system by flavour self-tagging.

Furthermore, a search has been performed for orbitally excited strange B mesons in the decay $B_s^{**} \rightarrow B^{(*)}K^{\pm}$. Inclusive B reconstruction methods, secondary vertex reconstruction and the DELPHI particle identification capabilities lead to the observation of a two-peak structure in the $B^{(*)}K$ Q-value distribution at $Q = 70 \pm 4$ (stat.) ± 8 (syst.) MeV/c^2 and

$Q = 142 \pm 4$ (stat.) ± 8 (syst.) MeV/c^2. It can consistently be interpreted as originating from the predicted narrow B_s^{**} states B_{s1} and B_{s2}^*. Accepting this interpretation, the masses of the two states are determined to be

$$\boxed{\begin{array}{rcl} m(B_{s1}) & = & 5888 \pm 4\,(\text{stat.}) \pm 8\,(\text{syst.})\ \text{MeV/c}^2 \\ m(B_{s2}^*) & = & 5914 \pm 4\,(\text{stat.}) \pm 8\,(\text{syst.})\ \text{MeV/c}^2\ . \end{array}} \tag{6.4}$$

Upper limits at 95% c.l. for the widths of these states have been evaluated: $\Gamma(B_{s1}) < 60$ MeV/c^2 and $\Gamma(B_{s2}^*) < 50$ MeV/c^2. The corresponding production rates are measured to be

$$\boxed{\begin{array}{rcl} \sigma_{B_{s1}} \cdot Br(B_{s1} \to B^* K)/\sigma_b & = & 0.021 \pm 0.005\,(\text{stat.}) \pm 0.006\,(\text{syst.}) \\ \sigma_{B_{s2}^*} \cdot Br(B_{s2}^* \to BK)/\sigma_b & = & 0.016 \pm 0.005\,(\text{stat.}) \pm 0.007\,(\text{syst.})\ . \end{array}} \tag{6.5}$$

Combining the results from the DELPHI B^{**} and B_s^{**} analyses, one obtains the production ratio

$$\boxed{(\sigma_{B_{s1}} + \sigma_{B_{s2}^*})/\sigma_{B^{**}} = 0.154 \pm 0.030\,(\text{stat.}) \pm 0.054\,(\text{syst.})\ ,} \tag{6.6}$$

which is consistent with the expected strangeness suppression of 1 : 6. The measurements are in general agreement with predictions. Additional analyses are needed by the LEP experiments in order to confirm these results. A sizeable production of B_s^{**} mesons will make an observation of B_s mixing harder at LEP, since it reduces the B_s production rate.

First experimental evidence for the beauty baryons $\Sigma_b^\pm$ and $\Sigma_b^{*\pm}$ is presented in an analysis of $\Lambda_b\pi$ Q-value distribution using an inclusive Λ_b reconstruction method, secondary vertex reconstruction and baryon enrichment techniques. The observed structure in the Q-value distribution can consistently be described by the production of $\Sigma_b^\pm$ and $\Sigma_b^{*\pm}$ baryons leading to the following mass difference measurements:

$$\boxed{\begin{array}{rcl} m(\Sigma_b^\pm) - m(\Lambda_b) & = & 173 \pm 3\,(\text{stat.}) \pm 14\,(\text{syst.})\ \text{MeV/c}^2 \\ m(\Sigma_b^{*\pm}) - m(\Lambda_b) & = & 229 \pm 3\,(\text{stat.}) \pm 8\,(\text{syst.})\ \text{MeV/c}^2\ . \end{array}} \tag{6.7}$$

The widths of both peaks are compatible with detector resolution leading to $\Gamma(\Sigma_b^\pm) < 32$ MeV/c^2 and $\Gamma(\Sigma_b^{*\pm}) < 39$ MeV/c^2 (at 95% c.l.). The total production rate of Σ_b and Σ_b^* baryons per b-jet and the relative fraction of each state are measured to be

$$\boxed{\begin{array}{rcl} (\sigma_{\Sigma_b} + \sigma_{\Sigma_b^*})/\sigma_b & = & 0.048 \pm 0.006\,(\text{stat.}) \pm 0.015\,(\text{syst.}) \\ \sigma_{\Sigma_b}/(\sigma_{\Sigma_b} + \sigma_{\Sigma_b^*}) & = & 0.24 \pm 0.06\,(\text{stat.}) \pm 0.10\,(\text{syst.})\ . \end{array}} \tag{6.8}$$

The $\pm 3/2$ helicity states of the Σ_b^* baryon seem to be suppressed. The sizeable production rate and the suppression of the $\pm 3/2$ helicity states could account for the small measured Λ_b polarisation. The results are in general agreement with predictions. Additional analyses are needed by the LEP experiments in order to confirm these results.

References

[1] DELPHI Collaboration, Phys. Lett. **B 345** (1995) 598

[2] OPAL Collaboration, Z. Phys. **C 66** (1995) 19

[3] S.L. Glashow, Nucl. Phys. **22** (1967) 579;
S. Weinberg, Phys. Rev. Lett. **19** (1967) 1264;
A. Salam, Proc. 8th Nobel Symposium, Aspenäsgarden 1968, ed. N. Svartholm (Almquist & Wiksell, Stockholm, 1968)

[4] J. Schwinger, Phys. Rev. Lett. **12** (1964) 237;
J. Schwinger, Phys. Rev. **B 135** (1964) 816;
R.P. Feynman, Phys. Rev. Lett. **23** (1969) 1415

[5] UA1 Collaboration, Phys. Lett. **B 126** (1983) 398;
UA2 Collaboration, Phys. Lett. **B 129** (1983) 130

[6] CDF Collaboration, Phys. Rev. Lett. **74** (1995) 2626;
D0 Collaboration, Phys. Rev. Lett. **74** (1995) 2632

[7] CFS Collaboration, Phys. Rev. Lett. **39** (1977) 252

[8] DELPHI Collaboration, M. Feindt, C. Kreuter, O. Podobrin, *Observation of Orbitally Excited B and B_s Mesons*, DELPHI-Note 95-105 PHYS 540, Brussels EPS95, Ref. eps0563, 1995

[9] DELPHI Collaboration, M. Feindt, C. Kreuter, O. Podobrin, *First Evidence for Σ_b and Σ_b^* Baryons*, DELPHI-Note 95-107 PHYS 542, Brussels EPS95, Ref. eps0565, 1995

[10] M. Feindt, *B quark fragmentation*, CERN-PPE/95-76 (1995);
M. Feindt, *Heavy Quark Spectroscopy at LEP*, CERN-PPE/95-139 (1995);
O. Podobrin, Nucl. Phys. **B 39** (1995) 373;
G. Sciolla, *Observation of excited B hadrons in DELPHI*, DELPHI-Note 95-144 PHYS 569 (1995)

[11] M. Gell-Mann, Y. Ne'emen, *The Eightfold Way*, W.A. Benjamin Inc., New York 11 (1964)

[12] The American Physical Society, Physics Review **D**, Particles and Fields, Part I, Review of Particle Properties, Volume 50, 3rd series, Number 3 (1994)

[13] N. Isgur, M.B. Wise, Phys. Lett. **B 232** (1989) 113;
M.B. Wise, Procs. XVI International Symposium on Lepton and Photon Interactions, Ithaca, New York, 1993, Ed. P. Drell, D. Rubin, page 253

[14] Sheldon Stone, *B Decays*, World Scientific, 1992, page 158

[15] W. Lucha, F. F. Schöberl, *Die Starke Wechselwirkung*, BI-Wiss.-verl., Mannheim Wien Zürich, 1989

[16] E. Eichten, K. Gottfried, T. Kinoshita, J. Koghut, K. D. Lane, T.-M. Yan, Phys. Rev. Lett. **34** (1975) 369;
E. Eichten, K. Gottfried, T. Kinoshita, K. D. Lane, T.-M. Yan, Phys. Rev. **D 17** (1978) 3090; **D 21** (1980) 313 (E);
E. Eichten, K. Gottfried, T. Kinoshita, K. D. Lane, T.-M. Yan, Phys. Rev. **D 21** (1980) 203

[17] C. Quigg, J. L. Rosner, Phys. Lett. **B 71** (1977) 153

[18] A. Martin, Phys. Lett. **B 93** (1980) 338;
A. Martin, Phys. Lett. **B 100** (1981) 511

[19] W. Buchmüller, G. Grunberg, S.-H. H. Tye, Phys. Rev. Lett. **45** (1980) 103

[20] T. Hebbeker, *Tests of Quantum Chromodynamics in Hadronic Decays of Z^0-Bosons Produced in e^+e^- Annihilation*, Phys. Rep. **217** (1979) 69

[21] K. Fabricius, G. Kramer, G. Schierholz I. Schmitt, Z. Phys. **C 11** (1981) 315;
F. Gutbrodt, G. Kramer, G. Schierholz, Z. Phys. **C 21** (1984) 235;
R.K. Ellis, D.A. Ross, E.A. Terrano, Phys. Rev. Lett. **45** (1980) 1225;
R.K. Ellis, D.A. Ross, E.A. Terrano, Nucl. Phys. **B 178** (1981) 421

[22] T. Sjöstrand, Comp. Phys. Comm. **39** (1986) 347;
T. Sjöstrand, M. Bengtsson, Comp. Phys. Comm. **43** (1987) 367;
T. Sjöstrand, Comp. Phys. Comm. **82** (1994) 74

[23] J.E. Campagne, R. Zitoun, Z. Phys. **C 43** (1989) 469

[24] G. Altarelli, G. Parisi, Nucl. Phys. **B 126** (1977) 298

[25] A. Krzywicki, B. Peterson, Phys. Rev. **D 6** (1972) 924;
J. Finkenstein, R.D. Peccei, Phys. Rev. **D 6** (1972) 2606;
F. Niedermeyer, Nucl. Phys. **B 79** (1974) 355;
A. Casher, J. Koghut, L. Susskind, Phys. Rev. **D 10** (1974) 732

[26] Jade Collaboration, W. Bartel *et al.*, Phys. Lett. **B 101** (1981) 129

[27] B. Anderson, G. Gustavson, G. Ingelman, T. Sjöstrand, Phys. Rep. **97** (1983) 31

[28] X. Artru, G. Mennessier, Nucl. Phys. **B 70** (1974) 93;
G.C. Fox, S. Wolfram, Nucl. Phys. **B 168** (1980) 285;
R. Field, S. Wolfram, Nucl. Phys. **B 213** (1983) 65

[29] G. Marchesini *et al.*, Comp. Phys. Comm. **67** (1992) 465

[30] L3 Collaboration, Phys. Lett. **B 345** (1995) 589

[31] DELPHI Collaboration, Z. Phys. **C 68** (1995) 353

[32] ALEPH Collaboration, *Production of Excited Beauty States in Z Decays*, CERN-PPE/95-108 (1995)

[33] L3 Collaboration, unnumbered contribution to the EPS conference, Brussels EPS95, 1995

[34] W. de Boer, H. Fürstenau, *Comparison of DELPHI data with QCD models*, DELPHI-Note 91-75 PHYS 129;
K. Hamacher, M. Weierstall, *The Next Round of Hadronic Generator Tuning Heavily Based on Identified Particle Data*, DELPHI-Note 95-80 PHYS 515

[35] R. Forty, *CP violation and B-$\bar{B}$ mixing*, CERN-PPE/94-154 (1994)

[36] CLEO Collaboration, *Observation of $D_1(2430)^+$ and $D_2^*(2470)^+$*, Glasgow ICHEP94, Ref. gls0386, 1994

[37] CLEO Collaboration, Phys. Rev. **D 41** (1990) 774;
CLEO Collaboration, Phys. Lett. **B 331** (1994) 236

[38] CLEO Collaboration, Phys. Lett. **B 303** (1993) 377

[39] CLEO Collaboration, Phys. Rev. Lett. **72** (1994) 1972

[40] E.J. Eichten, C.T. Hill, C. Quigg, Phys. Rev. Lett. **71** (1993) 4116

[41] E.J. Eichten, C.T. Hill, C. Quigg, *Orbitally Excited Heavy-Light Mesons Revisited*, Fermilab-Conf-94/118-T (1993) 4116

[42] DELPHI Collaboration, *Study of Charm Meson Production in Z^0 Decays and Measurement of Γ_c/Γ_h*, DELPHI-Note 95-101 PHYS 536, Brussels EPS95, Ref. eps0557, 1995

[43] ALEPH Collaboration, *D^{**} Production in Z^0 Decays*, Glasgow ICHEP94, Ref. gls0577, 1994

[44] OPAL Collaboration, *A Study of Charm Meson Production in Semileptonic B Decays*, CERN-PPE/95-02 (1995)

[45] ARGUS Collaboration, Phys. Lett. **B 221** (1989) 422

[46] ARGUS Collaboration, Phys. Lett. **B 232** (1989) 398

[47] ARGUS Collaboration, Z. Phys. **C 57** (1993) 533

[48] DELPHI Collaboration, *Determination of $|V_{cb}|$ from the semileptonic decay $B \to D^{*-} l^+ \nu$*, Brussels EPS95, Ref. eps0569, 1995

[49] CLEO Collaboration, Phys. Rev. **D 43** (1991) 651

[50] A.F. Falk, T. Mehen, *Excited Heavy Mesons Beyond Leading Order in the Heavy Quark Expansion*, JHU-TIPAC-950008, HEP-PH/9507311

[51] J.L. Rosner, Comm. Nucl. Part. Phys. **16** (1986) 109

[52] W. A. Bardeen, C. T. Hill, Fermilab-Pub-93/59-T, unpublished

[53] M. Gronau, A. Nippe, J.L Rosner, Phys. Rev. **D 47** (1993) 1988

[54] M. Gronau, Phys. Rev. Lett. **63** (1989) 1451;
M. Gronau, Phys. Lett. **B 300** (1993) 163

[55] J.G. Körner, M. Krämer, D. Pirjol, *Heavy Baryons*, DESY 94-095, 1994

[56] S. Plaszczynski, LAL-94-17, May 1994

[57] ALEPH Collaboration, Λ_b *exclusive decay*, Brussels EPS95, Ref. eps0401, 1995

[58] DELPHI Collaboration, *Search for exclusive hadronic decays of the* Λ_b *baryon with the DELPHI detector at LEP*, Brussels EPS95, Ref. eps0561, 1995

[59] ALEPH Collaboration, *Measurements of the b Baryon Lifetime*, CERN-PPE/95-65 (1995)

[60] DELPHI Collaboration, *Beauty-baryons production properties and lifetimes*, Brussels EPS95, Ref. eps0564, 1995

[61] OPAL Collaboration, *A Measurement of the* Λ_b^0 *Lifetime*, CERN-PPE/95-51 (1995)

[62] ALEPH Collaboration, *Measurement of the* Λ_b *polarisation in* Z^0 *decays*, Brussels EPS95, Ref. eps0400, 1995

[63] DELPHI Collaboration, *Lifetime and production rate of beauty baryons from Z decays*, CERN-PPE/95-54 (1995)

[64] OPAL Collaboration, *Measurement of the Average b-Baryon Lifetime and Product Branching Ratio* $f(b \to \Lambda_b) \cdot BR(\Lambda_b \to \Lambda l^- \bar{\nu} X)$, CERN-PPE/95-90 (1995)

[65] DELPHI Collaboration, *Production of strange B-baryons decaying into* $\Xi^\pm - l^\mp$ *pairs at LEP*, CERN-PPE/95-29 (1995)

[66] ALEPH Collaboration, *Evidence for strange b baryon production in Z decays*, Brussels EPS95, Ref. eps0406, 1995

[67] OPAL Collaboration, *Search for Strange b-flavoured Baryons Using* Ξ^- *Lepton Correlations*, Brussels EPS95, Ref. eps0272, 1995

[68] R. Roncaglia *et al.*, Phys. Rev **D 51** (1995) 1248

[69] A. Martin, Phys. Lett. **B 103** (1981) 51

[70] T.-M. Yan *et al.*, Phys. Rev. **D 46** (1992) 1148

[71] A.F. Falk, M.E. Peskin, Phys. Rev. **D 49** (1994) 3320

[72] V. Hatten *et al.*, LEP Performance Note 12 (1990);
R. Baily *et al.*, CERN-SL/90-95 (1990)

[73] World Wide Web, CERN accelerator division (SL), LEP statistics

[74] L. Arnaudon *et al.*, CERN-PPE/92-125 (1992);
Notes of the 16th Meeting of the Working Group on LEP Energy from 15 April 1992 at CERN, unpublished

[75] DELPHI Collaboration, *DELPHI Technical Proposal*, CERN-LEPC/83-3 (1983);
DELPHI Collaboration, *The DELPHI detector at LEP*, Nucl. Instr. Meth. **A 303** (1991) 233

[76] DELPHI Collaboration, *Proposal for the DELPHI Surround Muon Chambers* DELPHI-Note 92-139 TRACK 71 (1992);
DELPHI Collaboration, *Proposal for the Replacement of the Small Angle Calorimeter of DELPHI*, CERN-LEPC/92-6 (1992);
S.J. Alvsvaag *et al.*, *The DELPHI Small Angle Tile Calorimeter*, DELPHI-Note 94-157 CAL 120 (1994)

[77] N. Bingefors *et al.*, Nucl. Instr. Meth. **A 328** (1993) 447;
V. Chabaud *et al.*, *The DELPHI Silicon Strip Microvertex Detector with Double Sided Readout*, CERN-PPE/95-86 (1995)

[78] DELPHI Collaboration, *Performance of the DELPHI Detector*, DELPHI-Note 95-112 PHYS 547, Brussels EPS95, Ref. eps0764, 1995

[79] C. Kreuter, *Longitudinal Shower Development in the DELPHI Electromagnetic Calorimeter HPC*, Diploma Thesis, IEKP-KA/93-9

[80] G. Van Apeldoorn *et al.*, *Performance of the Barrel Ring Imaging Cherenkov Counter of DELPHI*, DELPHI-Note 94-18 RICH 61 (1994)

[81] DELPHI Collaboration, *The Design and Operation of the Slow Controls for the DELPHI Experiment at LEP*, DELPHI-Note 94-14 DAS-151 (1994)

[82] J.A. Valls *et al.*, *Architecture and Performance of the DELPHI Trigger System*, DELPHI-Note 92-162 DAS 135 (1992)

[83] B. Bouquet, P. Gavillet, J.-P. Laugier, *The fourth level Trigger of DELPHI*, DELPHI-Note 93-29 DAS 141 (1993)

[84] B. Franek *et al.*, *Architecture of the DELPHI on-line Data Acquision Control System*, DELPHI-Note 92-104 DAS 130 (1992)

[85] DELPHI Collaboration, *DELPHI Data Analysis Program (DELANA) User's Guide*, DELPHI-Note 89-44 PROG 137 (1989)

[86] Y. Sacquin, *Description of the DELPHI DST Content*, Version 3.15, DELPHI-Note 94-161 PROG 210 (1994)

[87] DELPHI Collaboration, *DELSIM – DELPHI Event Generation and Detector Simulation*, DELPHI-Note 89-15 PROG 130 (1989)

[88] F.A. Behrends, W. Hollik, R. Kleiss, Nucl. Phys. **B 304** (1988) 712

[89] S. Jadach *et al.*, Comp. Phys. Comm. **79** (1994) 503

[90] R. Brun *et al.*, CERN report DD/EE/84-1 (1986)

[91] W.R. Nelson *et al.*, *EGS4 User Manual*, SLAC-265 (1985)

[92] K. Brand, M. Feindt, C. Kreuter, O. Podobrin, *ELEPHANT Users Manual*, DELPHI-Note in preparation

[93] DELPHI Collaboration, Z. Phys. **C 54** (1992) 55

[94] S. Brandt, C. Peyrou, R. Sosnowski, A. Wroblewski, Phys. Lett. **12** (1964) 57;
E. Fahri, Phys. Rev. Lett. **39** (1977) 1587

[95] Torbjörn Sjöstrand, *Pythia 5.6 and Jetset 7.3*, CERN-TH 6488/92

[96] G. Borisov, *Lifetime Tag of events* $Z^0 \to b\bar{b}$ *with the DELPHI detector*, DELPHI-Note 94-125 PROG 208 (1994)

[97] ALEPH Collaboration, Phys. Lett. **B 313** (1993) 535;

[98] O. Podobrin, *An algorithm for inclusive B hadron reconstruction*, DELPHI-Note, in preparation

[99] DELPHI Collaboration, M. Feindt, O. Podobrin, *Inclusive measurement of the B fragmentation function*, DELPHI-Note 95-103 PHYS 538, Brussels EPS95, Ref. eps0560, 1995

[100] C. Bourdarius *et al.*, *User guide of the HADIDENT/RICH software*, 8 August 1995, unpublished; C. Bourdarius *et al.*, *A few plots about the barrel RICH performance*, 23 July 1995, unpublished

[101] DELPHI Collaboration, Phys. Lett. **B 334** (1994) 435

[102] J. Bartelt, *Recent Results in Charmed Meson Spectroscopy from CLEO*, Transparencies precented at the Hadron Conference, Manchester, July 1995

[103] V. Blobel, *Unfolding in High Energy Physics*, Procs. CERN School of Computing, Aiguablava (Spain), CERN, Geneva, 1985

[104] ALEPH Collaboration, *Resonant Structure and Flavor-tagging in the* $B\pi^{\pm}$ *System Using Fully Reconstructed B Decays*, Brussels EPS95, Ref. 0403, 1995

[105] Chi-Keung Chow, *Radiative Decays of Excited* Λ_Q *Baryons in the Bound State Picture*, CLNS-95/1367, 1995

[106] ARGUS Collaboration, Phys. Lett. **B 317** (1993) 227;
CLEO Collaboration, *Observation of excited charmed baryon states decaying to* $\Lambda_c^+\pi^+\pi^-$, CLNS 94/1304, 1994

[107] T. Mannel, G. A. Schuler, Phys. Lett. **B 279** (1992) 194

[108] F.E. Close *et al.*, J. Phys. **G 18** (1992) 1716

Members of the DELPHI Collaboration

AUSTRIA - VIENNA

W.Adam, W.Bartl, R.Fruhwirth, J.Hrubec, M.Krammer, G.Leder, D.Liko, J.MacNaughton, W.A.Mitaroff, N.Neumeister, H.Pernegger, M.Pernicka, M.Regler, J.Strauss

BELGIUM - BRUSSELS

D.Bertrand, C.Bricman, F.Cao, H.De Boeck, S.De Brabandere, C.De Clercq, P.Herquet, K.Huet, V.Lefebure, J.Lemonne, A.Tomaradze, C.Vander Velde, W.K.Van Doninck, F.Verbeure, J.H.Wickens

BRAZIL - RIO DE JANEIRO

M.Begalli, M.Gandelman, L.M.Mundim, M.E.Pol, R.C.Shellard, D.Souza-Santos

UFRJ

S.Amato, P.Carrilho, L.De Paula, B.Marechal

CZECH REPUBLIC - PRAHA

M.Lokajicek, S.Nemecek, J.Rames, J.Ridky, V.Vrba

NC

R.Leitner

CIS - JINR - DUBNA

G.D.Alekseev, D.Y.Bardin, M.S.Bilenky, G.A.Chelkov, B.A.Khomenko, N.N.Khovanski, Z.Krumstein, V.Malychev, A.G.Olshevski, V.Pozdniakov, N.Pukhaeva, A.Sadovsky, Y.Sedykh, A.N.Sisakian, O.Smirnova, L.G.Tkatchev, I.A.Tyapkin, L.S.Vertogradov, A.S.Vodopyanov, N.I.Zimin

SERPUKHOV

I.Ajinenko, G.Borisov, P.Chliapnikov, L.Gerdyukov, Yu.Gouz, V.Kostioukhine, V.Lapin, V.Obraztsov, V.Ronjin, N.Smirnov, O.Tchikilev, V.Uvarov, E.Vlasov, O.Yushchenko, A.Zaitsev

DENMARK - NBI

E.Dahl-Jensen, G.Damgaard, N.J.Kjaer, R.Moeller, B.S.Nielsen

FINLAND - HELSINKI

M.Battaglia, R.A.Brenner, S.Czellar, R.Keranen, K.Kurvinen, R.Lauhakangas, R.Orava, K.Osterberg, H.Saarikko

FRANCE - CDF

P.Beilliere, J-M.Brunet, C.Defoix, J.Dolbeau, Y.Dufour, P.Frenkiel, G.Tristram

GRENOBLE

M.L.Andrieux, R.Barate, F.Dupont, F.Ledroit, F.Naraghi, L.Roos, G.Sajot

LPNHE - PARIS

M.Baubillier, P.Billoir, L.Brillault, J.Chauveau, W.Da Silva, C.De La Vaissiere, N.Ershaidat, F.Kapusta, S.Lamblot, J.P.Tavernet

LYON

P.Antilogus, L.Chaussard, I.Laktineh, L.Mirabito, G.Smadja, P.Vincent, F.Zach

MARSEILLE

P.Delpierre, A.Tilquin

LAL - ORSAY

J-E.Augustin, P.Bambade, B.Bouquet, J.L.Contreras, G.Cosme, B.Dalmagne, F.Fulda-Quenzer, G.Grosdidier, B.Jean-Marie, V.Lepeltier, A.Lipniacka, P.Paganini, S.Plaszczynski, P.Rebecchi, F.Richard, P.Roudeau, A.Stocchi, A.Trombini, G.Wormser

SACLAY

R.Aleksan, Y.Arnoud, J.Baudot, T.Bolognese, C.De Saint-Jean, P.Jarry, J-P.Laugier, Y.Lemoigne, P.Lutz, A.Ouraou, F.Pierre, I.Ripp, V.Ruhlmann-Kleider, Y.Sacquin, P.Siegrist, S.Simonetti, M-L.Turluer, D.Vilanova, M.Zito

CRN - STRASBOURG

D.Bloch, F.Djama, M.Dracos, J-P.Engel, D.Gele, J-P.Gerber, P.Juillot, V.Nikolaenko, P.Pages, R.Strub, T.Todorov, M.Winter

GERMANY - KARLSRUHE

W.-D.Apel, A.Daum, W.De Boer, R.Ehret, D.C.Fries, U.Haedinger, M.Hahn, M.Kaiser, C.Kreuter, G.Maehlum, H.Mueller, W.Oberschulte-Beckmann, O.Podobrin, H.Schneider, A.Seitz, M.Wielers

WUPPERTAL

K-H.Becks, M.Blume, J.Dahm, J.Drees, K.-A.Drees, M.Elsing, F.Hahn, S.Hahn, K.Hamacher, P.-H.Kramer, P.Langefeld, G.Lenzen, R.Lindner, T.Maron, W.Neumann, M.Reale, M.A.E.Schyns, H.Staeck, B.Ueberschaer, S.Ueberschaer, H.Wahlen, A.Wehr, M.Weierstall, D.Wicke

UNITED KINGDOM - LANCASTER

P.N.Ratoff

LIVERPOOL

P.P.Allport, P.S.L.Booth, T.J.V.Bowcock, L.Carroll, A.Galloni, M.Gibbs, M.Houlden, J.N.Jackson, B.King, I.Last, R.Mc Nulty, J.Richardson, S.Tzamarias

OXFORD

G.J.Barker, S.Blyth, S.Bosworth, N.Demaria, F.J.Harris, P.J.Holt, J.G.Loken, L.Lyons, G.Myatt, A.Normand, C.Parkes, D.Radojicic, P.B.Renton, A.M.Segar, N.Vassilopoulos, G.R.Wilkinson, W.S.C.Williams, K.Yip, R.Zuberi

RUTHERFORD

T.Adye, M.J.Bates, D.Crennell, P.D.Dauncey, B.Franek, G.Gopal, J.Guy, G.Kalmus, W.J.Murray, H.T.Phillips, R.Sekulin, G.R.Smith, M.Tyndel, W.Venus

GREECE - ATHENS

P.Ioannou, S.Katsanevas, C.Kourkoumelis, R.Nicolaidou, L.K.Resvanis

NTU-ATHENS

M.Dris, D.Fassouliotis, T.A.Filippas, E.Fokitis, E.N.Gazis, E.C.Katsoufis, Th.D.Papadopoulou, H.Rahmani

DEMOKRITOS

E.Karvelas, P.Kokkinias, D.Loukas, A.Markou, E.Zevgolatakos

ITALY - BOLOGNA

A.C.Benvenuti, F.R.Cavallo, F.L.Navarria, A.Perrotta, T.Rovelli, G.Valenti

GENOVA

M.Bozzo, M.Canepa, C.Caso, R.Contri, G.Crosetti, F.Fontanelli, V.Gracco, O.Kouznetsov, M.R.Monge, P.Morettini, F.Parodi, A.Petrolini, G.Piana, I.Roncagliolo, M.Sannino, S.Squarcia

MILANO

A.Andreazza, M.Bonesini, W.Bonivento, M.Caccia, M.Calvi, A.De Min, C.Matteuzzi, C.Meroni, P.Negri, M.Paganoni, A.Pullia, S.Ragazzi, N.G.Redaelli, T.Tabarelli, C.Troncon, G.Vegni

PADOVA

K.D.Brand, P.Checchia, U.Gasparini, T.Lesiak, I.Lippi, M.Margoni, M.Mazzucato, M.Michelotto, A.Nomerotski, M.Pegoraro, P.Ronchese, F.Simonetto, I.Stavitski, L.Ventura, M.Verlato

ROMA2

V.Bocci, V.Canale, L.Cerrito, L.Di Ciaccio, G.Matthiae, P.Privitera

SANITA

A.Baroncelli, C.Bosio, P.Branchini, E.Graziani, C.Mariotti, A.Passeri, E.Spiriti, C.Stanescu, L.Tortora

TORINO

F.Bianchi, M.Bigi, R.Chierici, D.Gamba, E.Migliore, G.Rinaudo, A.Romero, G.Sciolla

TRIESTE/UDINE

F.Cossutti, G.Della Ricca, B.De Lotto, L.Lanceri, C.Petridou, P.Poropat, M.Prest, F.Scuri, L.Vitale, F.Waldner

NETHERLANDS - NIKHEF

E.Agasi, A.Augustinus, W.Hao, D.Holthuizen, P.Kluit, B.Koene, M.Nieuwenhuizen, W.Ruckstuhl, I.Siccama, J.Timmermans, D.Z.Toet, G.W.Van Apeldoorn, P.Van Dam, J.Van Eldik

NORWAY - BERGEN

S.J.Alvsvaag, G.Eigen, A.G.Frodesen, A.Klovning, B.Stugu

OSLO

L.Bugge, T.Buran, M.Dam, A.L.Read, T.B.Skaali, S.Stapnes

POLAND - KRAKOW

P.Bruckman, Z.Hajduk, P.Jalocha, K.Korcyl, W.Krupinski, W.Kucewicz, B.Muryn, H.Palka, G.Polok, A.Zalewska

WARSZAWA

K.Doroba, R.Gokieli, M.Gorski, J.Krolikowski, R.Sosnowski, K.Stepaniak, M.Szczekowski, M.Szeptycka, P.Zalewski

PORTUGAL - LIP

P.Abreu, F.Barao, M.Espirito Santo, R.Henriques, A.Maio, L.Peralta, M.Pimenta, T.Spassov, B.Tome

SLOVAKIA - BRATISLAVA

P.Chochula, R.Janik, P.Kubinec, B.Sitar

SLOVENIA - LJUBLJANA

V.Cindro, B.Erzen, B.Golob, D.Zavrtanik, D.Zontar

SPAIN - MADRID

J.A.Barrio, J.Sanchez

SANTANDER

M.Berggren, A.J.Camacho Rozas, J.Garcia, J.M.Lopez, M.A.Lopez Aguera, J.Marco, C.Martinez-Rivero, F.Matorras, A.Ruiz

VALENCIA

M.V.Castillo Gimenez, E.Cortina, A.Ferrer, J.Fuster, C.Garcia, J.J.Hernandez, E.Higon, C.Lacasta, F.Martinez-Vidal, S.Marti i Garcia, S.Navas, J.Salt

OVIEDO

J.Cuevas Maestro

SWEDEN - LUND

S.Almehed, O.Barring, E.Falk, V.Hedberg, G.Jarlskog, L.Jonsson, P.Jonsson, I.Kronkvist, B.Loerstad, U.Mjoernmark, G.Transtromer, C.Zacharatou

STOCKHOLM

B.Å, sman K.Cankocak, G.Ekspong, P.Gunnarsson, S-O.Holmgren, K.Hultqvist, R.Jacobsson, E.K.Johansson, M.Karlsson, T.Moa, P.Niss, C.Walck, G.C.Zucchelli

UPPSALA

O.Botner, T.Ekelof, M.Gunther, A.Hallgren, J.Medbo, K.Woschnagg

SWITZERLAND - CERN

U.Amaldi, P.Baillon, Yu.Belokopytov, C.Bourdarios, R.C.A.Brown, A.Buys, T.Camporesi, F.Carena, A.Cattai, V.Chabaud, Ph.Charpentier, V.Chorowicz, P.Collins, M.Davenport, A.De Angelis, H.Dijkstra, M.Donszelmann, M.Feindt, H.Foeth, F.Formenti, H.Furstenau, C.Gaspar, Ph.Gavillet, D.Gillespie, H.Herr, T.L.Hessing, H.J.Hilke, C.Joram, H.Klein, M.Koratzinos, A.Lopez-Fernandez, J-C.Marin, M.Mc Cubbin, K.Moenig, L.Pape, D.Reid, E.Rosso, F.Stichelbaut, D.Treille, W.Trischuk, A.Tsirou, O.Ullaland, E.Vallazza, P.Weilhammer, A.M.Wetherell, M.Witek

USA - AMES

H.B.Crawley, D.Edsall, A.Firestone, L.Gorn, T.S.Hill, J.W.Lamsa, D.W.Lane, C.K.Legan, R.Mc Kay, W.T.Meyer, E.I.Rosenberg

Acknowledgements

I would like to thank Prof. Dr. W. de Boer for his continuous support and providing me with the possibility to work in the DELPHI group at CERN. I am grateful to Prof. Dr. Th. Müller for accepting to be my *Korreferent*.

Many thanks go to Dr. M. Feindt for the exciting working topics, many valuable discussions and the good working atmosphere. It is also a pleasure to thank Dr. O. Podobrin for his close collaboration.

I am grateful to my colleagues in DELPHI, especially to D. Edsall, Dr. M. Feindt, Prof. Dr. A. Firestone, D. Lane, W. Oberschulte, Dr. O. Podobrin, A. Seitz, C. Weiser, and M. Wielers.

Furthermore, I would like to thank Prof. Dr. A. Firestone, D. Lane, Dr. O. Podobrin, and C. Weiser for carefully reading the manuscript.

I would especially like to thank my family and friends. Their support was essential for my studies and for the work on this thesis.